University of Sheffield

Thermomechanical Processing of Ferrite-Martensite Steels for Power Plant Applications

Ahmad Alsalman

Thesis Submitted for the Degree of Doctor of Philosophy

School of Chemical, Materials and Biological Engineering
The University of Sheffield
June 2025

Dedication

We descended the iron, in which there is severe might, and benefits for the people (Quran 57:25).

With ultimate faith that mankind has not been granted knowledge except a little, may this piece of work reveal unexposed knowledge regarding the thermomechanical processing of an iron alloy from which people may benefit.

While inquisitiveness to discover causes of matters is the motive behind this research, the dynamic generator driving this motivation is a conservative family that acknowledges morals, values, ethics, and education. Words are inadequate to transcribe the sincere pride of being a member of this family.

Declaration

This research was conducted under the supervision of Professor Eric J Palmiere within the School of Chemical, Materials and Biological Engineering, The University of Sheffield, whose expertise and feedback shaped its direction and quality, with support obtained from the Government of the State of Kuwait through the Kuwait Institute for Scientific Research (KISR), together with the Engineering and Physical Sciences Research Council (EPSRC)-funded Strategic University Steel Technology and Innovation Network (SUSTAIN) Future Manufacturing Research Hub, and with base steel provided by LIBERTY Steel UK, while the experimental work was enabled through the technical facilities and professional support available within The University of Sheffield.

Abstract

Steel, combining strength, high-temperature performance, and corrosion resistance when derived from suitable alloying design, remains among the most widely utilized materials in the energy sector, including oil and gas, nuclear power, and renewables. Ensuring reliable operation in aggressive environments requires a deeper understanding of its metallurgy and the behavior of advanced steel adaptations. Despite extensive studies on supermartensitic stainless steels, a limited quantitative understanding persists of how deformation temperature, strain amount, and alloying additions collectively govern the evolution of the austenitic microstructure, interfacial area per unit volume, and transformation behavior. This research aims to understand the role of the prior austenite microstructure in supermartensitic stainless steel on the final transformed microstructure. Particular emphasis is placed on the influence of controlled nickel and manganese additions on critical processing temperatures and transformation behavior. Specifically, this research aims to investigate the influence of austenite being deformed either above the recrystallization-limit temperature $T_{95\%}$ or below the recrystallization-stop temperature $T_{5\%}$, providing a comprehensive understanding of the influence of the difference in the microstructure on the difference in the interfacial area per unit volume S_v which will affect the transformation behavior and accordingly, the transformation product. Successful achievement of this research has been accomplished through carrying out plane strain compression (PSC) tests to address the identified purpose of this work. The principal findings demonstrated distinct compositional effects arising from variations in nickel and manganese content, with manganese increasing total S_v and strength across the studied conditions, while nickel contributed to higher ductility and a greater suppression of the martensitic transformation temperature. In addition, deformation below $T_{5\%}$ resulted in significantly higher total S_v values, more refined martensitic structures, and enhanced mechanical strength. Conversely, deformation above $T_{95\%}$ produced equiaxed austenitic grains with lower total S_v values, enhancing ductility and offering a controllable pathway for balancing strength and toughness via thermomechanical processing.

Table of Contents

List of Figures

List of Tables

Nomenclature

Acronyms

BA	Base alloy
BA ↗ Mn	Base alloy with higher manganese content
BA ↗ Ni	Base alloy with higher nickel content
bcc	Body-centered cubic
bct	Body-centered tetragonal
CCT	Continuous cooling transformation
EBSD	Electron Backscatter Diffraction
EDS	Energy Dispersive Spectroscopy
fcc	Face-centered cubic
FTTU	Fast thermal treatment unit
HAGB	High-angle grain boundaries
IPF	Inverse pole figure
KAM	Kernel Average Misorientation
LTD	Long transverse direction
OECD	Organisation for Economic Co-operation and Development
OES	Optical emission spectroscopy
PAG	Prior Austenite Grains
PSC	Plane strain compression
SE	Secondary electron
SUSTAIN	Strategic University Steel Technology and Innovation Network
SEM	Scanning electron microscopy
STD	Short transverse direction
TMP	Thermomechanical processing
TMTS	Thermomechanical treatment simulator
UN	United Nations
UNS	Unified numbering system
VIM	Vacuum induction melting

Parameters

α	Ferrite
γ	Austenite
ε	Strain
σ_y	Yield stress
σ_0	Friction stress
$\sigma_{0.2}$	Yield strength
σ_t	Tensile Strength
A_0	Original cross-sectional area before fracture
A_f	Smallest cross-sectional area after fracture
A_{c1}	Ferrite to austenite start transformation temperature
A_{c3}	Ferrite to austenite finish transformation temperature
A_{cm}	Austenite to cementite start transformation temperature
A_{e1}	Equilibrium temperature for the lower austenite/ferrite boundary
A_{e3}	Equilibrium temperature for the upper austenite/ferrite boundary
A_{r1}	Austenite to ferrite finish transformation temperature
A_{r3}	Austenite to ferrite start transformation temperature
d	Average grain size
D_γ	Average recrystallized austenite grain size
$D_{\gamma'}$	Initial grain size of austenite
$\Delta l/l_o$	Fractional change in length
k_y	Material-dependent constant
M_s	Martensitic start transformation temperature
R	Ratio of rolling reduction in thickness
R^2	Coefficient of determination
RA	Reduction of area
S_v	Interfacial area per unit volume
S_v^{GB}	Grain boundary contribution
S_v^{IPD}	Intragranular planar defect contribution
T	Temperature
$T_{95\%}$	Recrystallization-limit temperature
$T_{5\%}$	Recrystallization-stop temperature

Abbreviations

e.g. (*exempli gratia*)	for example
et al. (*et alia*)	and others
etc. (*et cetera*)	and so on
i.e. (*id est*)	that is
avg.	Average
std dev	Standard deviation

Units

%	Percent
°C	Celsius
µm	Micrometer
g	Gram
h	Hour
kW	Kilowatt
mbar	Millibar
min	Minute
mL	Milliliter
mm	Millimeter
MPa	Megapascal
N	Newton
rpm	Revolutions per minute
s	Second

Chapter 1 Introduction

1.1 Insights on the Energy Industry

Energy industries have been relying on conventional sources to generate power from fossil fuels, whereas coal, oil, and gas have been considered to be the primary energy sources for decades despite their financial cost and environmental impact. Some unconventional sources have been unleashed in recent years enabling the world not to be dependent on a sole source of energy and broadening it to include nuclear power and renewable energy as promising alternative sources to address the continuous concerns regarding the increasing prices and security of supply during global conflicts and pandemics.

Oil prices, for instance, experienced throughout the past fifty years a variability of price ranges more than once in direct connection with invasions, revolutions, and other sorts of crisis; BP plc reported hyperinflation in the price of all energy sources with the lion's share of the increase observed for natural gas prices which increased by more than 400% in 2021 along with an increase of about 150% and 70% in coal and oil prices, respectively[1].

McKinsey & Company expected that depending on three energy transition scenarios, global fossil fuels will make up between 39% to 61% of global energy demand by 2050 when the compass gravitates towards nuclear and renewable energy, in accordance with the current analytics projecting that coal demand will continue to decrease after reaching its peak in 2013 while oil and gas demands will continue to plateau until 2030 firmly highlighting that a delayed decrease in demand is expected if the key goals of Paris Agreement are failed to be realistically achieved; represented by continued momentum and slow evolution scenarios as opposed to the sustainable transformation (Figure 1.1)[2].

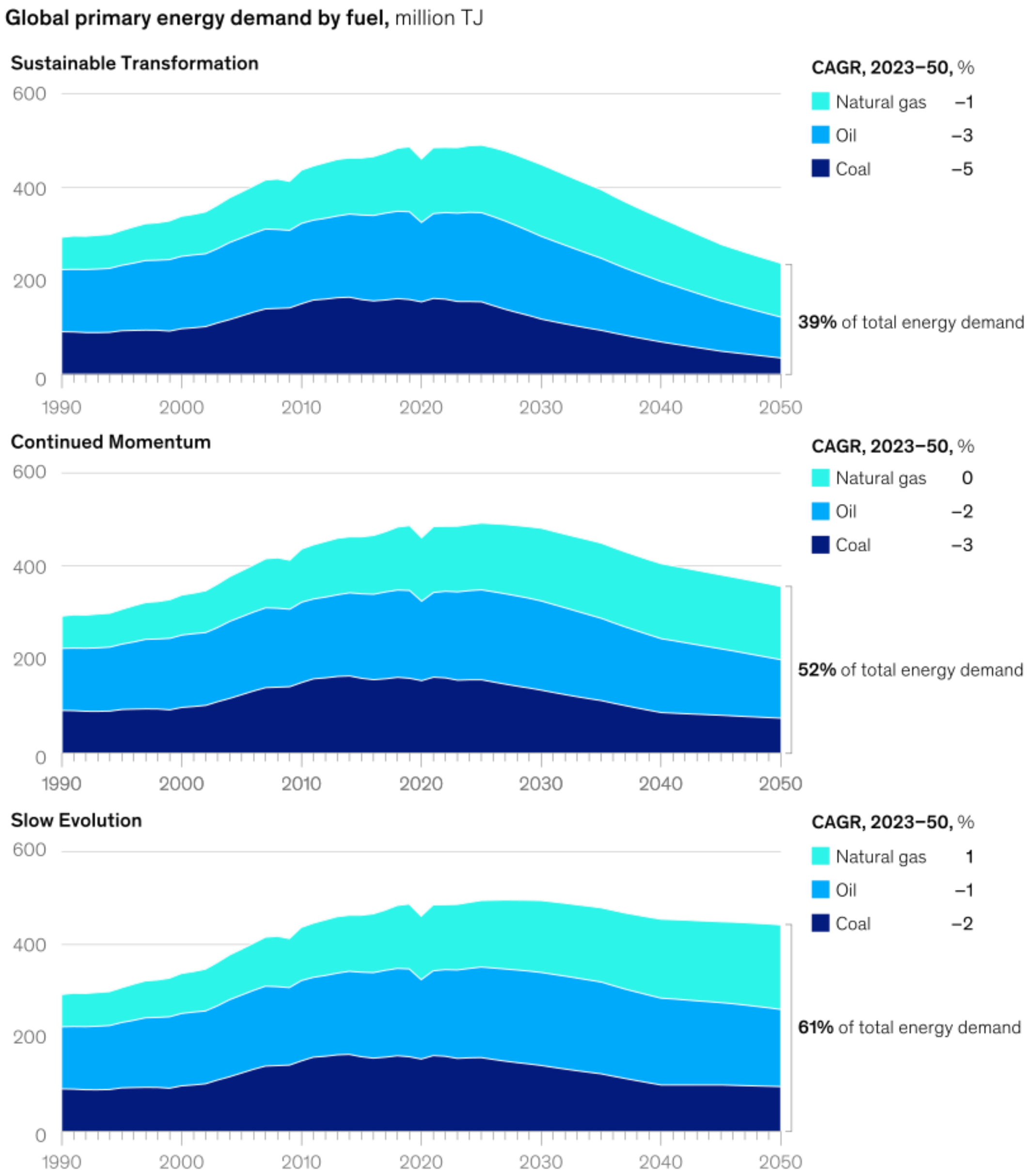

Figure 1.1 Historical and projected global fossil fuel demand revealing a dramatic decline by 2050 depending on power generation alternatives and successful global commitment to sustainability (above), a gradual decline anticipating a precarious deployment of low-carbon technologies by 2050 (middle), and a consistent demand as a result of reduced investments into low-carbon technologies(reproduced)[2].

According to the Organisation for Economic Co-operation and Development (OECD), a large proportion of coal power plants existing in many countries all over the world, as presented in Figure 1.2, should be under an obligation to shut down to meet the commitments outlined in the Paris Agreement which has been adopted by the vast majority of the parties of the United Nations (UN); highlighting that unabated coal generation should be globally reduced to minimal levels by 2030 and phased out within the following few years[3,4].

The UK, for instance in the case, has reached an advanced stage towards the full implementation of its policy to phase out unabated coal generation by October 2025; considering that the number of power stations has been significantly reduced over the past decade and only one coal-fired station was in operation until September 2024, when it was finally shut down after decades of service, turning the page of coal age in the UK and advancing further towards decarbonization of the power sector, corresponding to international efforts[5–9].

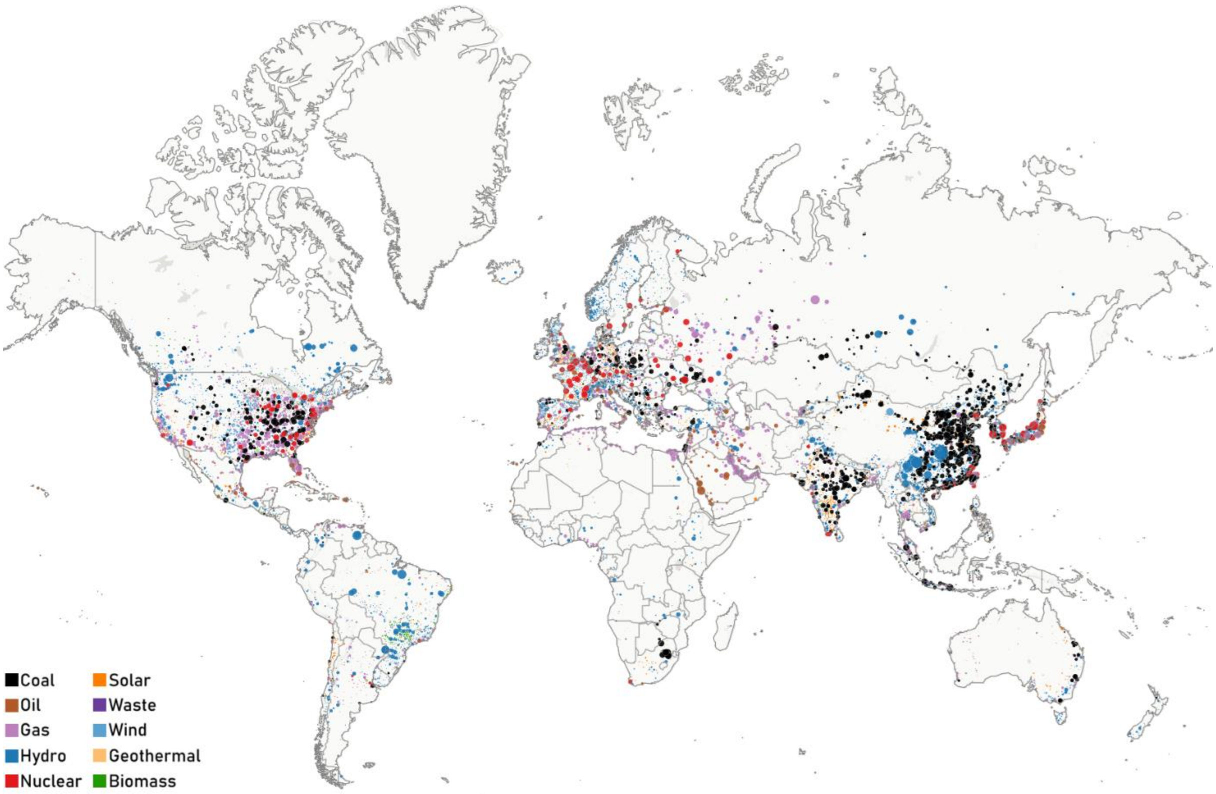

Figure 1.2 Global power plants by capacity and fuel type turning the spotlight on tens of thousands of different energy sources spread worldwide; where some are hypothesized to grow in the future while others are presumed to diminish (adapted)[10].

1.2 Insights on the Steel Industry

Steel production in its first solid form that is often processed further to be employed in various product applications is in continual growth in response to high global demand[11]. Although sophisticated steels are less common when compared to traditional steels, the era of lower-performance steel grades is expected to decline in the years to come as global quality requirements continue to rise.

Steel is recognized to be one of the most widely utilized materials in energy industries including oil and gas industries, nuclear power industries, and renewable energy industries. Managing the integrity of energy applications is a complex activity and careful attention shall be paid to the materials used in the construction of equipment utilized to avoid failures that sometimes culminate in unexpected incidents[12].

The combination of mechanical properties which can be tailored for various product applications through combinations of alloy chemistry and thermomechanical processing of steels, at a relatively lower cost than other engineering materials, have unanimously played a vital role in the deployment of numerous improved steel variations within diverse challenging environments within energy industries.

Nevertheless, there are challenging operational factors that restrict the use of steel and its newly developed adaptations, in particular their operation in critical aggressive environments (i.e. high-temperature environments, corrosive environments, and high irradiation conditions).

1.3 Turning Challenges into Opportunities

Stainless steel is a ferrous alloy composed primarily of iron with at least 10.5% chromium and it was first ever developed commercially in 1913 when Harry Brearley cast martensitic steel with a composition of 12.86% chromium and 0.24% carbon in Sheffield, England[13]. From that point forward, various grades of stainless steel were developed which all fall under one of the five stainless steel categories: austenitic, ferritic, martensitic, duplex, and precipitation-hardening[14,15]. The first four families are characterized according to their crystalline structure, while the precipitation hardening stainless steel corresponds to a special strengthening mechanism in the austenitic or martensitic structures[13,16].

Identification of limitations restricting the use of stainless steel opens the door widely for researchers to break a specific challenge down and concentrate on delivering an attainment solution that forms an addition to knowledge via the establishment of a systematic study leading to a tangible advancement in the field of materials science; with regards to this matter, supermartensitic stainless steels have the tendency to fall within the category of trending materials worth to be evaluated.

Supermartensitic stainless steels are improved low-carbon martensitic stainless steels developed in the last quarter of the 20th century and introduced enhanced mechanical and corrosion resistance properties[17–20]. In contrast to other expensive stainless steels employed in various applications to secure a stable operation of equipment, supermartensitic stainless steels are cost-effective alloys giving rise to substituting some of the more expensive alloys within the family of steels leading to added profitability and increased productivity of industrial operations[17,18,21–29].

Notwithstanding the fact that supermartensitic stainless steels are already in operation to some measures, future applications in sensitive environments depend on further understanding of their principal parameters which have not been studied yet. An advanced level of knowledge will facilitate placing these steels in service and finding their path into power plant applications as they demand operating at high temperatures.

Hence, it is necessary to design the microstructure in a conservative manner, i.e. tailoring the microstructure through balancing alloying elements, outlining the limits of the properties of the alloy, ensuring overall stability of the material under the demanded operation conditions, and avoiding groundless modifications leading to degradation on the short-term or long-term, aiming towards achieving outstanding properties.

Supermartensitic stainless steels are modified iron-based alloys containing chromium, nickel, molybdenum, manganese, and other alloying elements in particularly defined presence in specific percentage within the metallurgy of these steels on the one hand,

and reduced amount of carbon content on the other hand. The chemical composition is a significant aspect that has a partial impact on the microstructure and consequently a partial responsibility in determining the strength and toughness properties; hence, an outstanding metallurgical effort is required to enhance these properties by least possible alloy additions.

Thermomechanical processing (TMP) is another significant aspect with a direct influence on the final microstructure and mechanical properties, monopolizing the final product. In essence, it consists of a series of multiple stages of processing mechanisms that are required to be effectively controlled in the direction of designing a well-engineered microstructure and mechanical properties; such process requires deformation of alloys under specific conditions followed by explicit investigation of microstructural transformation where this process requires tensive attention due to the complexity of its mechanisms.

1.3.1 Scientific Perspective

The underlying method to control the mechanical properties of a particular alloy composition is through the understanding of the processing steps involved, where the dedicated approach to implement changes, e.g. increase or decrease certain properties, is carried out by creating variations in terms of processing route and this clear understanding of the initial process is the core component in the way of accomplishing the purpose in demand.

The relationship between the processing techniques, specifically with regard to deformation temperature, and the influence it has on the austenitic microstructure and the final structure and properties initially on the basis of quantifying the high total interfacial area per unit volume S_v (which will be defined in detail in Section 2.4) in conjunction with its influence upon cooling at a certain rate fall into the classification of unique research studies owing to the fact that this relation has not been investigated enough[30].

The proper combination of alloying elements and thermomechanical processing leads to a high total interfacial area per unit volume S_v value in the as-rolled austenite microstructure prior to transformation which subsequently leads to grain refinement. Although significant progress driven by the requirements of the industry has been conducted on supermartensitic stainless steels, there are still aspects of fundamental importance to understanding recrystallization that has not been studied yet[31].

1.3.2 Commercial Perspective

Supermartensitic stainless steels represent extreme importance to several steel-producing companies supplying products for different industries around the world including high-demand sectors such as aerospace, defense, construction, and particularly oil and gas, where these alloys are extensively used in offshore pipelines, flowlines, risers, and subsea components. In the UK, for instance, multiple manufacturers are producing supermartensitic stainless steels for various applications while looking forward towards a higher production efficiency by virtue of ongoing research and development, where the outcome of this research matches with the interest of those manufacturers and necessarily creating a driving force to proceed forward with the study.

In principle, the investigated compositions in this study are variations of an alloy that is already available in the market, specifically derived from the commercially recognized UNS S41427 grade currently used in oil and gas transport systems and hydrocarbon handling equipment as well as other subsea applications owing to its combination of high strength, moderate corrosion resistance and good weldability that ensure reliable operation under sour service and high-pressure conditions, which continues to demand further property optimization; thus, it is feasible to intelligently explore the possible prospects leading to enhancing this alloy on the basis of experimenting different compositions following the same process, experimenting different processes while the composition remains as is, or implementing slight changes to both processes and compositions[32].

Recognizing that minor compositional or processing adjustments can substantially alter microstructural stability and transformation behavior, such modifications are representative of the continuous industrial practice of refining existing grades to achieve improved mechanical strength, corrosion performance, long-term service reliability, and processing efficiency without altering the established manufacturing infrastructure. Nevertheless, this should be performed through an appropriate procedures to ensure reaching optimum quality while maintaining balance between cost, time, and scope, in accordance with the fundamentals of the project management triangle.

Over and above that, the work carried out in this research including but not limited to the new processes of new products along with understanding the metallurgical aspects tolerating the development of microstructural features, directly supports the industrial objectives of achieving improved steel performance in critical service environments, where durability, reliability, and process efficiency are of paramount importance. The outcomes of this work extend beyond laboratory-scale experimentation to offer practical insights applicable to industrial alloy design and manufacturing optimization, particularly in sectors driven by safety, performance, and cost-effectiveness.

This research makes a substantive contribution to advancing sustainable and technologically adaptive production practices, supporting the ongoing transformation of the steel industry toward low-carbon and resource-efficient manufacturing models, and reinforcing the collaborative link between academic innovation and industrial implementation. The study is in line with the core research tasks of Strategic University Steel Technology and Innovation Network (SUSTAIN) Future Manufacturing Research Hub and falls, more specifically, under the umbrella of Task 9/Task 17[33].

1.4 Research Aim, Scope, and Objectives

The thrust of this research is to study the influence of different processing temperatures and deformation amounts on the phase transformation and mechanical properties of ferrite-martensite steels with moderately manipulated chemical compositions.

The scope of this research is to understand the role of the austenite microstructure of the supermartensitic stainless steels and investigate whether or not the austenite is deformed above the recrystallization-limit temperature $T_{95\%}$ or below the recrystallization-stop temperature $T_{5\%}$; correspondingly, to understand the influence of the difference in the microstructure on the difference in the total interfacial area per unit volume S_v which shall affect the transformation behavior and accordingly, the transformation product.

Plane strain compression (PSC) tests were carried out accompanied by deep-rooted microstructural characterization and evaluation, outlined in Chapter 3, to address the identified purpose of this work and achieve the following objectives:

I. To study the behavior of supermartensitic stainless against the critical processing temperatures and evaluate the influence of nickel and manganese additions on these temperatures.

II. To investigate and quantify the total interfacial area per unit volume S_v when these alloys are deformed above or below the critical processing temperatures, and to investigate its effect on the subsequent transformation microstructures.

III. To investigate and quantify the contribution of the reconstructed prior austenite grains to the total interfacial area per unit volume S_v for the extreme identified conditions, and to investigate its effect on the transformation product.

1.5 Structure of Thesis

This thesis is composed of six interlinked chapters, each building systematically upon the preceding one to establish a coherent narrative that traces the progression from conceptual motivation to mechanistic understanding, quantitative analysis, and final interpretation of findings within the broader context of thermomechanical processing of supermartensitic stainless steels, thereby providing both deeper fundamental insights and extended applied relevance to industrial alloy development and thermomechanical process optimization.

I. Chapter 1 introduces the global and industrial context of the research, outlining the contemporary challenges facing the steel and energy sectors and framing the scientific and commercial motivations for developing advanced supermartensitic stainless steels with improved strength-ductility synergy. It defines the overarching research problem, articulates the aims, scope, and objectives, and positions the study within the broader materials science and engineering landscape, thereby setting the foundation for subsequent chapters.

II. Chapter 2 presents the current understanding of microstructural constituents, alloying element effects, and thermomechanical processing parameters that govern the behavior of supermartensitic stainless steels. It consolidates knowledge on microstructural restoration mechanisms, interfacial phenomena, and critical transformation temperatures, identifying key scientific gaps that the present research addresses through a quantitative approach based on interfacial area per unit volume and prior austenite grain reconstruction.

III. Chapter 3 provides the systematic methodology adopted to design and execute the thermomechanical tests, including alloy manufacturing by vacuum induction melting, plane-strain compression experiments, metallographic preparation, and microstructural and mechanical characterization. This chapter establishes the experimental foundation by defining the compliance framework, test matrix, and analytical techniques employed for quantifying S_v and assessing mechanical performance under varied deformation conditions.

IV. Chapter 4 outlines the experimental findings in a structured manner encompassing dilatometric assessment, microstructural evolution, quantitative measurements, and mechanical testing outcomes. The chapter interrelates observed microstructural changes with processing parameters, thereby generating a quantitatively data-driven perspective on how deformation temperature, strain amount, and chemical composition collectively influence the transformation behavior and mechanical response of the studied alloys.

V. Chapter 5 discusses the results to establish a comprehensive understanding of the governing phenomena that define the processing-structure-property relationships. It systematically examines the influence of finish deformation temperature, strain amount, and alloy composition on microstructural refinement and mechanical performance, thereby elucidating their interdependence while providing practical insights for process control and industrial applicability.

VI. Chapter 6 synthesizes the principal findings and reflects on their scientific and practical implications. It summarizes the contributions of the research to the understanding of deformation-induced microstructural evolution in supermartensitic stainless steels and proposes future directions encompassing advanced characterization, multiscale modeling, and industrial-scale validation to further develop the field of high-performance structural alloys.

Chapter 2 Literature Review

2.1 Microstructure Elements

With regard to martensitic stainless steels, a crystal structure of martensite with a body-centered tetragonal (bct) lattice is formed through a shear mechanism during a diffusionless transformation of austenite with face-centered cubic (fcc) lattice as a consequence of cooling at very high rates; in addition, the transformation from austenite to martensite, which leads to increased strength due to increased dislocations, depends on the chemical composition where the microstructure shall transform almost entirely to martensite only if cooling is performed at a specific temperature that is below the martensitic start temperature noting that retained austenite may persist either due to chemical stabilization in steels with relatively high carbon content or due to partial mechanical stabilization in low-carbon martensitic stainless steels, where residual stresses and dislocation substructures locally hinder the completion of the transformation[31,34–43].

2.2 Alloying Elements

Martensitic stainless steels are designed principally based upon balancing between a set of different elements; in the first place, the chromium content in their chemical composition typically ranges roughly between 11 wt% and 18 wt% on the side of carbon content reaching up to 1 wt%, along with relatively small amounts of some other alloying elements acknowledging that these elements are the main characteristics to distinguish and differentiate between the different UNS grades of martensitic stainless steels as illustrated in Figure 2.1[44]. It is critical to establish a precise combination of these alloying elements to achieve a well-balanced martensitic stainless steel with the desired properties.

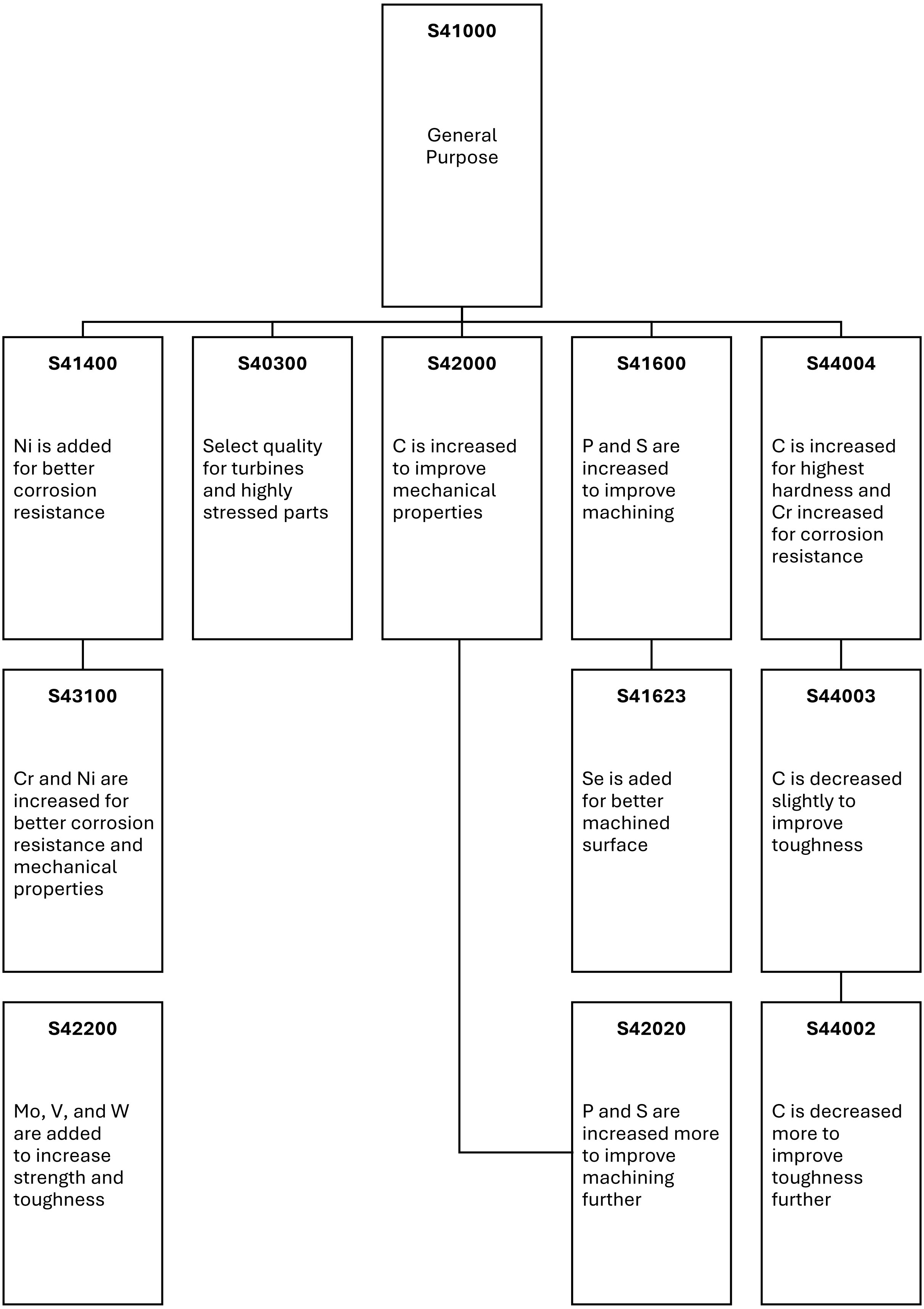

Figure 2.1 Chart of various grades of martensitic stainless steels and, notably, nickel appears only in the composition of UNS S41400 series (adapted)[15].

Supermartensitic stainless steels are advanced derivatives of conventional martensitic stainless steels, achieved through carefully controlled compositional optimization designed to enhance corrosion resistance, toughness, and weldability while maintaining high strength. They possess a predominantly martensitic microstructure, resulting from reduced carbon content and balanced alloying design that collectively improve phase stability and mechanical performance compared with traditional martensitic grades.

The microstructural morphology of supermartensitic stainless steels is predominantly composed of lath martensite arranged within packets that are confined by prior austenite grain boundaries, as shown in Figure 2.2, which presents representative micrographs of a typical supermartensitic stainless steel at two magnifications. At lower magnification, the microstructure exhibits a lath morphology distributed across several prior austenite grains, reflecting a transformation structure that developed upon rapid cooling from the austenitic phase. At higher magnification, the lath arrangements are revealed in greater detail, where the individual martensite laths are separated by low-angle dislocation boundaries and substructure interfaces formed through the diffusionless shear transformation.

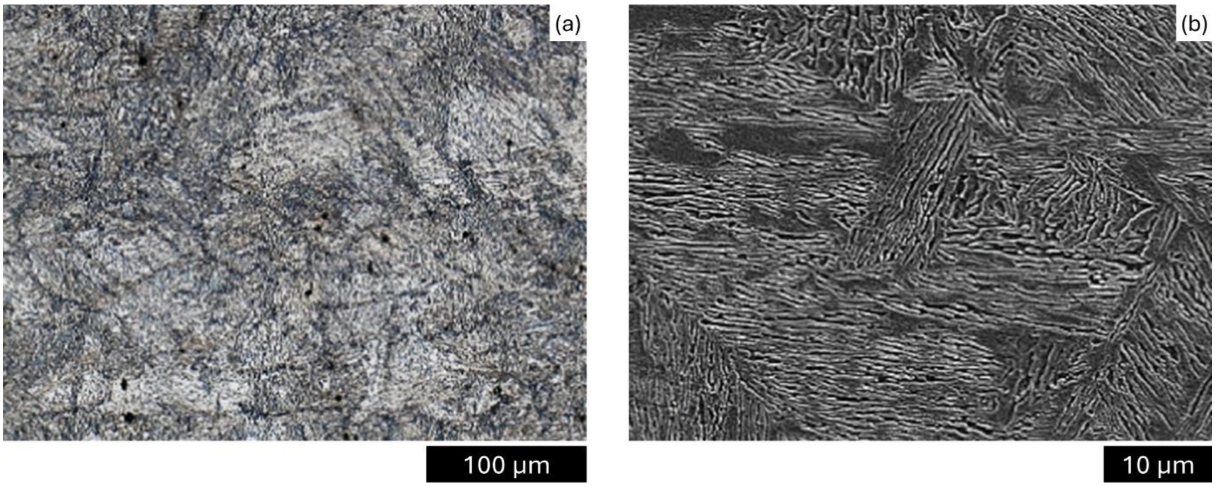

Figure 2.2 Representative microstructure of supermartensitic stainless steel (C 0.013%, Si 0.60%, Mn 0.86%, P 0.019%, S 0.002%, Cr 13.14%, Mo 0.78%, Ni 4.64%) castings: (a) low-magnification micrograph showing lath martensite packets within prior austenite grains, and (b) high-magnification micrograph revealing the detailed lath morphology characteristic of the martensitic structure (adapted)[45].

Distortions in the body-centered tetragonal (bct) crystal structure are restricted due to the particularly low-carbon content[46]. The first solid phase to form during solidification is delta ferrite with a body-centered cubic (bcc) crystal structure. With decreasing temperature, it will be transformed to austenite with a face-centered cubic (fcc) crystal structure followed by a transformation to martensite that is attributed to rapid cooling from elevated temperature. The stability of microstructure is contingent upon constituents of supermartensitic stainless steels where chromium, molybdenum, silicon, and titanium are prominent ferrite stabilizing elements whilst nickel, manganese, carbon, nitrogen, and copper are prominent austenite stabilizing elements.

The addition of elements has a notable influence on microstructure leading to enhancement in a lot of characteristics beyond material strength; evidence demonstrated that alloying alters multiple properties i.e. mechanical properties such as hardenability, fatigue, and creep resistance; service properties such as hardness, corrosion, and wear resistance; processing properties such as castability, weldability, and machinability; and physical properties such as density, elastic modulus, and thermal expansion[47,48].

The effects of a wide variety of alloying additions that shall modify the behavior of steels during thermomechanical processing are summarized in Table 2.1; it is worth mentioning that while the presence of an element may improve a specific property, it may deteriorate another. Furthermore, a contrast to a certain extent is expected as an outcome of different alloying elements corresponding to their concentration meaning that the same amount of nickel or manganese, for instance, will not stabilize the austenite in the same manner.

It is worth highlighting that the influence of alloying elements on the critical points of a phase diagram is associated with the condition of their existence in solid solution and not precipitation as second phases; hence, the presence of an alloying element in the chemical analysis on its own does not necessarily indicate the effectiveness of such element[49].

Table 2.1 Summary of the effects of alloying elements on the properties and processing of carbon and alloy steels (adapted)[47].

	Alloying element													
Property	C	Mn	Si	Cr	Ni	Mo	V	Nb	Al	B	Ti	N	P	S
Room-temperature properties														
Strength	✓	✓	✓[a]		✓[a]		✓[a]					✓	✓	
Ductility	x											x	x	x
Fatigue	✓				✓									
Hardness	✓	✓					✓					✓	✓	
Hardenability	✓	✓		✓	✓[b]	✓	✓[c]			✓	✓[d]	x[e]		
Charpy impact	x				✓		✓						x	x
Fracture (KTc) toughness	x			✓[f]	✓		✓	x[g]				✓[h]	x	
High-temperature properties														
Strength				✓[i]		✓								
Creep resistance						✓								
Low-temperature properties														
Strength					✓									
Toughness	x				✓		✓							
Microstructure														
Segregation*	Mod.	Sl.	Sl.											Max.
Grain refiner							✓		✓			✓		
Slows grain growth							✓		✓		✓	✓[h]		
Deoxidizer		✓	✓						✓		✓			
Eliminates hot shortness		✓												
Carbide former				✓		✓	✓	✓						
Reduces temper embrittlement						✓							x	
Austenite stabilizer	✓	✓			✓									
Ferrite stabilizer			✓	✓		✓		✓						

✓ = effective. **x** = detrimental. [a]Ferrite strengthener. [b]Nickel improves hardenability in conjunction with chromium. [c]Additions of vanadium up to 0.05% increase hardenability; larger additions result in carbide formation which is detrimental to hardenability. [d]Titanium is effective because it protects boron from nitrogen in boron-treated steels. If carbides form, it is detrimental. [e]Nitrogen can reduce the effect of boron on the hardenability of steel. [f]Chromium improves toughness in conjunction with nickel. [g]Detrimental unless grain is refined. [h]Effective in aluminum-killed steels because nitrogen forms AlN particles that control grain size and improve strength and toughness. Nitrogen lowers toughness in aluminum-free steels. [i]Chromium increases high-temperature strength in conjunction with molybdenum. *Segregation ratings: Mod. = moderate; Sl. = slight; and Max. = Maximum.

2.2.1 Chromium

Chromium, which is a ferrite stabilizer, is the main alloying element of supermartensitic stainless steels which assumes the fundamental role of outlining the main mechanical properties, e.g. strength, hardness, toughness, etc[50]. Chromium effectively enhances these properties along with its effectiveness in the enhancement of corrosion resistance owing to a coherent oxidation layer formed by its virtue; conversely, chromium may detriment the properties of an alloy when it combines with carbon if an inaccurate treatment process is carried out because of its nature as a carbide former[47,48,51–53].

Elaborating further, the passive barrier is primarily composed of chromium oxide, Cr_2O_3, which protects the surface of stainless steels from the penetration of corrosive agents such as oxygen as presented in Figure 2.3; hence, the presence of chromium is crucial in this context[54]. However, the effectiveness of chromium is governed by the presence of excess amounts of carbon combined with improper processing conditions, particularly at elevated temperatures[55,56]. Under such conditions, carbide precipitates at grain boundaries leading to decreased toughness and increased susceptibility to corrosion. Fortunately, supermartensitic stainless steels are low-carbon steels which significantly reduce the concerns and fears associated with the precipitation of carbide.

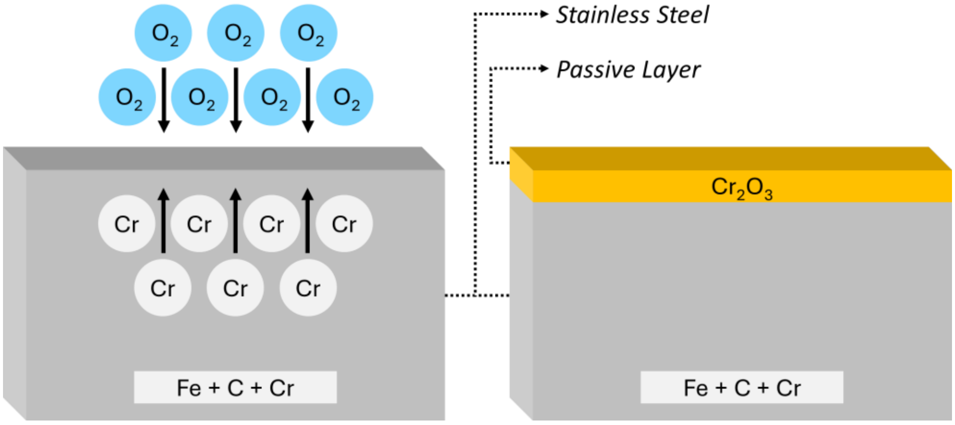

Figure 2.3 Formation of the passive layer on a stainless steel surface where chromium in the material reacts with oxygen from the air (left) to form an ultra-thin Cr_2O_3 protective film (right).

In addition, chromium plays a substantive role in determining the final microstructure of low-carbon steels, depending on its weight percent within the composition as well as the presence or absence of other alloying elements[57,58]. A fully martensitic microstructure is typically achieved when the chromium content is less than 12 wt%, as the transformation to martensite occurs upon rapid cooling from austenite, which forms from ferrite during heating at elevated temperatures[58]. Conversely, a fully ferritic microstructure is obtained when the chromium content exceeds 14 wt%, while a dual-phase microstructure, consisting of both ferrite and martensite, is observed when the chromium content lies approximately between these two ranges, depending on the specific alloy composition and processing conditions[57,58].

2.2.2 Molybdenum

Molybdenum, which is a ferrite stabilizer, is in the group of the significant alloying elements of supermartensitic stainless steels and minor addition of it would positively influence hardenability as well as its influence on the continuous cooling transformation when it is combined with nickel and manganese, where a consequent effect will be reflected on the martensitic transformation start temperature that is decreasing by the addition of molybdenum due to its role in reducing the free energy and reducing the accompanying equilibrium temperature[47,48,59–61].

2.2.3 Vanadium

Vanadium, which is a ferrite stabilizer, is in the group of the significant alloying elements of supermartensitic stainless steels; however, its presence is limited where it is added to the composition mainly to refine grain size and retard the growth of grains during the austenitization process; in addition, it is worth to highlight that even the small amount of vanadium tends to increase material strength, hardness, and toughness[47,48,61–65].

2.2.4 Nickel

Nickel is one of the significant alloying elements of supermartensitic stainless steels contributing to enhanced strength and improved toughness together with greater hardenability, particularly when combined with chromium; in addition, it is comprehended as the strongest austenite stabilizer among all other alloying elements, with the exception of nitrogen, whereas the unwanted delta ferrite formation is limited when nickel is presented in adequate amounts around 5% where it solidifies to austenite crystals taking into account that austenitic structure is stabilized further with increasing nickel content as illustrated in Figure 2.4[44,47,48,66–78].

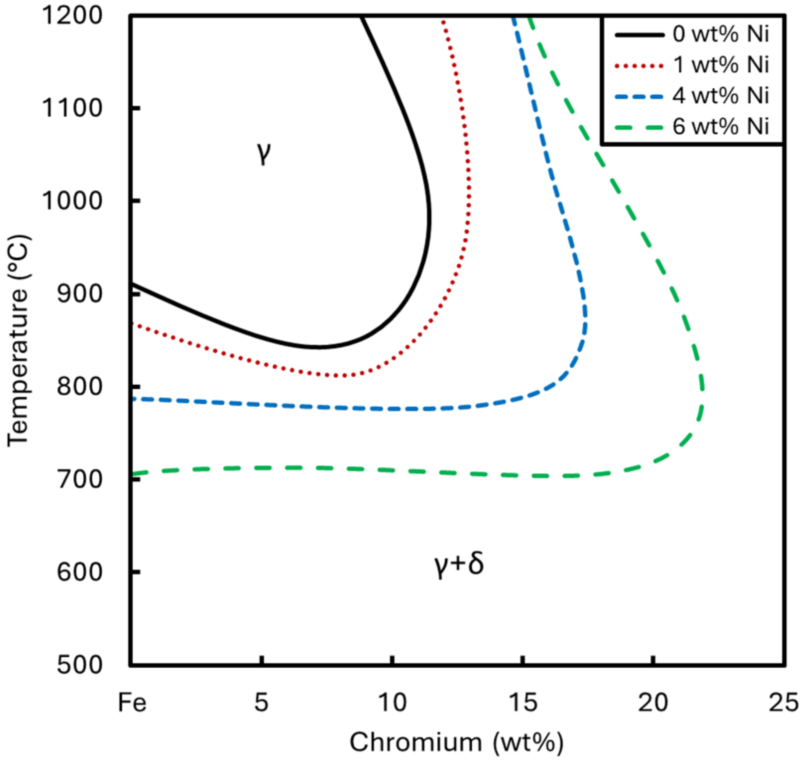

Figure 2.4 Influence of nickel concentrations on the range of the austenite phase in the iron-chromium system with a carbon content of 0.05 wt% (adapted)[75].

2.2.5 Manganese

Manganese is another significant alloying element of supermartensitic stainless steels which has a strong influence on increasing the hardenability and limited contribution to the strength and hardness enhancement; it is often proposed as a moderate alternative to nickel despite that it is not a strong austenite stabilizer as nickel as demonstrated in Figure 2.5, yet it will influence the phase transformation temperature by increasing the recrystallization temperature of austenite to higher temperatures and decreasing the start temperature of martensite transformation to lower temperatures implying that further reduction passes can be conducted at lower temperatures while being in single phase region[44,47,48,63,73–80].

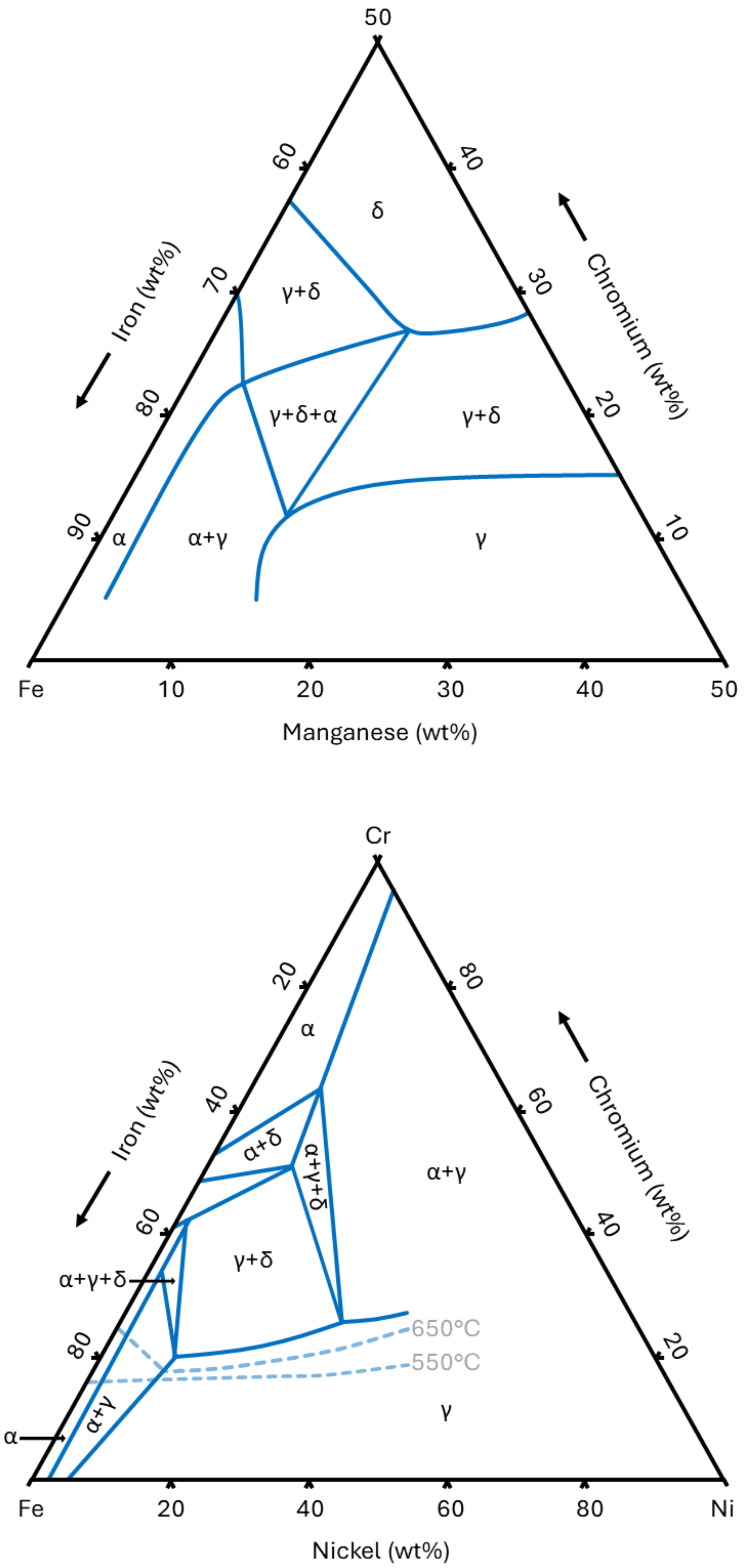

Figure 2.5 Isothermal profile in the ternary iron-chromium-manganese constitution diagram at 700°C and ternary iron-chromium-nickel constitution diagram at 800°C (adapted)[75].

2.3 Thermomechanical Processing

At the same hierarchical level, alloy design, and thermomechanical processing are complementary approaches that contribute towards tailoring the microstructure of the material to achieve the essential physical or mechanical properties necessary for optimal performance under specific operational conditions. On one hand, alloy design is a structure-guided approach that involves a methodical manipulation of the microstructure to engineer steels with higher material strength fine-tuned through the careful addition of alloying elements which may be presented in the form of solutes, precipitates, or a combination of the two forms[81,82].

On the other hand, thermomechanical processing is a key component in achieving higher material strength and toughness by primarily controlling the final microstructure through the refinement of austenite grains during deformation at elevated temperatures which subsequently leads to the refinement of transformation products such as polygonal ferrite, Widmanstätten ferrite, acicular ferrite, bainitic ferrite, martensite[81,83,84]. This process adheres to a defined schedule to obtain the maximum possible amounts of fine homogenized grains as opposed to the minimum possible amounts of inhomogeneous grains considering that this process is governed by several interrelated factors, e.g. processing temperatures, strain rate, and cooling rate[85–89].

The principle of thermomechanical processing of ferrous alloys is strongly related to the control of the microstructure of steels which can be accomplished through deforming the material in a series of well-designed and carefully controlled processes that can best be categorized under four determinant headings: reheating, rough rolling in the fully recrystallized region, finish rolling in the fully recrystallized region, the fully unrecrystallized region, or the partially recrystallized region, and cooling (air-cooled, water-quenched, or a combination of both methods depending on the desired final product properties). The metallurgical mechanisms and the associated microstructural evolution during each critical stage of thermomechanical processing are thoroughly detailed and illustrated in Figure 2.6.

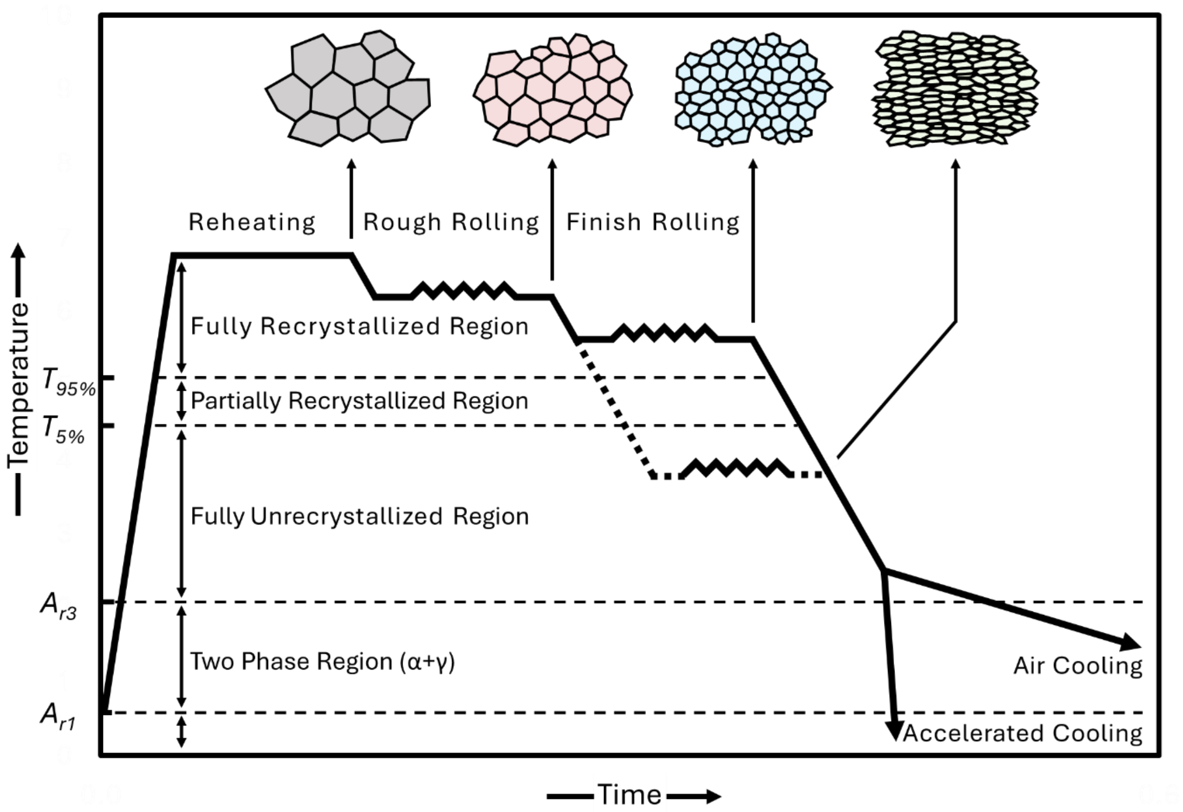

Figure 2.6 Schematic illustration of the four stages of thermomechanical processing where coarsen equiaxial microstructure is obtained after reheating (gray) followed by finer equiaxial microstructure resulting from a rough rolling pass (red) preceding an even finer equiaxial microstructure or elongated morphology due to a finish rolling pass in the fully recrystallized region (blue) or the fully unrecrystallized region (green), and finally cooling by air, immersion or other techniques.

Successful thermomechanical processing can be attributed to the control of the as-rolled austenite microstructure prior to its transformation. The as-rolled austenite microstructure may be fully recrystallized when deformed above $T_{95\%}$, fully unrecrystallized when deformed below $T_{5\%}$, or partially recrystallized when deformed between $T_{95\%}$ and $T_{5\%}$. Furthermore, the grain boundary area per unit volume depends primarily on the starting grain size and the aspect ratio of the deformed grains when the microstructure is not fully recrystallized, i.e. in partially or fully unrecrystallized microstructures[90].

Optimum mechanical properties of alloyed steels are achieved through thermomechanical processing bearing in mind on the one hand that unprocessed alloyed steels exhibit less favorable properties and on the other hand that thermomechanical processing of steels in the absence of alloying elements is difficult as essential microstructural control mechanisms are often deficient[89]. Hence, the correlation between alloying elements and thermomechanical processing is associated with their direct impact on the final microstructure and their critical responsibility in determining the mechanical properties.

While thermomechanical processing can lead to improved toughness caused by refined austenite microstructure, alloying elements combined with unrefined austenite microstructure consisting of large grains lead to a lower material toughness caused by the presence of large ferrite grains and the possible formation of low-temperature transformation products, i.e. martensite, with this effect becoming more pronounced in highly alloyed steels. Furthermore, it is evident that grain refinement is the only adequate mechanism to improve strength along with toughness, whereas other strength-increasing mechanisms deteriorate toughness[84,91].

The influence of grain size on material strength is expressed by the classic Hall-Petch relationship:

$$\sigma_y = \sigma_0 + k_y d^{-1/2} \quad \text{Equation 2.1}$$

where σ_y is the yield stress, σ_0 is the friction stress, d is the average grain size, and k_y is the material-dependent constant[92,93]. Despite that several alternative relationships were developed at later periods of time; this grain size relationship which represents the first quantification and implementation of a model to relate microstructure to a mechanical property remains the most widely applicable equation for evaluating the effect of grain size on strength, taking into account that it depends on the precise value of k_y[94–96].

Nevertheless, the Hall-Petch relationship in its classical sense becomes less relevant for heavily deformed microstructure at high strain rates and low temperatures whereupon the concept of the average grain size vanishes attributed to the highly elongated grains; accordingly, a more suitable parameter supersedes this relationship and embodies grain size with other structural defects e.g. shear bands or dislocation networks[97].

2.4 Interfacial Area per Unit Volume S_v

Nucleation of the low-temperature transformation product can occur from either fully recrystallized or fully unrecrystallized austenite grains, where the number of nucleation sites is governed by the grain boundary area per unit volume, which in turn is directly related to the initial grain size of austenite[84]. In physical terms, martensite commonly nucleates at prior austenite grain boundaries and at intersections of deformation bands within grains, particularly where local strain accumulation and crystallographic misorientation are pronounced. Practically, the finest grain size of the final product is attained at a high nucleation rate, which depends primarily on subdividing austenite grains along with the presence of structures built into them, e.g. deformation bands[84].

In addition, the density of deformation bands is related to the temperature at which the material is deformed where higher density is attained at lower deformation temperatures falling within the fully unrecrystallized region and vice versa[89]. These deformation-induced features provide additional nucleation sites, supplementing those at prior austenite grain boundaries. This enhanced subdivision contributes to an increased total interfacial area per unit volume, thereby elevating S_v and increasing the number of available nucleation sites, both of which critically influence the transformation pathway and the final morphology of ferritic or martensitic structures[81,98].

Research carried out during the early years of the last quarter of the 20th century defined a stereological parameter, S_v, to measure the frequency of nucleation occurring at austenite grain boundary area per unit volume which was introduced in 1970 by Underwood through the advancement of quantitative metallography techniques[85,99]. The empirical relationship between S_v and ferrite grain size is represented in Figure 2.7 for a transformation product consisting of ferrite and pearlite, where higher S_v values are shown to correspond with finer ferrite grains.

This correlation primarily depends on the state of austenite, whether it is recrystallized or unrecrystallized, prior to transformation. Despite that intentional grain refinement is generally intended to increase S_v following deformation in the recrystallized or unrecrystallized regions, the rate of nucleation significantly increases in the condition of deformation in the unrecrystallized region leading to further refinement of the microstructure[89].

This phenomenon is particularly relevant in thermomechanical processing where deformation at low temperatures restricts dynamic recovery, encouraging dislocation accumulation and storage. Accordingly, martensitic nucleation is spatially heterogeneous and governed by the availability of boundaries and deformation substructures that locally raise the driving force for transformation. These stored dislocations, along with the formation of sub-grain structures and deformation bands contribute not only to grain subdivision but also to a higher interfacial area density within the austenitic microstructure, encompassing both grain boundaries and deformation-induced internal interfaces; consequently, S_v becomes a powerful indicator of transformation potential and microstructural refinement[81].

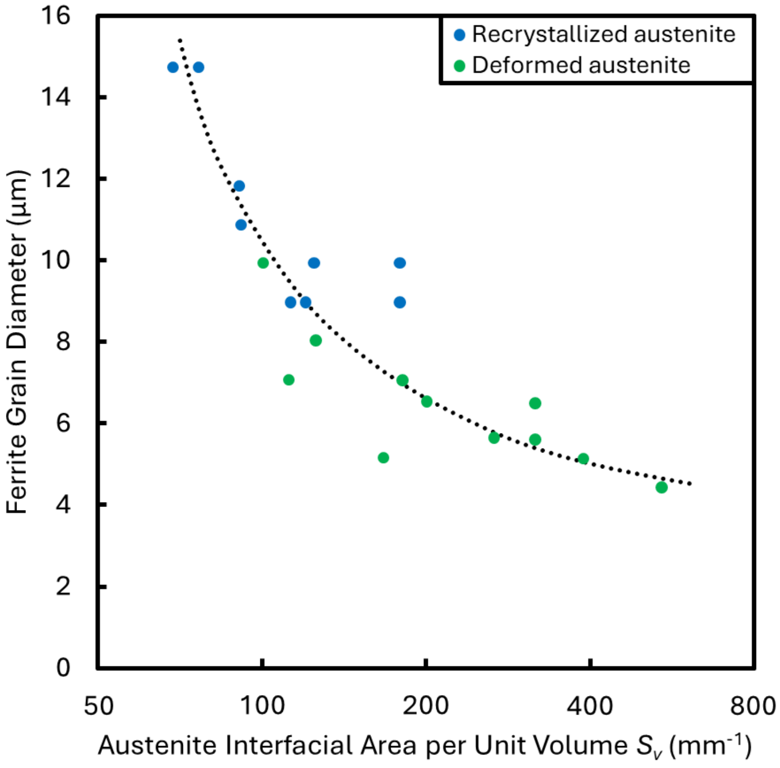

Figure 2.7 Ferrite grain sizes produced from recrystallized and unrecrystallized austenite at various S_v values, with the unit of mm^2/mm^3 or simply mm^{-1} (adapted)[100].

The total interfacial area per unit volume tends to be larger for unrecrystallized austenite than recrystallized austenite primarily attributed to distinct factors for each of the two conditions. The refinement of the recrystallized microstructure occurring at a temperature above the recrystallization-limit temperature is the one and only factor influencing the interfacial area per unit volume with an inverse variation denoting that the larger values of S_v depend straight forward on the smaller equiaxed grains which substituted the original larger equiaxed grains, as a direct consequence of complete dynamic recrystallization, where the relationship under this condition can be expressed by the following:

$$S_v = \frac{2}{D_\gamma} \qquad \text{Equation 2.2}$$

where S_v is the total effective interfacial area per unit volume of recrystallized austenite, and D_γ is the average recrystallized austenite grain size[85,99].

However, the highly elongated grains along with the intragranular crystalline defects occurring at a temperature below the recrystallization-stop temperature are the two factors influencing the interfacial area per unit volume and standing behind the larger values of S_v in this condition where the relationship between these parameters can be expressed by the following:

$$S_v = S_v^{GB} + S_v^{IPD} \qquad \text{Equation 2.3}$$

where S_v is the total effective interfacial area per unit volume of unrecrystallized austenite, S_v^{GB} is the grain boundary contribution, and S_v^{IPD} is the intragranular planar defect contribution[85,100].

The grain boundary contribution to the total interfacial area per unit volume is affected by rolling reduction and initial grain size prior to deformation as illustrated in Figure 2.8; accordingly, this contribution can be expressed by the following:

$$S_v^{GB} = \frac{1}{D_{\gamma'}}\left(1 + R + \frac{1}{R}\right) \qquad \text{Equation 2.4}$$

where $D_{\gamma'}$ is the initial grain size of austenite, and R is the ratio of rolling reduction in thickness from original to final[85,100].

The intragranular planar defect contribution to the total interfacial area per unit volume is affected by a minimum rolling reduction percentage of 30 when a linear increase initiates thenceforth as illustrated in Figure 2.9; accordingly, this contribution can be expressed by the following:

$$S_v^{IPD} = 0.63\ (Reduction\% - 30)mm^{-1} \qquad \text{Equation 2.5}$$

where deformation bands are associated with a rolling reduction of 30% and above; otherwise, the contribution of intragranular planar defect to S_v does not anticipate being captured[85,101]. Such dual contributions make S_v a more versatile and accurate indicator of interface density than average grain size, especially in heavily deformed or thermomechanically processed steels[102].

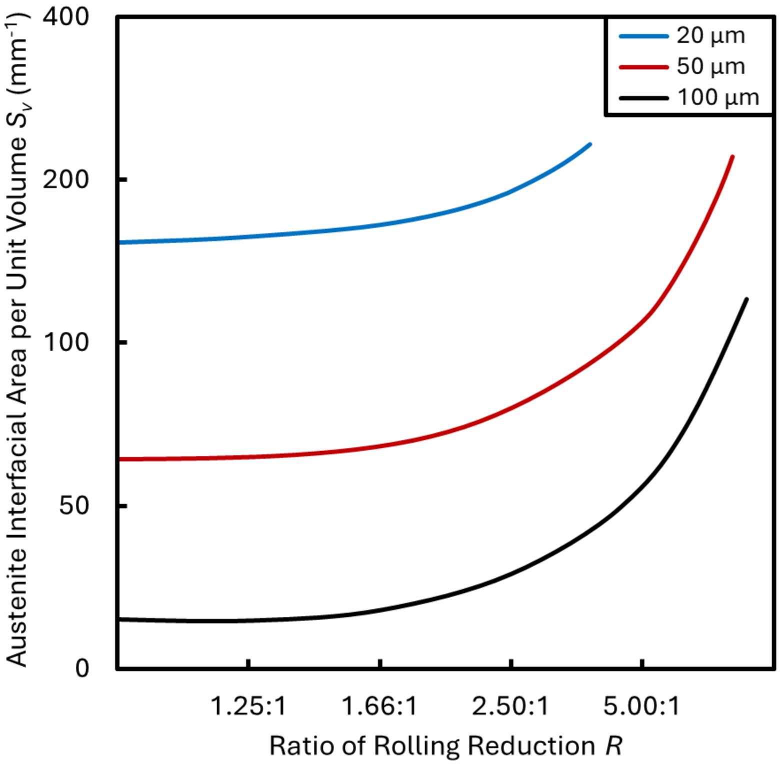

Figure 2.8 Grain boundary contribution to S_v for a hypothetical array of cube-shaped grains of variable initial grain size (adapted)[100].

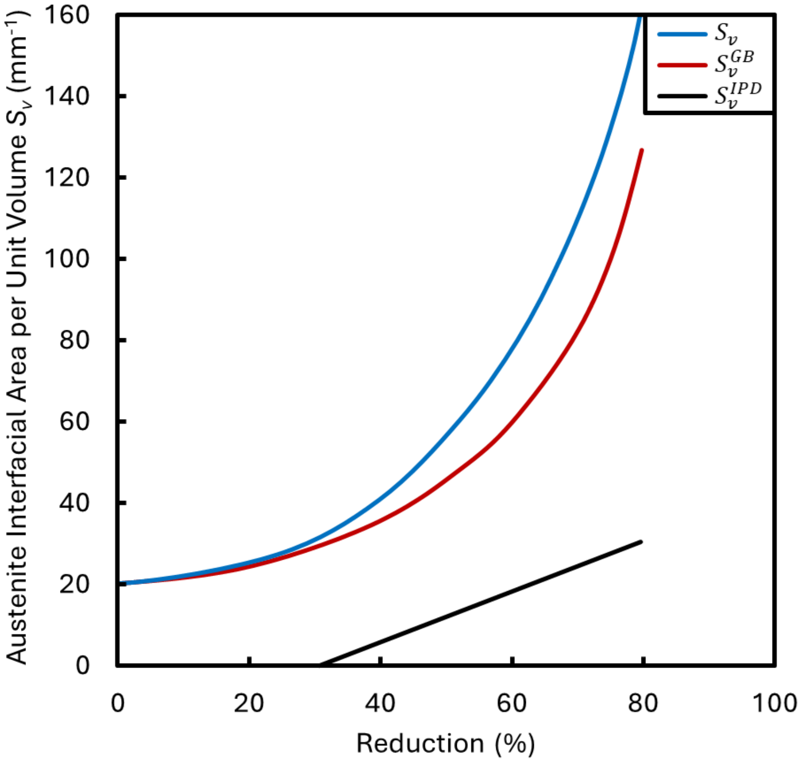

Figure 2.9 Intragranular planar defect contribution to S_v along with grain boundary contribution to S_v for an austenite grain diameter of 100 µm (adapted)[100].

2.5 Microstructural Changes during Deformation

The deformation of austenite during thermomechanical processing results in the generation of dislocations which serve as the primary carriers of plastic strain, and as deformation progresses, the dislocation density increases substantially, particularly at lower processing temperatures where the rate of dynamic recovery is reduced and dislocation annihilation becomes limited, thereby promoting the subdivision of austenite grains and the formation of intragranular features such as deformation bands and sub-grains[102].

This, in turn, contributes to elevated S_v values due to the increased interfacial area generated by grain boundary refinement and the presence of internal planar defects; consequently, the evolution of S_v is directly related to the intensity and nature of the deformation process; for instance, dislocations and their associated stored energy accumulate significantly when dynamic recovery and recrystallization mechanisms are largely suppressed[103].

The dislocations generated during deformation are not passive defects but active reservoirs of stored energy that drive subsequent microstructural evolution. While the majority of mechanical work applied to the material is dissipated as heat, a fraction is retained as internal energy associated with dislocation networks and lattice distortions; furthermore, the density and distribution of these dislocations are influenced by various factors including but not limited to deformation temperature, strain rate, and alloying composition.

In supermartensitic stainless steels, the presence of specific alloying elements in the austenitic phase reduces the stacking fault energy, which promotes planar slip over cross-slip, thus leading to localized strain accumulation and the development of persistent dislocation structures, which not only act as barriers to further plastic deformation but also impede dislocation mobility, amplify the effects of strain hardening, and elevate the driving force for thermally activated restoration processes such as recovery and recrystallization during subsequent annealing[104].

Understanding the evolution of dislocations during deformation, aside from being fundamental to controlling S_v, is also significant in anticipating the onset and progression of microstructural restoration mechanisms that are inherently driven by the internal energy, whereupon, throughout and following the course of deformation, the material exhibits an intrinsic tendency to reduce its accumulated energy, initiating a series of structural rearrangements governed by the balance between the stored energy associated with dislocation networks and the opposing energy barriers to lattice reconfiguration.

In this regard, the character of the dislocation configurations established during deformation not only governs the immediate austenitic response but also critically influences the path and extent of restoration, ultimately defining the final microstructure and mechanical performance of the material[105].

2.6 Microstructural Restoration Processes

2.6.1 Restoration Driving Forces

Approximately 90-95% of the total energy generated via steel deformation is dissipated in the form of heat and only a relatively small yet critical fractional amount of the deformation is stored in the alloy leaving it in an energetically unstable and structurally distorted state where the microstructure represented in grains and grain boundaries is directly affected by the continuous generation of dislocations and defects, leading to increasing amounts of stored energy depending on multiple factors including deformation temperature and strain amount[102].

This energy is the primary driving force for microstructural restoration processes which are best categorized into two distinct types: recovery and recrystallization. Recovery refers to the rearrangement of dislocations into lower-energy configurations and the elimination of vacancies while maintaining the existing grain shape and orientation; despite the slight overall decrease in dislocation density, the pre-existing grain framework is essentially preserved, with only limited boundary migration[48,102,106]. In contrast, recrystallization refers to the reduction of dislocations and the formation of new grains with significantly lower dislocation density and varying sizes, shapes, and orientations, accompanied by the migration of grain boundaries[48,102,106].

On one hand, recovery is a process occurring in advance of recrystallization where a partial restoration of properties and microstructure to their original condition prior to deformation is often achieved through the elimination of point defects and dislocations; apparently, most of the point defects anneal out at low temperatures while dislocations rearrange into other configurations such as sub-grains, under a phenomenon known as polygonization[102]. This process involves a sequence of multiple recovery mechanisms which typically occur in the order illustrated in Figure 2.10.

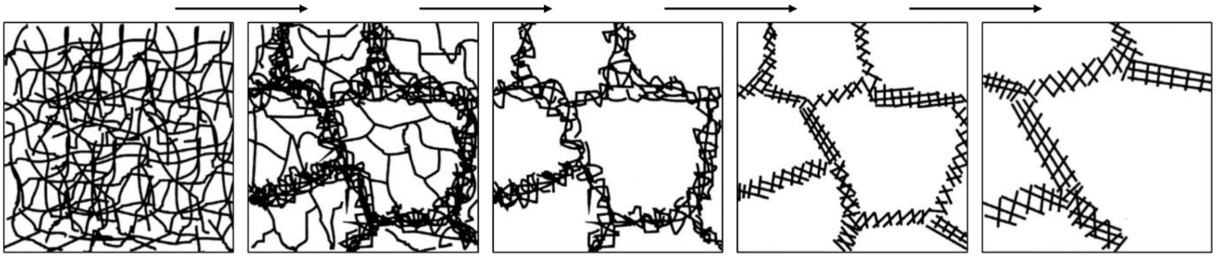

Figure 2.10 Schematic illustration of the different stages of dislocation recovery starting with tangled dislocations subsequent to plastic deformation, followed by cell structure formation, then dislocation annihilation within cells, reaching sub-grain structures formation and growth (adapted)[102].

On the other hand, recrystallization is the process of restructuring the deformed microstructure during annealing through the formation of new grains and the migration of grain boundaries toward states of lower free energy; meanwhile, the driving force for further migration and growth decreases significantly due to the substantial reduction in dislocation density by virtue of newly originated grains as illustrated in Figure 2.11, and this decrease in the driving force for grain migration and growth subsequently leads to an increase in S_v[31,102,106].

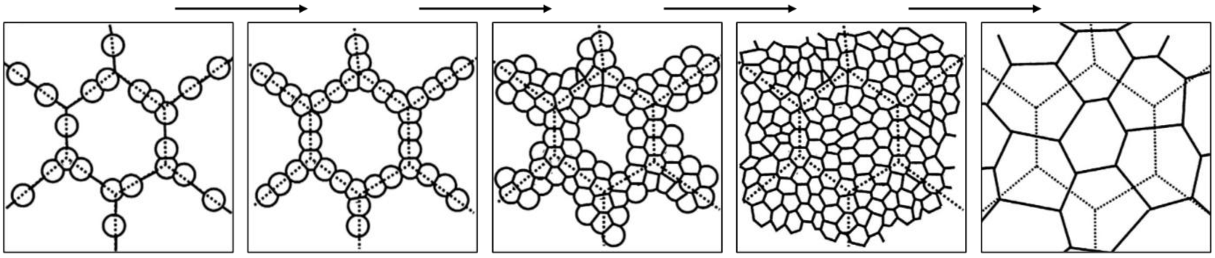

Figure 2.11 Schematic illustration of the different stages of recrystallization starting with the formation of grains at the old grain boundaries (dotted lines), followed by continuous nucleation of new grains at the new grain boundaries, reaching fully recrystallized structure with finer grains (adapted)[102].

Fundamentally, recrystallization is driven by the stored strain energy accumulated within the deformed microstructure, primarily arising from the high density of dislocations, sub-boundaries, and lattice distortions generated during plastic deformation; this stored energy provides the thermodynamic potential required to nucleate new strain-free grains and to activate boundary migration that eliminates regions of high internal energy[102].

The magnitude of this driving force increases with greater deformation and lower processing temperatures that suppress recovery, whereas it decreases as recovery proceeds and dislocation density is reduced; nevertheless, the balance between the driving force from stored energy and the retarding forces from solute drag or particle pinning ultimately governs the onset, rate, and extent of recrystallization in supermartensitic stainless steels[102,107].

2.6.2 Restoration Retarding Forces

Microstructural restoration processes are subject to certain conditions proceeding only when the driving forces exceed the retarding forces; in other words, restoration is inhibited when retarding forces dominate. The basic and essential aspects of retarding forces are associated with restraining grains from further restoration following their deformation, driven by mechanisms such as solute drag and particle pinning which are the cause of inhibition of further grain boundary migration leading to stabilization of smaller grains and an increase in S_v as a consequence[102,108–110].

Specifically, solute drag creates a drag force when solute atoms segregate at grain boundaries, effectively restricting their movement, whereas particle pinning forms a physical barrier when phase particles pin at grain boundaries, thereby preventing their growth[111]. Furthermore, the high interfacial area per unit volume acts as a stumbling block to the motion of dislocations, intensifying resistance by creating obstacles that hinder deformation[112].

2.6.3 Recrystallization Mechanisms

Recrystallization in supermartensitic stainless steels occurs during or following the deformation of austenite depending primarily on deformation temperature, strain amount, and the stored energy accumulated during plastic deformation;

more specifically, it represents a fundamental restoration stage that dictates subsequent transformation behavior, and in this context, the mechanisms that govern this process include dynamic recrystallization, static recrystallization, and, under certain intermediate conditions, continuous recrystallization, each of which contributes differently to the restoration and refinement of the austenitic microstructure[102].

When deformation is carried out above the recrystallization-limit temperature, the simultaneous accumulation of dislocations and the migration of existing boundaries lead to dynamic recrystallization, which is characterized by the nucleation and growth of new strain-free grains along high-angle boundaries, deformation bands, and triple junctions; during this thermally activated process, localized nucleation events progressively consume regions of high dislocation density, as this process progresses, the deformed microstructure is gradually replaced by finer equiaxed grains, thereby enhancing homogeneity and reducing dislocation density[102].

In contrast, deformation below the recrystallization-limit temperature, yet above the recrystallization-stop temperature, restricts boundary mobility and suppresses the formation of new grains through dynamic recrystallization; nevertheless, recovery processes dominate, allowing sub-grain structures to evolve through dislocation rearrangement and gradual rotation of low-angle boundaries, eventually facilitating a progressive transition from recovery to recrystallization, ultimately producing new grains through continuous recrystallization as strain increases[102].

When deformation ceases while sufficient thermal energy remains available, static recrystallization proceeds as new grains nucleate and grow into the previously deformed matrix, driven by the release of stored strain energy; however, in supermartensitic stainless steels, the rate and extent of static recrystallization are strongly influenced by alloying additions that modify boundary mobility, where elements such as chromium and molybdenum tend to retard grain boundary migration through solute drag, while manganese enhances recrystallization locally by increasing dislocation density and providing favorable nucleation sites that promote uniform grain subdivision and microstructural homogenization[102,113].

Consequently, the dominant mechanism depends on the thermomechanical regime, whereby dynamic recrystallization governs grain refinement above the recrystallization-limit temperature, continuous recrystallization becomes significant between the recrystallization-limit temperature and the recrystallization-stop temperature, and static recrystallization completes restoration once deformation stops; collectively, these processes control the evolution of austenite prior to martensitic transformation and thus determine the total interfacial area per unit volume and the resulting balance between strength, ductility, and toughness in supermartensitic stainless steels[102,107,114].

2.6.4 Grain Coarsening

Grain coarsening represents a later stage in microstructural evolution process occurring after restoration processes such as recovery and recrystallization; in fact, this process, also referred to as grain growth, involves a gradual increase in grain size due to the consumption of smaller grains and the growth of larger grains driven by the reduction of grain boundary energy and governed by the tendency to minimize total free energy achieved through the migration of grain boundaries toward their centers of curvature during annealing[90,115].

While the presence of fine particles or solute atoms may retard grain coarsening through mechanisms such as Zener pinning or solute drag, impurities or second phases may accelerate grain growth leading to significant consequences affecting material properties as larger grain sizes generally result in a reduction of principal properties such as strength and hardness, yet improve other properties such as ductility and toughness[102,116].

2.7 Critical Processing Temperatures

2.7.1 Phase Transformation Temperatures

There are several phase transformation temperatures important to define for better understanding of the microstructural evolution of steels during heating and cooling processes; A_{e1} refers to the equilibrium eutectoid temperature for the lower boundary of the α+γ region at which steel is fully ferritic and similar to that, A_{e3} refers to the carbon concentration of austenite in equilibrium with ferrite and represents the upper boundary of the α+γ region, above which the steel is fully austenitic. Four phase transformation temperatures can be integrated from A_{e1} and A_{e3} depending on whether the transformation is occurring during heating or cooling i.e. A_{c1}, A_{c3}, A_{r1}, and A_{r3}.

While A_e is denoted by the letter "e" as an indication of equilibrium conditions, A_c and A_r are denoted by the letters "c" and "r" as an indication of heating or cooling conditions which comes from the French words *chauffage* and *refroidissement* which means heating and cooling, respectively[77,117]. The Fe-Fe_3C phase diagram with the main boundaries representing the phase transformation temperatures is illustrated in Figure 2.12. From an industrial processing point of view, transformation temperatures during heating and cooling are considerably more important than those at equilibrium since they play a role in identifying TMP limits.

In addition to these transformation temperatures, it is necessary to define the martensitic start temperature, M_s, which is an important phase transformation temperature at which the microstructure starts to transform from the austenitic phase into the martensitic phase; it is worth recalling that this temperature, as do other transformation temperatures, is influenced by alloying elements[80]. Figure 2.13 represents the effect of alloying elements on A_{c1}, and Figure 2.14 represents the effect of alloying elements on M_s; additionally, Figure 2.15 represents a dilation diagram of a supermartensitic stainless steel with titanium addition indicating that A_{c1} is around 680°C, and M_s is around 220°C[118].

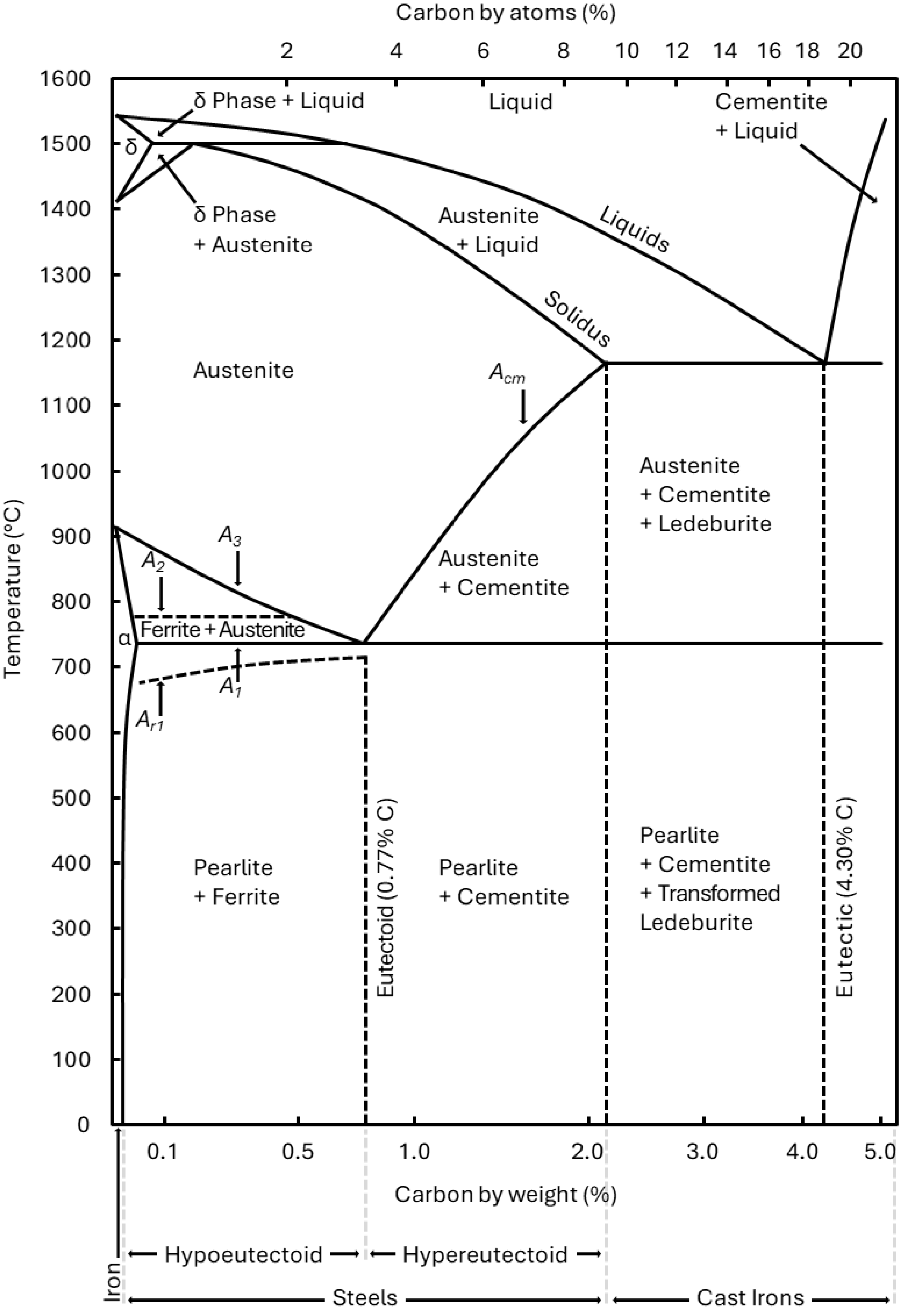

Figure 2.12 Iron-carbon phase diagram exhibiting the different phases of steels at different temperatures with respect to carbon content (adapted)[117].

Austenite to martensite transformation during cooling occurs at a specific temperature which varies depending on the composition of the alloy; however, this temperature does not depend significantly on the cooling rate where this transformation may take place at various cooling rates[119]. Due to the nature of martensitic transformation that is associated with rapid cooling after heating to a very high temperature, the iron-carbon phase diagram is no longer sufficient[120].

It is significant to identify the phase transformation temperatures due to their influence on the final microstructure and consequently, the mechanical properties. Multiple empirical equations tend to estimate various transformation temperatures and several of them have shown satisfactory predictions; however, these equations are not precise enough as they take into account the chemical composition of a variety range of steels and without paying attention to heating and cooling effects which play an important role in determining these temperatures, yet they possessed the ability to provide an adequate approximate estimation with an accepted margin of error[121].

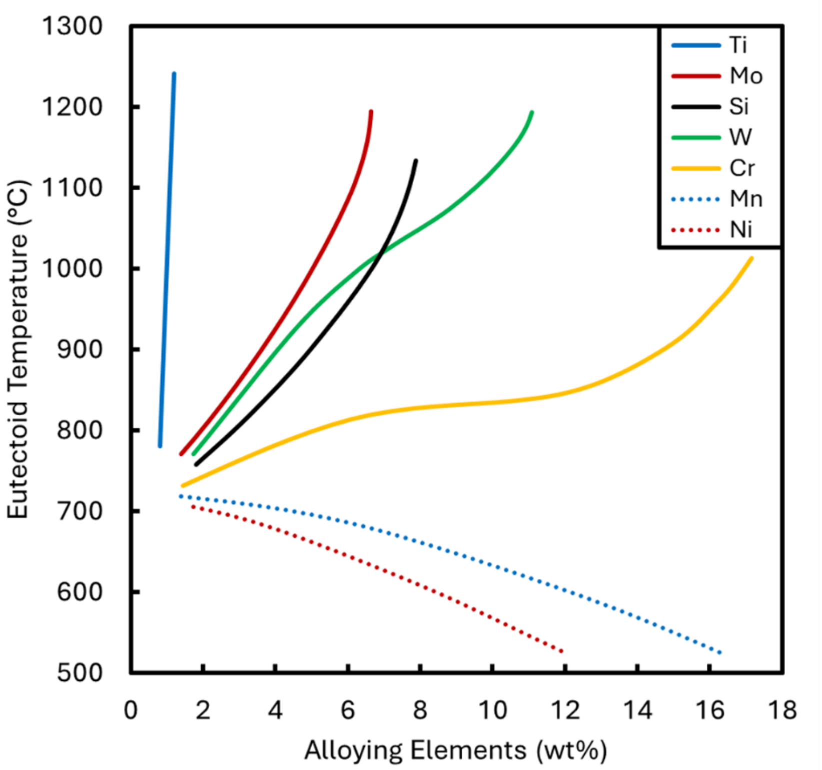

Figure 2.13 Effect of alloying elements on A_{c1} where a steady decrease is anticipated with the addition of nickel or manganese (adapted)[119].

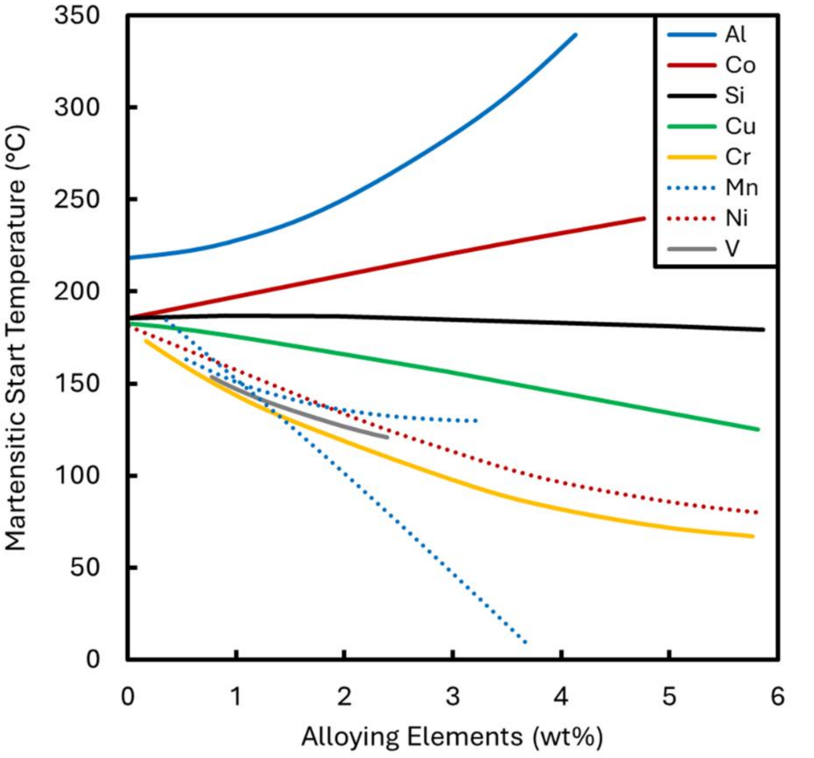

Figure 2.14 Effect of alloying elements on M_s where a decrease is anticipated with the addition of most elements, except cobalt and aluminum (adapted) [119].

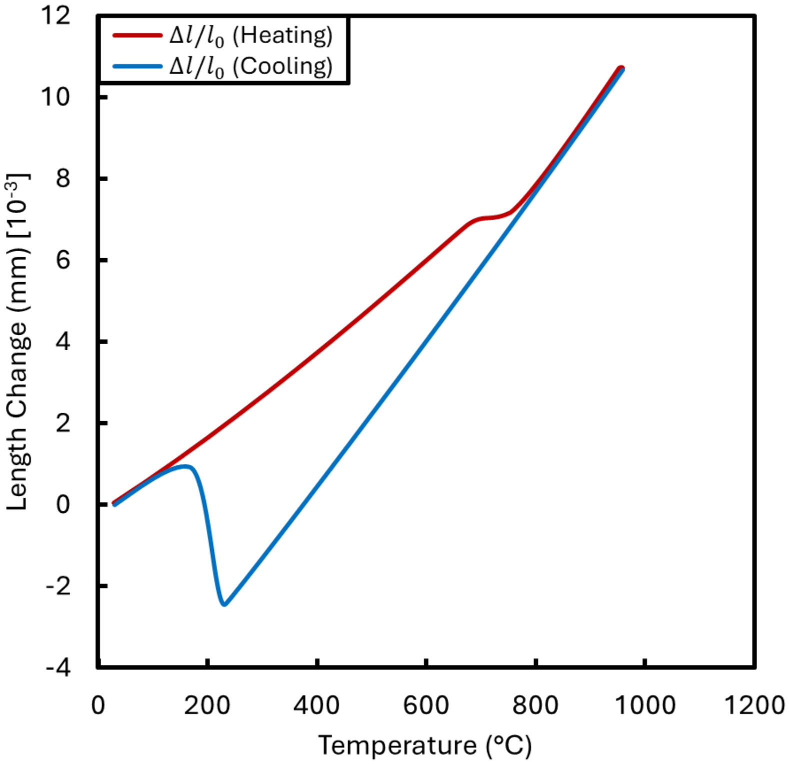

Figure 2.15 Dilation diagram of a low-carbon supermartensitic stainless steel heated to 1000°C at a rate of 0.33°C/s, and then cooled to ambient temperature at a rate of 0.2°C/s (adapted)[118].

2.7.2 Critical Recrystallization Temperatures

Austenite recrystallization is associated with two critical processing temperatures defining the three recrystallization regions: fully recrystallized, partially recrystallized, and fully unrecrystallized. The recrystallization-limit temperature $T_{95\%}$ represents the temperature above which a fully recrystallized region exists; by contrast, the recrystallization-stop temperature $T_{5\%}$ represents the temperature below which a fully unrecrystallized region exists due to the insufficient stored energy from prior deformation to drive further nucleation and growth of new grains[122]. As a matter of course, the partially recrystallized region exists within these two recrystallization-limit temperatures: $T_{95\%}$ and $T_{5\%}$.

Whereas a maximum percentage of 5% of recrystallized austenite grains may exist at $T_{5\%}$, a minimum of 95% of recrystallized austenite grains must exist at $T_{95\%}$. These temperatures have a direct influence on the final microstructure resulting from thermomechanical processing; hence, it is significant to identify them precisely taking into consideration that both temperatures are strongly affected by the chemical composition of the alloy and the particular deformation conditions as well as initial grain size and recrystallization kinetics[49,87,89,122–124].

2.8 Critical Processing Conditions

Deformation of austenite is possible to be conducted in different regions; it can be deformed above the recrystallization-limit temperature $T_{95\%}$ and can be also deformed below the recrystallization-stop temperature $T_{5\%}$ where the final microstructure will be significantly different[88,89].

The degree of importance of these two parameters is that $T_{95\%}$ and $T_{5\%}$ are both extremely critical to two out of the four stages of thermomechanical processing; therefore, understanding their fundamentals is a significant contributory cause to achieving the desired final product.

2.8.1 Deformation Above $T_{95\%}$

The process of rough rolling in the fully recrystallized region results in fine equiaxed austenite grains and when the finish rolling is performed also at high temperatures in this region, a much finer equiaxed microstructure is achieved due to the repeated reduction passes where the final microstructure depends on the initial grain size at the early processing stages and on the amount of strain applied[87,89]. Deformation in this region results in the formation of strain-free grains that refine and homogenize the microstructure through continuous dynamic recrystallization which promotes the elimination of dislocation networks. Furthermore, the conditioning of austenite grains improves material strength and toughness; moreover, it eventually increases the value of S_v.

2.8.2 Deformation Below $T_{5\%}$

Deformation in the fully unrecrystallized region below $T_{5\%}$ and above A_{r3} results in elongated austenite grains and the effectiveness of finish rolling in this region is influenced by the temperature window where the larger the magnitude of the unrecrystallized region is, the more reduction passes can be performed[87,89]. Deformation in this region results in the formation of sub-grains that lead to the gradual rearrangement of dislocations dominated by dynamic recovery which delays the onset of recrystallization. In fact, this process will subsequently result in a microstructure with a high density of dislocations and deformation bands due to the repeated reduction passes which correspondingly results in higher S_v values, compared to deformation above $T_{95\%}$.

2.8.3 Controlled Cooling

The final microstructure transformation of a material is significantly influenced by cooling parameters; therefore, it is critical to control the overall cooling process from the austenitic region and determine the optimum cooling rates by considering the continuous cooling transformation (CCT) diagrams to mitigate any undesirable phase formation aiming towards enhanced material performance. The cooling rate is calculated via the following equation:

$$\dot{T} = \frac{\Delta T}{\Delta t} \qquad \text{Equation 2.6}$$

where $\dot{T}$ is the cooling rate, ΔT is the change in temperature, and Δt is the change in time associated with the temperature change[125].

For supermartensitic stainless steels, austenitic to martensitic transformation is obtained at a wide range of cooling rates because of the high hardenability of these steels where a fully martensitic single-phase structure with absolutely no other transformation products is expected at a cooling rate of 0.2°C/s or even higher as presented in Figure 2.16 which emphasizes a relatively low M_s temperature; hence, either water quenching or air cooling is sufficient to attain the desired final microstructure.

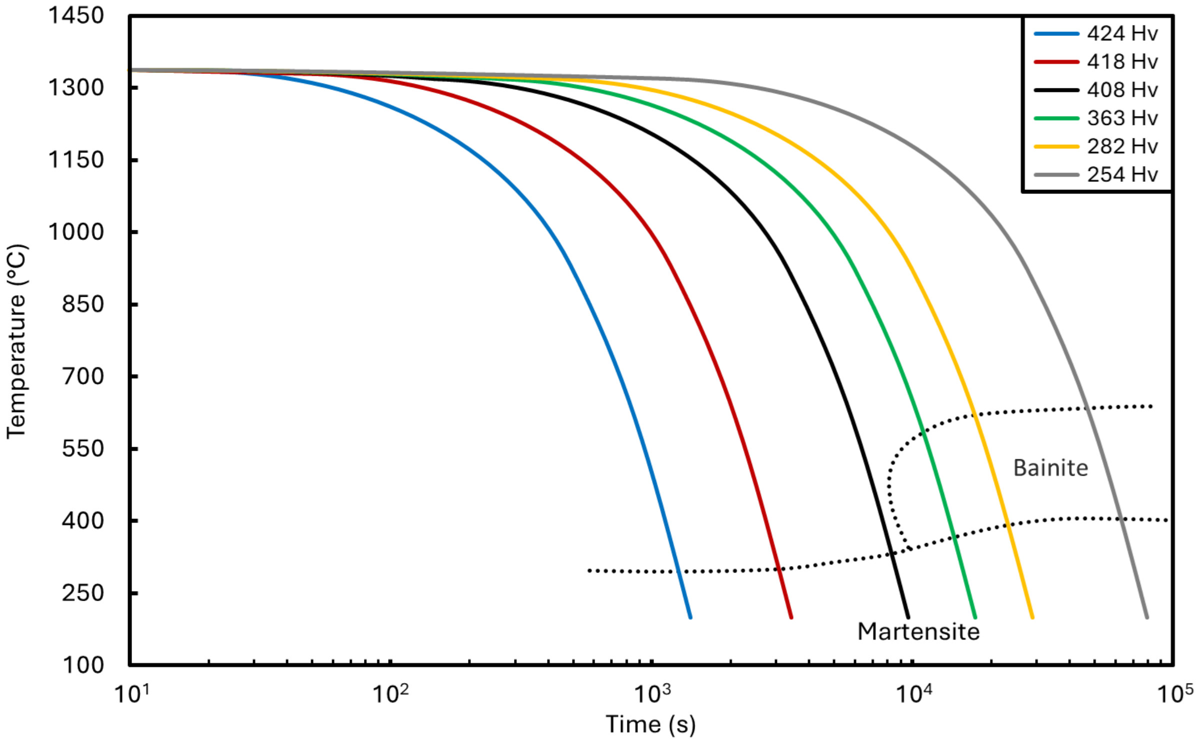

Figure 2.16 CCT diagram of a low-carbon supermartensitic stainless steel (C-0.04%, Si-0.55%, Mn-0.80%, P-0.018%, S-0.008%, Cr-12.8%, Mo-0.28%, Ni-5.25%) cooled from 1350°C (adapted)[126].

2.9 Summary of Literature Review

Increasing interfacial area per unit volume to the highest possible value is an essential purpose of this study and should be delivered by increasing the number of defects within unit volume giving rise to the number of nucleation sites which will eventually lead to a finer transformed microstructure which is acknowledged to be the only mechanism that causes to not only a higher strength but also a higher toughness. The primary methods to increase S_v value are associated with the refinement of initial austenite grain size prior to deformation, and deformation of austenite above $T_{95\%}$ or below $T_{5\%}$.

While the magnitude of S_v is influenced by the initial grain size refinement that is achieved through reheating followed by deformation above $T_{95\%}$ where large S_v values are to be expected, larger S_v values are attained with much finer transformation product traceable to a reduction below $T_{5\%}$ where the number of passes of deformation in the fully unrecrystallized region is directly related to the final value of S_v. In connection with this, alloying elements furnish the ground for further passes to be conducted within this region based on their impact on $T_{5\%}$ which, in practice, direct to higher S_v values due to enhanced microstructural control[87].

Controlling the as-rolled austenite microstructure of supermartensitic stainless steels preceding transformation is a principal target of TMP and furnishes the ground for the successful development of the desired mechanical properties. In addition, understanding the core metallurgical aspects of thermomechanical processing enables designing a specific microstructure with certain properties e.g. high strength and high toughness.

Chapter 3 Experimental Procedure

3.1 Research Compliance

All experimental work including testing, characterization, and evaluation was meticulously performed and determined in compliance with relevant specifications and practices developed by trusted sources such as ASTM standards, where applicable. Strict adherence to recognized guidelines ensures not only the reliability and reproducibility of the research outcomes but also their consistency with industry best practices. Additionally, instruction manuals and user guides for all equipment and testing procedures were thoroughly reviewed and followed to obey the same principle of compliance, with a zero-tolerance level maintained for all matters related to health and safety measures, thus ensuring a secure working environment throughout the research process.

3.2 Research Concept

Plane strain compression (PSC) testing was conducted incorporating a diverse range of processing conditions as outlined in the concept map in Figure 3.1, including deformation in both recrystallized and unrecrystallized regions, to systematically vary S_v. A series of experimental steps were planned, prepared, and executed before, during, and after PSC tests to construct a comprehensive sequence of outcomes that enabled accurate data acquisition and contributed to a deep understanding of the complex relationships and the notable differentiations between the various processing conditions and their effect on mechanical properties across three different material compositions, thereby allowing for an assessment of their response to different deformation regimes.

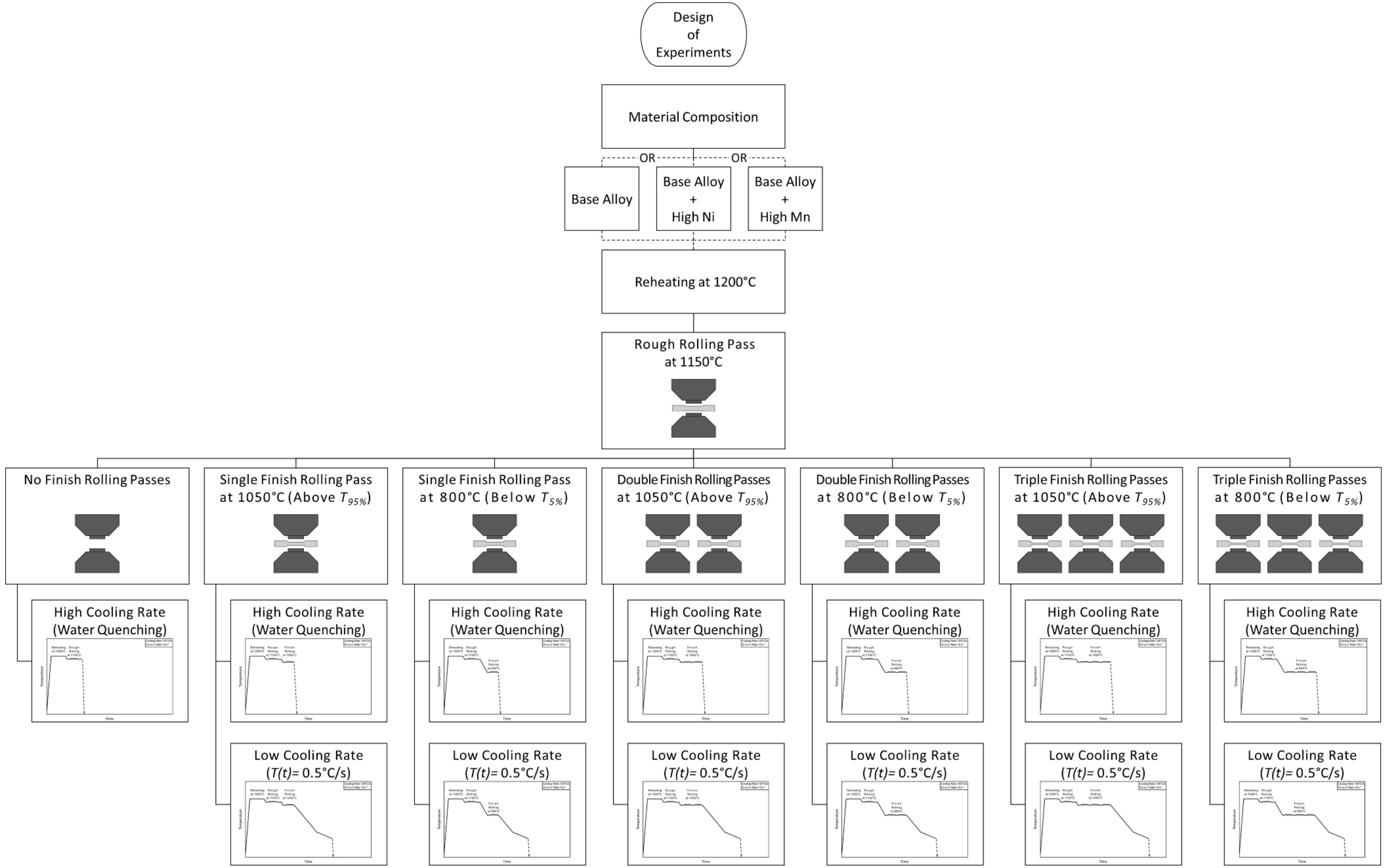

Figure 3.1 Design of experiments chart presenting the different processing conditions to be followed in this research project.

3.3 Material Manufacturing

Three supermartensitic stainless steel bars were cast using an Arcast Arc 200 arc melting furnace and homogenized at a temperature of 1200°C for 1 h and then hot rolled with a rolling reduction of 50%. The chemical composition of the alloys manufactured by arc melting is represented in Table 3.1, as determined by optical emission spectroscopy (OES), where the main difference between the three compositions is the higher nickel content in the second and the higher manganese content in the third, while the majority of other elements are within the identified range of UNS S41427 composition limits as per ANSI/NACE MR0175/ISO 15156 standard recognizing that the base steel was provided from LIBERTY Steel UK[32].

Larger homogeneous alloy casts were manufactured by Consarc small R&D vacuum induction melting furnace (VIM) presented in Figure 3.2, using the same nominal charge and weight ratios as the arc-melted alloys, and accordingly, the composition of the VIM-processed materials is considered equivalent to that reported in Table 3.1, with variations remaining within the analytical uncertainty of OES. The base steel, electrolytic iron, ferrovanadium, ferromolybdenum, ferrochromium, and nickel were placed in an alumina AL68S one-shot crucible developed by Capital Refractories; in addition, graphite, carbon, and manganese were placed in an over-melt charger to be introduced into the crucible at a later stage of melting, taking into account that the chamber was backfilled with argon from the outset to suppress element evaporation.

A mold with a footprint of 80 mm x 80 mm made of a copper base and steel plates, lined with boron nitride to prevent welding during the casting of the molten alloy, was assembled to accommodate the melt after magnetic stirring at 1550°C for 300 s when all components were completely melted and thoroughly homogenized at a medium frequency of 35 kW initiated by an induction generator in the system which was then vacuumed down to an ultralow pressure of 5×10^{-4} mbar by a diffusion pump to ensure precise control during the casting process, i.e. to maintain uniform cooling rates and minimize thermal gradients.

A total of the three rectangular cuboid ingots presented in Figure 3.3 were made via VIM where the weight of each was around 5000 g with initial dimensions of 80 mm in length x 80 mm in depth x 100 mm in height; these ingots were then homogenized at a temperature of 1200°C and hot rolled to plates down to 12 mm in thickness using FENN rolling mill machine presented in Figure 3.4. It is worth mentioning that the leftover materials that remain in each of the three crucibles were collected and preserved for additional microstructural investigation of the as-cast condition versus the as-rolled condition.

The hot rolling process was conducted on each of the three casts where each ingot underwent a total of 14 reduction passes; the first 13 passes were done with a reduction of 5 mm in thickness during each pass followed by a final pass with a reduction of 2 mm to reach the final desired thickness and the reason behind choosing this specific thickness is to ensure that specimens of 10 mm in thickness are obtained after machining taking into consideration that the end product resulting from hot rolling would have a non-even surface to a certain degree, which could influence subsequent machining precision if adequate attention is not given.

Out of these plates, plane strain compression (PSC) specimens were machined with the dimensions of 60 mm in length x 30 mm in width x 10 mm in thickness as presented in Figure 3.5; indeed, these specimens were used for subsequent PSC testing. Henceforth, the alloy with no further additions, the alloy with higher nickel content, and the alloy with higher manganese content will be referred to as Base Alloy (BA), Base Alloy ↗ High Ni (BA ↗ Ni), and Base Alloy ↗ High Mn (BA ↗ Mn), respectively, to simplify data presentation.

Table 3.1 Chemical compositions (wt%) of supermartensitic stainless steel.

Material Identification		C	Si	Mn	P	S	Cr	Mo	Ni	Ti	V
BA		0.019	0.18	0.30	0.011	0.005	12.10	1.95	5.38	<0.01	0.15
BA ↗ Ni		0.019	0.19	0.33	0.011	0.005	12.10	1.93	6.42	<0.01	0.15
BA ↗ Mn		0.017	0.19	1.02	0.010	0.005	12.06	1.93	5.32	<0.01	0.15
UNS S41427	Min.	-	-	-	-	-	11.50	1.50	4.50	-	0.10
	Max.	0.300	0.05	1.00	0.020	0.005	13.50	2.50	6.50	0.01	0.50

Figure 3.2 Vacuum induction melting furnace used for casting of the three homogeneous 5000 g ingots, located at Royce Discovery Centre.

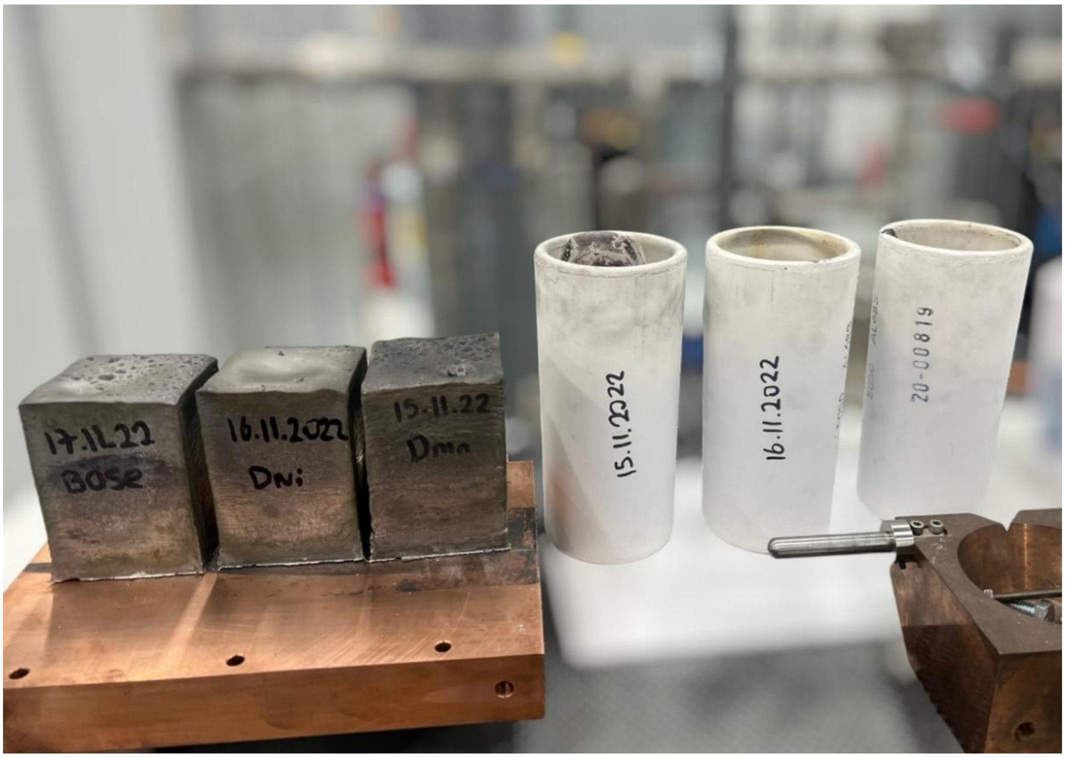

Figure 3.3 The three 5000 g ingots cast via VIM (left) along with the one-shot liners which were dried and conditioned by applying a low induction power that was increased gradually until the alloys were melted (right).

Figure 3.4 Hot rolling mill used to roll the three ingots into plates, reducing their thickness to 12 mm, where one of these plates appears at the bottom right corner.

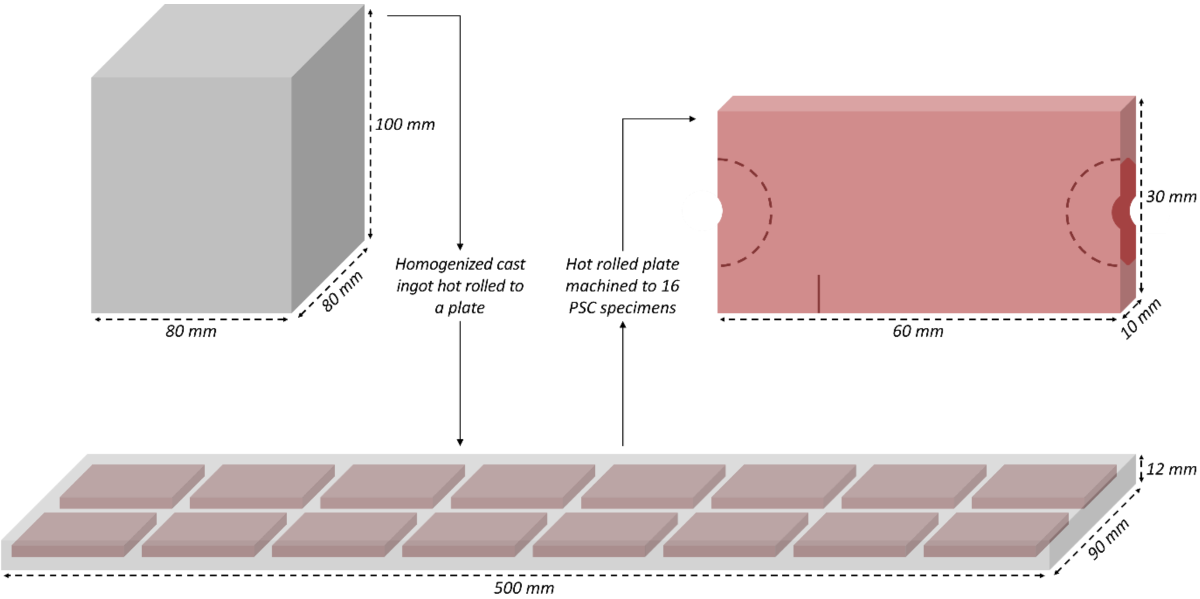

Figure 3.5 Illustration of the process followed to manufacture the PSC specimens; taking into consideration that all were aligned with the rolling direction.

3.4 Dilatometric Assessment

In advance of dilatometry, simulations were done via a simulation software, JMatPro 7.0, to identify the phase transformation temperatures, A_{c1} and A_{c3}, for the three different compositions with an estimated austenite grain size of 200 µm. Within this framework and for more precise determination, phase transformation temperatures were determined by dilatometry where small cylindrical specimens with dimensions of 10 mm in length and a diameter of 6 mm were machined along the rolling direction to measure the thermal expansion as a function of temperature in a controlled atmosphere where specimens were heated to 1200°C at a rate of 5.0°C/min (0.08°C/s) and then cooled to ambient temperature at the same rate[127,128].

Curves representing the fractional change in length against temperature during heating and cooling were acquired from a computerized system connected to the dilatometer DIL 402 Expedis Classic presented in Figure 3.6, which were used to determine these temperatures for the three different compositions as these two temperatures are associated with the chemical composition taking into account that the system was vacuumed in order to prevent possible oxidation.

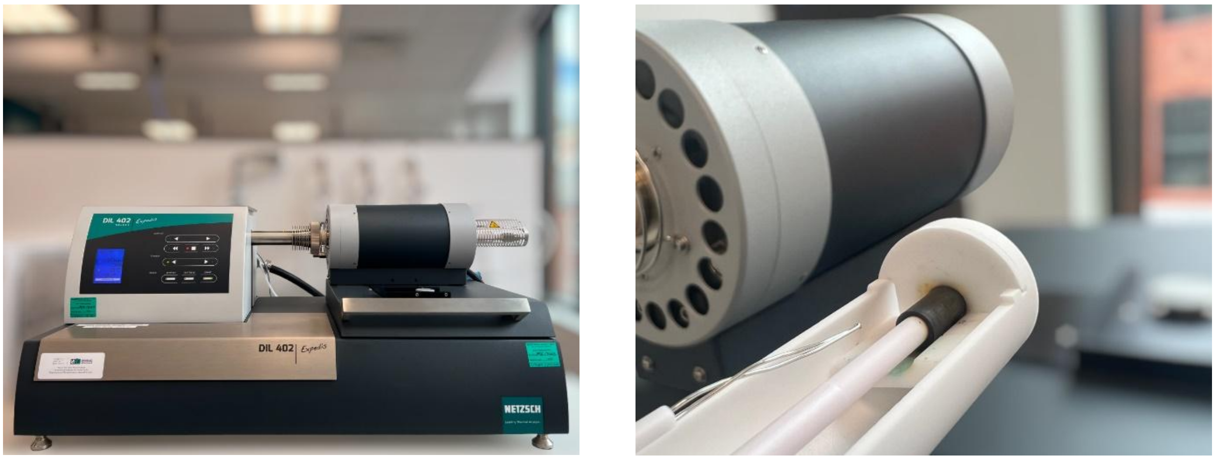

Figure 3.6 Dilatometer apparatus used for measurement and identification of critical transformation temperatures during continuous heating and cooling, temperatures were measured by a thermocouple located in close proximity to the sample to maintain the accuracy of dilation readings.

The determination of the critical transformation temperatures (A_{c1}, A_{c3}, and M_s) followed the procedure described in the ASTM A1033 standard, where the measurements were derived directly from the length-temperature curves obtained during dilatometry[129]. A_{c1} and A_{c3} were obtained by constructing tangent lines on the heating portion of the curve; in practice, the first tangent was drawn to the linear segment preceding the contraction associated with the transformation from martensite to austenite, and the second tangent was drawn to the segment after the transformation region where thermal expansion resumed.

The intersections of these lines defined A_{c1} and A_{c3}, marking the characteristic slope changes where strain first decreased and then increased with temperature. During cooling, the martensitic start temperature, M_s, was identified at the inflection point where the linear contraction of austenite deviated toward expansion, indicating the onset of transformation from austenite to martensite; this approach followed the derivative and extrapolation method outlined in ASTM A1033, where slope deviations and extrapolated austenite baselines are used to identify the start and progress of transformation, with an an example of this method illustrated in Figure 3.7[129].

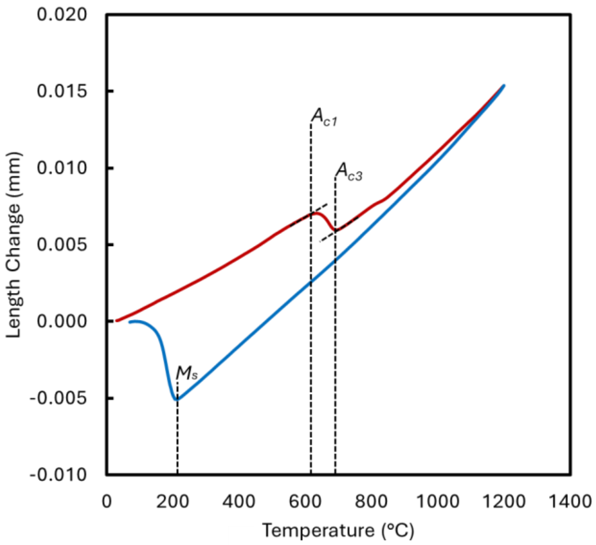

Figure 3.7 An example of a dilatometer curve used for determination of critical transformation temperatures during continuous heating and cooling of the alloy with higher manganese content where the black dashed lines represent the extrapolation process used to define A_{c1}, A_{c3}, and M_s.

3.5 Thermomechanical Compression

Plane strain compression (PSC) tests were carried out as per the revised version of the measurement good practice guide NPL-CMMT (GPG)027; in principle, specimens that were machined from plates to the dimensions illustrated in Figure 3.8 were deformed at specified pre-defined conditions of different temperatures and strains to measure the change in load and displacement against temperature using the thermomechanical compression (TMC) machine presented in Figure 3.9 which is a modified system of the oldest TMC that was developed for the first time in its history by Servotest in cooperation with the University of Sheffield[130].

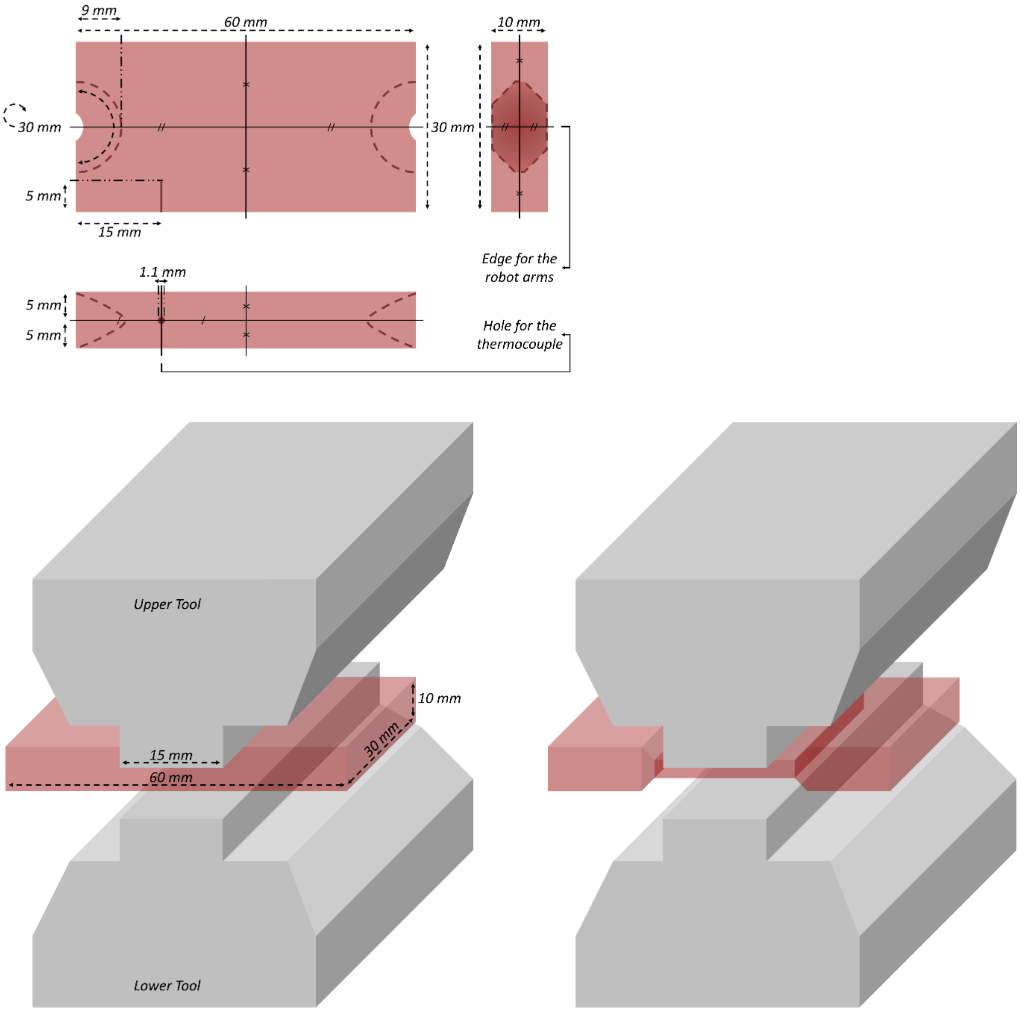

Figure 3.8 Schematic diagram of a plane strain compression test illustrating the standard dimensions and position of a test piece, highlighted in red, equally distant between the upper and lower tools prior to deformation (left) and post deformation (right).

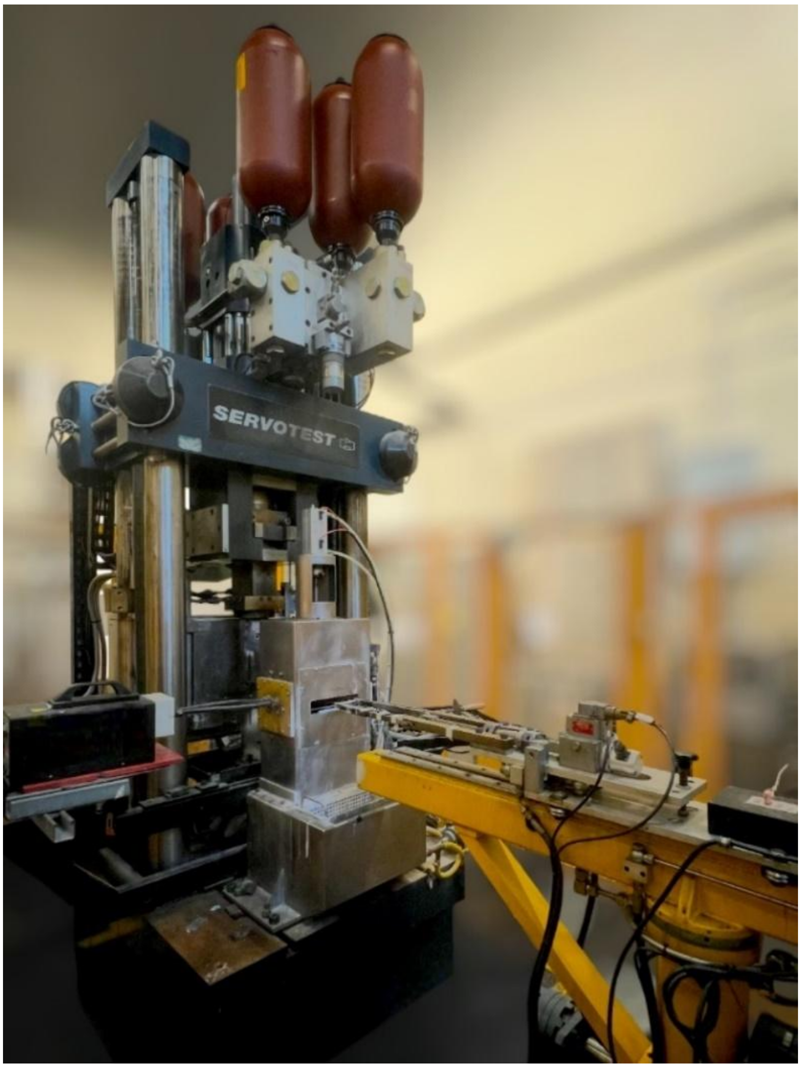

Figure 3.9 Thermomechanical compression (TMC) machine used for deformation at a specified temperature and strain rate.

Experiments were conducted above the recrystallization-limit temperature $T_{95\%}$ and below the recrystallization-stop temperature $T_{5\%}$ with an initial strain of 0.3 and a final strain that was increasing gradually by 0.3 resulting in a final total strain of 0.6, 0.9, or 1.2; in operation, a rough rolling pass was done at 1150°C followed by a finishing pass or more at 1050°C or 800°C, which were identified as the temperatures above and below $T_{95\%}$ and $T_{5\%}$, respectively. A comprehensive full testing assessment was performed starting from controlled heating to controlled cooling, where different sets of strain compression tests were conducted to investigate the deformation impact on the final product where S_v was the significant parameter in determining this influence.

Based upon the historical understanding of the thermomechanical behavior of supermartensitic stainless steels, it was initially anticipated that 1050°C would be positioned above $T_{95\%}$ and 800°C would fall below $T_{5\%}$. With the intention of promoting either fully recrystallized or fully unrecrystallized austenitic microstructures, these assumptions regarding both selected temperatures were later validated through detailed microstructural characterization, as presented in Section 4.3.2. To clarify, if a given condition failed to yield the expected transformation state during microstructural examination, i.e. if austenite was not fully recrystallized at the presumed temperature above $T_{95\%}$ or not fully unrecrystallized at the presumed temperature below $T_{5\%}$, then alternate finishing temperatures would be selected through progressive trial-and-error adjustment.

For the avoidance of doubt, if austenite exhibited partial recrystallization instead of fully recrystallized or fully unrecrystallized austenite, the finishing deformation temperatures would simply be increased or decreased accordingly, depending on the observed outcome. The reason for not precisely determining these temperatures beforehand is due to the fact that the primary aim of this study was to investigate the development of S_v as a function of strain and composition in a systematic and comparative manner; evaluating how it evolves from microstructures transformed from fully recrystallized versus fully unrecrystallized austenite, rather than focusing on exact thermodynamic thresholds.

Several measures were adopted prior to conducting any PSC test including but not limited to repositioning the crosshead of the thermomechanical treatment simulator to an ideal height where the upper and lower tools would be slightly in contact, zeroing the transducers to ensure that the crosshead was not tremendously lowered or considerably elevated, and testing the stiffness to ensure the compliance of the machine, in addition to other precautions of a similar instrumentation and calibration nature that are typically required for achieving consistent and repeatable experimental conditions.

A number of functions were fulfilled to accommodate the test in a systematic configuration minimizing the probability of testing deficiencies or biased outcomes, key aspects of appropriate test embraced setting up the temperature of the preheat furnace and the main furnace, identifying the sample parameters including height, width, and geometric factor as well as the logged signals to be recorded including displacement, load, velocity, temperature and other parameters of interest, and delineating the test sequence through outlining the various segments and their parameters which were the most critical aspect before running the plane strain compression test.

A massive number of segments could be outlined, segments of interest depended mainly on the fast thermal treatment unit (FTTU) where all tests commenced by heating the sample from ambient temperature to 1200°C and holding it for 300 s, followed by cooling it down to 1150°C where it was prepared to handle a rough rolling pass in advance of further FTTU segments as per the predefined processing conditions, e.g. finish rolling passes at 1050°C or 800°C ahead of cooling by air, mist or water spry, where an example of a full test profile for one of the 39 PSC tests which were conducted following the design of experiments, outlined earlier in Figure 3.1, is presented in Figure 3.10.

A particular emphasis was placed on the thermocouple by securing its functionality and firm connection with the sample through precise alignment and controlled positioning to avoid bending or tilting, ensuring it remained parallel to the robotic arms of the testing system. The thermocouple was fixed in place using high-temperature adhesive tape, allowing sufficient free space for movement while ensuring it was carried exclusively by the motion of the arms rather than moving independently, considering the fact that the test would fail for an eventuality of thermocouple failure; in addition, the test piece was lubricated with boron nitride to protect the surface from possible oxidation as presented in Figure 3.11. A successful test would lead to further processing of certain recorded variable parameters with time such as changes in load, crosshead velocity and displacement, and many others to identify the true stress and equivalent strain providing valuable flow curves as outlined in the revised version of the measurement good practice guide NPL-CMMT (GPG)027 bearing in mind the fact that further microstructural investigation would be carried on the test piece itself[130].

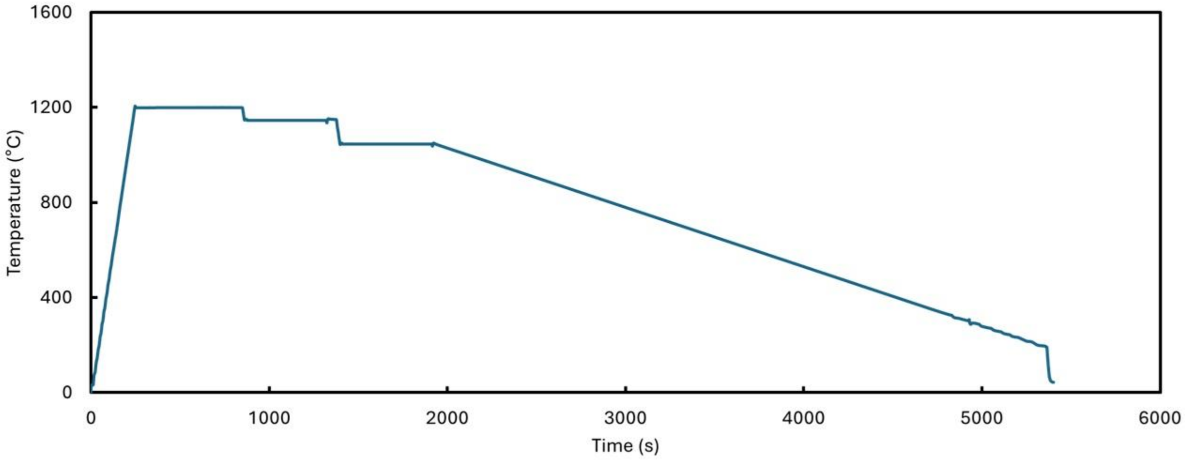

Figure 3.10 PSC test profile illustrating temperature as a function of time during the different segments of the test, shedding light on the fact that real-time readings were transmitted by the thermocouple and displayed on the main dashboard for instant monitoring purposes.

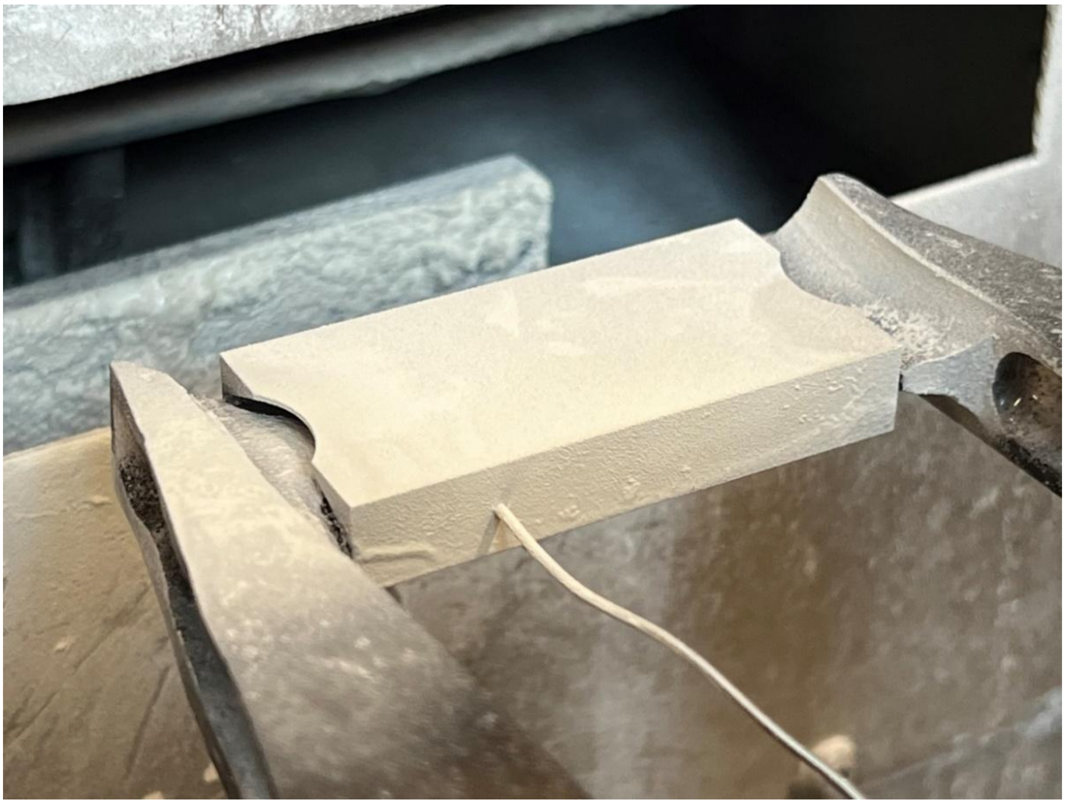

Figure 3.11 SPC test piece lubricated by boron nitride, connected with the thermocouple, and held by the robot arms.

3.6 Metallographic Preparation

3.6.1 Prior to Deformation

As a matter of material characterization, metallographic preparation of specimens was performed as per ASTM E3 standard to reveal the general microstructure where a sample from each alloy composition was sectioned along the rolling direction via Secotom-20, hot-compression mounted in a conductive Bakelite resin via SimpliMet 1000, and mechanically ground by with conventional silicon carbide papers ranging from P120 up to P2500 and then, mechanically polished with diamond particles down to 1 µm in diameter; detailed procedure followed throughout each stage of the modified automated preparation method which was done via EcoMet 250 Pro is presented in Table 3.2[131].

Table 3.2 Stages of the specimen preparation method utilizing grinding papers and polishing cloths (adapted)[132].

	Abrasive parameters			Mechanical Parameters				
Stage	Type	Grade	Fluid	Speed[a]	Speed[b]	Direction	Force[c]	Time[d]
1	SiC	P120 - P2500	Water	60	240	Comp[e]	22	120
2	Diamond	6 µm	Suspension	60	150	Comp[e]	18	180
3	Diamond	3 µm	Suspension	60	150	Comp[e]	18	180
4	Diamond	1 µm	Suspension	60	150	Contra[f]	18	300

[a]Powerhead speed, in rpm. [b]Platen speed, in rpm. [c]Applied to 25 mm diameter mount, in N. [d]Stage time, in s. [e]Work wheel and specimen holder rotate in the same direction. [f]Work wheel and specimen holder rotate in the opposite direction.

Once a mirror-like surface was obtained, specimens were etched in a fume hood at ambient temperature with Vilella's reagent to reveal the general microstructure for the three compositions as per ASTM E407 standard; further details regarding this etchant are presented in Table 3.3[30,133].

Table 3.3 Composition of Vilella's reagent and procedure to reveal microstructure (adapted)[133].

Etchant	Composition	Procedure
Vilella's Reagent	5 mL HCl 1 g picric acid 100 mL ethanol (95%) or methanol (95%)	Immerse for a few seconds at a time until the desired results are obtained

3.6.2 During Deformation

Metallographic preparation of specimens was performed as per ASTM E3 standard to reveal the deformed microstructure where each of the PSC test pieces was sectioned from the middle and a sample towards the long transverse direction perpendicular to the rolling direction was acquired for all processing conditions, i.e. deformation in recrystallized and unrecrystallized regions, in conjunction with another sample towards the short transverse direction only for the deformation condition in which unrecrystallized microstructures were attained; an illustration of the orientation and location of the area under characterization is presented in Figure 3.12.

Deformed specimens were mounted, ground, and polished in the same manner as the undeformed specimens were prepared; however, these specimens were etched in a fume hood at ambient temperature with ASTM 36 ferric chloride etch to reveal the deformed microstructure as per ASTM E407 standard; further details regarding this etchant are presented in Table 3.4[30,133].

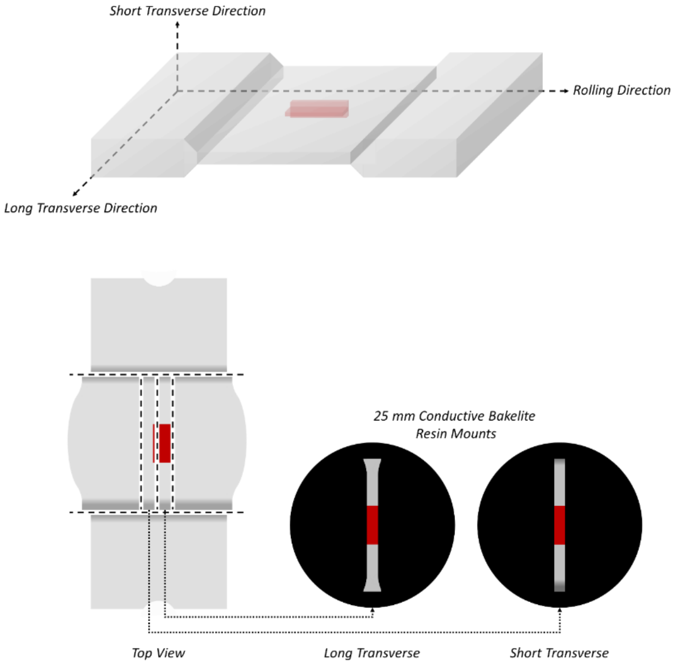

Figure 3.12 Schematic view of the PSC test piece clarifying the location of the samples sectioned for further examination, highlighted in red, in the center of the test piece towards the long and short transverse directions.

Table 3.4 Composition of ASTM 36 etch and procedure to reveal microstructure (adapted)[133].

Etchant	Composition	Procedure
ASTM 36 Ferric Chloride Etch	25 g $FeCl_3$ 25 mL HCl 100 mL water	Immerse for a few seconds at a time until the desired results are obtained

3.7 Microstructural Analysis

Beyond a shadow of a doubt, optical microscopy provided an acceptable general overview of the general microstructure, but its resolution is limited, and greater depth of field at the same magnification and higher magnifications attracted attention to the value of utilizing some more powerful tools including scanning electron microscopy (SEM) and its based techniques such as energy dispersive spectroscopy (EDS) and electron backscatter diffraction (EBSD) to define the microstructure and proceed with the quantitative analysis of the three different compositions processed under different conditions. Hence, only the microstructure prior to deformation was evaluated via optical microscopy, while the microstructure post deformation was evaluated via electron microscopy. Together, SEM, EDS, and EBSD formed an integrated characterization suite combining surface morphology, elemental composition, and crystallographic orientation. SEM provided detailed imaging of deformation features and grain morphology; EDS confirmed compositional uniformity and identified segregation; and EBSD quantified orientation, phase distribution, and substructure development. The complementary use of these techniques ensured a comprehensive and quantitative understanding of how thermomechanical processing influenced the morphology, chemistry, and crystallography of the studied alloys.

3.7.1 Scanning Electron Microscopy

Specimens of each and all deformation conditions were characterized by SEM to reveal the morphology of the deformed microstructure and highlight the grain boundaries and other main microstructural features to be quantified. SEM operates by scanning a finely focused beam of high-energy electrons across the specimen surface. As the incident beam interacts with atoms, it generates secondary electrons that emerge from the top few nanometers of the surface and backscattered electrons that depend on atomic number, together forming an image with topographic and compositional contrast[134]. The technique therefore enables visualization of grain morphology, phase distribution, and deformation features with a resolution much higher than optical microscopy.

Rigorously, the different microstructures of polished samples were observed at a high resolution via FEI Inspect F50 which is presented in Figure 3.13 where the parameters used were the same all along the line to ensure consistency of reported total S_v values, and in particular while comparing between the morphologies of different conditions, e.g. two different compositions at a constant temperature and strain. Accordingly, the Everhart-Thornley detector was operated in combination with a high-vacuum in secondary electron (SE) mode at an accelerating voltage of 20 kV, an analytical working distance of 10 mm, a spot size of 3.5, and a magnification of x1000 which provided satisfactory micrographs of the sophisticated surface morphology.

Figure 3.13 Inspect F50 scanning electron microscope used to acquire high resolution images of the deformed microstructure.

3.7.2 Energy Dispersive Spectroscopy

Selected specimens were characterized by SEM coupled with an X-Max 80mm^2 EDS silicon drift detector for elemental analysis purposes, i.e. determination of the presence of specific elements, and to confirm the homogeneity of the presented elements. EDS operates by detecting the characteristic X-rays emitted when the electron beam displaces inner-shell electrons from atoms in the specimen. As outer-shell electrons fill these vacancies, X-rays with element-specific energies are produced; measurement of these energies enables qualitative and quantitative elemental analysis[134]. This method therefore provides a direct means of confirming elemental distribution and identifying segregation or compositional gradients within the investigated alloys.

Consequently, a few EDS maps were captured and analyzed by an acquisition and analysis software, AZtec 6.1. The decision on which specimens to characterize and whether to proceed with further characterization was made based upon the initial EDS maps representing whether segregation was presented or not. If segregation was detected, additional characterization would be carried out to evaluate its extent and assess its implications on microstructural evolution.

3.7.3 Electron Backscatter Diffraction

Specimens of various deformation conditions which trigger attention for further investigation via EBSD were mounted, ground, and polished following the same procedure outlined previously in Table 3.2; however, these specimens were vibratory polished for 1.5 h at a vibration amplitude of 30% with a 0.02 µm non-crystallizing colloidal silica suspension; furthermore, these specimens were ultrasonically cleaned in distilled water for 10 min to remove any residuals of colloidal silica remained following vibratory polishing via VibroMet 2.

Thereafter, specimens were etched for 2 h at an ion beam energy of 5.0 keV and a rotation speed of 6 rpm with a tilt angle of 4° for both argon ion guns using a precision etching coating system, PECS II 685, which is presented in Figure 3.14 noting that specimens during this stage were mounted onto 12.5 mm x 10 mm aluminum cylinder stubs using fast drying silver paint post to their extraction from Bakelite mounts; an illustration of the orientation and location of the area under characterization is presented in Figure 3.15.

EBSD is a crystallographic technique integrated within the SEM that determines local crystal orientation and phase by analyzing the Kikuchi diffraction patterns formed when backscattered electrons satisfy Bragg diffraction conditions on a tilted, polished crystalline surface, where each pattern corresponds to a distinct lattice orientation, and automated indexing across the scanned area yields orientation maps that reveal grain morphology, misorientation, and boundary character[135]. Low-angle boundaries correspond to sub-grains or dislocation arrays, whereas high-angle boundaries delineate prior grains or recrystallized regions. This capability made EBSD essential for quantifying deformation, recovery, and recrystallization mechanisms in this study.

It matters to remark that the total S_v findings were the main criteria for identifying the extreme conditions to be investigated via JSM-7900F which is presented in Figure 3.16 where a total of eight EBSD maps were captured to reconstruct the prior austenite grains of the base alloy with no further additions versus the base alloy with higher manganese content when those alloys were deformed at high and low temperatures with final strains of 0.6 and 1.2; while neither the base alloy with higher nickel content was investigated nor all alloys with a final strain of 0.9 considering that those conditions were outside of the above-mentioned criteria.

Reconstruction of PAG relying on the captured inverse pole figure (IPF) maps obtained via EBSD, using a step size not exceeding the threshold of ~0.1 µm, was achieved via a processing software, AZtecCrystal 6.1, to identify the austenitic microstructure and reveal its boundaries prior to deformation, employing the Nishiyama-Wasserman crystallographic orientation relationship targeting high-angle grain boundaries (HAGB) with misorientation angles greater than 10°.

Thereafter, the relationship was refined to improve the reconstruction of PAG further and accurately define parent and child phases, i.e. fcc austenite and bcc martensite, respectively, which enabled quantification of PAG contribution to the total S_v for selected processing conditions outlined previously which were acknowledged to exhibit an extreme behavior[136–138]. In addition, PAG was reconstructed by another processing software, i.e. MTEX 6.0, yet in the same vein outlined previously while explaining data processing aided by AZtecCrystal 6.1, where the underlying reasons were to validate the accuracy of the reconstruction and pinpoint intrinsic differences between the outcomes of the two software, if any[136–140].

Following the reconstruction of PAG, quantitative evaluation of PAG size and, where appropriate, transverse intercept distance was performed using two distinct approaches matched to the microstructural geometry of each condition. All measurements were refined by applying the internal noise-reduction and data-cleaning filters that excluded dubious grains and removed polygons intersecting the map borders to ensure statistical validity and eliminate artifacts from edge truncation.

Both recrystallized and unrecrystallized morphologies were analyzed using procedures suited to their geometry. For equiaxed grains (recrystallized), statistical grain size determination followed ASTM E2627, reported as average grain size[141]. For elongated grains (unrecrystallized), a separate directional line-intercept method based on ASTM E112 was used to characterize effective grain thickness orthogonal to the elongation axis, reported as an average transverse intercept distance[142]. This ensured that all reported grain metrics reflected the physical dimensions relevant to each microstructural state, rather than orientation distortions caused by deformation.

For the conditions deformed at 1050°C with total strain amounts of 0.6 and 1.2, the ASTM E2627 grain size numbers were extracted directly from AZtecCrystal 6.1, as these microstructures were fully recrystallized and exhibited equiaxed morphologies amenable to automated statistical quantification. Via the standard ASTM relation between grain size number and mean grain area, these values were converted to average prior austenite grain size and reported as equivalent circle diameters. At these conditions, the reconstructed PAG were well defined and continuous across the analyzed areas, allowing accurate grain size determination based on complete polygonal segmentation without the need for directional correction or manual adjustment.

Conversely, for the conditions deformed at 800°C with total strain amounts of 0.6 and 1.2, where recrystallization was incomplete and the microstructure remained elongated, average PAG thickness was evaluated via a directional line-intercept method. Five equidistant test lines of fixed length, i.e. 85 µm, were drawn at ~90° to the elongation direction, the number of reconstructed PAG boundary intercepts along each line was counted, and the average transverse intercept distance was obtained by dividing line length by intercept count and averaging over the five lines, where smaller values indicated a thinner effective grain thickness and larger values a greater transverse dimension. Since the PAG were elongated primarily along the rolling direction, intercepts measured orthogonal to that axis provided a representative measure of effective transverse grain thickness, whereas intercepts along 0° would exaggerate aspect ratios due to deformation-induced elongation.

Quantitative parameters such as Kernel Average Misorientation (KAM), martensite lath and block size, and retained austenite fraction were not extracted in the present analysis. The EBSD step size of approximately 0.1 µm is comparable to the expected martensitic lath width of 0.1-0.3 µm, which would cause under-sampling and limit the reliability of such measurements, while KAM is highly sensitive to step size, pattern noise, and neighbor-definition criteria. In addition, retained austenite present in very low volume fractions is more accurately quantified by X-ray diffraction with Rietveld refinement than by EBSD indexing. The analysis therefore focused on total S_v and reconstructed PAG, which provide a more robust basis for microstructural quantification under the present conditions.

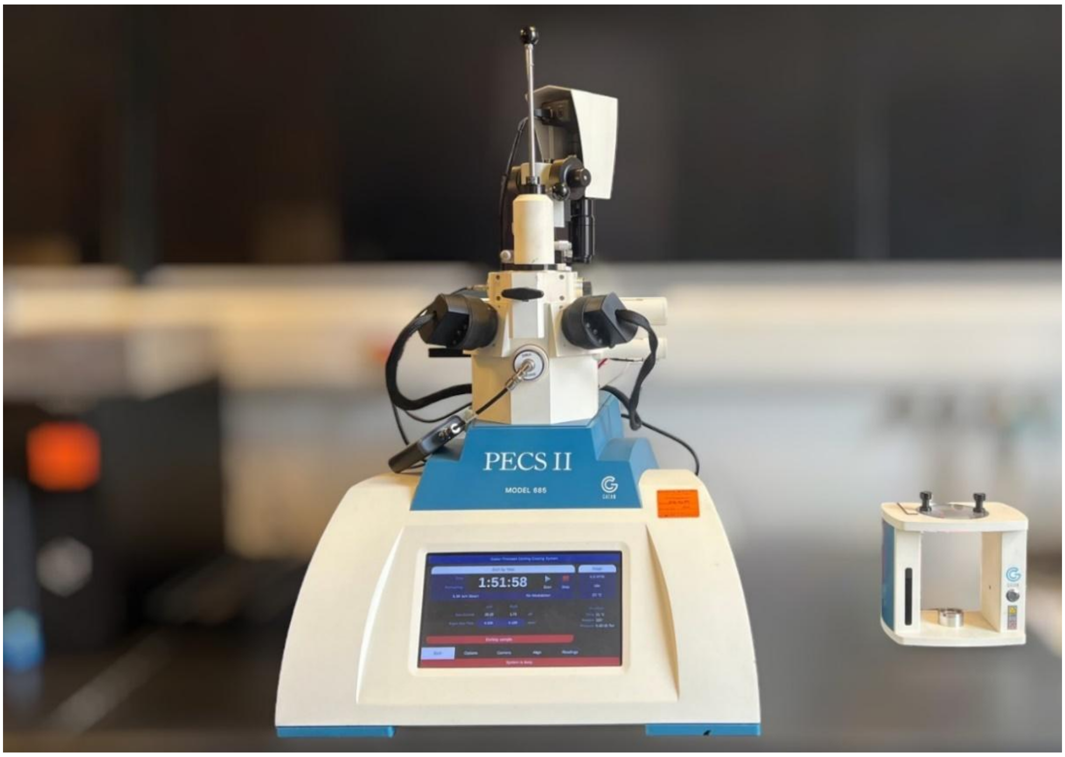

Figure 3.14 Automated argon ion polishing system used to accomplish damage-free surfaces securing successful EBSD analysis; the loading dock on the right-hand side is used to adjust the height of the mounted specimen before transferring it into the system.

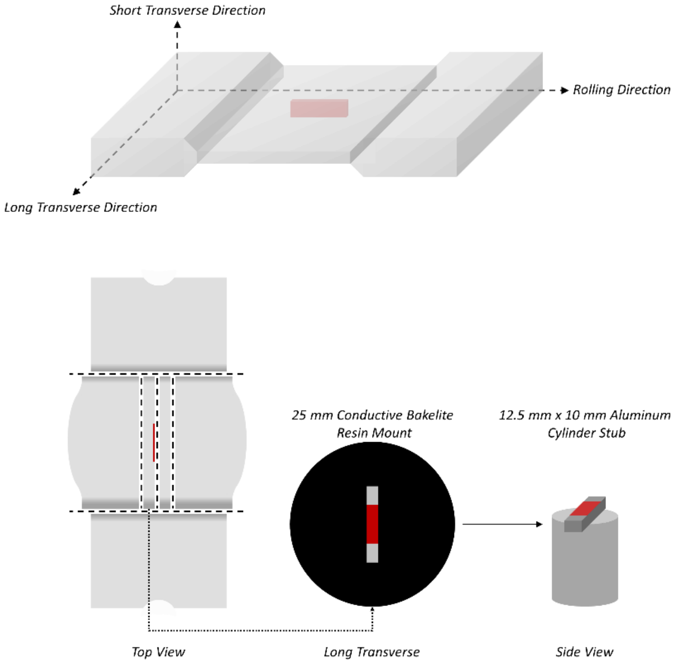

Figure 3.15 Schematic view of the PSC test piece clarifying the location of the samples sectioned for EBSD examination, highlighted in red, in the center of the test piece towards the long transverse directions.

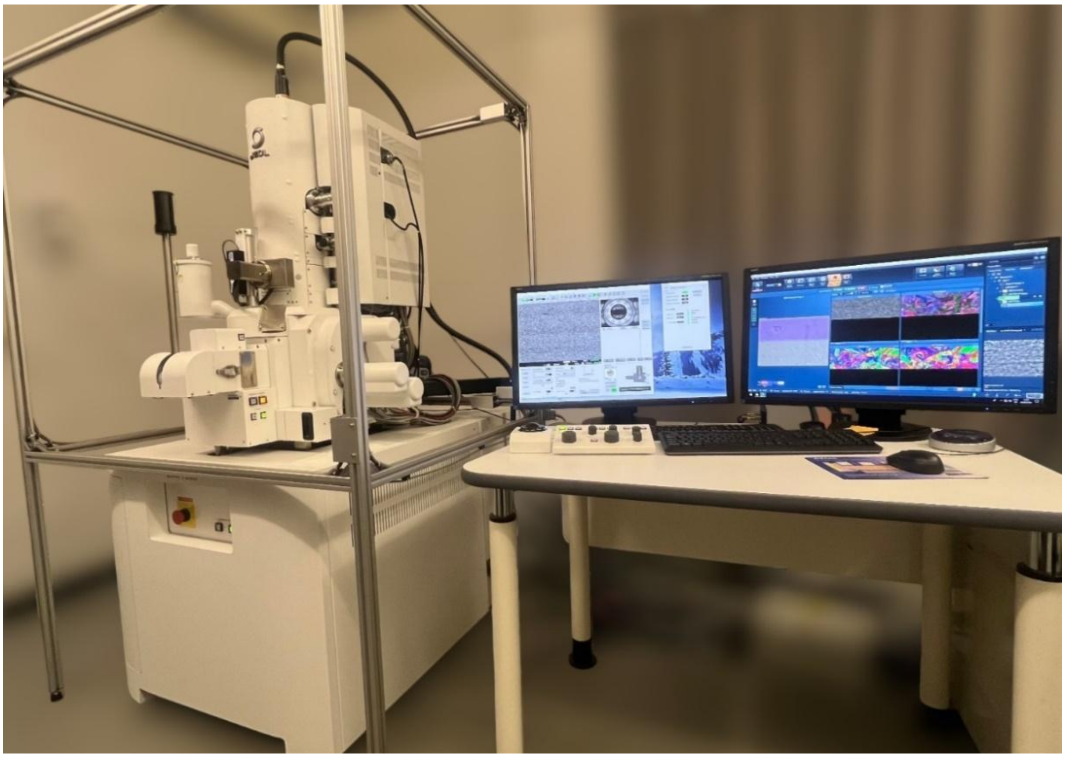

Figure 3.16 Schottky field emission scanning electron microscope used to perform distortion-free EBSD analysis.

3.8 Microstructure Quantification

3.8.1 Interfacial Area per Unit Volume S_v

S_v is the key element in this research for understanding the behavior of alloys deformed under various conditions; precise quantitative measurements were carried out for every condition applied to each and all compositions relying on the resulted microstructure as a reference for quantitative evaluation where, for every condition, four separate fields-of-view under the same magnification of x1000 were captured via SEM to ensure higher confidence of the reported S_v values. These S_v values were determined by analyzing the deformed microstructure through the Abrams Three-Circle Procedure as per ASTM E112 standard, relying on the geometric analysis of the intersecting circles within the microstructure to quantify grain size[142].

An example of how this methodology was followed is presented in Figure 3.17 and details regarding the analyzed fields are provided in Table 3.5 taking into consideration that this data was directed toward determining total S_v values for conditions under investigation by:

$$N_L = \frac{N_i}{L/M} \qquad \text{Equation 3.1}$$

where N_L is the number of intercepts per unit length of the test line, N_i is the number of intercepts counted on each field, L is the total test line length, and M is the magnification[142]. Once this parameter was determined, total S_v was then calculated straight forward equation that is:

$$S_v = 2N_L \qquad \text{Equation 3.2}$$

where S_v is the total effective interfacial area per unit volume of recrystallized austenite, and N_L is the number of intercepts per unit length of the test line[142]. The average and standard deviation of total S_v were then calculated based on the quantified fields for each deformation condition highlighting that circular methodology was followed in particular to avoid possible bias caused by taking measurements in a linear fashion. While it would not matter with the recrystallized microstructure; it would matter significantly for the unrecrystallized microstructure where the circles compile different directional orientations into a sort of plane field. For this reason, a circular methodology was adopted to reflect rigorous quantification of the microstructure based on composition differences and processing conditions leading to establishing a relationship between the quantified microstructure and the measured mechanical properties[98,142–144].

Table 3.5 An example of data from which total S_v was quantified via the Abrams Three-Circle procedure for an alloy with higher manganese content deformed at 1050°C and quenched in water.

Field	Magnification	Circumference (µm)	Number of Intercepts	Total S_v (mm^{-1})
A	x1000	700	229	612000
		500	137	
		300	93	
B	x1000	700	198	592000
		500	164	
		300	82	
C	x1000	700	182	556000
		500	158	
		300	77	
D	x1000	700	172	548000
		500	168	
		300	71	

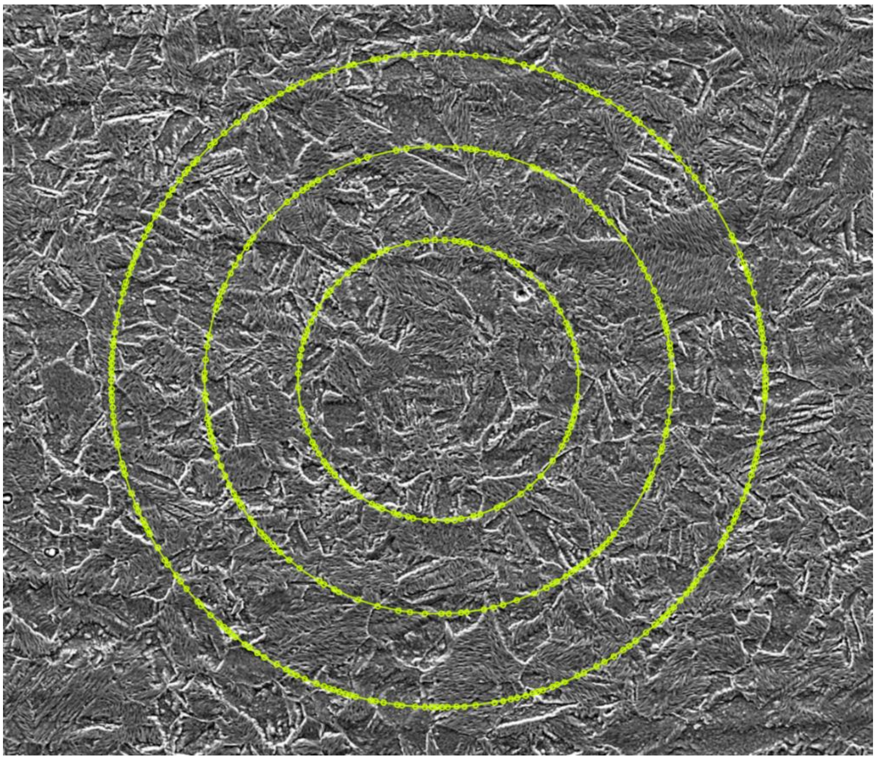

Figure 3.17 An example of Abrams Three-Circle methodology for an alloy with higher manganese content deformed at 1050°C and quenched in water.

3.8.2 Prior Austenite Grains (PAG) Contribution to Total S_v

The contribution of prior austenite grains (PAG) to the total S_v for the extreme conditions was investigated and quantified adhering to the same procedure followed to analyze the total S_v, i.e. Abrams Three-Circle Procedure as per ASTM E112 standard[142]. However, only a single field of view at a magnification of x1000 was captured for each extreme condition explaining the absence of error bars for the reported PAG contribution to total S_v despite their presence for the reported total S_v, yet the reconstructed EBSD maps revealed reliable results.

Pondering these considerations, investigation of the austenite grains at the point of transformation was performed by breaking the confusing martensitic microstructure apart and measuring only the contribution of the reconstructed PAG to the total S_v excluding all other defects present in the deformed microstructure, for the selected conditions. An example of how this methodology was followed is presented in Figure 3.18.

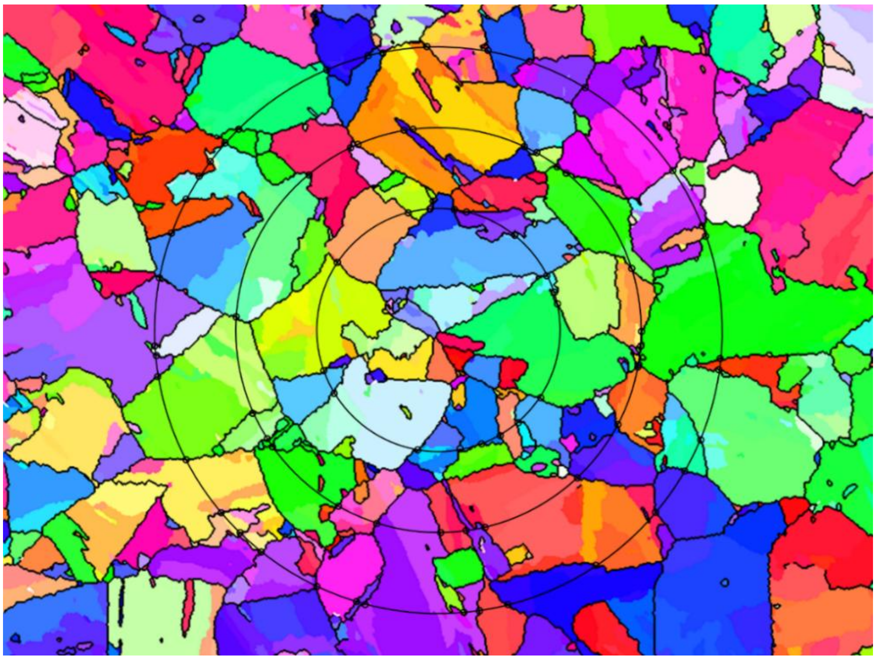

Figure 3.18 An example of Abrams Three-Circle methodology for the same alloy whose microstructure is presented in Figure 3.17.

3.9 Mechanical Properties

3.9.1 Instrumented Indentation Testing

Nanoindentation tests were performed at ambient temperature as per ASTM E2546 standard using the NanoTest Vantage system presented in Figure 3.19, where a controlled load of 1000 µN was applied at a loading and unloading rate of 200 µN/s with a holding time of 2 s to measure the mean contact pressure, p_m, of some of the alloys under study and investigate their response to the different processes to which the material was subjected, from which Vickers hardness was evaluated via the following equation:

$$HV = H \times 0.094495 \qquad \text{Equation 3.3}$$

where HV is the Vickers hardness, and H is the Meyer hardness that is equivalent to the mean contact pressure, i.e. $H = p_m$[145,146]. A 2 x 5 grid pattern equally spaced by an offset of 20 µm in the vertical and horizontal directions was defined to conduct ten indentation measurements on the long transverse surface mounted in a conductive Bakelite resin and etched with ASTM 36 ferric chloride after polishing down to 1 µm as presented earlier in Figure 3.12.

3.9.2 Uniaxial Tension Testing

Tensile tests were performed at ambient temperature as per ASTM E8 standard using the ZwickRoell ProLine materials testing machine presented in Figure 3.20 to evaluate the properties of the alloys under study and compare the different processes to which the material was subjected, where test pieces with a gage length of 12 mm and gage width of 2 mm were machined from the middle section of the PSC specimens which were previously deformed at 800°C and 1050°C, perpendicular to the rolling direction as illustrated in Figure 3.21[147].

Figure 3.19 NanoTest Vantage system used to perform depth versus load hysteresis nanoindentation testing.

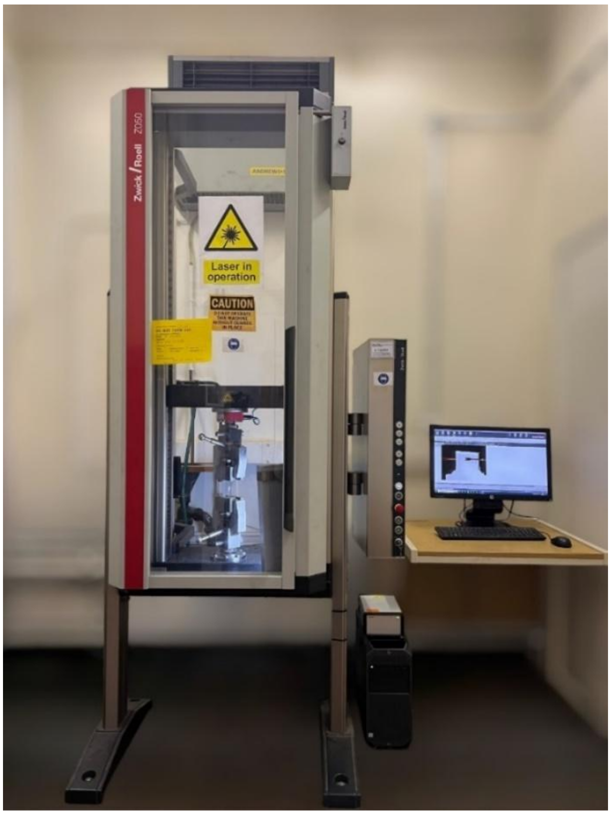

Figure 3.20 Universal testing machine used for tensile testing through applying a specific force and capturing the elongation of material until fracture.

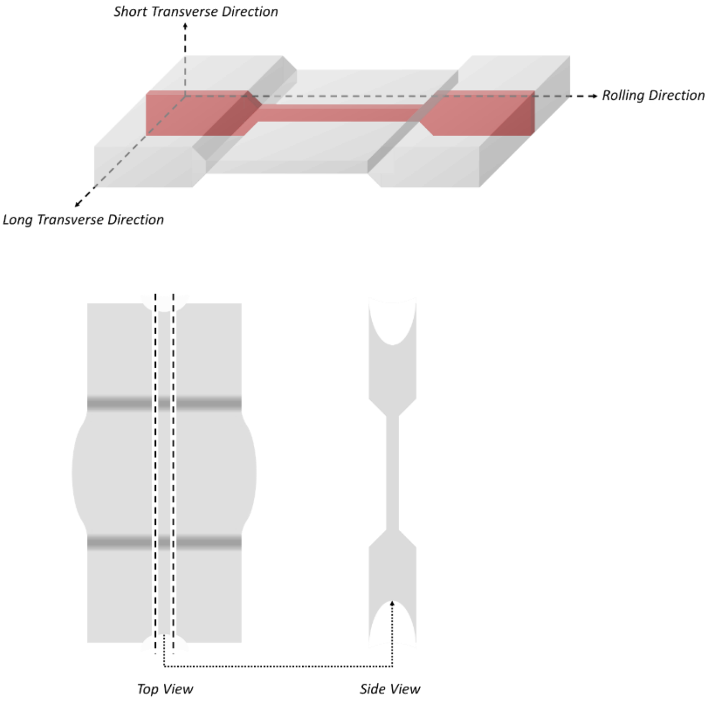

Figure 3.21 Schematic view of the PSC test piece clarifying the location of the tensile test piece sectioned for tensile testing, in the middle of the test piece perpendicular to the rolling direction.

Strain measurement was conducted using a calibrated clip-on extensometer firmly attached to the gage section of each specimen, thereby recording the actual specimen elongation rather than the crosshead displacement. This configuration eliminated machine compliance and grip deformation effects, ensuring that the measured strain accurately represented the true local deformation within the uniform gage length. Accordingly, the engineering stress-strain curves obtained from these measurements were constructed from the instantaneous applied load and the extensometer-measured strain in strict accordance with the standard testing methodology.

A couple of important mechanical properties including the yield strength and tensile strength were determined straight from the graphically constructed engineering stress-strain curves by applying the standard methodologies for mechanical testing and acknowledging that the 0.2% strain offset criterion was laid out parallel to the straight-line portion of these curves as presented in Figure 3.22 for one condition as an example.

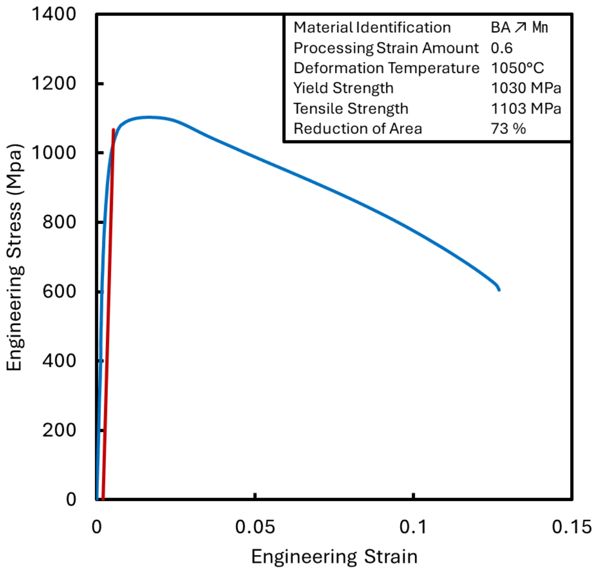

Figure 3.22 An example of an engineering stress-strain curve for an alloy with higher manganese content deformed at 1050°C followed by cooling at a rate of 0.5°C/s where the red straight-line represents the 0.2% offset.

Furthermore, the ratio between the yield strength and tensile strength was calculated to evaluate work hardening while the reduction of area was calculated to evaluate the ductility of the material after fracture. This reduction of area is expressed by the following:

$$RA = \left(\frac{A_0 - A_f}{A_0}\right) \times 100 \qquad \text{Equation 3.4}$$

where RA is the reduction of area occurring during tensile testing, A_0 is the original cross-sectional area of the test piece, and A_f is the smallest cross-sectional area after fracture[148].

3.10 Summary of Experimental Procedure

Several activities were carried out following a structured and detailed experimental procedure allowing interested researchers to execute experiments of interest as necessary. The well-constructed design of experiments presenting the different implemented processing conditions assisted in understanding the research concept and was treated as the roadmap to be followed which commenced by manufacturing the material via a vacuum induction melting furnace to meet certain specifications regarding composition followed by hot rolling the homogenized cast ingots to plates from which PSC specimens were machined.

Characterization of microstructure before and after deformation was performed using advanced analytical techniques including SEM and EBSD to evaluate the impact of the alloy additions as well as the various deformation amounts and deformation temperatures on the final product; in addition to other tests such as tensile and nanoindentation tests which were performed in order to determine the mechanical properties.

Chapter 4 Results and Discussion

4.1 Dilatometric Assessment

Dilatometric curves, shown in Figure 4.1, introduced changes in the slope during continuous heating corresponding to a significant volume contraction in connection with the transformation from martensite (bct) to austenite (fcc) where the temperatures at which this transformation is projected to start, A_{c1}, and end, A_{c3}, for the three studied compositions are provided in Table 4.1; in addition to the martensitic start temperature that is representing the transformation from austenite (fcc) to martensite (bct) which was estimated based on the slope change occurred during continuous cooling corresponding to significant volume expansion and phase transformation behavior[127,149,150].

Transformation temperatures obtained from simulations conducted using the JMatPro 7.0 software were consistent with the dilatometry results; indeed, the CCT diagrams presented in Figure 4.2 support the measurements made by dilatometric assessment, demonstrating that the final transformed microstructure shall be fully martensitic upon cooling. In other words, martensite was the only phase present, with no evidence of other transformation products such as ferrite, pearlite, or bainite. It is evident from the CCT diagrams that the martensitic transformation starts at temperatures comparable to those obtained from dilatometry, and that the minor differences observed can be attributed to the fact that these calculations were done on the basis of an austenite grain size and/or grain shape, which was estimated and may not precisely reflect the actual grain size. In the present work, no direct experimental austenite or martensite grain size quantification was performed at this stage; thus, the simulated transformation temperatures should be interpreted without implying a measured grain size baseline.

It should also be noted that the CCT diagrams generated by JMatPro do not conform to the standard convention where cooling initiates from the A_{e3}; instead, the software automatically commences cooling from the calculated equilibrium austenitization temperature that reflects its thermodynamic modeling framework. Accordingly, these simulations represent theoretical projections rather than experimentally standardized CCT curves, and they are intended to provide comparative insight into the relative transformation tendencies of the studied alloys rather than to define exact transformation start points.

Furthermore, an earlier study on a supermartensitic stainless steel with a relatively similar composition reported moderately consistent transformation temperatures; specifically, A_{c1} was 565°C, A_{c3} was 843°C, and M_s ranged between 230°C and 280°C[126]. These transformation temperatures align well with the experimental dilatometry results as well as the predictions from the software simulations, thereby reinforcing their reliability.The slight variations observed between the temperature values obtained in the current study and those reported in the literature may stem from differences in key factors such as alloying element concentrations, processing conditions, and austenite grain size and/or grain shape.

While carbon content has a significant influence on M_s, results indicate that the addition of nickel and manganese influences not only the thermodynamic stability of austenite but also the onset of the martensitic transformation, as evidenced by the observed variations in the M_s temperatures. Notably, manganese tends to decrease M_s to a greater degree than nickel in alloys with relatively low chromium concentrations; however, the effect of nickel becomes progressively less pronounced relative to manganese when chromium is present in sufficiently high concentrations, suggesting a shift in transformation behavior depending on the specific alloy composition[119]. Hence, it is essential to consider the combined effects of complex interactions between these alloying elements and carbon, rather than evaluating their individual or isolated contributions.

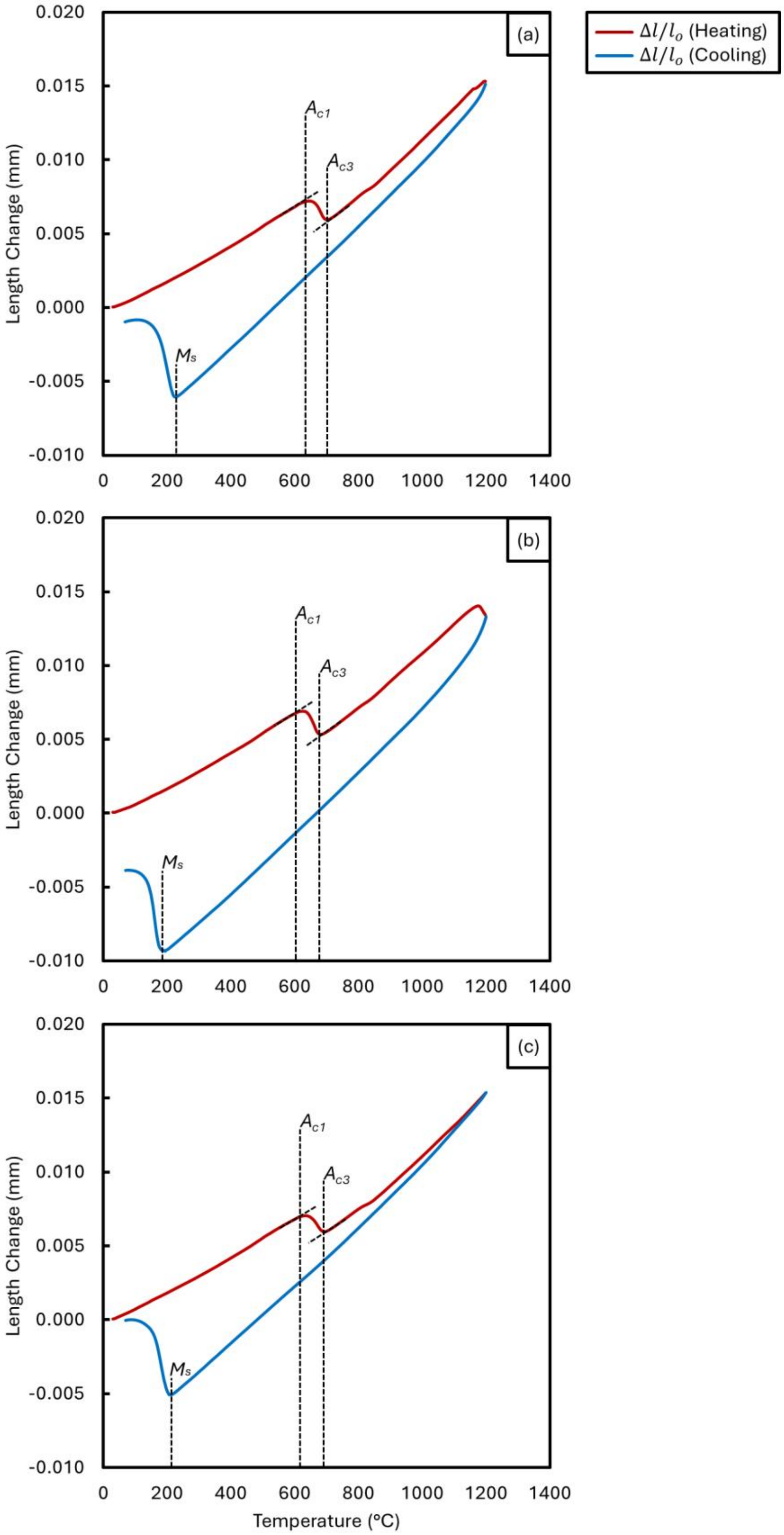

Figure 4.1 Dilatometer curves used for determination of critical transformation temperatures during continuous heating and cooling of: (a) BA, (b) BA ↗ Ni, and (c) BA ↗ Mn.

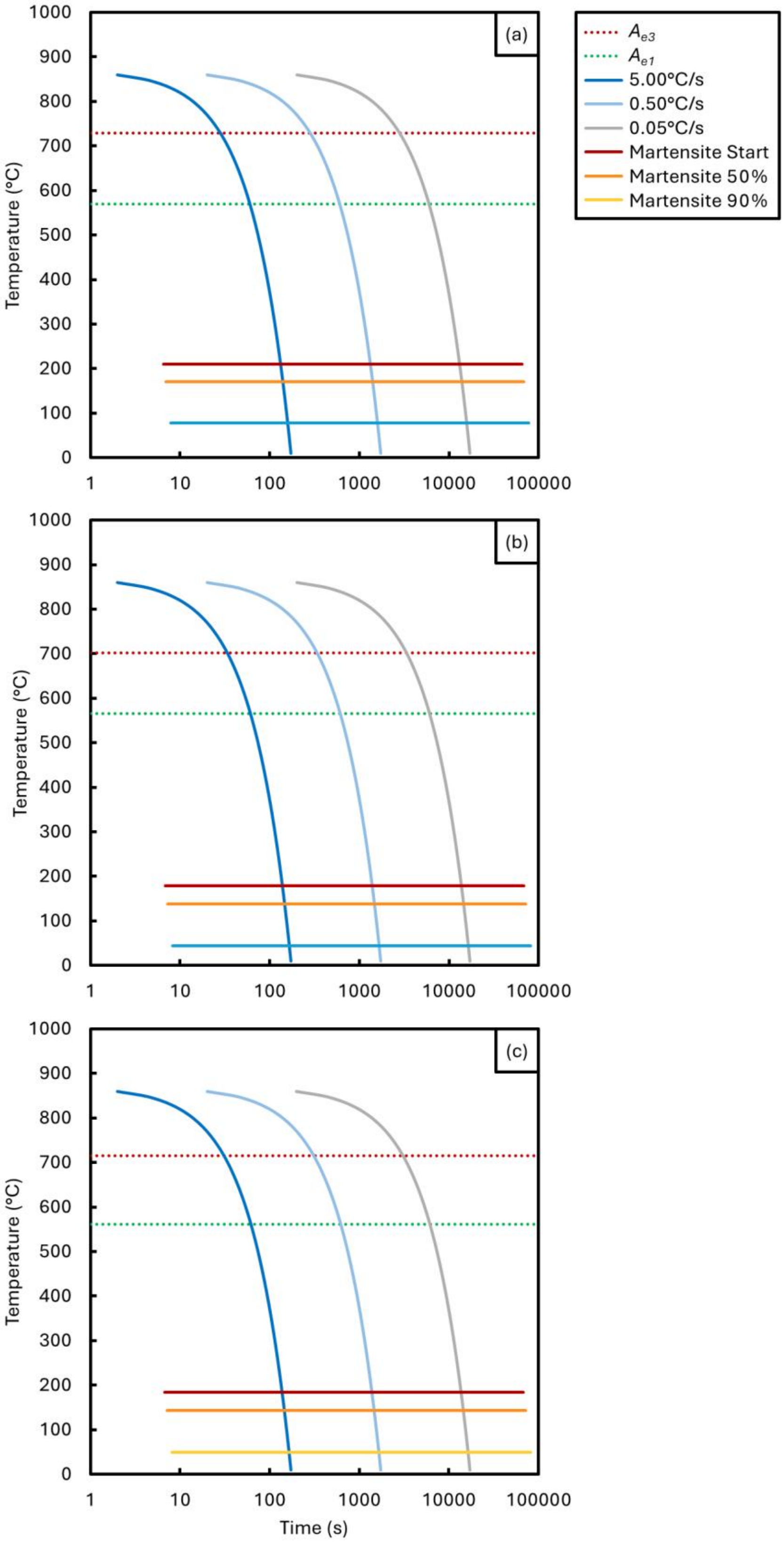

Figure 4.2 CCT curves used for estimation of critical transformation temperatures during continuous cooling of: (a) BA, (b) BA ↗ Ni, and (c) BA ↗ Mn.

Table 4.1 Critical transformation temperatures (°C) extracted from the dilatometric analysis.

Material Identification	A_{c1}	A_{c3}	M_s
BA	620	700	230
BA ↗ Ni	600	680	190
BA ↗ Mn	610	690	210

In brief, these findings provide a foundation for optimizing the parameters of the thermomechanical composition and processing routes to control microstructure via refining grain size and, consequently, paving the way for improved mechanical properties. The identification of deformation temperatures would lead to precise control of grain morphology; for instance, deformation at a temperature of 1050°C would result in a recrystallized microstructure consisting of refined and equiaxed grains, while deformation at a temperature of 800°C would promote an unrecrystallized microstructure consisting of refined and elongated grains associated with higher strength and fracture resistance.

4.2 Thermomechanical Compression

The macroscopic flow behavior is presented in Figure 3.4 in the form of true stress-strain curves obtained from the analyzed plane strain compression data for each of the three compositions at a constant true strain rate of 10 s^{-1} with a single rough rolling pass at 1150°C and a strain of 0.3 followed by single, double, or triple finish rolling passes at 1050°C or 800°C with a varied total strain amounts of 0.6, 0.9, or 1.2, respectively. Excellent consistency in deformation behavior was observed across all processing conditions for the three compositions. Considering the differences and similarities into account, the overall response of the different compositions was both similar and consistent, whereas softening effects became more pronounced at the higher deformation temperatures compared to the lower deformation temperatures.

The flow curves are comparable to their dependence on the temperature at which the alloy was deformed, where the stress level increased as the deformation temperature decreased from 1150°C to 1050°C; more distinctly, the stress escalated by decreasing the deformation temperature down to 800°C. This behavior is indicative of work hardening where softening mechanisms such as dynamic recovery and dynamic recrystallization were suppressed which was reflected by the characteristic drooping nature of the flow curves in some conditions with a high strain amount, such as BA ↗ Mn deformed at a temperature of 800°C and a strain of 1.2. The short period of time available for energy accumulation when the deformation occurs at a lower deformation temperature promoted the nucleation and growth of dynamically recrystallized grains while facilitating the annihilation of dislocations at grain boundaries[102].

Distinctly, the BA ↗ Mn exhibited a unique stress-strain response at 800°C where the flow stress notably dropped at high strain, suggesting the onset of dynamic recrystallization. However, this behavior was less evident in the other compositions, suggesting that Mn increases grain boundary mobility and facilitates recrystallization nucleation by reducing stacking fault energy (SFE) and increasing dislocation accumulation, leading to an acceleration of dynamic recrystallization kinetics[103,151]. It should be noted, however, that this interpretation is qualitative, as no direct dislocation mapping or saturation analysis was carried out within this study.

It is acknowledged that the stress-strain curves obtained from the thermomechanical compression experiments are subject to certain inherent limitations despite being conducted using the modified TMC system in accordance with the good practice guide NPL-CMMT (GPG)027[130]. Minor frictional effects at the tooling interfaces, slight temperature gradients across the sample thickness, and localized adiabatic heating during high-strain deformation could have introduced small variations in the recorded stress levels.

Furthermore, the conversion of load-displacement data to true stress-strain form followed the procedures described in the referenced good practice guide, using measured spread to determine a spread coefficient and account for friction, thereby reducing barreling and edge effects. These experimental factors were minimized through precise control of strain rate, temperature, and lubrication; nevertheless, they may still introduce minor uncertainty in stress magnitudes without affecting relative deformation trends or mechanistic interpretations of the overall flow behavior.

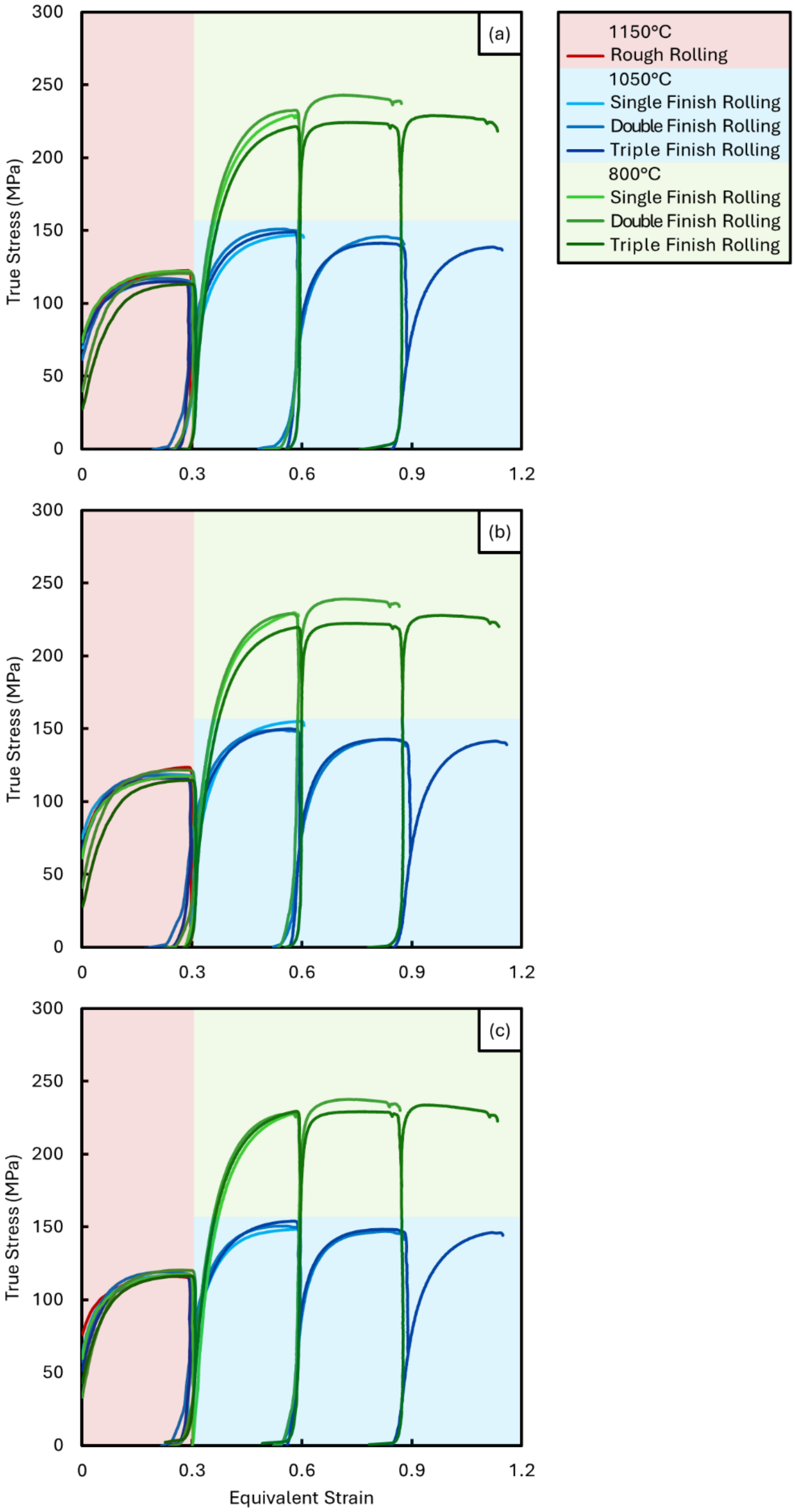

Figure 4.3 Stress-strain flow curves of (a) BA, (b) BA ↗ Ni, and (c) BA ↗ Mn where rough rolling at 1150°C, finish rolling at 1050°C, and 800°C are highlighted in red, blue, and green, respectively.

4.3 Microstructural Analysis

4.3.1 Prior to Deformation

Optical micrographs of the as-cast and as-hot rolled structures are presented in Figure 4.4 where a coarse equiaxed microstructure is observed in the as-cast state, compared to a finer equiaxed microstructure composed of prior austenite grain boundaries along with amounts of transformed needle-like martensite that formed as a result of hot rolling at a high temperature of 1200°C followed by subsequent rapid cooling to inhibit diffusional transformations, including ferrite and pearlite formation, and facilitate the martensitic transformation. It is worth noting that rapid cooling plays an essential role in the formation or absence of phases, where high cooling rates suppress the formation of softer equilibrium phases while promoting the formation of harder non-equilibrium phases, ensuring a fully martensitic microstructure[81,124,152].

The micrographs indicate that all three compositions exhibit a similar recrystallized microstructure. Furthermore, this revealed microstructure closely resembles UNS S41427 and other supermartensitic stainless steels that share similar chemical compositions to the alloys under study, highlighting that a certain acceptable degree of variation is noticeable which is to be expected and is primarily arising from compositional modifications in these alloys; nevertheless, none of the examined microstructures exhibited any anomalous characteristics, unexpected deviations, or abnormal features when compared to earlier findings that have been comprehensively reported in the existing literature[25,26,28,29,118].

EDS analysis demonstrated a uniform elemental distribution of elements with no evidence of segregation from the casting via VIM before reheating; as a matter of course, even if any segregation had been present at the casting stage, it would have been eliminated after hot rolling at 1200°C and subsequent reheating at 1150°C. To provide additional clarity, individual elemental distribution maps for Fe, Cr, Ni, Mo, Mn, Si, V, and C are provided in Figure 4.5, Figure 4.6, and Figure 4.7, further confirming the homogeneity of the elemental distribution and the absence of segregation across all three alloys. Hence, EDS for the as-rolled state would not provide further insightful information since a similar level of chemical homogeneity would be expected across the three alloys, i.e. the base alloy, the alloy with higher nickel content, and the alloy with higher manganese content.

The faint banded morphology observable in Figure 4.4, particularly within the as-cast microstructure, corresponded to subtle microsegregation bands that developed during solidification and were partially retained after hot rolling, originating from compositional variations between dendritic and interdendritic regions that evolved as solute elements such as Cr, Mo, and Mn partitioned during the final stages of solidification under non-equilibrium conditions, where rapid cooling limited complete solute redistribution before solidification completion and produced local chemical heterogeneity that is inherently characteristic of steels processed by VIM[42,153].

Upon subsequent reheating and hot rolling, these solute fluctuations were substantially reduced through diffusion and dynamic recovery yet not entirely eliminated, as hot rolling at 1200°C and reheating at 1150°C promoted partial homogenization without fully eradicating compositional gradients which, upon cooling, locally influenced the martensitic transformation kinetics, giving rise to alternating regions of slightly differing transformation temperatures and etching responses that appeared as microstructural banding, a phenomenon widely recognized as a residual effect of segregation contrasts in multi-component steels containing strong carbide and ferrite stabilizers with differing diffusion coefficients rather than a manifestation of thermomechanical deformation effects[31,81].

These banded regions did not represent deformation-induced flow lines, recrystallization artifacts, or abnormal austenite morphology, but instead reflected minor and non-critical solidification inhomogeneities whose influence was negligible in structural or mechanical terms, as confirmed by the EDS elemental distribution maps which verified chemical uniformity at the microscale, thereby affirming that the observed banding was a visual remnant of primary solidification history typical of vacuum melted steels and not indicative of any compositional segregation or instability within the as-rolled condition[30,154].

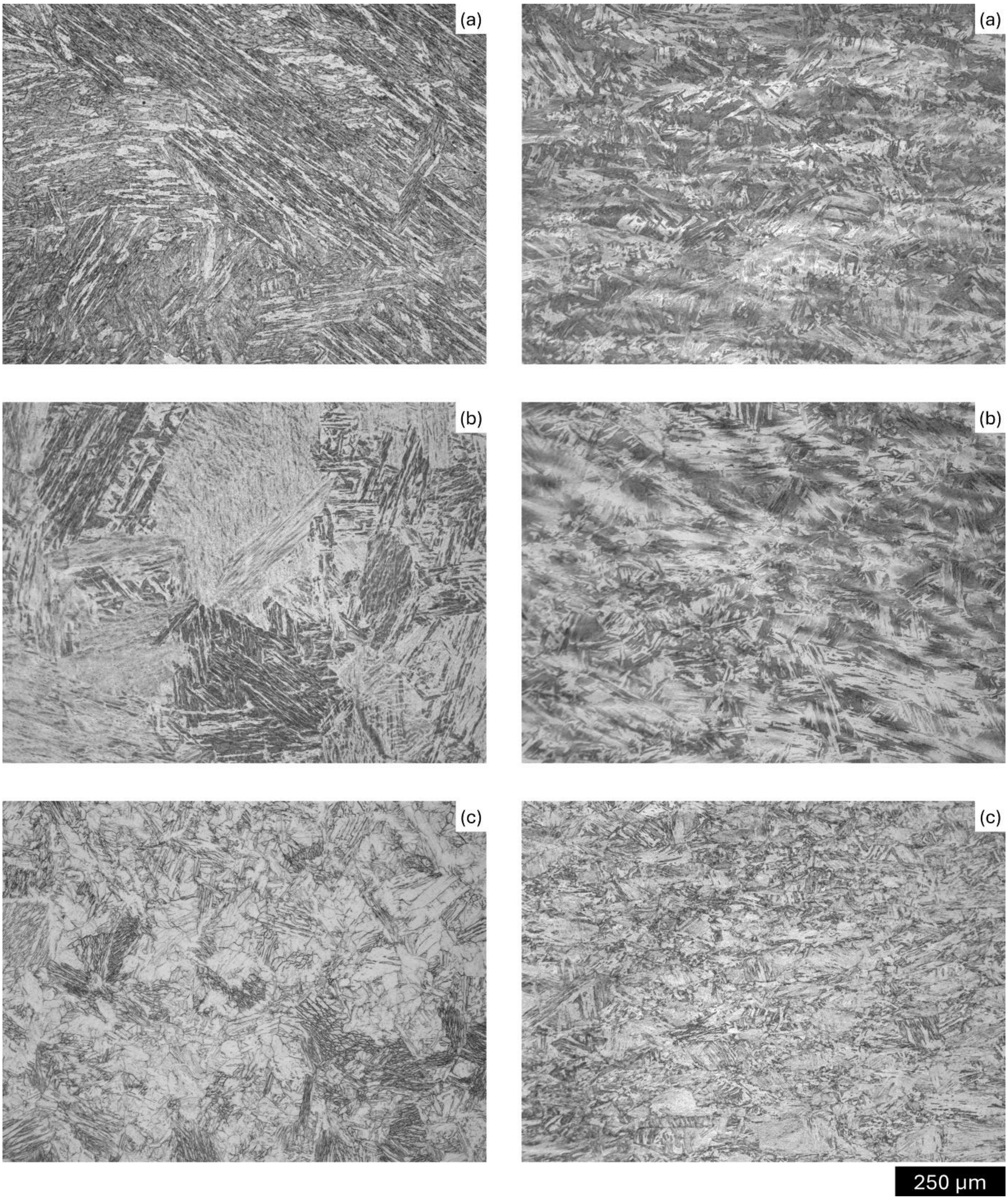

Figure 4.4 Optical micrographs representing the as-cast (left) and as-hot rolled (right) general microstructures of: (a) BA, (b) BA ↗ Ni, and (c) BA ↗ Mn.

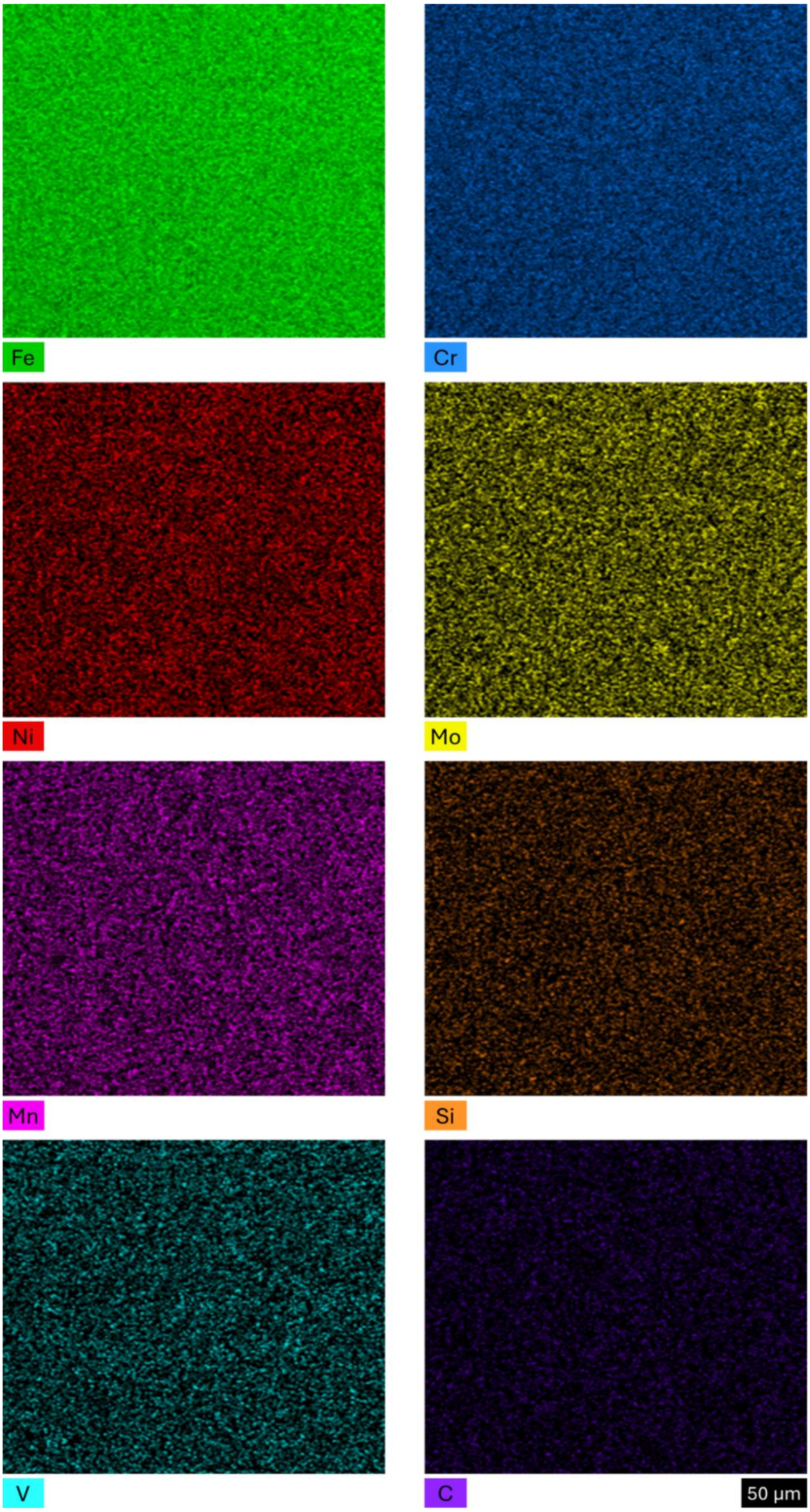

Figure 4.5 Individual elemental distribution maps (Fe, Cr, Ni, Mo, Mn, Si, V, C) for the as-cast BA, showing homogeneous chemical distribution and the absence of segregation.

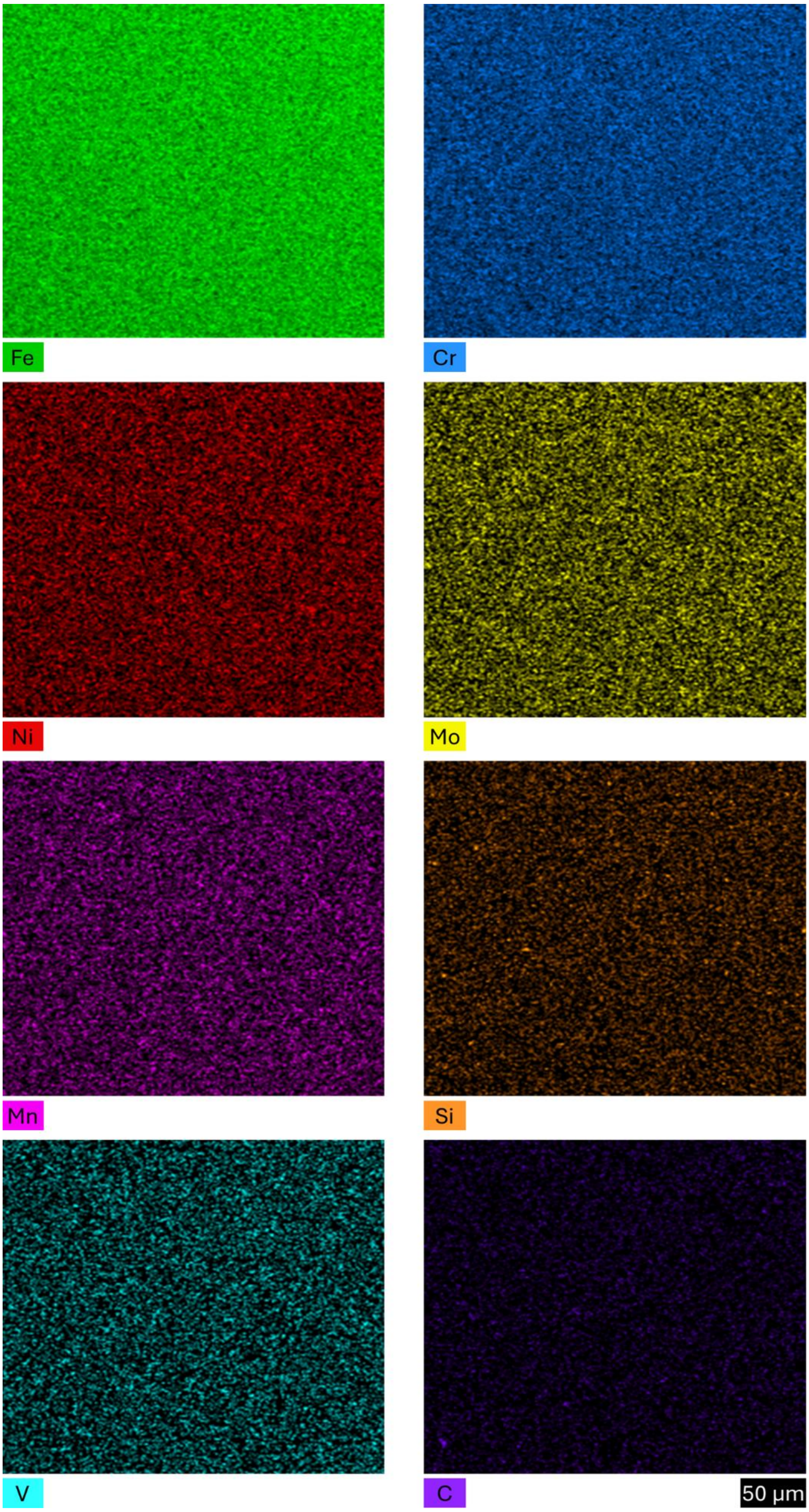

Figure 4.6 Individual elemental distribution maps (Fe, Cr, Ni, Mo, Mn, Si, V, C) for the as-cast BA ↗ Ni, showing homogeneous chemical distribution and the absence of segregation.

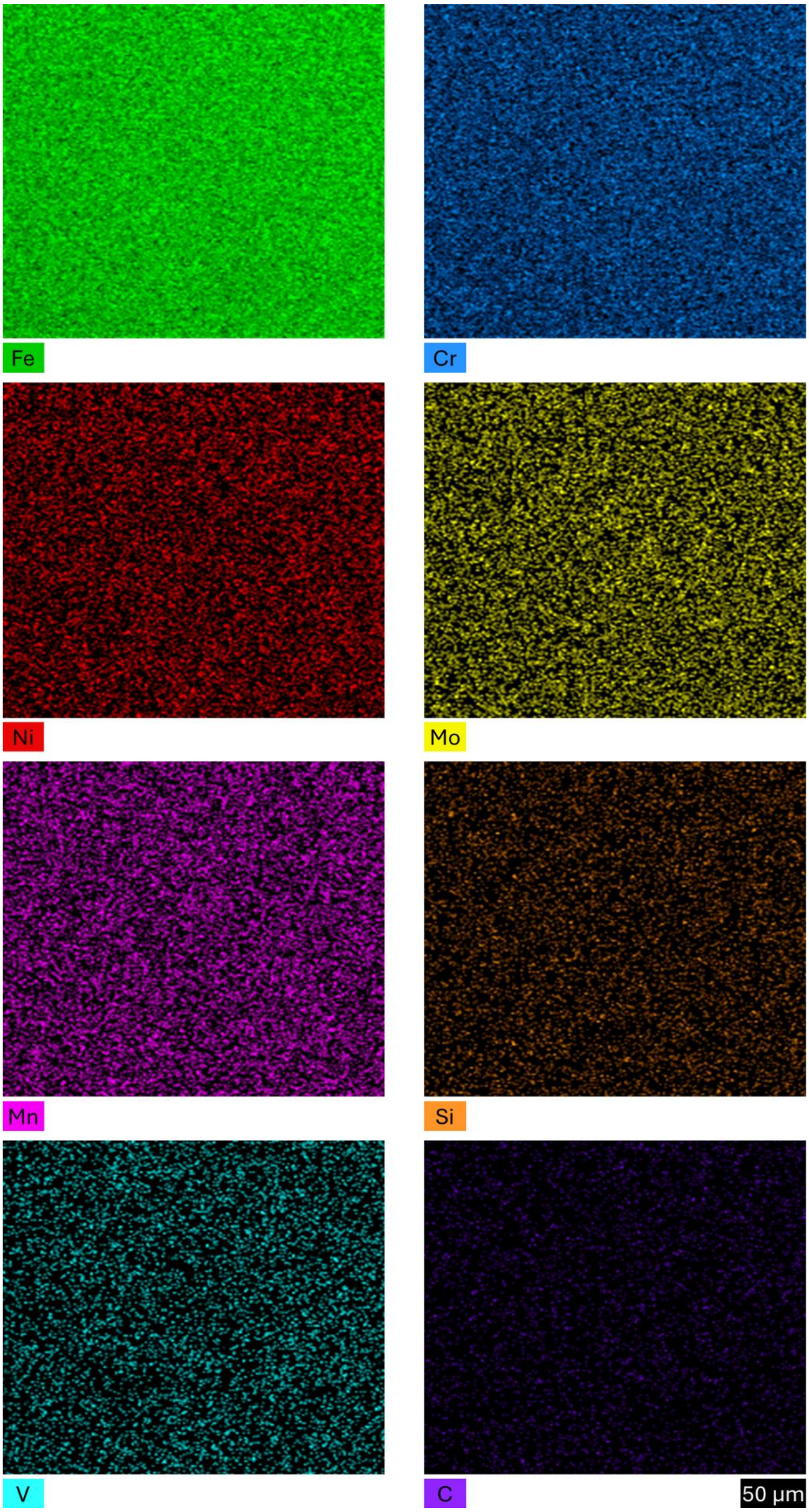

Figure 4.7 Individual elemental distribution maps (Fe, Cr, Ni, Mo, Mn, Si, V, C) for the as-cast BA ↗ Mn, showing homogeneous chemical distribution and the absence of segregation.

4.3.2 During Deformation

SEM micrographs of the deformed microstructure reflecting the microstructural evolution from rough rolling to finish rolling, which is influenced by high-temperature and low-temperature finish rolling, are presented in the following sub-sections. These micrographs provide significant insights, from a microstructural point of view, into the roles of deformation temperature and strain amount in tailoring the final microstructure, characterized by extensive grain refinement.

4.3.2.1 Rough Rolling at 1150°C

The three compositions, i.e. BA, BA ↗ Ni, and BA ↗ Mn, underwent rough rolling at a temperature of 1150°C and a strain of 0.3 as introduced in the schematic diagram represented in Figure 4.8. This initial processing stage aimed to simulate a controlled deformation environment representative of industrial conditions, allowing for the analysis of the behavior of these alloys under applied processing parameters. The resulting microstructures post rough rolling, obtained under the processing conditions outlined in the schematic diagram, are represented in Figure 4.9 alongside their corresponding individual stress-strain flow curves.

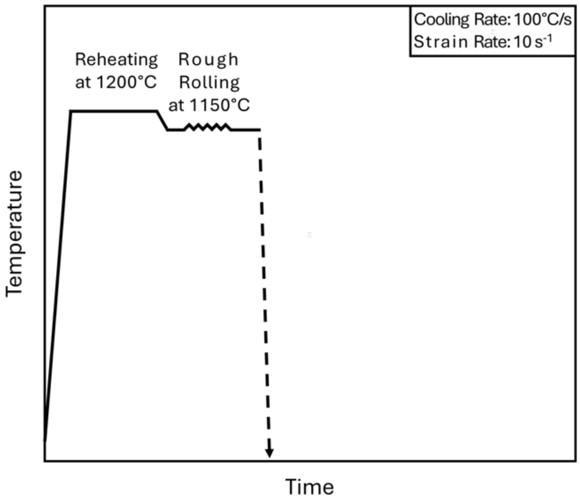

Figure 4.8 Schematic diagram illustrating the processing conditions of deformation at 1150°C with a final strain reaching ~0.3, followed by rapid cooling at a rate of 100°C/s.

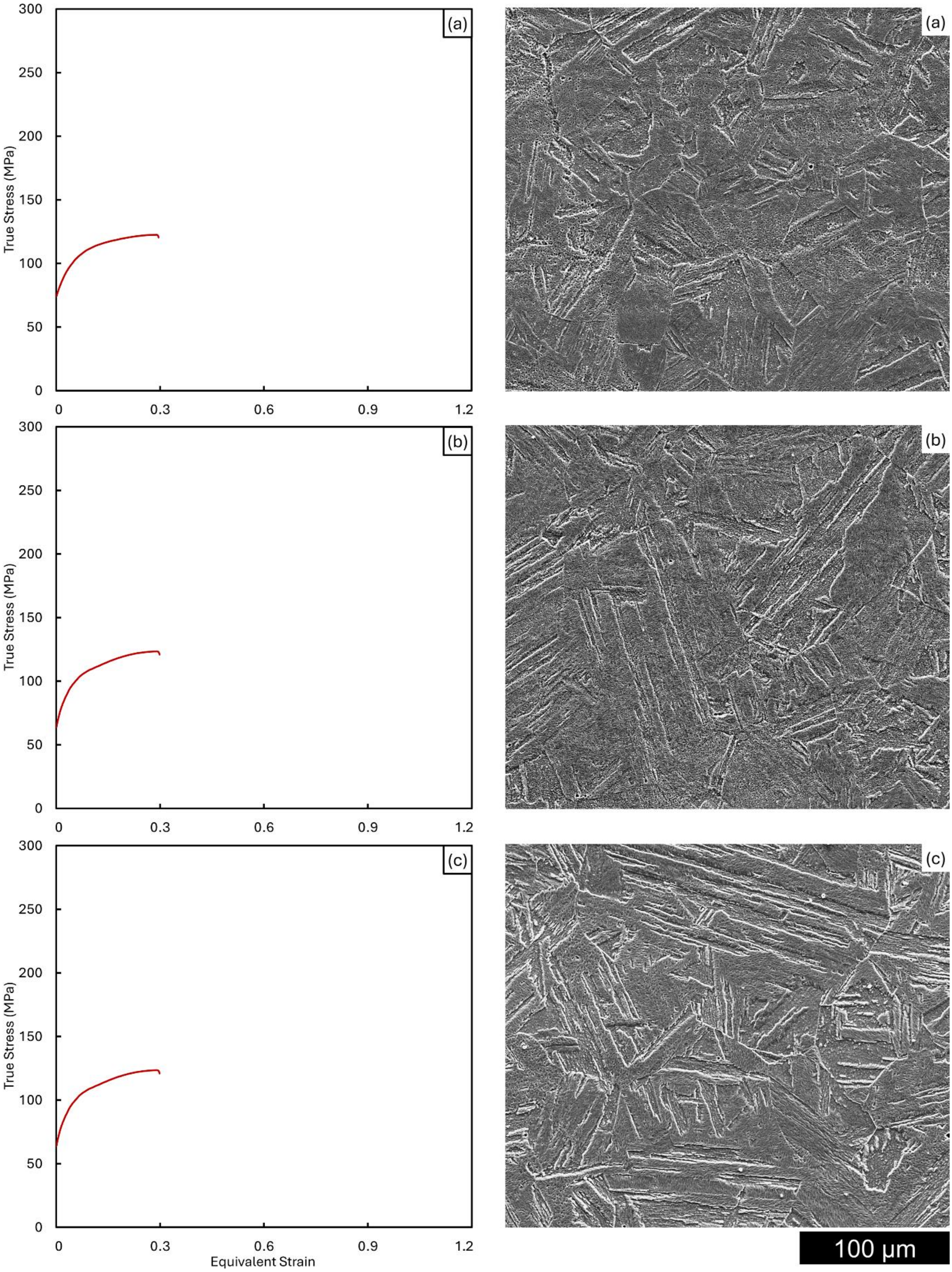

Figure 4.9 SEM micrographs representing microstructure, towards the long transverse direction, deformed at 1150°C with a final strain reaching ~0.3 followed by rapid cooling at a rate of 100°C/s along with corresponding stress-strain flow curve for: (a) BA, (b) BA ↗ Ni, and (c) BA ↗ Mn.

4.3.2.2 Finish Rolling at 1050°C

Following rough rolling at 1150°C, the alloys under study underwent single, double, and triple finish rolling at a relatively high temperature of 1050°C (above $T_{95\%}$) as introduced in the schematic diagrams represented in Figure 4.10, where each finishing pass had an equivalent strain of 0.3. The resulting microstructures post finish rolling, obtained under the three different processing conditions outlined in the schematic diagrams with total strain amounts of 0.6, 0.9, and 1.2, are represented in Figure 4.11, Figure 4.12, and Figure 4.13, respectively, alongside their corresponding individual stress-strain flow curves.

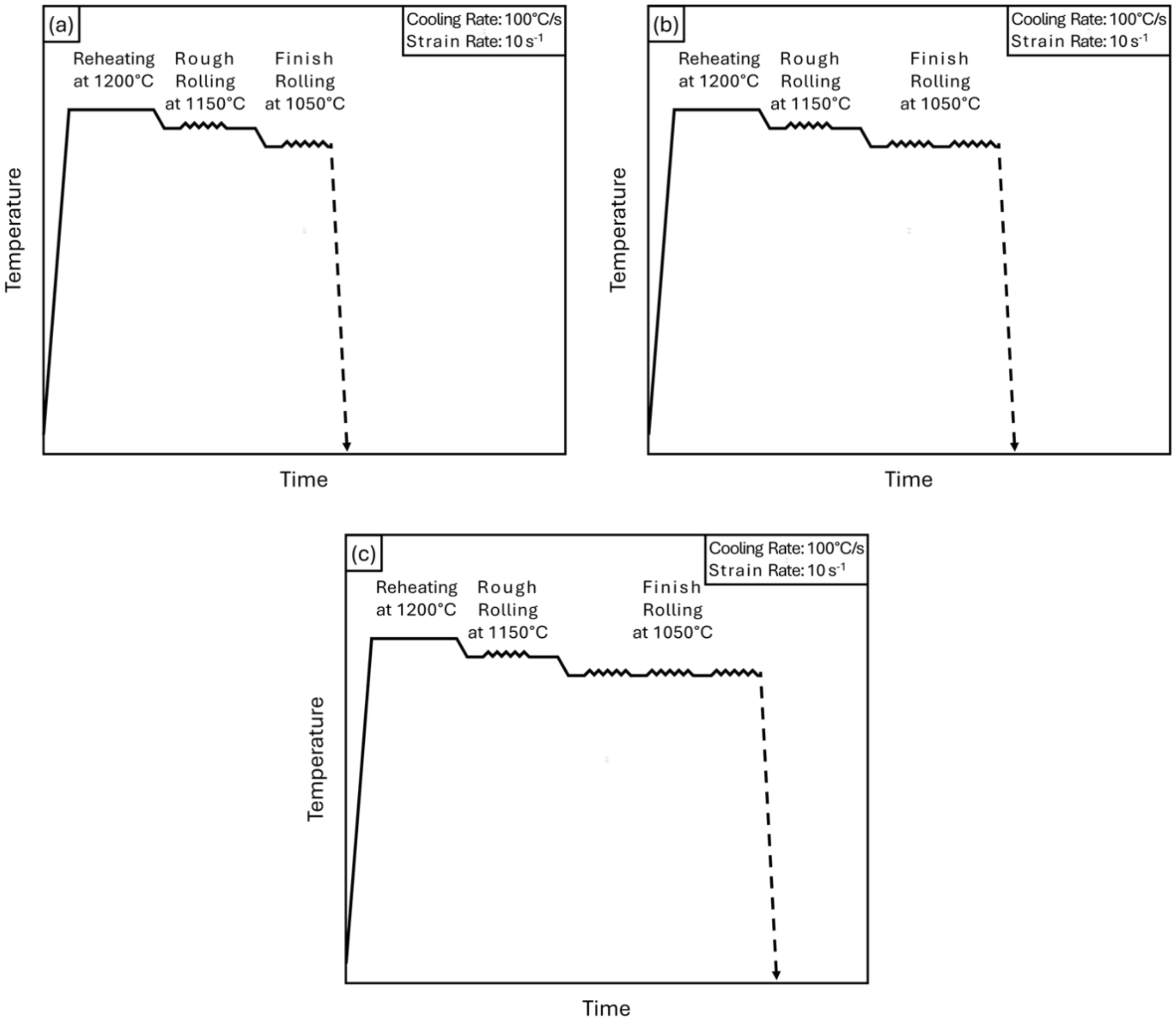

Figure 4.10 Schematic diagram illustrating the processing conditions of deformation at 1050°C with a final strain reaching (a) ~0.6, (b) ~0.9, and (c) ~1.2, followed by rapid cooling at a rate of 100°C/s.

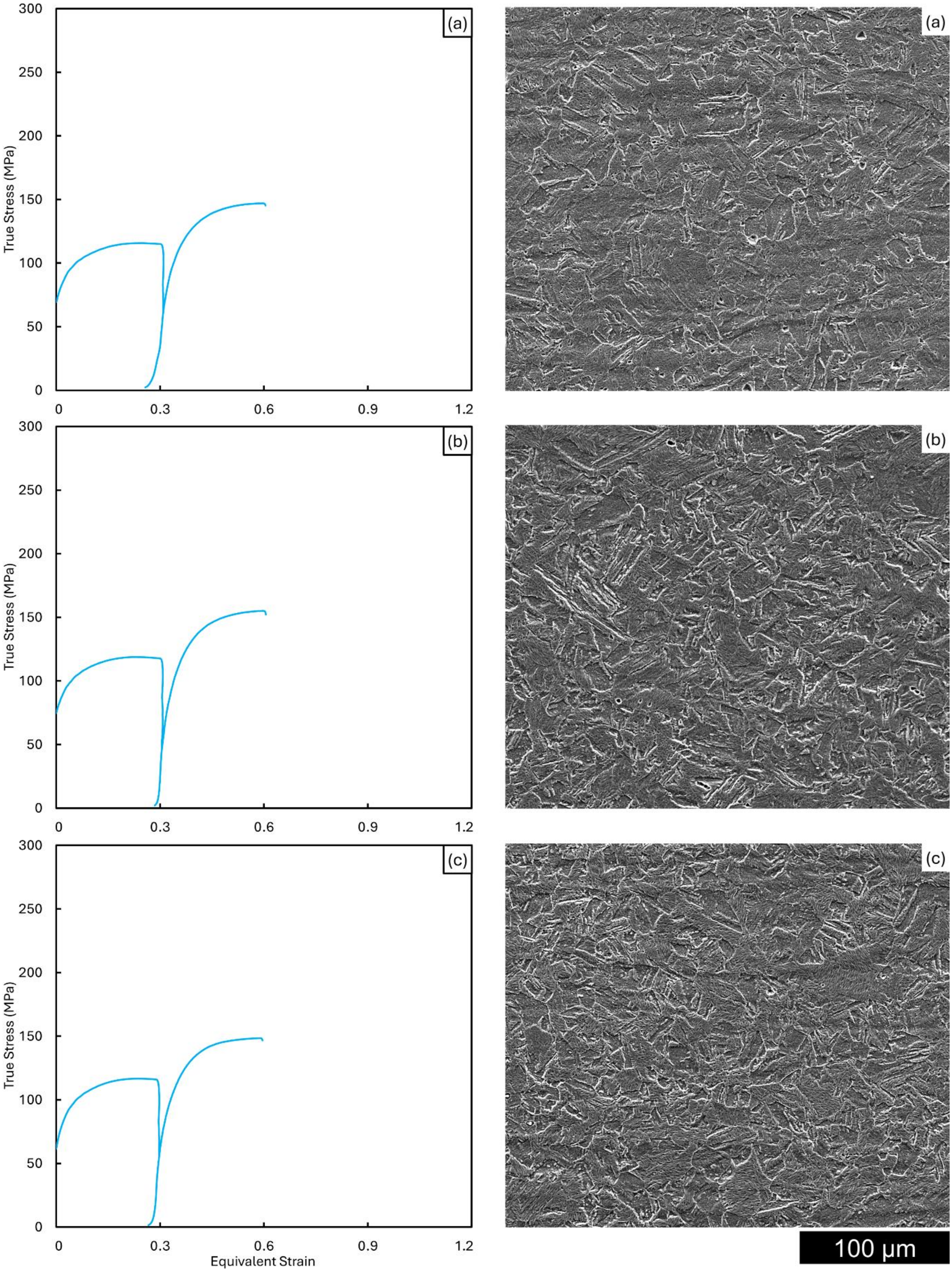

Figure 4.11 SEM micrographs representing microstructure, towards the long transverse direction, deformed at 1050°C with a final strain reaching ~0.6 followed by rapid cooling at a rate of 100°C/s along with corresponding stress-strain flow curve for: (a) BA, (b) BA ↗ Ni, and (c) BA ↗ Mn.

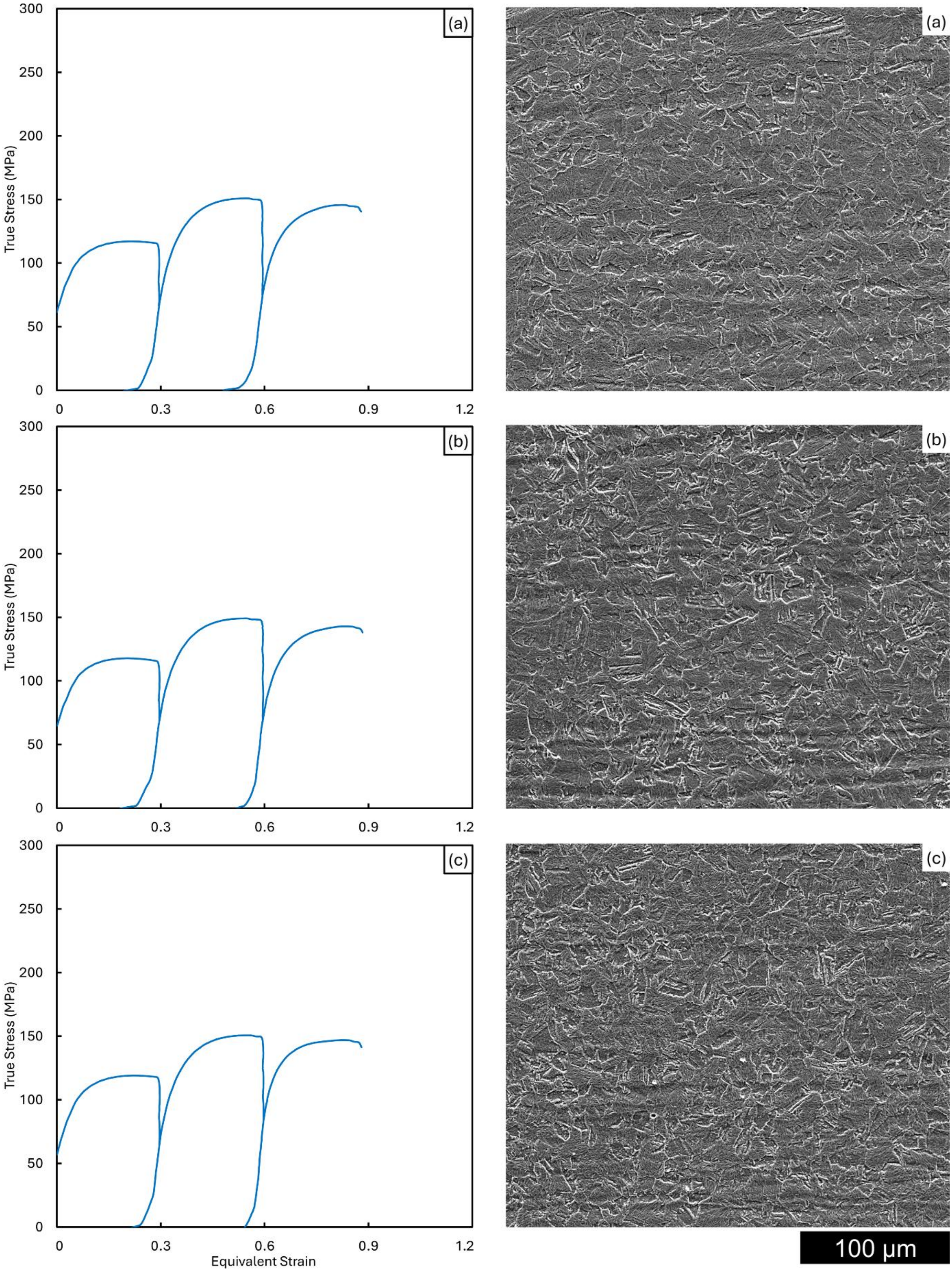

Figure 4.12 SEM micrographs representing microstructure, towards the long transverse direction, deformed at 1050°C with a final strain reaching ~0.9 followed by rapid cooling at a rate of 100°C/s along with corresponding stress-strain flow curve for: (a) BA, (b) BA ↗ Ni, and (c) BA ↗ Mn.

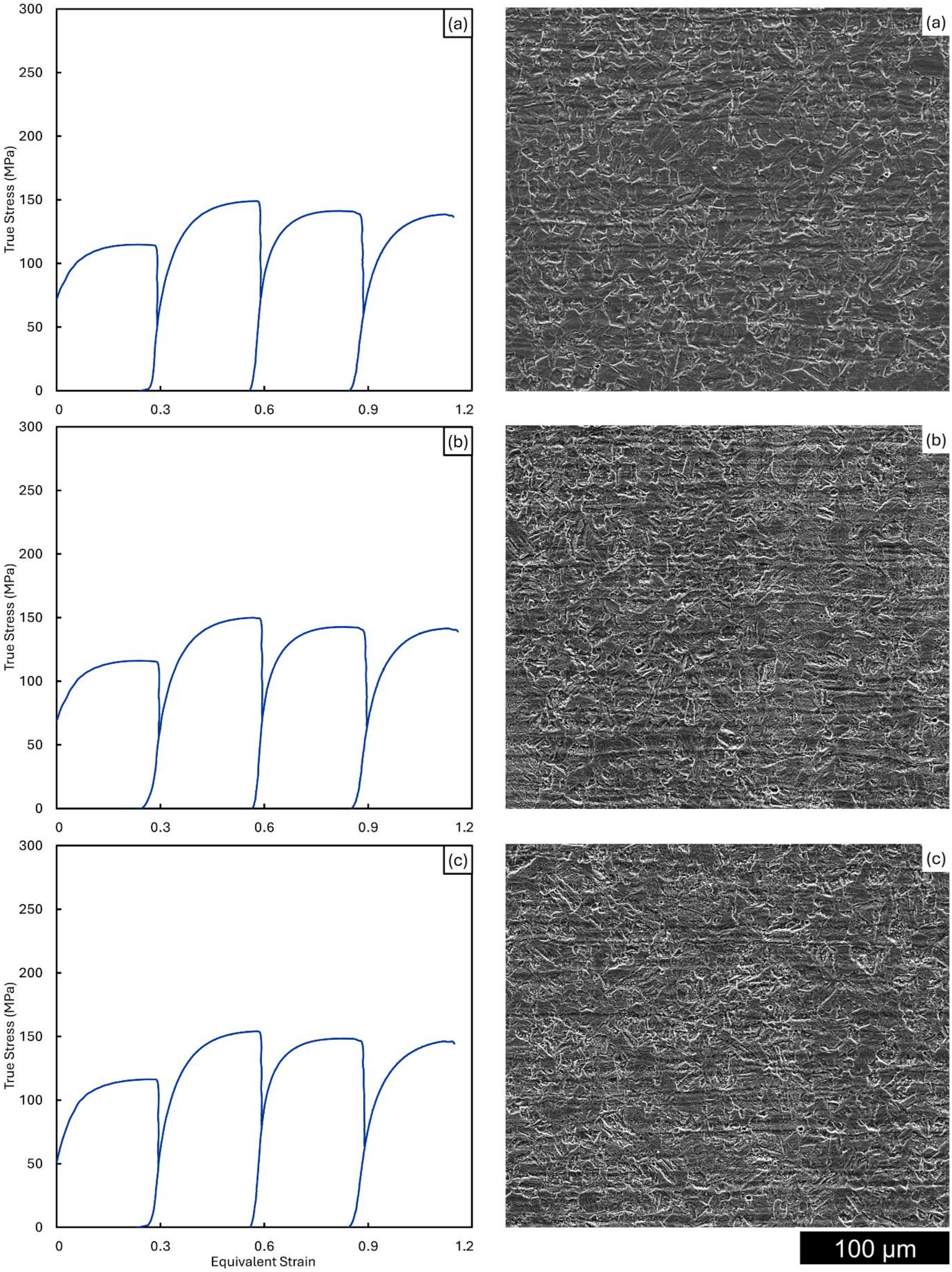

Figure 4.13 SEM micrographs representing microstructure, towards the long transverse direction, deformed at 1050°C with a final strain reaching ~1.2 followed by rapid cooling at a rate of 100°C/s along with corresponding stress-strain flow curve for: (a) BA, (b) BA ↗ Ni, and (c) BA ↗ Mn.

4.3.2.3 Finish Rolling at 800°C

Following rough rolling at 1150°C, the alloys under study underwent single, double, and triple finish rolling at a temperature of 800°C (below $T_{5\%}$) as introduced in the schematic diagrams represented in Figure 4.14. The resulting microstructures post finish rolling, obtained under the three different processing conditions outlined in the schematic diagrams with total strain amounts of 0.6, 0.9, and 1.2, are represented in Figure 4.15, Figure 4.16, and Figure 4.17, respectively, when viewed in the long transverse orientation, alongside their corresponding individual stress-strain flow curves. Additionally, the microstructures are presented from another orientation, i.e. the short transverse, in Figure 4.18, Figure 4.19, and Figure 4.20.

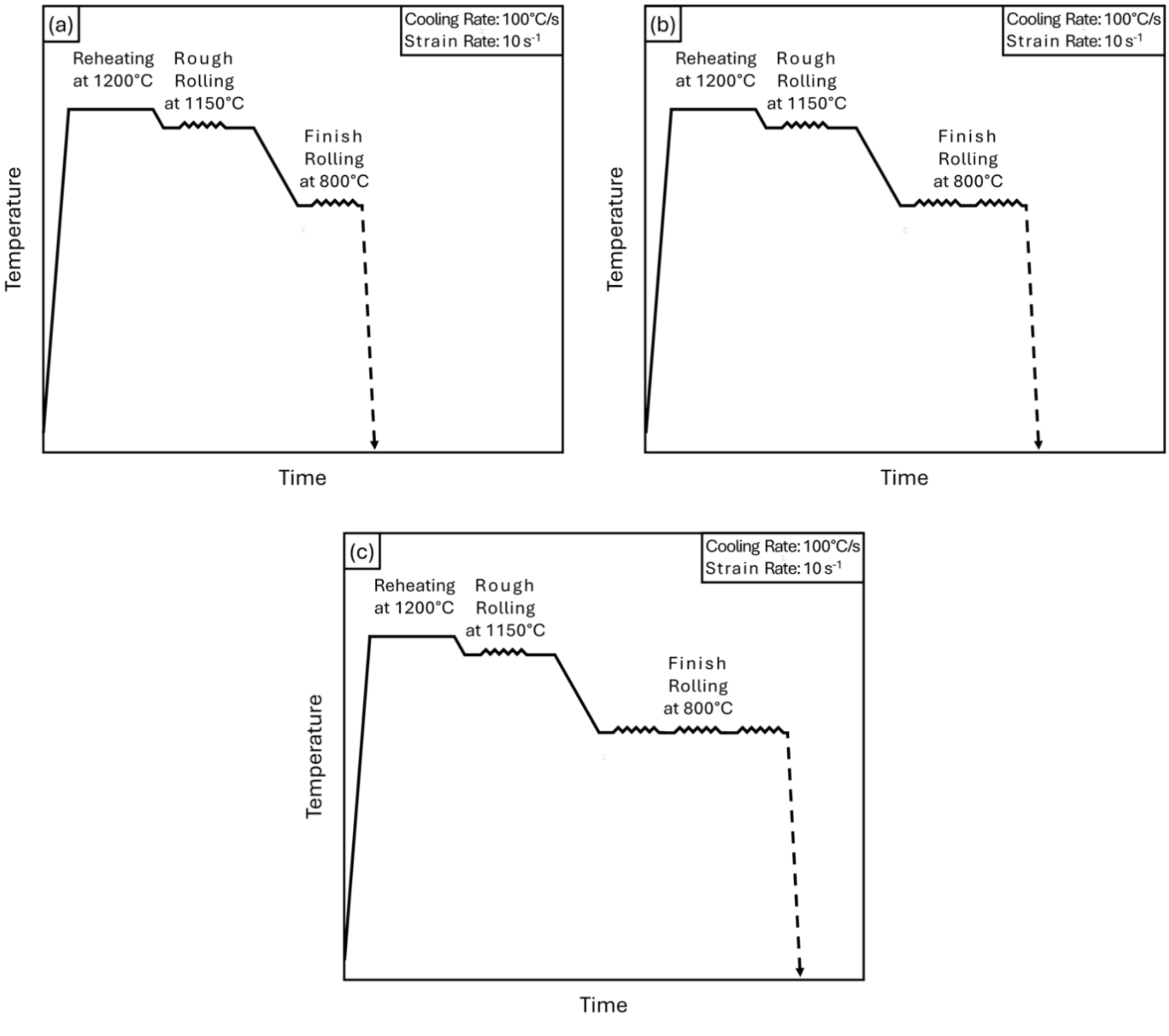

Figure 4.14 Schematic diagram illustrating the processing conditions of deformation at 800°C with a final strain reaching (a) ~0.6, (b) ~0.9, and (c) ~1.2, followed by rapid cooling at a rate of 100°C/s.

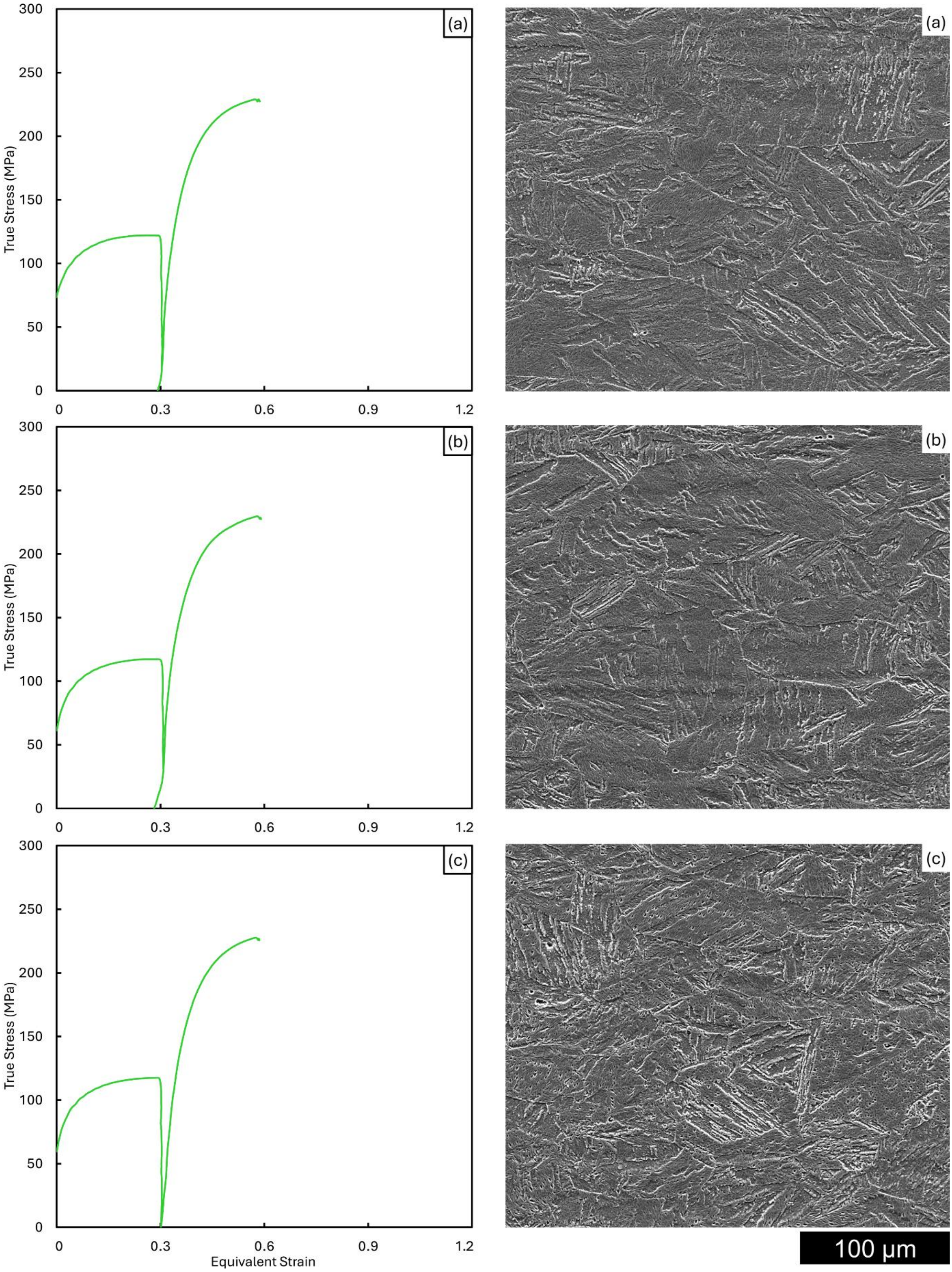

Figure 4.15 SEM micrographs representing microstructure, towards the long transverse direction, deformed at 800°C with a final strain reaching ~0.6 followed by rapid cooling at a rate of 100°C/s along with corresponding stress-strain flow curve for: (a) BA, (b) BA ↗ Ni, and (c) BA ↗ Mn.

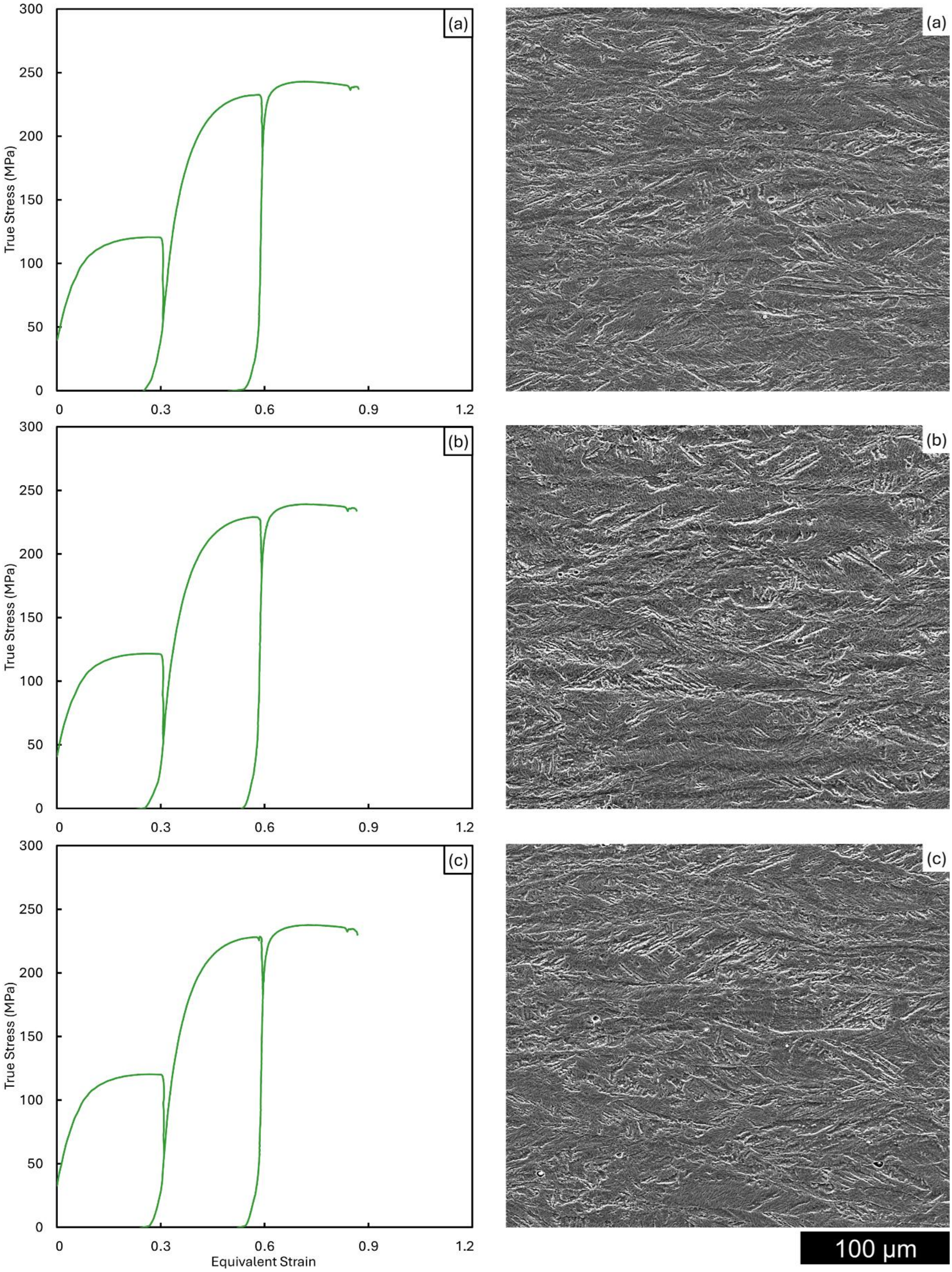

Figure 4.16 SEM micrographs representing microstructure, towards the long transverse direction, deformed at 800°C with a final strain reaching ~0.9 followed by rapid cooling at a rate of 100°C/s along with corresponding stress-strain flow curve for: (a) BA, (b) BA ↗ Ni, and (c) BA ↗ Mn.

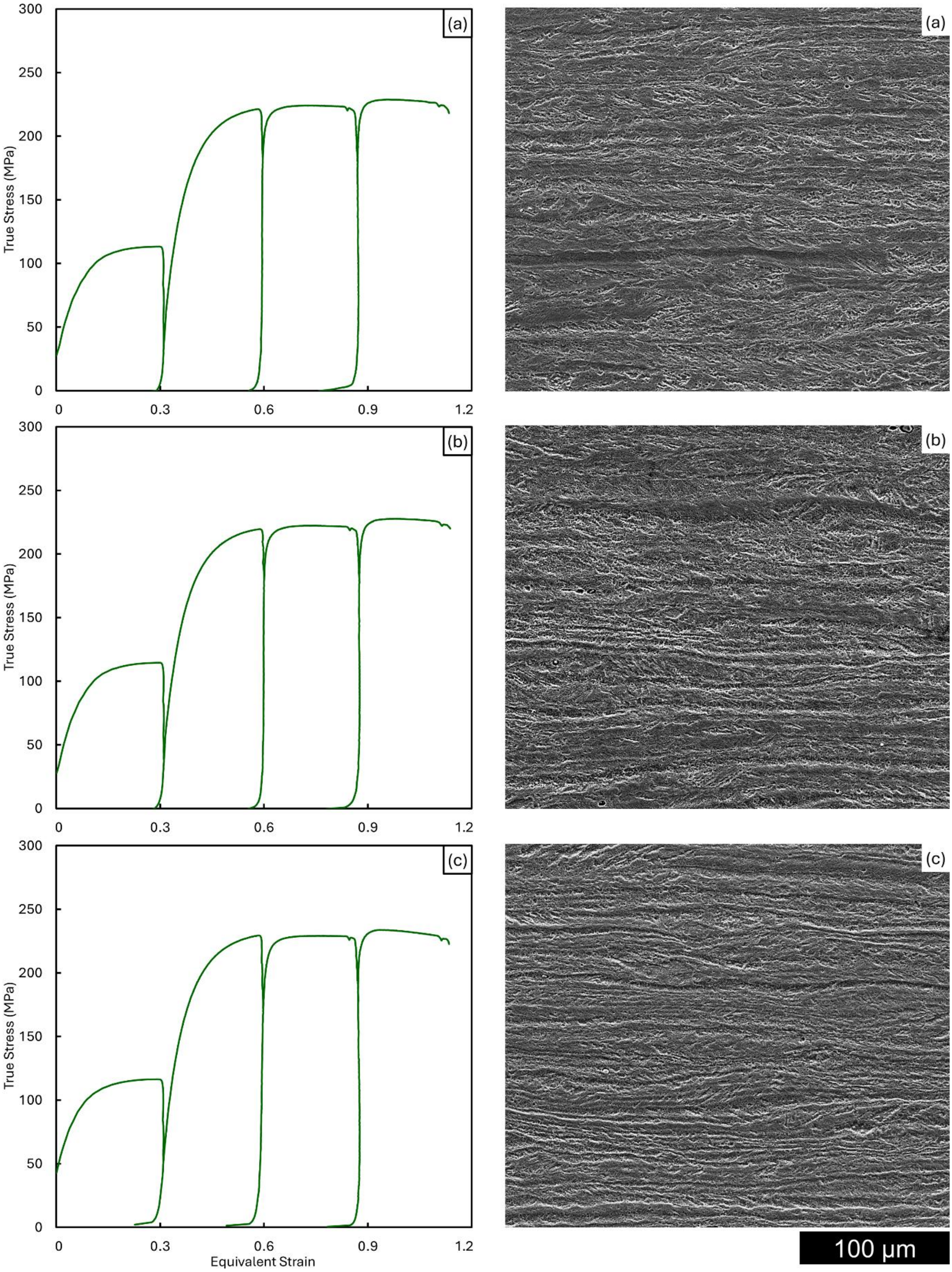

Figure 4.17 SEM micrographs representing microstructure, towards the long transverse direction, deformed at 800°C with a final strain reaching ~1.2 followed by rapid cooling at a rate of 100°C/s along with corresponding stress-strain flow curve for: (a) BA, (b) BA ↗ Ni, and (c) BA ↗ Mn.

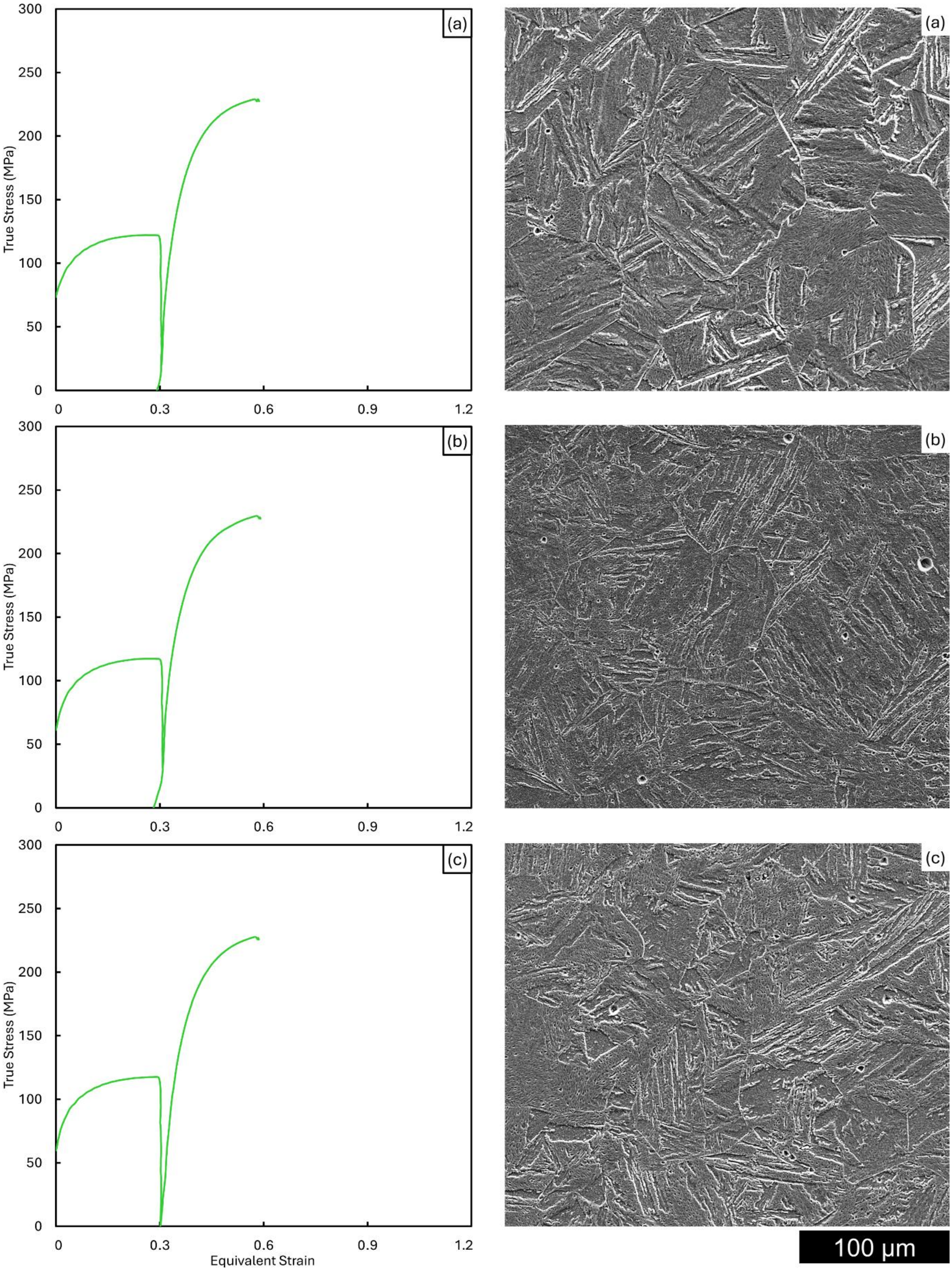

Figure 4.18 SEM micrographs representing microstructure, towards the short transverse direction, deformed at 800°C with a final strain reaching ~0.6 followed by rapid cooling at a rate of 100°C/s along with corresponding stress-strain flow curve for: (a) BA, (b) BA ↗ Ni, and (c) BA ↗ Mn.

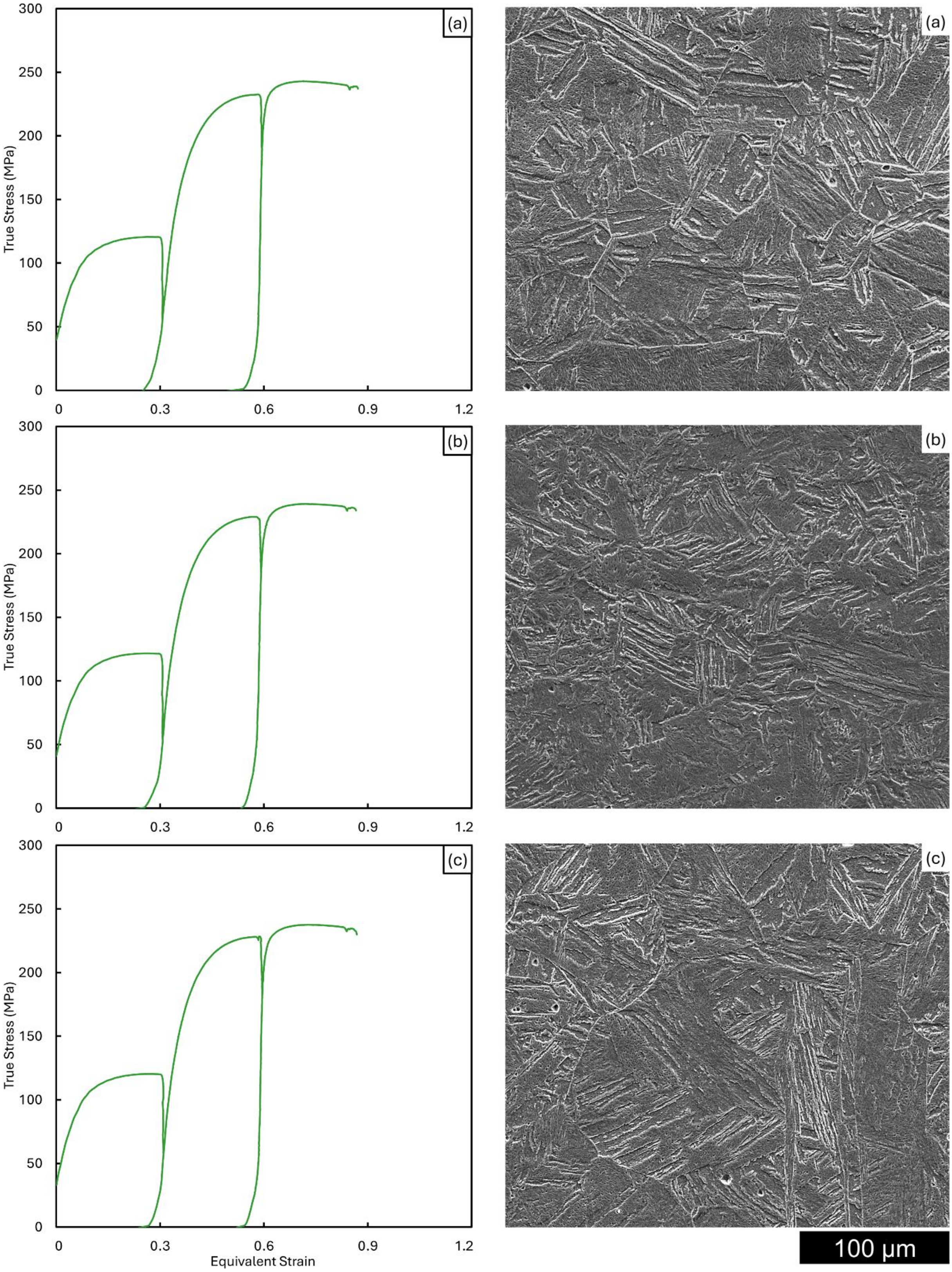

Figure 4.19 SEM micrographs representing microstructure, towards the short transverse direction, deformed at 800°C with a final strain reaching ~0.9 followed by rapid cooling at a rate of 100°C/s along with corresponding stress-strain flow curve for: (a) BA, (b) BA ↗ Ni, and (c) BA ↗ Mn.

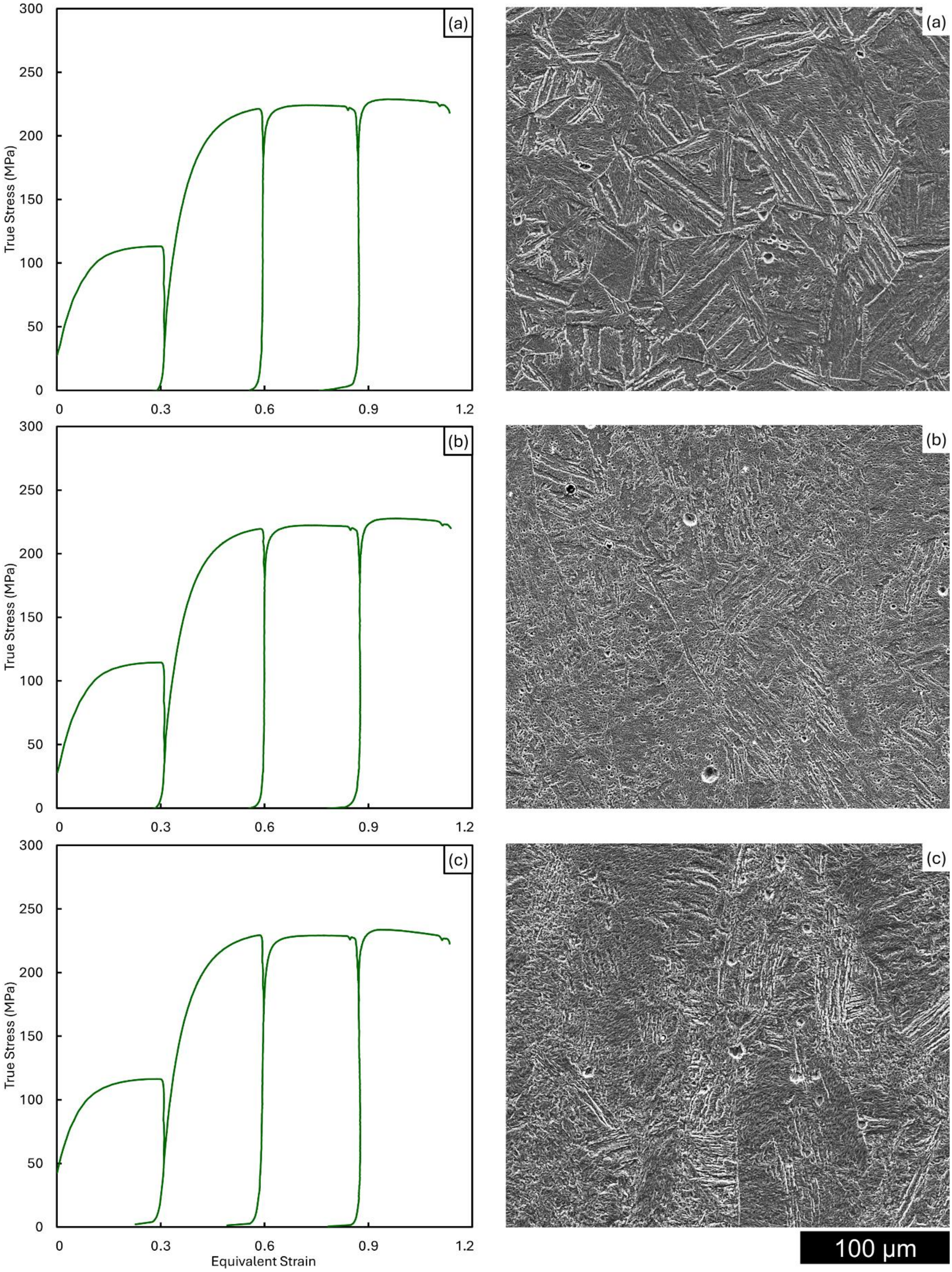

Figure 4.20 SEM micrographs representing microstructure, towards the short transverse direction, deformed at 800°C with a final strain reaching ~1.2 followed by rapid cooling at a rate of 100°C/s along with corresponding stress-strain flow curve for: (a) BA, (b) BA ↗ Ni, and (c) BA ↗ Mn.

4.3.2.4 Principal Observations from SEM Micrographs

In contrast to the microstructure obtained post rough rolling that is shown in Figure 4.9 for BA, BA ↗ Ni, and BA ↗ Mn, SEM micrographs presented in Figure 4.11, Figure 4.12, and Figure 4.13 indicated a marked increase in grain refinement and more consistent microstructural features of the microstructure following finish rolling at 1050°C where a recrystallized austenite microstructure was obtained as a consequence of deformation above the recrystallization-limit temperature $T_{95\%}$. It should be noted, however, that this interpretation was based on morphological evidence, i.e. equiaxed appearance and boundary contrast, rather than direct crystallographic confirmation. Neither KAM nor sub-grain orientation-gradient analysis was undertaken; therefore, classification of these regions as fully recrystallized should be regarded as indicative rather than definitive.

Furthermore, SEM micrographs presented in Figure 4.15, Figure 4.16, and Figure 4.17 also indicated a pronounced increase in grain subdivision and morphological definition following finish rolling at 800°C where an unrecrystallized austenite microstructure was obtained as a consequence of deformation below the recrystallization-stop temperature $T_{5\%}$. Similarly, the unrecrystallized description was inferred from the elongated grain morphology and retained deformation contrast in SEM images, without direct validation by orientation-based metrics such as KAM.

This microstructural refinement was evaluated on the basis of grain size evolution, where it is evident that progressively smaller grains were obtained with every strain increment, i.e. from 0.3 to 0.6, 0.9, and 1.2 even though differences in microstructure progressively diminished and became less pronounced with increased strain. While this refinement trend is consistent with deformation-driven subdivision and boundary formation, it was primarily inferred from morphological contrast rather than statistical grain size measurements. An assessment of martensitic grain size was not conducted, the quantitative treatment relied on total S_v, reported in subsequent sections.

Despite that the microstructures appear alike to the naked eye, closer observation would lead to remarking the overall differences in grain refinement particularly for the conditions in which the microstructure was heavily deformed. For instance, remnants of parent unrecrystallized austenite were observed along the elongated microstructure obtained post deformation below $T_{5\%}$ at a strain of 1.2 as presented in Figure 4.17, while an equiaxial microstructure was observed post deformation above $T_{95\%}$ at the same strain as presented in Figure 4.13. These features were interpreted on the basis of microstructural morphology and boundary continuity, and should therefore be considered qualitative indicators of recrystallization and recovery behavior.

Accordingly, the best straightforward approach for capturing a tangible magnitude manifesting the influence of grain refinement is based upon a quantitative analysis in which total S_v is determined by the number of intercepts encountered, reflecting the interface density within the microstructure. Since the entire prior austenite grains are challenging to detect in the majority of conditions, this restricts the possibility of a definite identification of grains or the precise demarcation of their boundaries.

However, it is indisputable that the final product, i.e. the final transformed microstructure, consisted entirely of martensite originating from either fully recrystallized austenite or fully unrecrystallized austenite; this austenitic microstructure could be reconstructed via EBSD maps to reveal the prior austenite grains (PAG) at the point of transformation. Within this framework, the EBSD-based reconstruction served as the principal means of corroborating the morphology-based observations, while orientation-gradient metrics, e.g. KAM, and lath-size distributions were not produced in the present dataset and are identified as potential extensions.

It is worth noting that only one field of view per processing condition and alloy composition was presented in the context of microstructural analysis to avoid repetition. The remaining fields that were analyzed within the scope of quantifying total S_v (explicitly discussed in Section 4.4), i.e. four fields of view for each condition, can be found in Appendix I, which provides a comprehensive compilation of all the fields investigated and ensures all relevant details are thoroughly documented.

4.3.3 Reconstruction of Prior Austenite Grains

EBSD maps of the deformed microstructure reflecting the reconstruction of PAG following single-pass and triple-pass finish rolling, under both high-temperature and low-temperature conditions, are presented in the following sub-sections. These maps enable the reconstruction of the prior austenitic microstructure allowing for the identification of its boundaries before deformation and facilitating the evaluation of the effects of various processing conditions, i.e. deformation temperature and strain amount, on tailoring the final deformed microstructure. Quantitative martensite lath, block, or packet size distributions and kernel average misorientation analyses were not generated in this section; therefore, references to martensite grain refinement are qualitative and are corroborated later only by interfacial metrics and reconstructed prior austenite grain topology.

In addition to the qualitative interpretation, limited quantitative grain size metrics were extracted directly from the reconstructed PAG data under conditions where such measurements were geometrically valid. The reconstruction followed the Nishiyama-Wasserman orientation relationship between austenite and martensite, which reliably delineated prior austenite boundaries for low-carbon supermartensitic stainless steels. All reconstructed datasets, for finish rolling at 1050°C and 800°C, were subjected to internal noise-reduction and confidence-index filtering to exclude poorly indexed points, dubious grains, and polygons intersecting the map borders, ensuring that the derived quantitative data represented physically meaningful grains free from edge truncation or artefactual segmentation.

For finish rolling at 1050°C, where the reconstructed prior austenite grains were equiaxed and statistically well-defined, the prior austenite grain size was obtained in accordance with ASTM E2627 and reported as the average equivalent circle diameter. Conversely, for finish rolling at 800°C, where the reconstructed grains exhibited pronounced elongation and incomplete recrystallization, quantitative assessment relied on a directional line-intercept method normal to the elongation axis, as the ASTM E2627 approach would not be applicable to such non-equiaxed morphologies.

The reconstructed austenite morphology was interpreted in terms of topology and misorientation distribution, without invoking sub-grain orientation gradients or dislocation density quantification, ensuring that all structural interpretations remain strictly morphological. This reconstruction provides critical insight into how the deformation process influences the evolution of the grain structure. In other words, the differences observed in the reconstructed PAG maps lead to a better understanding of the influence of deformation on the preservation and transformation of the original austenitic grains.

Furthermore, by understanding how deformation affects the microstructural evolution of these grains, it becomes possible to refine processing techniques that promote key microstructural characteristics such as grain refinement and controlled phase transformation behavior. This provides significant insight into whether the original grain structure is preserved or altered, thus forming the basis for the evaluation of the mechanical properties and performance of the material. Retained austenite was not quantified by diffraction or EBSD phase mapping within the present dataset; the interpretations in this section therefore treat retained austenite as negligible in accordance with the dilatometry and CCT indications of fully martensitic products.

4.3.3.1 Finish Rolling at 1050°C

EBSD maps along with the corresponding reconstructed PAG maps were generated for the two studied alloys, i.e. BA and BA ↗ Mn, following single-pass finish rolling with a strain of 0.6 and triple-pass finish rolling with a strain of 1.2 at a high temperature of 1050°C. The data were processed using AZtecCrystal, and these maps are presented in Figure 4.21 and Figure 4.22; additionally, the maps presented in Figure 4.23 and Figure 4.24 yield similar results when processed using MTEX, albeit with slight variations in the interpretation of grain boundaries, highlighting the importance of the processing method in microstructural analysis. The EBSD outputs were interpreted on the basis of inverse pole figure colouring, and reconstructed austenite topology.

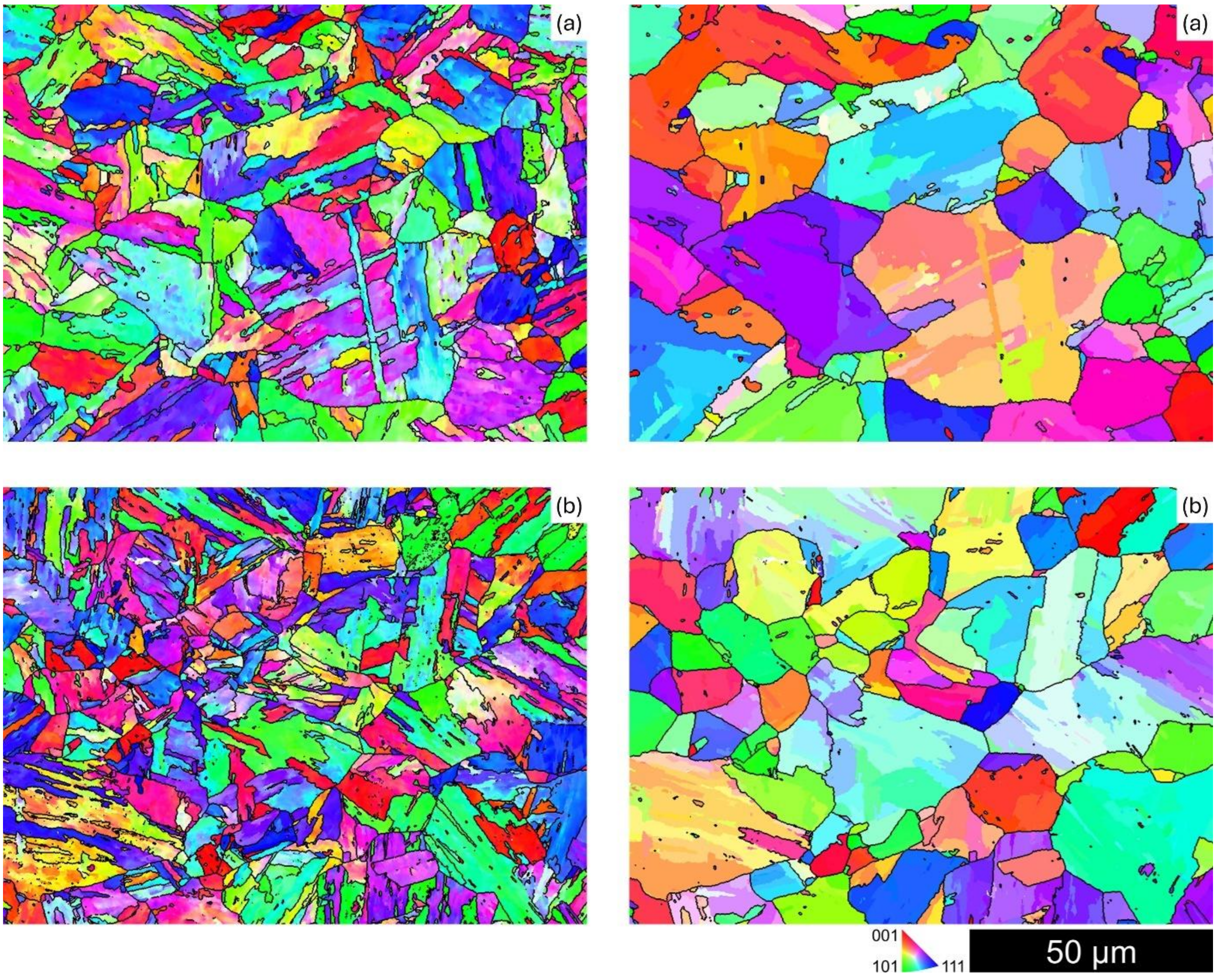

Figure 4.21 EBSD IPF maps representing microstructure, towards the long transverse direction, deformed at 1050°C with a final strain reaching ~0.6 followed by rapid cooling at a rate of 100°C/s (left) along with corresponding reconstructed PAG maps (right) for (a) BA and (b) BA ↗ Mn, processed using AZtecCrystal.

The effect of strain on grain morphology and PAG reconstruction is evident when comparing the single-pass and triple-pass finish rolling conditions. In the single-pass finish rolling condition presented in Figure 4.21 and Figure 4.23, the EBSD maps revealed elongated grains with retained deformation substructures such as deformation bands and low-angle grain boundaries indicating partial recrystallization, whereas the corresponding reconstructed PAG maps exhibited a refined prior austenite grain structure due to the onset of recrystallization, which helped fragment the initially larger grains. Furthermore, a comparison of the microstructure before and after PAG reconstruction indicates that BA ↗ Mn exhibited finer grains compared to BA, emphasizing the role of manganese addition in accelerating grain refinement and recrystallization processes, derived from morphology and boundary continuity in the EBSD maps.

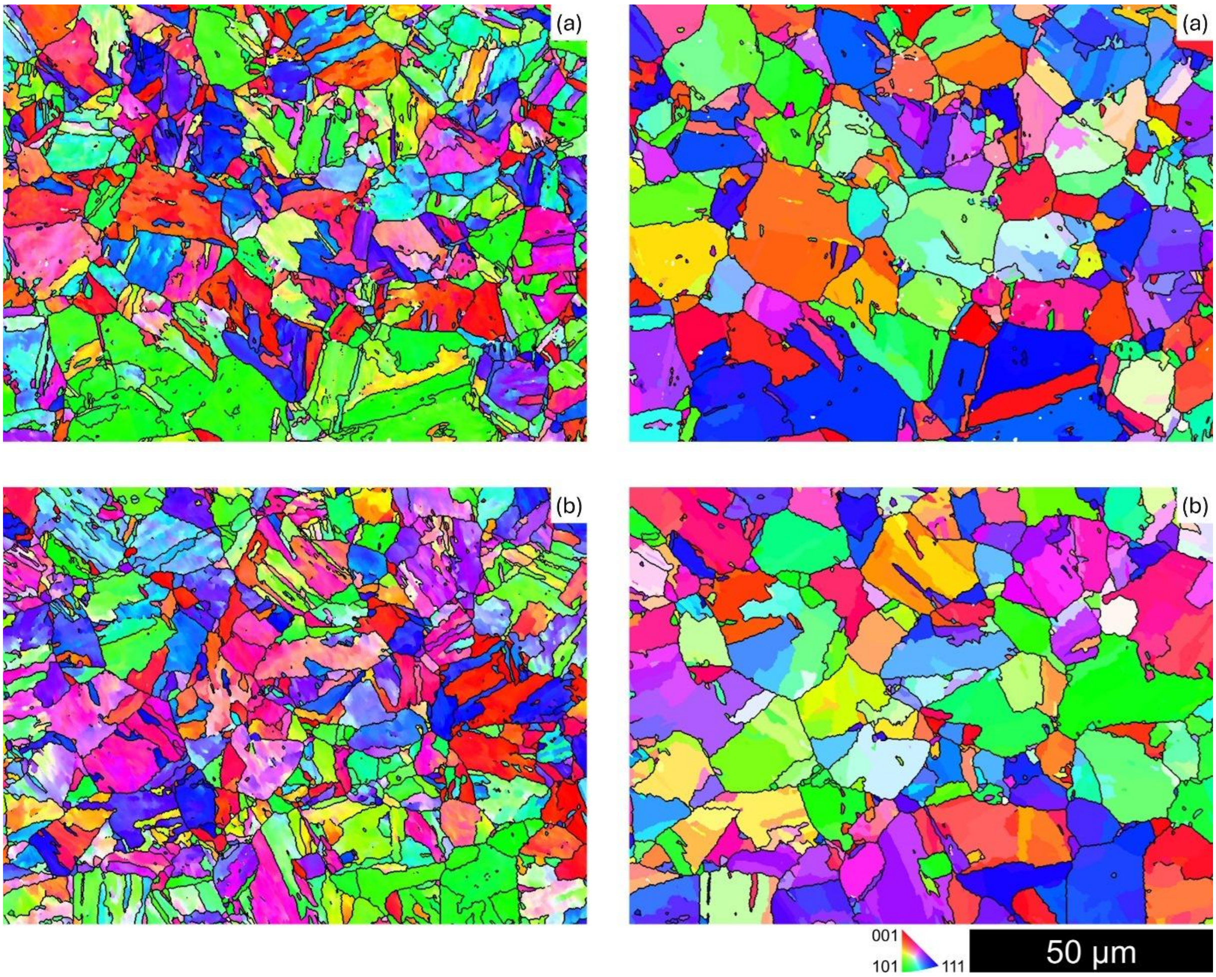

Figure 4.22 EBSD IPF maps representing microstructure, towards the long transverse direction, deformed at 1050°C with a final strain reaching ~1.2 followed by rapid cooling at a rate of 100°C/s (left) along with corresponding reconstructed PAG maps (right) for (a) BA and (b) BA ↗ Mn, processed using AZtecCrystal.

This difference was captured numerically, as the reconstructed PAG were sufficiently equiaxed to permit determination of prior austenite grain size, and the measured grain size decreased with both increasing strain and manganese addition. At a total strain of 0.6, BA exhibited a grain size of 25.2 µm, whereas BA ↗ Mn exhibited 18.6 µm; at a total strain of 1.2, BA and BA ↗ Mn showed further refinement to 14.8 µm and 12.7 µm, respectively. These values, listed in Table 4.2, were obtained after reconstruction via AZtecCrystal in conjunction with automated cleanup and therefore reflect the refined equiaxed PAG morphology associated with deformation at 1050°C, consistent with the observed increase in boundary definition and grain topology in the reconstructed PAG maps, confirming the convergence between quantitative metrics and qualitative features in indicating improved grain refinement with increasing strain and manganese content.

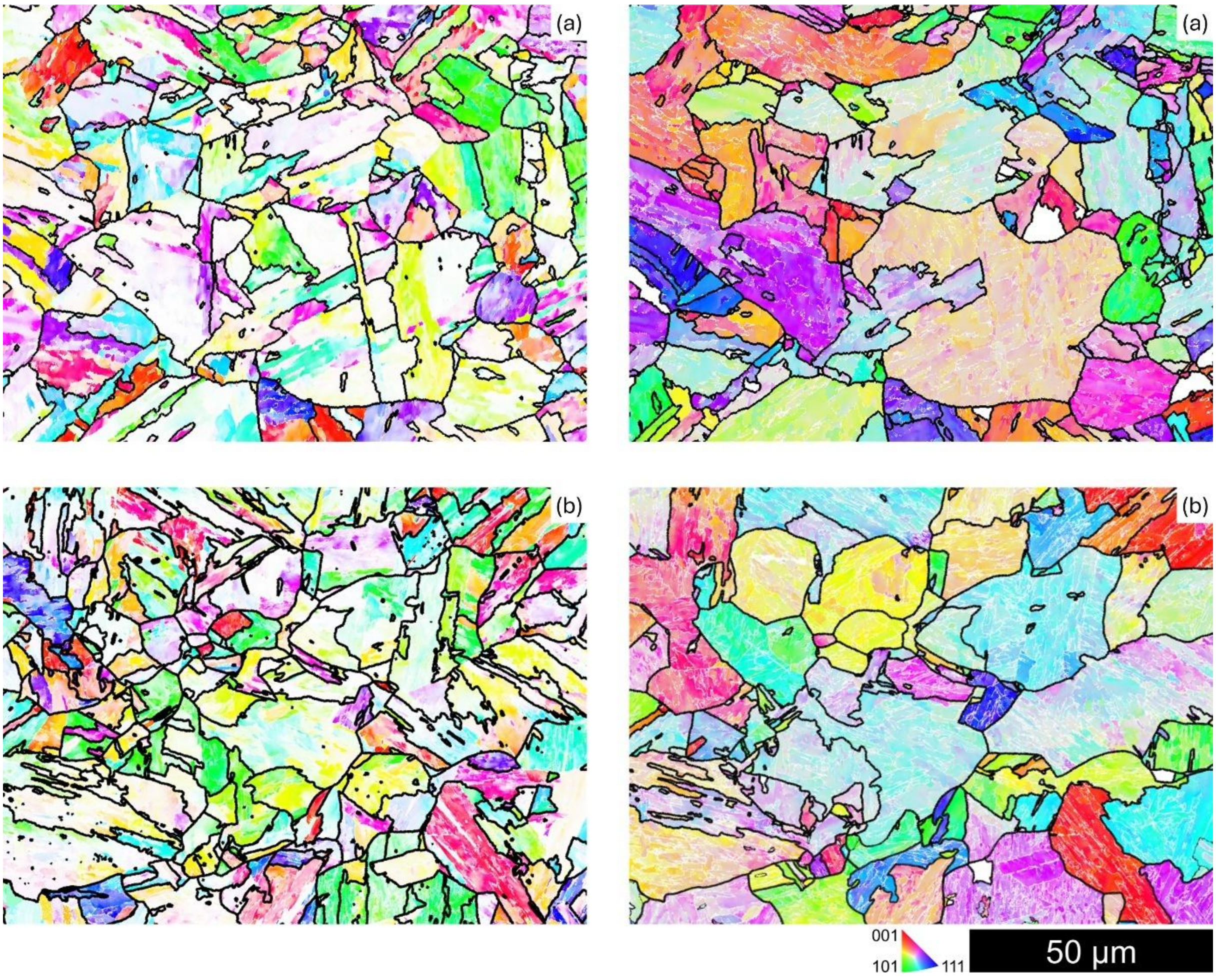

Figure 4.23 EBSD IPF maps representing microstructure, towards the long transverse direction, deformed at 1050°C with a final strain reaching ~0.6 followed by rapid cooling at a rate of 100°C/s (left) along with corresponding reconstructed PAG maps (right) for (a) BA and (b) BA ↗ Mn, processed using MTEX.

The EBSD maps of the triple-pass finish rolling condition presented in Figure 4.22 and Figure 4.24 indicated that deformation at a higher strain resulted in a more refined and fragmented microstructure with a consistent grain distribution. In essence, increased deformation boosted the recrystallization already active at this temperature, leading to the formation of smaller grains and a reduction in dislocation density. This was driven by greater stored strain energy, particularly in BA ↗ Mn, where manganese promoted dislocation retention and boundary stability, thereby intensifying grain refinement. Additionally, the reconstructed PAG maps of the higher strain condition revealed more equiaxed grains and a more distinct prior austenite grain structure with well-defined boundaries, confirming a more complete transformation compared to the lower strain condition. The apparent reduction in stored deformation and increase in equiaxed boundary fractions are inferred from boundary maps.

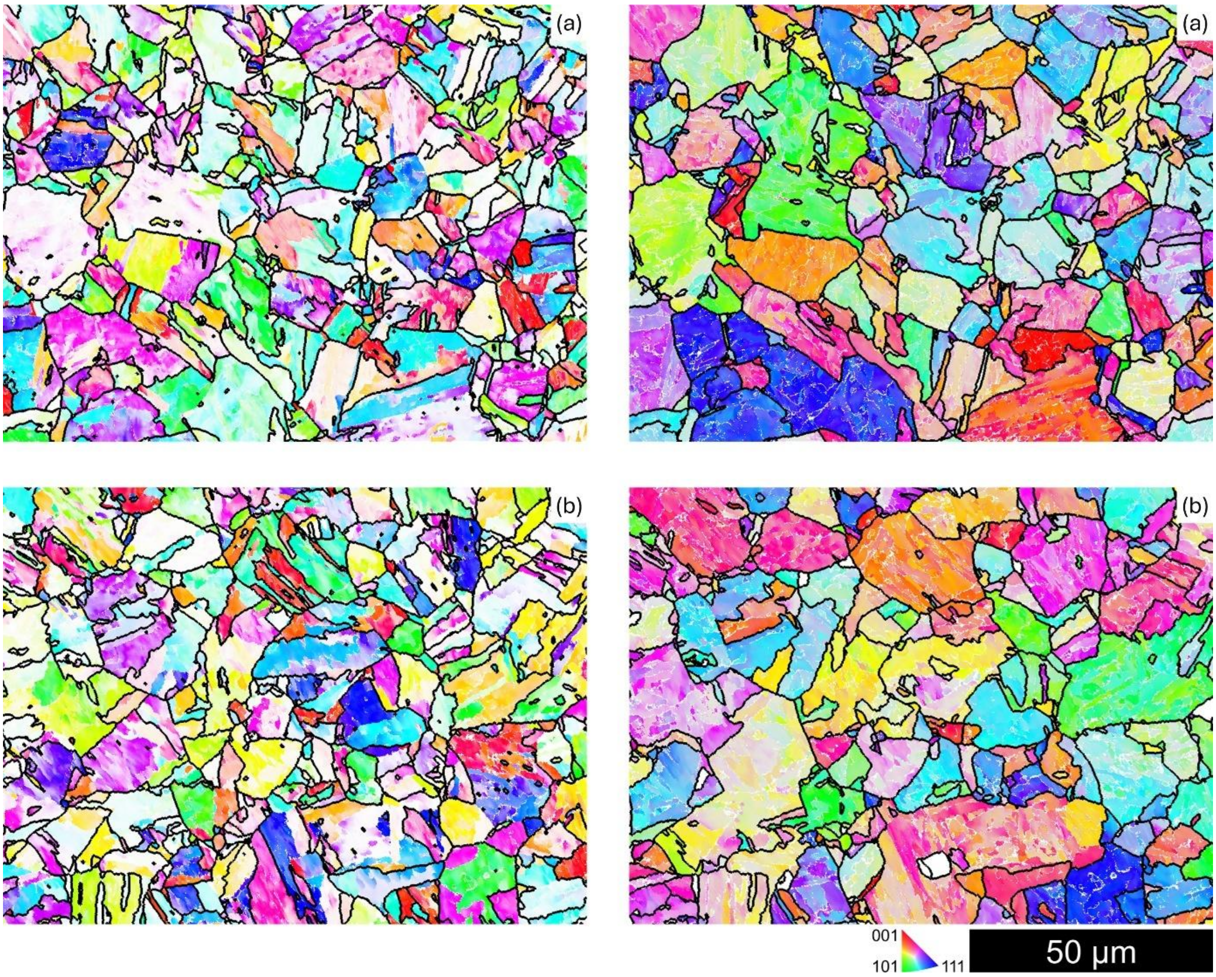

Figure 4.24 EBSD IPF maps representing microstructure, towards the long transverse direction, deformed at 1050°C with a final strain reaching ~1.2 followed by rapid cooling at a rate of 100°C/s (left) along with corresponding reconstructed PAG maps (right) for (a) BA and (b) BA ↗ Mn, processed using MTEX.

Table 4.2 Average PAG size, expressed as equivalent circle diameter, for BA and BA ↗ Mn at 1050°C.

Temperature	Strain	Material Identification	Average Grain Size (μm)
1050°C	0.6	BA	25.2
		BA ↗ Mn	18.6
1050°C	1.2	BA	14.8
		BA ↗ Mn	12.7

4.3.3.2 Finish Rolling at 800°C

EBSD maps along with the corresponding reconstructed PAG maps were generated for the two studied alloys, i.e. BA and BA ↗ Mn, following single-pass finish rolling with a strain of 0.6 and triple-pass finish rolling with a strain of 1.2 at a low temperature of 800°C. The data were processed using AZtecCrystal, and these maps are presented in Figure 4.25 and Figure 4.26; additionally, the maps presented in Figure 4.27 and Figure 4.28 yield similar results when processed using MTEX, albeit with slight variations in the interpretation of grain boundaries, highlighting once again the importance of the processing method in microstructural analysis.

The reconstructed PAG at 800°C are described here as unrecrystallized because they retain elongated morphology, pronounced intragranular banding, and boundary continuity consistent with deformation substructure rather than equiaxed recrystallized grains. The classification of the microstructure as unrecrystallized is based on elongated morphology and boundary character revealed by EBSD.

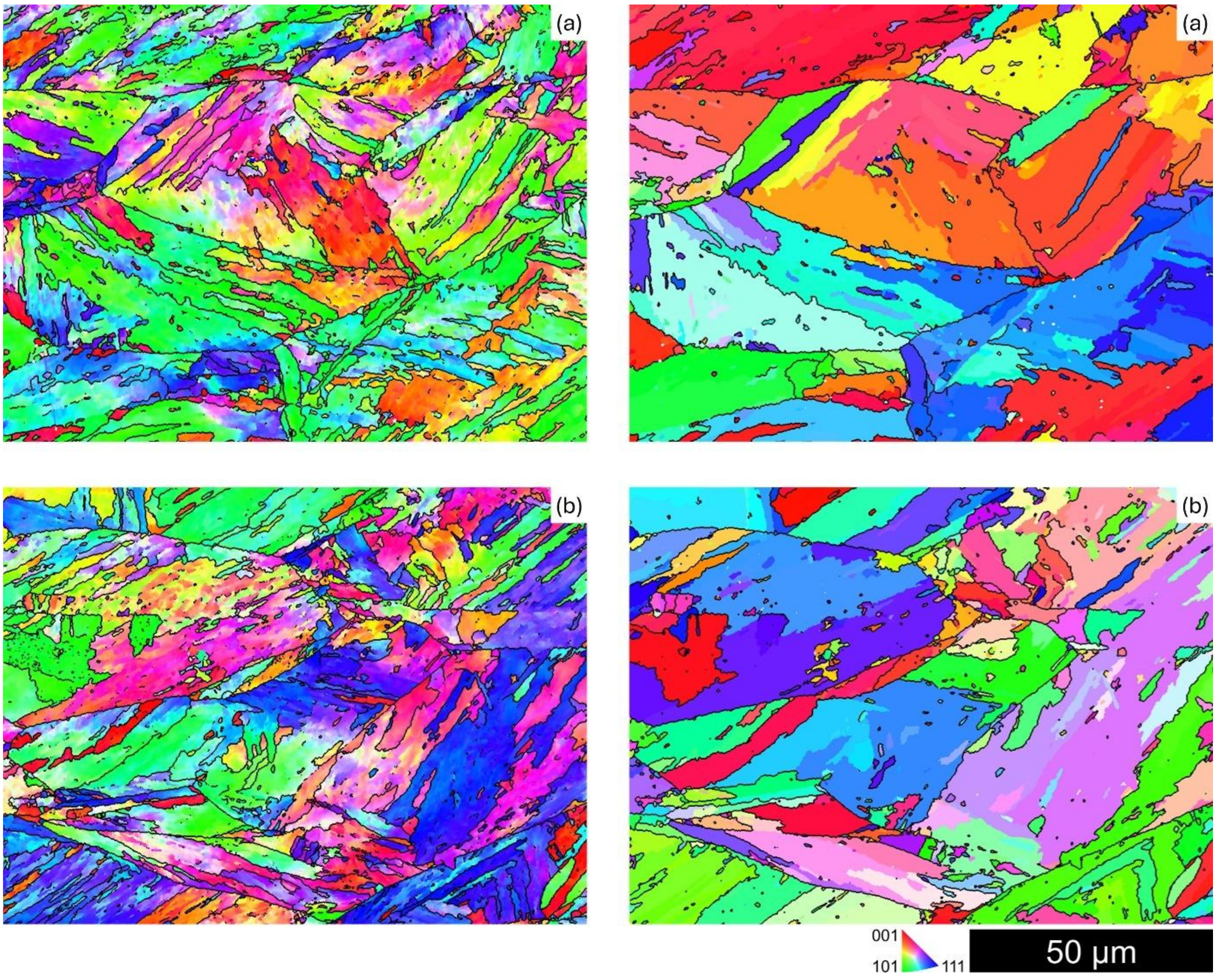

Figure 4.25 EBSD IPF maps representing microstructure, towards the long transverse direction, deformed at 800°C with a final strain reaching ~0.6 followed by rapid cooling at a rate of 100°C/s (left) along with corresponding reconstructed PAG maps (right) for (a) BA and (b) BA ↗ Mn, processed using AZtecCrystal.

The effect of strain on grain morphology and PAG reconstruction is evident when comparing the single-pass and triple-pass finish rolling conditions. In the single-pass finish condition shown in Figure 4.25 and Figure 4.27, the EBSD maps revealed a heterogeneous microstructure with some regions containing relatively coarse and elongated grains, indicating that recrystallization was strongly suppressed, whereas the corresponding reconstructed PAG maps exhibited a lower density of HAGB confirming that the prior austenite grains remained largely intact with limited subdivision. However, BA↗Mn displayed higher boundary definition and HAGB density than BA, indicating that manganese stabilized boundary segments and restricted migration, thereby preserving a finer effective grain thickness even without full recrystallization, noting that the term finer refers to reduced transverse grain intercept thickness rather than an equiaxed grain diameter.

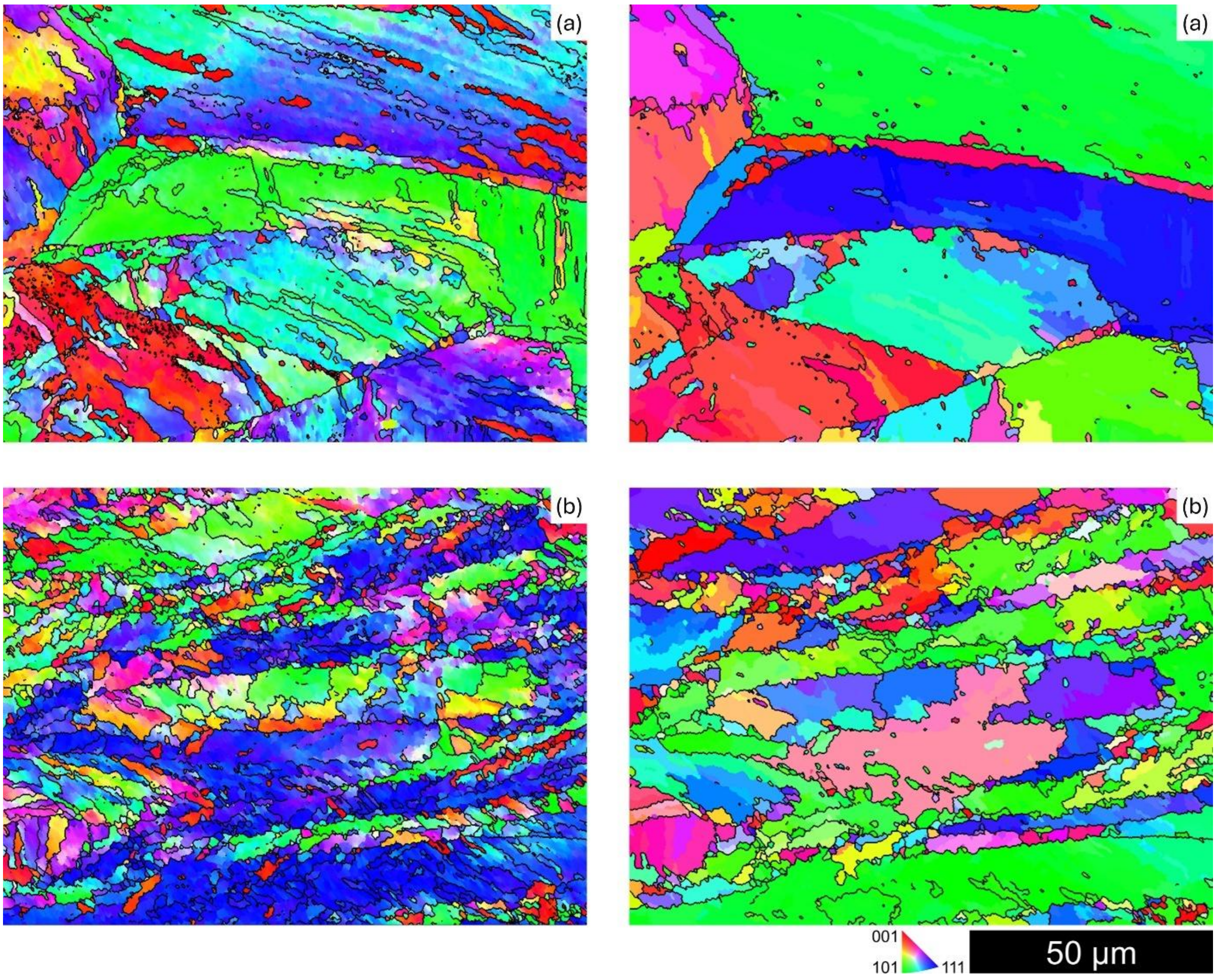

Figure 4.26 EBSD IPF maps representing microstructure, towards the long transverse direction, deformed at 800°C with a final strain reaching ~1.2 followed by rapid cooling at a rate of 100°C/s (left) along with corresponding reconstructed PAG maps (right) for (a) BA and (b) BA↗Mn, processed using AZtecCrystal.

Because the reconstructed prior austenite grains at 800°C were elongated rather than equiaxed, grain size was not attainable in this condition. Instead, the characteristic PAG thickness normal to the elongation direction was assessed by a directional line-intercept method, where five parallel test lines of 85 µm length were drawn approximately perpendicular to the elongation axis, i.e. at an angle of 90°, and the number of PAG boundary intercepts on each line was counted. The average transverse intercept distance was then calculated by dividing the test line length by the number of intercepts on each line and averaging the lineal distances over the five lines, so that smaller values indicate a thinner effective grain thickness and larger values a greater transverse dimension. This approach is therefore targeted to the relevant dimension, i.e. the thickness of the elongated prior austenite grains rather than their full aspect ratio.

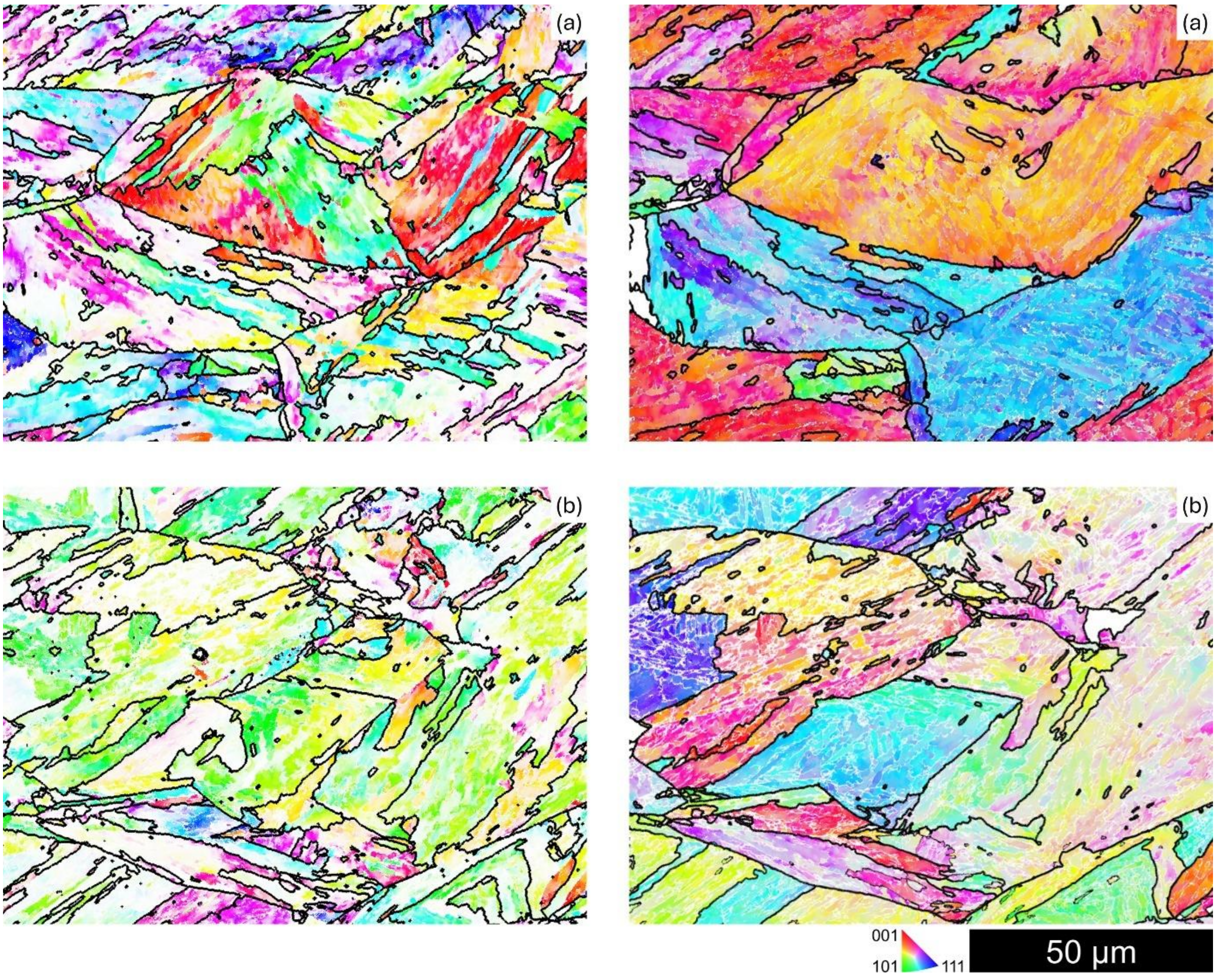

Figure 4.27 EBSD IPF maps representing microstructure, towards the long transverse direction, deformed at 800°C with a final strain reaching ~0.6 followed by rapid cooling at a rate of 100°C/s (left) along with corresponding reconstructed PAG maps (right) for (a) BA and (b) BA ↗ Mn, processed using MTEX.

Under the 0.6 strain condition at 800°C, BA exhibited an average transverse intercept distance of ~30.4 µm, whereas BA ↗ Mn exhibited ~26.6 µm. At the higher strain of 1.2, BA and BA ↗ Mn showed further refinement to ~25.0 µm and ~18.5 µm, respectively. Decreasing transverse intercept distance from 0.6 to 1.2 indicated progressive thinning of the elongated PAG in the transverse direction, while at each strain level, BA ↗ Mn consistently exhibited a shorter transverse intercept distance, confirming a finer effective PAG thickness in the manganese-enriched condition. These findings, summarized in Table 4.3, align with the qualitative EBSD observations in Figure 4.25 to Figure 4.28, where the 1.2 strain condition displayed a more segmented elongated morphology than 0.6, and BA ↗ Mn appeared more finely partitioned than BA, confirming that strain accumulation and manganese addition both intensified directional refinement.

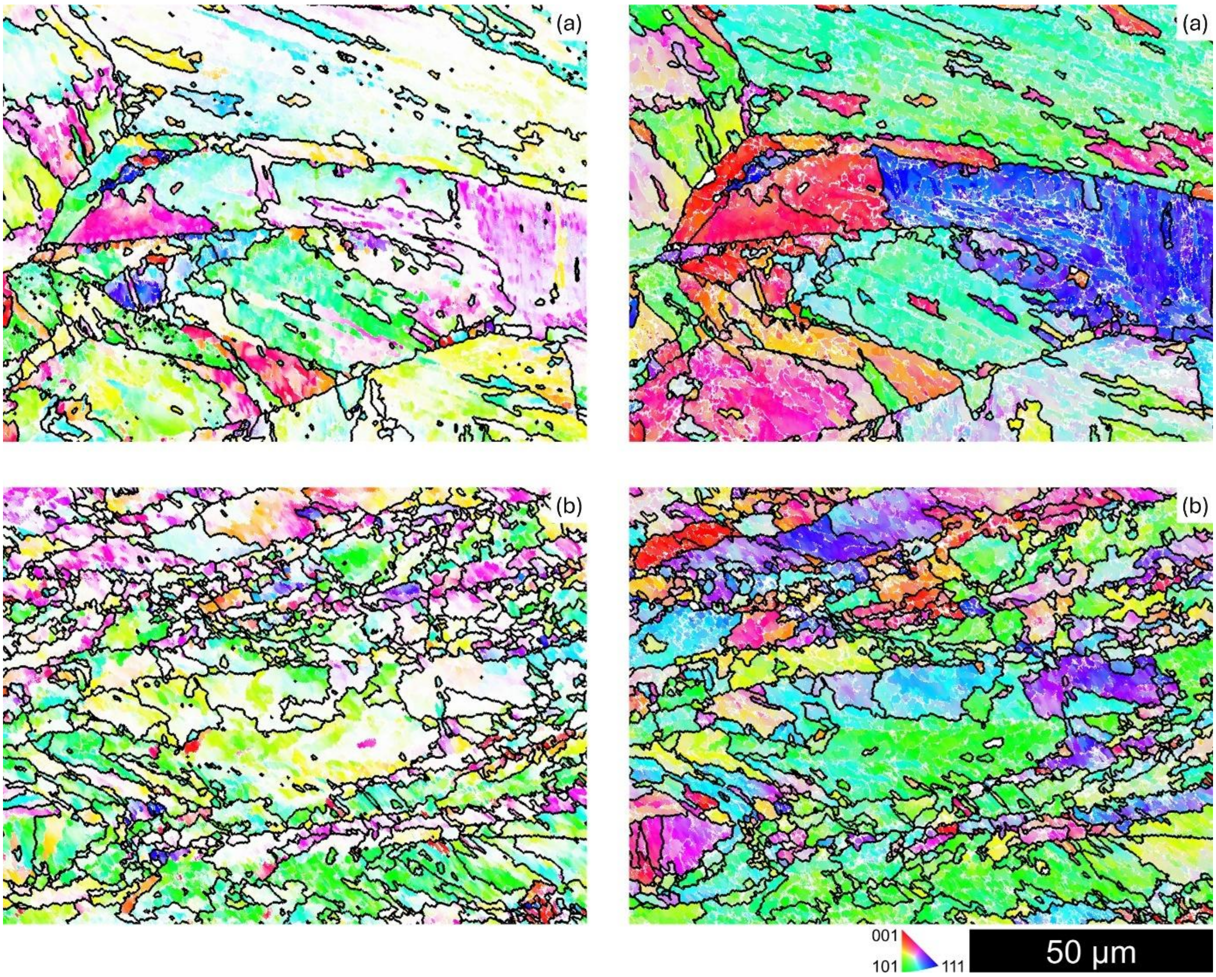

Figure 4.28 EBSD IPF maps representing microstructure, towards the long transverse direction, deformed at 800°C with a final strain reaching ~1.2 followed by rapid cooling at a rate of 100°C/s (left) along with corresponding reconstructed PAG maps (right) for (a) BA and (b) BA ↗ Mn, processed using MTEX.

Table 4.3 Average transverse PAG intercept distance normal to the elongation direction for BA and BA ↗ Mn at 800°C.

Temperature	Strain	Material Identification	Average Transverse Intercept Distance (µm)
800°C	0.6	BA	30.4
		BA ↗ Mn	26.6
800°C	1.2	BA	25.0
		BA ↗ Mn	18.5

In contrast to the single-pass finish rolling condition, the EBSD maps of the triple-pass finish rolling condition presented in Figure 4.26 and Figure 4.28 indicated that deformation at a higher strain facilitated the breakdown of larger grains and resulted in a more fragmented and elongated microstructure due to the accumulation of strain. In addition, the maps revealed an increase in HAGB with increased strain which is indicative of recovery processes occurring within certain regions of the microstructure. However, these HAGB at 800°C are embedded within elongated grain fragments rather than surrounding equiaxed recrystallized grains, implying boundary sharpening without complete boundary replacement.

The addition of manganese led to a higher density of HAGB reflected by the pronounced increase in grain boundary definition for BA ↗ Mn compared to BA. Rather than promoting recrystallization directly, manganese acted to retard recovery and grain boundary migration, thereby suppressing coarsening and preserving stored strain energy, leading to the development of a finer martensitic microstructure upon cooling; distinguishing recovery from recrystallization in these conditions would benefit from KAM mapping.

The influence of strain and manganese on grain orientation and boundary characteristics is further highlighted through closer observation of the reconstructed PAG maps. Notably, PAG reconstruction presented in Figure 4.26 and Figure 4.28 revealed a lower density of retained deformation features in BA ↗ Mn compared to BA when deformed at a strain of 1.2 indicating that manganese accelerated dislocation rearrangement and recovery even before recrystallization. Additionally, the presence of manganese stabilized HAGB, promoted the development of misoriented sub-grains within the parent grains, and restricted prior austenite grain coarsening by influencing transformation kinetics. Consequently, the finer austenite grains prior to transformation resulted in the finest martensitic morphology among all the studied conditions, reflected by the segmented EBSD contrast, increased boundary definition, and a higher reconstructed prior austenite boundary density, rather than by a directly measured martensite lath width.

4.3.3.3 Principal Observations from EBSD Maps

Regarding the effect of deformation temperature on grain morphology and boundary characteristics, temperature significantly influenced the evolution of prior austenite grains where a high deformation temperature of 1050°C led to finer and more equiaxed grains which was indicative of a recrystallized microstructure. Conversely, a lower deformation temperature of 800°C resulted in larger and more elongated prior austenite grains remaining in their deformed state without undergoing significant recrystallization. In addition, the unrecrystallized grains at 800°C exhibited higher strain accumulation and contained more lattice defects compared to the fully recrystallized grains at 1050°C, further highlighting the role of temperature in governing the balance between deformation and recrystallization, where deformation alone dictated the microstructural features at lower temperatures, whereas recrystallization played a dominant role in refining the grain structure at higher temperatures[155].

Regarding the effect of deformation amount on grain morphology and boundary characteristics, a clear trend emerged, wherein increased strain led to a more refined microstructure in both temperature regimes, but through different pathways. At 1050°C, higher strain promoted recrystallization, producing a higher density of equiaxed grains and HAGB. At 800°C, higher strain intensified subdivision of elongated unrecrystallized grains and increased local HAGB density within those elongated fragments. Quantitative martensite grain size metrics were not compiled for this comparison; the refinement trend is supported indirectly by the interfacial area per unit volume and reconstructed prior austenite grain statistics presented in Section 4.4.

In effect, this trend was particularly pronounced in BA ↗ Mn which suggested that manganese facilitated the formation of a greater amount of equiaxed grains, as revealed in the reconstructed PAG maps, confirming the critical role of manganese in intensifying the recrystallization response through increased dislocation storage and local strain energy accumulation while stabilizing grain boundaries against excessive growth, ultimately contributing to finer grain morphology and higher boundary density within the microstructure[156]. These interpretations are inferential rather than directly evidenced by dislocation structure analysis and should be regarded as consistent with expected thermomechanical trends rather than confirmed mechanisms. A definitive separation of recovery, sub-grain formation, and recrystallization would require kernel average misorientation or high-resolution transmission electron microscopy.

Regarding the effect of chemical composition on grain morphology and boundary characteristics, manganese promoted more complete boundary refinement and accelerated recrystallization at 1050°C; in addition, BA ↗ Mn alloy consistently exhibited a higher density of misoriented sub-grains, particularly at a higher strain of 1.2, which ultimately contributed to the refinement of prior austenite grain size and improved the final microstructure. Furthermore, the increased density of HAGB in the triple-pass finish rolling of BA ↗ Mn confirmed the role of manganese in influencing transformation kinetics by restricting prior austenite grain coarsening, leading to a more resistant microstructure with reduced susceptibility to grain growth evidenced by a finer and more consistent martensitic structure upon cooling[157].

Regarding the effect of processing methods on grain morphology and boundary characteristics, both AZtecCrystal and MTEX yielded comparable overall microstructural morphologies; however, differences in boundary interpretations were observed. The grain boundaries identified using AZtecCrystal appeared more defined, revealing prominent deformation substructures, whereas MTEX captured more subtle intragranular features that were less apparent in the EBSD maps processed by AZtecCrystal. These differences highlighted the influence of processing algorithms on microstructural analysis and their effect on the interpretation of grain size, shape, and distribution, which consequently impacts the quantitative analysis.

4.4 Microstructure Quantification

4.4.1 Interfacial Area per Unit Volume S_v

In correspondence with the significant microstructural refinement achieved through finish rolling in comparison to rough rolling as highlighted in the microstructural analysis during deformation (Section 4.3.2), total S_v values exhibited a substantial increase attributed to this major grain refinement associated with this pronounced grain size reduction. A gradual and significant increase in total S_v was remarked with an increasing amount of strain from 0.6 to 0.9 and 1.2, showing a direct correlation between strain increment and grain refinement; while only a slight increase in total S_v was remarked when comparing the temperature at which deformation occurred, specifically a minor increase in the conditions where deformation was carried out below the recrystallization-stop temperature $T_{5\%}$ at 800°C as opposed to deformation above the recrystallization-limit temperature $T_{95\%}$ at 1050°C. Although total S_v increases with strain and decreasing temperature, the present work does not deconvolute this increase into contributions from martensite lath, block, or packet size; explicit martensite grain size statistics were not reported.

As an analogy, the data reported appear to support the assumption that a noteworthy increase in total S_v values is correlated with the addition of specific alloying elements; into evidence, the presence of nickel and manganese contribute to increasing total S_v to a certain level higher than total S_v of base alloy with no further additions highlighting their potential to influence boundary mobility and structural stability during deformation and cooling. This relationship is considered a logical outcome since variations in solute content can alter recovery and recrystallization kinetics and, consequently, the evolution of interfacial area, yet this remains to be investigated. This reinforces the hypothesis that alloying elements play a fundamental role in driving microstructural refinement and could be strategically adjusted to tailor the desired property balance.

As a reference for evaluating the effectiveness of applied processing conditions on the final product when quantifying S_v as a function of deformation amount or deformation temperature, a total S_v range for each composition component was determined succeeding an intermediate stage of processing, i.e. roughing deformation at a relatively low strain of 0.3 and a relatively high temperature of 1150°C. Figure 4.29 represents these outcomes where the alloy with higher manganese content presented the highest total S_v ranging between 1.68-1.92 x 10^5 mm^{-1}, while the alloy with higher nickel content presented a lower total S_v ranging between 1.52-1.60 x 10^5 mm^{-1}, and the base alloy with no further additions presented the lowest total S_v ranging between 1.12-1.36 x 10^5 mm^{-1}.

In terms of S_v quantification as a function of deformation amount, Figure 4.30 and Figure 4.31 represent the total S_v values succeeding finishing deformation at a varied total strain of 0.6, 0.9, and 1.2 and a constant temperature of 1050°C or 800°C, respectively. A gradual increase in the total S_v associated with increased strain at a temperature of 1050°C is illustrated in Figure 4.30; BA ↗ Mn had an average total S_v of 5.77 x 10^5 mm^{-1} at a strain of 0.6, 6.72 x 10^5 mm^{-1} at a strain of 0.9, and 7.00 x 10^5 mm^{-1} at a strain of 1.2; BA ↗ Ni had an averaged total S_v of 3.86 x 10^5 mm^{-1} at a strain of 0.6, 4.81 x 10^5 mm^{-1} at a strain of 0.9, and 5.83 x 10^5 mm^{-1} at a strain of 1.2; and BA had an averaged total S_v of 2.51 x 10^5 mm^{-1} at a strain of 0.6, 4.05 x 10^5 mm^{-1} at a strain of 0.9, and 4.75 x 10^5 mm^{-1} at a strain of 1.2.

Comparatively, a gradual increase in the total S_v associated with increased strain at a temperature of 800°C is illustrated in Figure 4.31; BA ↗ Mn had an averaged total S_v of 6.47 x 10^5 mm^{-1} at a strain of 0.6, 6.91 x 10^5 mm^{-1} at a strain of 0.9, and 7.18 x 10^5 mm^{-1} at a strain of 1.2; BA ↗ Ni had an averaged total S_v of 4.18 x 10^5 mm^{-1} at a strain of 0.6, 5.49 x 10^5 mm^{-1} at a strain of 0.9, and 6.10 x 10^5 mm^{-1} at a strain of 1.2; and BA had an averaged total S_v of 3.67 x 10^5 mm^{-1} at a strain of 0.6, 4.65 x 10^5 mm^{-1} at a strain of 0.9, and 5.12 x 10^5 mm^{-1} at a strain of 1.2.

In terms of S_v quantification as a function of deformation temperature, Figure 4.32, Figure 4.33, and Figure 4.34 represent the total S_v values succeeding finishing deformation at a varied temperature of 1050°C and 800°C, and a constant total strain of 0.6, 0.9, or 1.2 respectively. A gradual increase in the total S_v associated with the decreased temperature at a strain of 0.6 is illustrated in Figure 4.32; BA ↗ Mn had an averaged total S_v of 5.77 x 10^5 mm^{-1} at a temperature of 1050°C, and 6.47 x 10^5 mm^{-1} at a temperature of 800°C; BA ↗ Ni had an averaged total S_v of 3.86 x 10^5 mm^{-1} at a temperature of 1050°C, and 4.18 x 10^5 mm^{-1} at a temperature of 800°C; and BA had an averaged total S_v of 2.51 x 10^5 mm^{-1} at a temperature of 1050°C, and 3.67 x 10^5 mm^{-1} at a temperature of 800°C.

Relatively, a gradual increase in the total S_v associated with decreased temperature at a strain of 0.9 is illustrated in Figure 4.33; BA ↗ Mn had an averaged total S_v of 6.72 x 10^5 mm^{-1} at a temperature of 1050°C, and 6.91 x 10^5 mm^{-1} at a temperature of 800°C; BA ↗ Ni had an averaged total S_v of 4.81 x 10^5 mm^{-1} at a temperature of 1050°C, and 5.49 x 10^5 mm^{-1} at a temperature of 800°C; and BA had an averaged total S_v of 4.05 x 10^5 mm^{-1} at a temperature of 1050°C, and 4.65 x 10^5 mm^{-1} at a temperature of 800°C.

In addition, a gradual increase in the total S_v associated with decreased temperature at a strain of 1.2 is illustrated in Figure 4.34; BA ↗ Mn had an averaged total S_v of 7.00 x 10^5 mm^{-1} at a temperature of 1050°C, and 7.18 x 10^5 mm^{-1} at a temperature of 800°C; BA ↗ Ni had an averaged total S_v of 5.83 x 10^5 mm^{-1} at a temperature of 1050°C, and 6.10 x 10^5 mm^{-1} at a temperature of 800°C; and BA had an averaged total S_v of 4.75 x 10^5 mm^{-1} at a temperature of 1050°C, and 5.12 x 10^5 mm^{-1} at a temperature of 800°C.

In brief, what stands out in this quantification is that higher total S_v values were achieved on the grounds of three aspects: deformation at lower temperatures, deformation at higher strains, and the addition of alloying elements. Within the context of alloying elements, manganese exerted the greatest effect on the microstructure refinement, whereby its presence in higher content resulted in the highest total S_v values peaked under all deformation conditions, whereas nickel exhibited a lower effect.

This is compared to the base alloy with no additional amounts of manganese or nickel, which had the lowest total S_v values. Furthermore, the total S_v increases with increasing deformation amount, and it increases with decreasing deformation temperature, which reinforces the importance of controlling these factors for achieving specific microstructural refinement objectives. Nevertheless, the effect of deformation temperature on total S_v moderately diminished with increasing deformation amount, indicating that strain increment plays a dominant role in achieving further grain refinement at higher strains.

Despite the total S_v findings obtained from analyzing the deformed microstructure along the long transverse direction for all processing conditions, an additional independent set of total S_v findings from another point of view, i.e. another orientation, is shown in Figure 4.35 manifesting the quantitative measurements of the deformed microstructure along the short transverse direction for the deformation condition in which unrecrystallized microstructures were attained; alternatively stated, deformation at a temperature of 800°C. While the recrystallized microstructure exhibited equiaxed grains in all three different orientations, i.e. long transverse, short transverse, and rolling direction, the unrecrystallized microstructure exhibited equiaxed grains only in the short transverse direction, whereas it contained elongated grains in the other two directions: long transverse and rolling directions.

The trend of total S_v findings for the microstructure towards the short transverse direction is comparable to that towards the long transverse direction as represented in Figure 4.36; however, with lower values, which can be rationalized by the directional nature of deformation during plane-strain compression, where the imposed strain is predominantly concentrated along the rolling and long transverse directions, resulting in reduced interface density and grain subdivision along the short transverse direction.

Reviewing the results towards the short transverse direction, it is illustrated once again that the foremost alloy is BA ↗ Mn which, towards the short transverse direction, had an averaged total S_v of 3.12 x 10^5 mm^{-1} at a strain of 0.6, 3.59 x 10^5 mm^{-1} at a strain of 0.9, and 3.94 x 10^5 mm^{-1} at a strain of 1.2; followed by BA ↗ Ni which had an averaged total S_v of 2.29 x 10^5 mm^{-1} at a strain of 0.6, 2.83 x 10^5 mm^{-1} at a strain of 0.9, and 2.97 x 10^5 mm^{-1} at a strain of 1.2; and finally BA which had an averaged total S_v of 1.87 x 10^5 mm^{-1} at a strain of 0.6, 2.36 x 10^5 mm^{-1} at a strain of 0.9, and 2.65 x 10^5 mm^{-1} at a strain of 1.2.

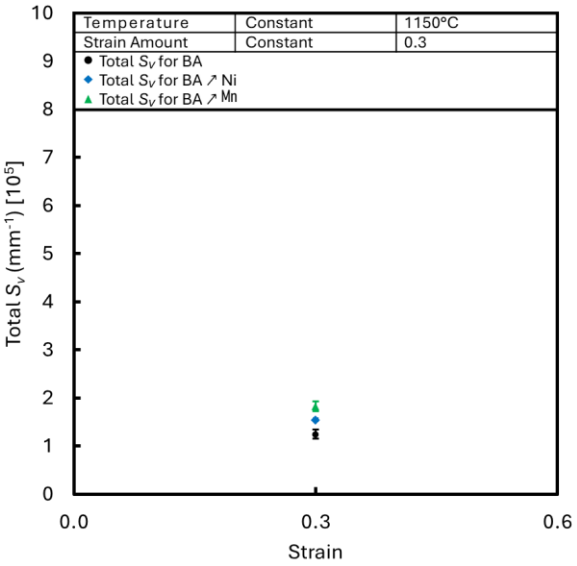

Figure 4.29 Total S_v of the three different compositions at a constant temperature of 1150°C and a constant strain of 0.3; towards the long transverse direction.

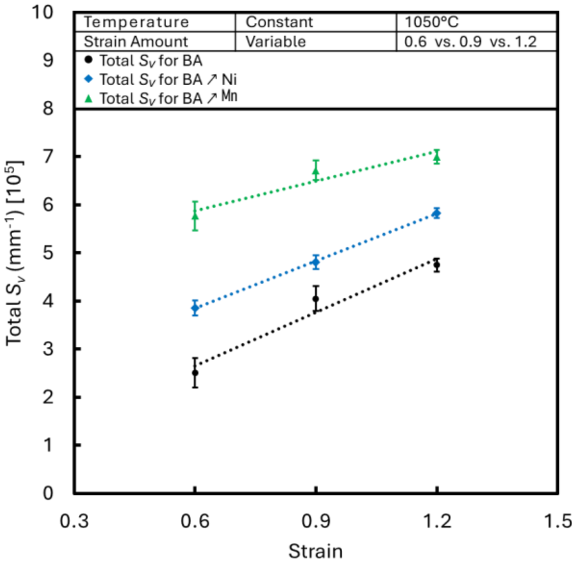

Figure 4.30 Total S_v of the three different compositions at a constant temperature of 1050°C and a varied total strain of 0.6, 0.9, and 1.2; towards the long transverse direction.

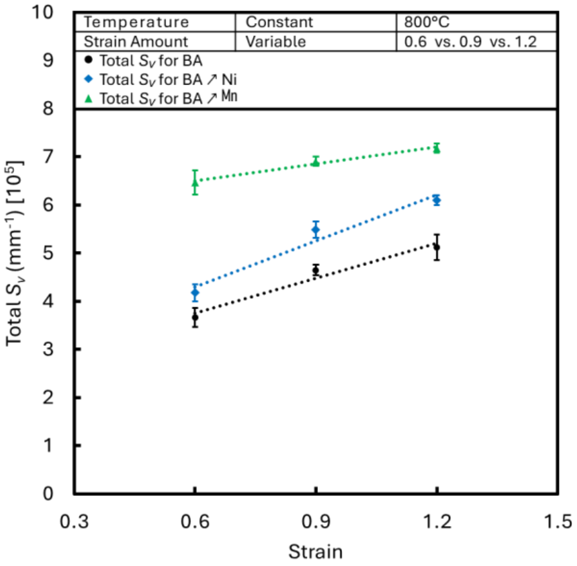

Figure 4.31 Total S_v of the three different compositions at a constant temperature of 800°C and a varied total strain of 0.6, 0.9, and 1.2; towards the long transverse direction.

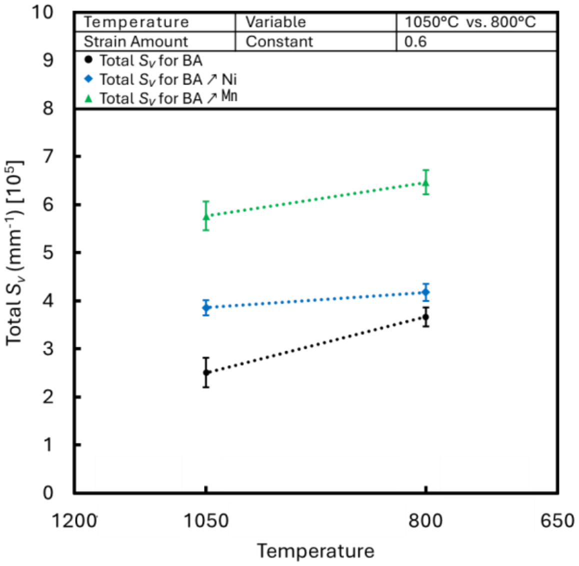

Figure 4.32 Total S_v of the three different compositions at a constant strain of 0.6 and a varied temperature of 1050°C and 800°C; towards the long transverse direction.

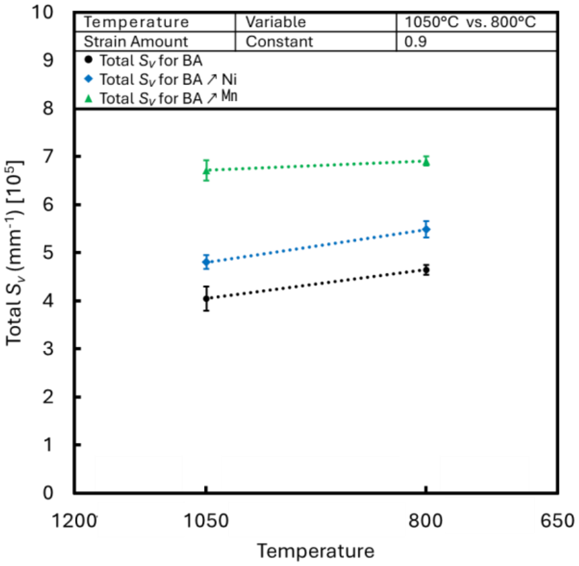

Figure 4.33 Total S_v of the three different compositions at a constant strain of 0.9 and a varied temperature of 1050°C and 800°C; towards the long transverse direction.

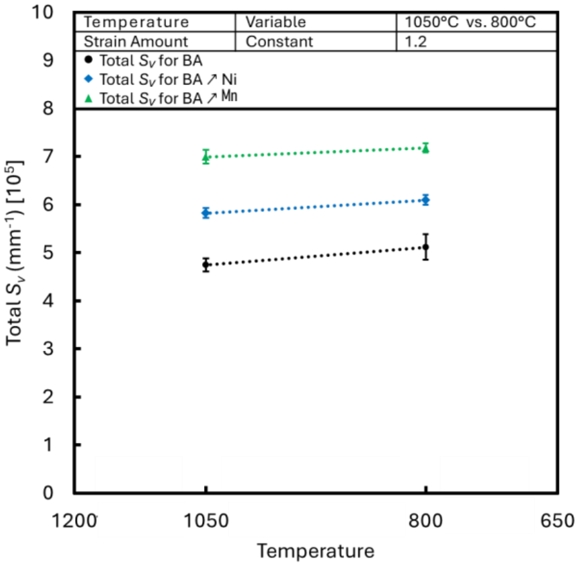

Figure 4.34 Total S_v of the three different compositions at a constant strain of 1.2 and a varied temperature of 1050°C and 800°C; towards the long transverse direction.

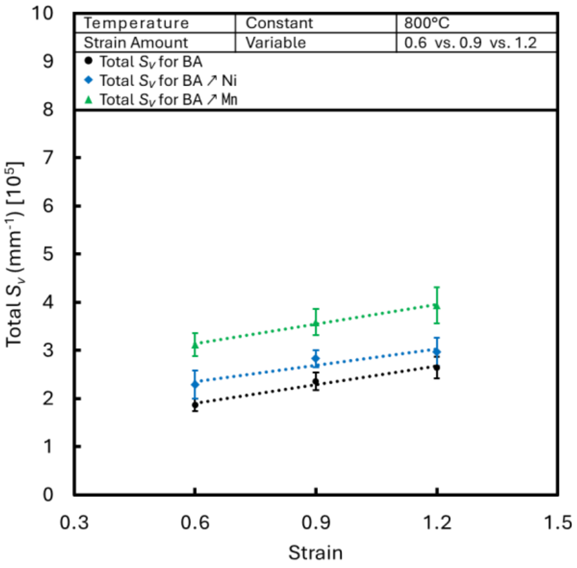

Figure 4.35 Total S_v of the three different compositions at a constant temperature of 800°C and a varied total strain of 0.6, 0.9, and 1.2; towards the short transverse direction.

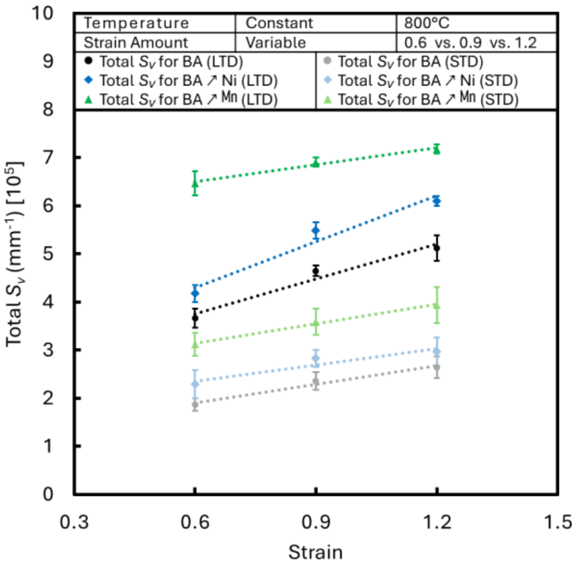

Figure 4.36 Total S_v of the three different compositions at a constant temperature of 800°C and a varied total strain of 0.6, 0.9, and 1.2; towards the long transverse direction (LTD) as well as the short transverse direction (STD).

4.4.2 Reconstructed PAG Contribution to Total S_v

The contribution of the reconstructed PAG to the total S_v is one of the critical aspects of microstructural quantification providing essential insights into the evolution of austenite grain boundaries during thermomechanical processing[136,158]. The analysis of this contribution revealed distinct trends based on two deformation temperatures of 1050°C and 800°C, two strain amounts of 0.6 and 1.2, and two alloy compositions, i.e. BA and BA ↗ Mn. These trends are presented in Figure 4.37, Figure 4.38, Figure 4.39, and Figure 4.40.

At a constant deformation temperature of 1050°C and a varied strain of 0.6 and 1.2, the reconstructed PAG contribution to total S_v increased with increasing strain as exhibited in Figure 4.37. On one hand, at a lower strain of 0.6, the reconstructed PAG contribution to the total S_v was 1.64×10^5 mm^{-1} for BA at a strain of 0.6, while it was 2.24×10^5 mm^{-1} for BA ↗ Mn. On the other hand, at a higher strain of 1.2, the reconstructed PAG contribution to the total S_v increased to 2.39×10^5 mm^{-1} for BA and 2.88×10^5 mm^{-1} for BA ↗ Mn, indicating an increase in the overall contribution of the reconstructed PAG to total S_v as the strain increased.

At a constant deformation temperature of 800°C and a varied strain of 0.6 and 1.2, the reconstructed PAG contribution to total S_v decreased with increasing strain as exhibited in Figure 4.38. On one hand, at a lower strain of 0.6, the reconstructed PAG contribution to the total S_v was 1.46×10^5 mm^{-1} for BA at a strain of 0.6, while it was 1.91×10^5 mm^{-1} for BA ↗ Mn. On the other hand, at a higher strain of 1.2, the reconstructed PAG contribution to the total S_v decreased to 1.35×10^5 mm^{-1} for BA and 1.68×10^5 mm^{-1} for BA ↗ Mn, indicating a decrease in the overall contribution of the reconstructed PAG to total S_v as the strain increased.

At a constant strain of 0.6 and a varied deformation temperature of 800°C and 1050°C, the reconstructed PAG contribution to total S_v decreased with decreasing deformation temperature as exhibited in Figure 4.39. Analogously, at a constant strain of 1.2 and a varied deformation temperature of 800°C and 1050°C, the reconstructed PAG contribution to total S_v also decreased with decreasing deformation temperature as exhibited in Figure 4.40.

On one hand, at a deformation temperature of 1050°C, recrystallization was promoted at a lower strain leading to a higher density of equiaxed grains and an initial increase in the reconstructed PAG contribution; however, the contribution of the reconstructed PAG to the total S_v decreased as recrystallization reached a more advanced stage and other microstructural features such as sub-grains and dislocation networks dominate at a higher strain. On the other hand, at a deformation temperature of 800°C, the contribution of the reconstructed PAG to total S_v decreased with increasing strain which exacerbated the elongation of grains in consistency with the suppression of recrystallization where mechanisms such as dislocation slip and deformation twinning dominate, although these were inferred from the deformation response rather than directly observed in microstructural characterization.

Furthermore, the addition of manganese significantly influenced the reconstructed PAG contribution as demonstrated by the lower reconstructed PAG contribution exhibited for BA ↗ Mn compared to BA, particularly at 800°C. This could be attributed to the role of manganese in stabilizing grain boundaries and facilitating a refined and consistent grain morphology. For example, at a deformation temperature of 800°C and a strain of 1.2, the reconstructed PAG contribution for BA ↗ Mn was 23% compared to 26% for BA. As further evidence, the percentage of the reconstructed PAG contribution to total S_v for all investigated conditions is summarized in Table 4.4.

It should be noted that orientation-gradient metrics such as KAM and detailed lath-size distributions were not reported in the present work, owing to the resolution limits described in Section 3.7.3. Accordingly, references to boundary stabilization, dislocation storage, or recovery are to be regarded as morphology-based correlations inferred from EBSD boundary topology and reconstructed PAG structure rather than as outcomes of direct crystallographic measurement, since quantitative assessment of dislocation density or orientation gradients would require additional techniques such as KAM mapping or diffraction-based line profile analysis.

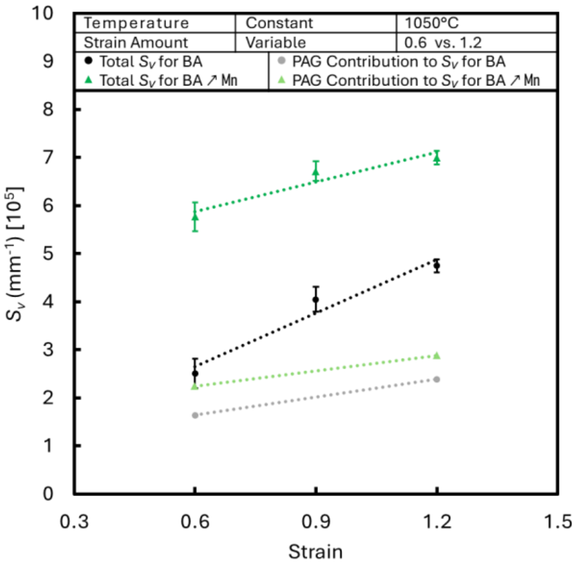

Figure 4.37 PAG contribution to the total S_v for two different compositions at a constant temperature of 1050°C and a varied strain of 0.6 and 1.2; towards the long transverse direction.

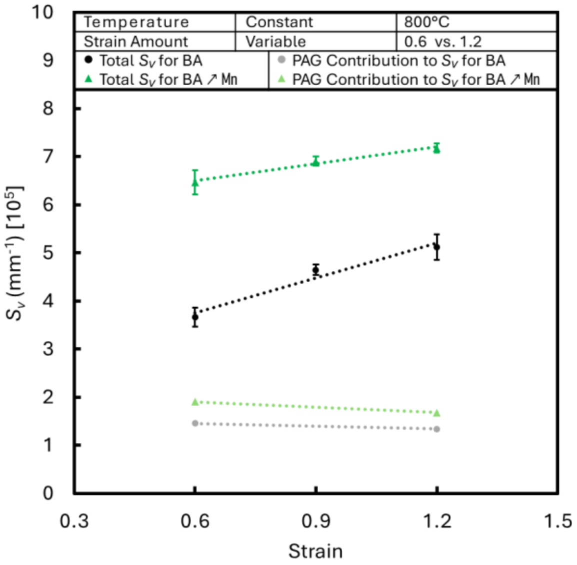

Figure 4.38 PAG contribution to the total S_v for two different compositions at a constant temperature of 800°C and a varied strain of 0.6 and 1.2; towards the long transverse direction.

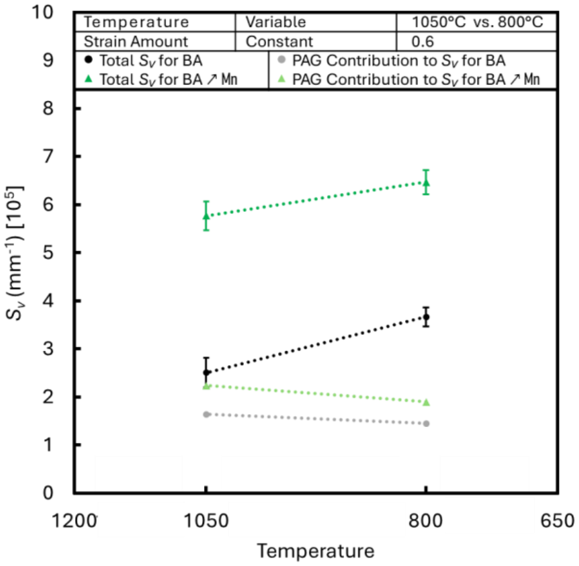

Figure 4.39 PAG contribution to the total S_v for two different compositions at a constant strain of 0.6 and a varied temperature of 1050°C and 800°C; towards the long transverse direction.

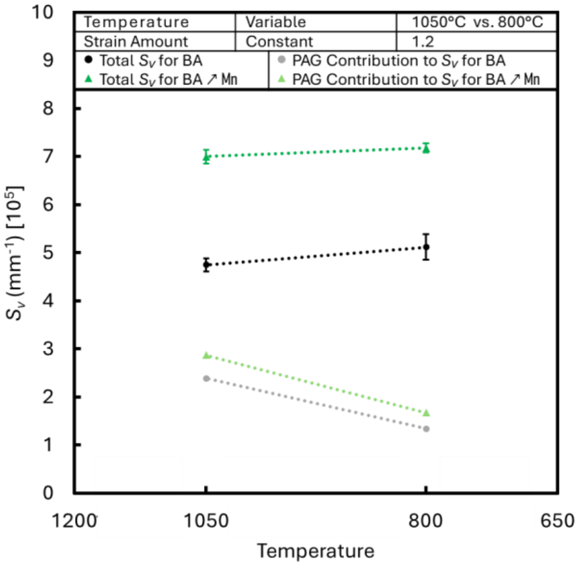

Figure 4.40 PAG contribution to the total S_v for two different compositions at a constant strain of 1.2 and a varied temperature of 1050°C and 800°C; towards the long transverse direction.

Table 4.4 Percentage of the reconstructed PAG contribution to total S_v considering variations in alloy composition, deformation temperature, and strain amount.

Temperature	Strain	Material Identification	Percentage of PAG Contribution to Total S_v
1050°C	0.6	BA	66%
		BA ↗ Mn	39%
800°C	0.6	BA	40%
		BA ↗ Mn	29%
1050°C	1.2	BA	50%
		BA ↗ Mn	41%
800°C	1.2	BA	26%
		BA ↗ Mn	23%

4.5 Mechanical Properties

4.5.1 Tensile Testing

Engineering stress-strain curves of test pieces deformed at 1050°C and 800°C with a cooling rate of 0.5°C/s and three different strain amounts are presented collectively in Figure 4.41 and independently in Figure 4.42, Figure 4.43, and Figure 4.44 for BA, BA ↗ Ni, and BA ↗ Mn, respectively. Additionally, the principal tensile properties of the deformed samples that encountered different deformation conditions, i.e. strain and temperature, are summarized in Table 4.5, contributing towards a comprehensive understanding of the impact of various manufacturing and processing factors significantly affecting the mechanical properties of the alloy.

For all tensile tests, yield strength was determined by a 0.2% offset method within the extensometer gauge length; results from specimens that fractured outside the extensometer gauge region are flagged with an asterisk in Table 4.5 and are reported for completeness only; however, these values are non-representative and are excluded from in-depth interpretation and discussion.

In practice, these curves offered significant insights into the mechanical behavior of the studied alloys under different deformation conditions by exhibiting the response of these alloys to tensile forces and highlighting the regions of material deformation, i.e. elastic deformation, yielding, plastic deformation, and fracture, which revealed information regarding significant parameters including but not limited to yield strength, tensile strength, and ductility[148].

The increase in strength and hardness during plastic deformation is referred to as work hardening, and although the ratio of tensile strength to yield strength does not provide the true rate of work hardening, it serves as a key indicator of the work hardening capacity of the studied alloys. As presented in Table 4.5, this ratio was greater than 1 under all conditions; notably, a higher ratio of tensile strength to yield strength suggests that the material undergoes significant strengthening during plastic deformation, while a lower ratio indicates less effective work hardening. Additionally, it is worth noting that ratios derived from conditions where fracture occurred outside the extensometer gauge were not considered in the analysis.

Figure 4.42 revealed that the yield strength and tensile strength of BA at a deformation temperature of 1050°C ranged from 550 MPa to 860 MPa and from 869 MPa to 988 MPa, respectively, whereas at a deformation temperature of 800°C, the yield strength and tensile strength ranged from 400 MPa to 900 MPa and from 993 MPa to 1052 MPa, respectively; in addition, the ratio of tensile strength to yield strength varied from 1.15 to 2.48. The lowest yield strength values and the highest tensile strength to yield strength ratios in these ranges correspond to tests where fracture occurred outside the extensometer gauge and were not used to infer material behavior; hence, more reliable outcomes following exclusion of these out-of-gauge values indicated yield strength averaging 811 MPa, a tensile strength to yield strength ratio averaging 1.27, and tensile strength averaging 1006 MPa, highlighting that all reported values are reliable when fracture occurred within the gauge length.

Figure 4.43 revealed that the yield strength and tensile strength of BA ↗ Ni at a deformation temperature of 1050°C ranged from 690 MPa to 855 MPa and from 939 MPa to 950 MPa, respectively, whereas at a deformation temperature of 800°C, the yield strength and tensile strength ranged from 430 MPa to 910 MPa and from 930 MPa to 1054 MPa, respectively; in addition, the ratio of tensile strength to yield strength varied from 1.08 to 2.16. The lowest yield strength values and the highest tensile strength to yield strength ratios in these ranges correspond to tests where fracture occurred outside the extensometer gauge and were excluded from the discussion dataset.

Figure 4.44 revealed that the yield strength and tensile strength of BA ↗ Mn at a deformation temperature of 1050°C ranged from 660 MPa to 1030 MPa and from 935 MPa to 1103 MPa, respectively, whereas at a deformation temperature of 800°C, the yield strength and tensile strength ranged from 930 MPa to 990 MPa and from 1074 MPa to 1174 MPa, respectively; in addition, the ratio of tensile strength to yield strength varied from 1.07 to 1.64. It is worth mentioning that all BA ↗ Mn yield strength and tensile strength values used for interpretation were obtained from compliant tests except for one test that occurred outside the extensometer gauge, yet its results were in line and within the range revealed by other tensile testing of this alloy composition.

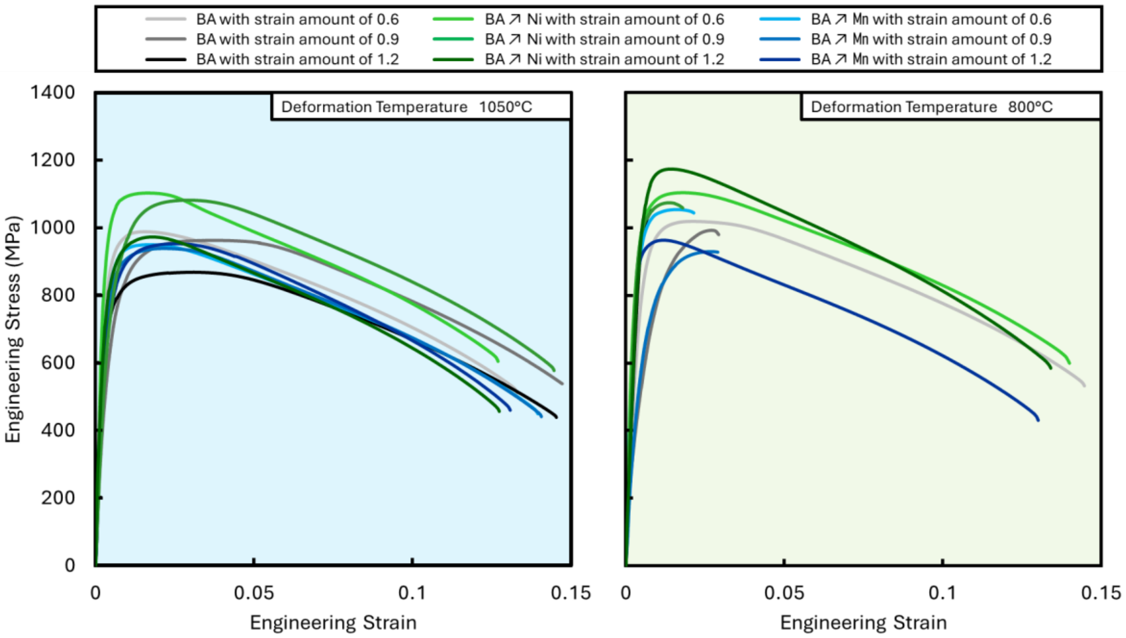

Figure 4.41 Engineering stress-strain curves of BA, BA ↗ Ni, and BA ↗ Mn test pieces following deformation at two different finishing temperatures shown above; at a cooling rate of 0.5°C/s with total strain amounts of 0.6, 0.9, and 1.2.

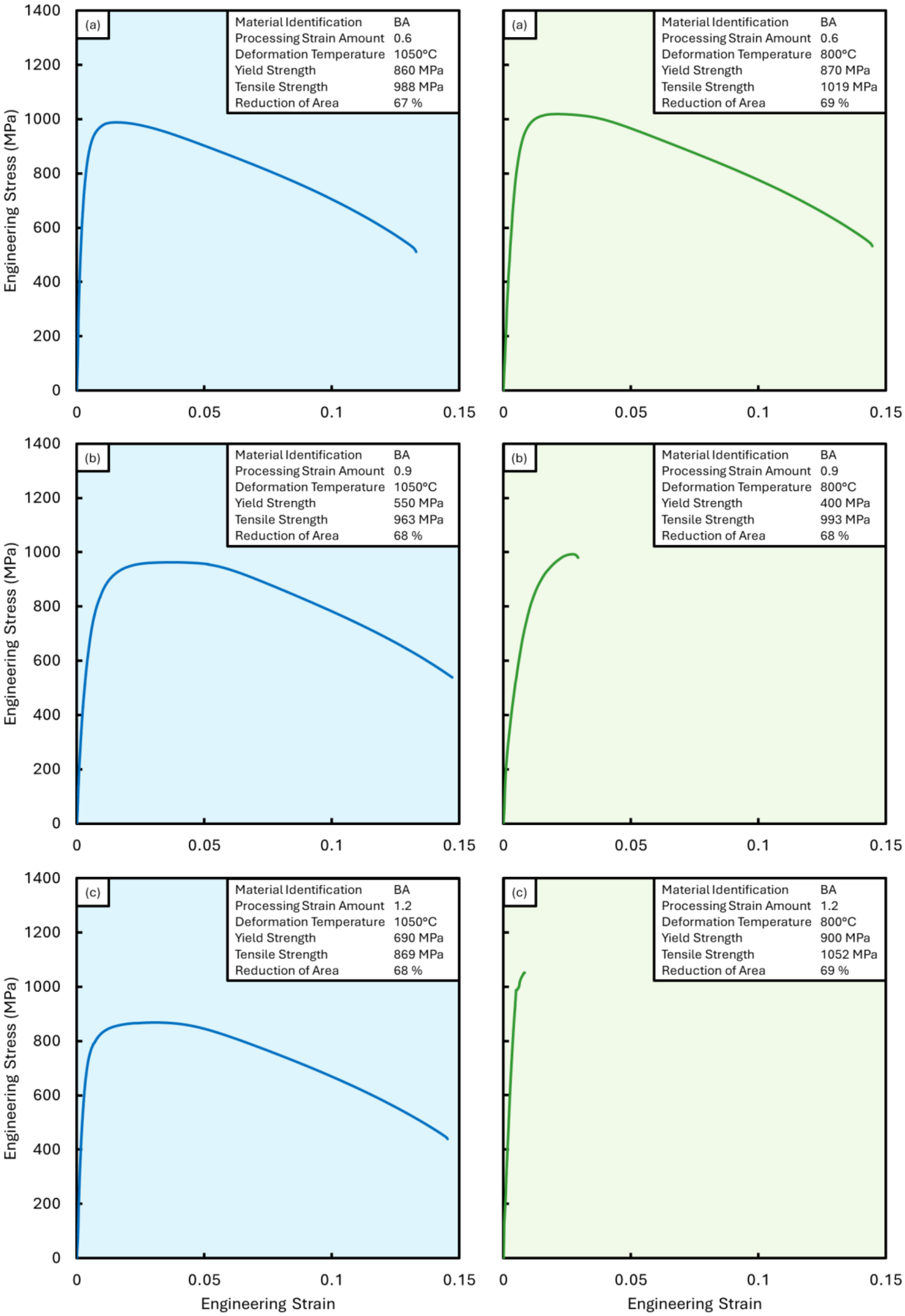

Figure 4.42 Engineering stress-strain curves of BA test pieces deformed at 1050°C (left) and 800°C (right) highlighted in blue and green, respectively; at a cooling rate of 0.5°C/s with strain amounts of: (a) 0.6, (b) 0.9, and (c) 1.2.

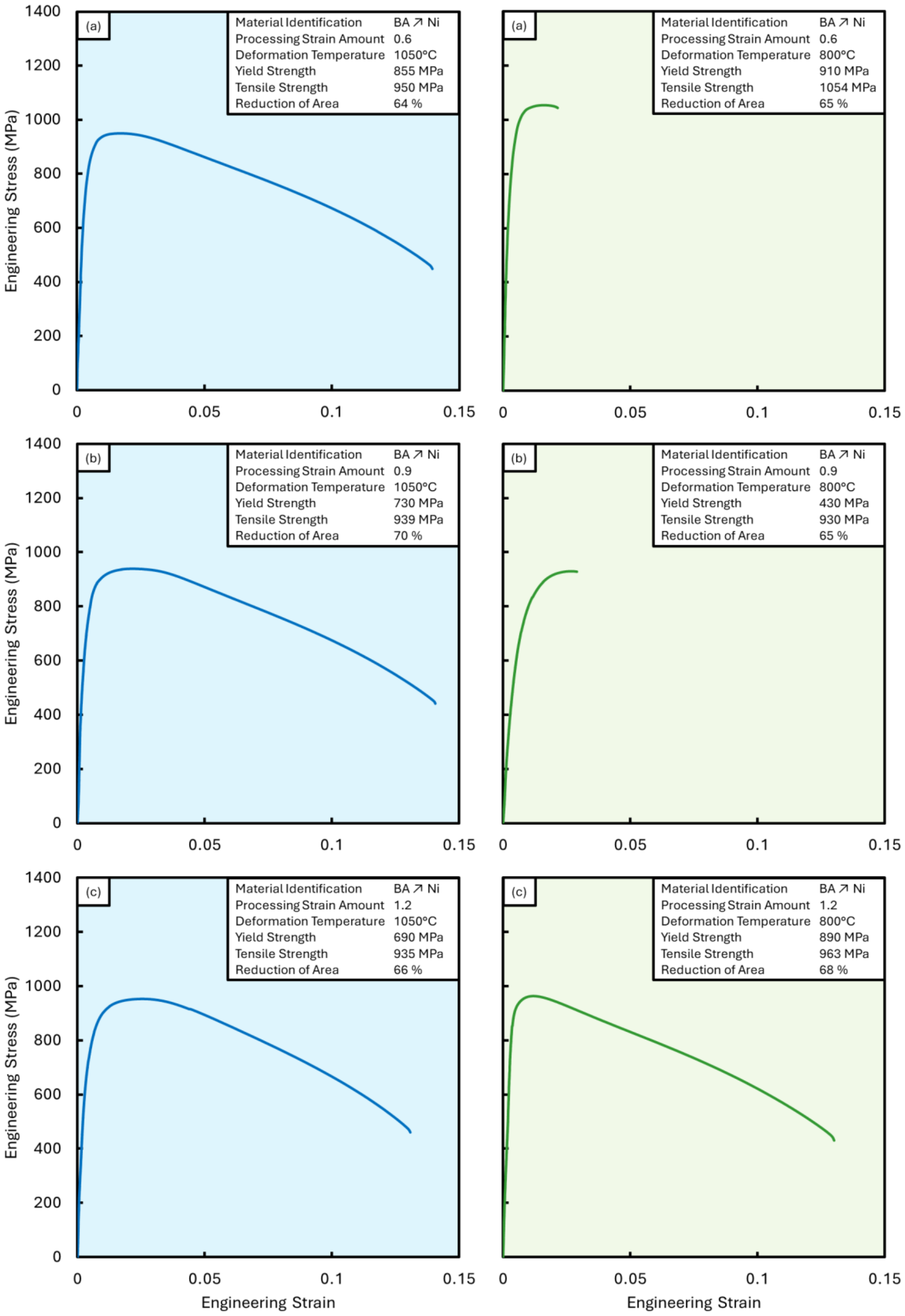

Figure 4.43 Engineering stress-strain curves of BA ↗ Ni test pieces deformed at 1050°C (left) and 800°C (right) highlighted in blue and green, respectively; at a cooling rate of 0.5°C/s with strain amounts of: (a) 0.6, (b) 0.9, and (c) 1.2.

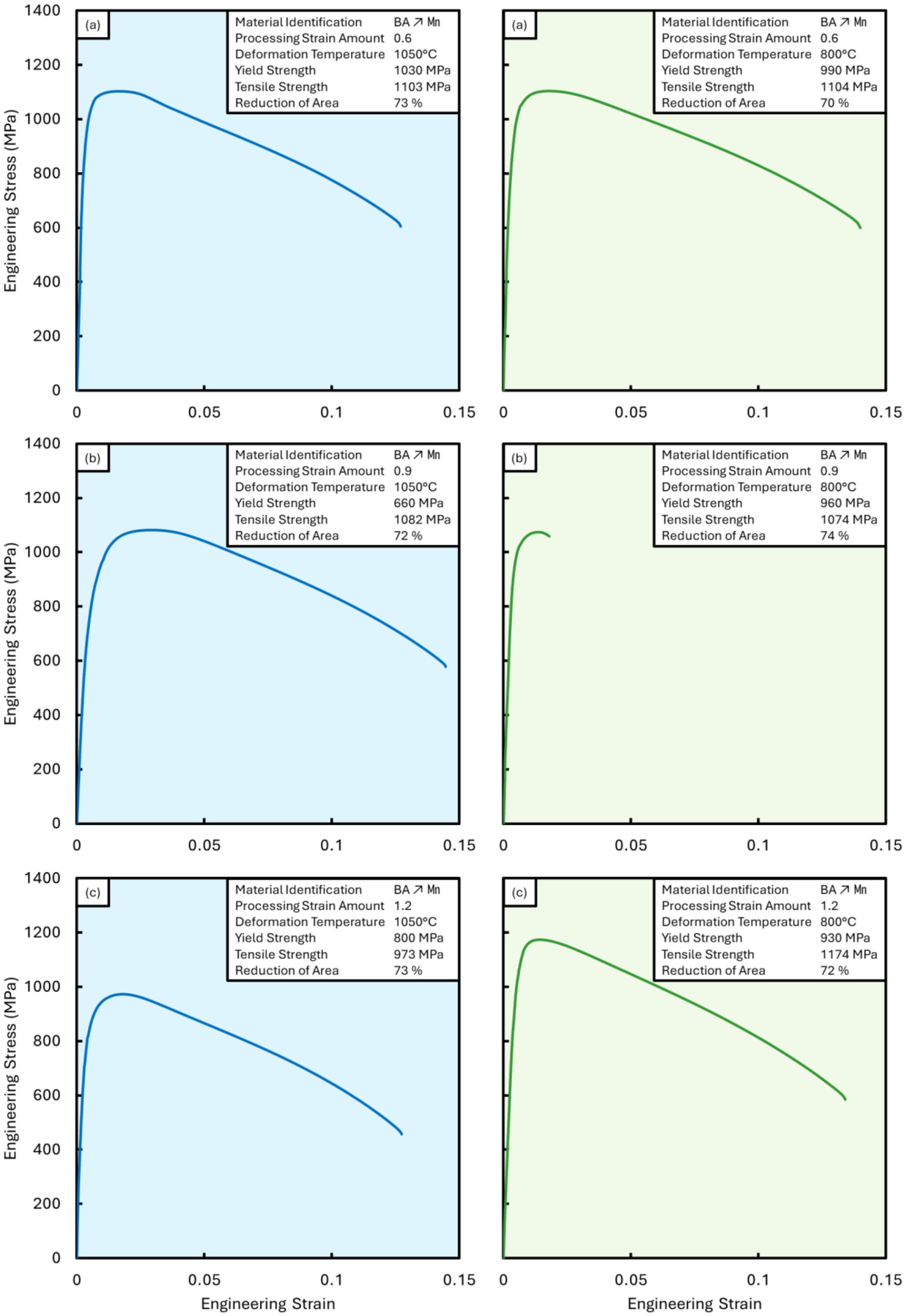

Figure 4.44 Engineering stress-strain curves of BA ↗ Mn test pieces deformed at 1050°C (left) and 800°C (right) highlighted in blue and green, respectively; at a cooling rate of 0.5°C/s with strain amounts of: (a) 0.6, (b) 0.9, and (c) 1.2.

Table 4.5 Summary of mechanical properties of the studied alloys resulting from tensile testing at an ambient temperature where $\sigma_{0.2}$, σ_t, and $\sigma_t/\sigma_{0.2}$ represent yield strength, tensile strength, and the ratio of tensile strength to yield strength.

Temperature	Strain	Material Identification	$\sigma_{0.2}$ (MPa)	σ_t (MPa)	$\sigma_t/\sigma_{0.2}$	Reduction of Area (%)
1050°C	0.6	BA	860	988	1.15	67
		BA ↗ Ni	855	950	1.11	64
		BA ↗ Mn	1030	1103	1.07	73
800°C	0.6	BA	870	1019	1.17	69
		BA ↗ Ni	910*	1054*	1.16*	65
		BA ↗ Mn	990	1104	1.12	70
1050°C	0.9	BA	550	963	1.75	68
		BA ↗ Ni	730	939	1.29	70
		BA ↗ Mn	660	1082	1.64	72
800°C	0.9	BA	400*	993*	2.48*	68
		BA ↗ Ni	430*	930*	2.16*	65
		BA ↗ Mn	960*	1074*	1.12*	74
1050°C	1.2	BA	690	869	1.26	68
		BA ↗ Ni	690	953	1.38	66
		BA ↗ Mn	800	973	1.22	73
800°C	1.2	BA	900*	1052*	1.17*	69
		BA ↗ Ni	890	963	1.08	68
		BA ↗ Mn	930	1174	1.26	72

* The fracture caused by these conditions occurred outside the extensometer gauge.

From an analytical point of view, BA demonstrated superior work hardening among the three alloys studied, based on the ratio of tensile strength to yield strength as well as the range of work hardening behavior observed across different deformation conditions, particularly under certain conditions, e.g. higher strain amount or lower deformation temperature. For clarity, work ardening assessments excluded ratios derived from entries where fracture occurred outside the extensometer gauge. However, some of the higher ratios reported for BA and BA ↗ Ni were for conditions in which fracture occurred outside the extensometer gauge, specifically the top two ratios of 2.48 for BA at 800°C with a strain of 0.9 and 2.16 for BA ↗ Ni at 800°C with a strain of 0.9, and are flagged as non-representative, so these specific ratios may not fully represent the intrinsic work hardening behavior. Nevertheless, BA exhibited an overall significant capacity for work hardening even after the exclusion of these ratios from the analysis.

In addition, the consistently high ratios of BA ↗ Mn indicated that the material could sustain significant plastic deformation before failure, driven by the ability of manganese to increase dislocation density and provide effective solid solution strengthening, as will be discussed in detail in Chapter 5. On the contrary, BA ↗ Ni was relatively less sensitive to deformation conditions in terms of work hardening, as evidenced by lower ratios with a narrower range, indicating limited to moderate work hardening. A notable aspect in terms of composition is that the addition of nickel tended to reduce work hardening as opposed to the addition of manganese; furthermore, higher strain amounts and lower deformation temperatures generally promoted work hardening as revealed by the higher ratios of tensile strength to yield strength in most of the conditions.

It is worth noting that BA ↗ Mn demonstrated the highest tensile strength across all conditions, indicating the contribution of manganese in increasing work hardening capacity; notably, this aligned with the higher reduction of area observed for BA ↗ Mn, further supporting its superior ductility and fracture resistance. In contrast, BA ↗ Ni exhibited the lowest tensile strength and reduction of area, indicating that nickel may not have contributed as effectively as manganese to work hardening or ductility. Moreover, the similarity in tensile strength between BA and BA ↗ Ni indicated the marginal and minimal impact of nickel on material strength; nevertheless, the slight increase in reduction of area for BA ↗ Ni in one condition, 2% higher than BA, alludes to a potential trade-off between strength and ductility.

Ductility, as measured by the reduction of area at fracture, is a critical parameter to indicate the plastic deformation limit at which the alloy should survive prior to fracture; in other words, the tougher material with a higher reduction of area percentage is more ductile and will generally withstand higher deformation levels and vice versa[148]. While BA ↗ Mn ranked top with an average reduction of area of 72%, BA ↗ Ni ranked last with an average reduction of area of 66%, and BA ranked in between them with an average reduction of area of 68%; taking into account that these averages were for both temperatures, i.e. 1050°C and 800°C, due to their negligible influence on the reduction of area.

Loose correlations of increased reduction of area with increasing deformation amount indicating an increase in ductility, irrespective of changes in deformation temperature, are represented in Figure 4.45 and Figure 4.46. The negligible influence of temperature on the reduction of area suggests that ductility is primarily governed by the amount of strain applied in addition to alloy composition, exemplified by the ability of BA ↗ Mn to withstand deformation, while BA ↗ Ni exhibited a diminished effect or even a detrimental impact of nickel on ductility.

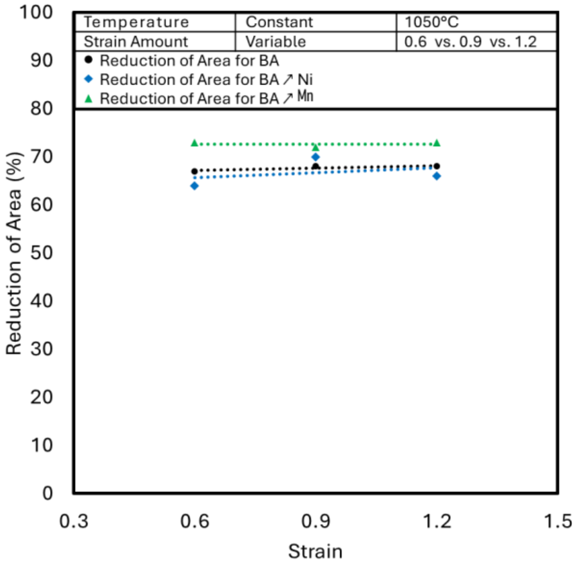

Figure 4.45 Reduction of area for the three different compositions at a constant temperature of 1050°C and a varied total strain of 0.6, 0.9, and 1.2.

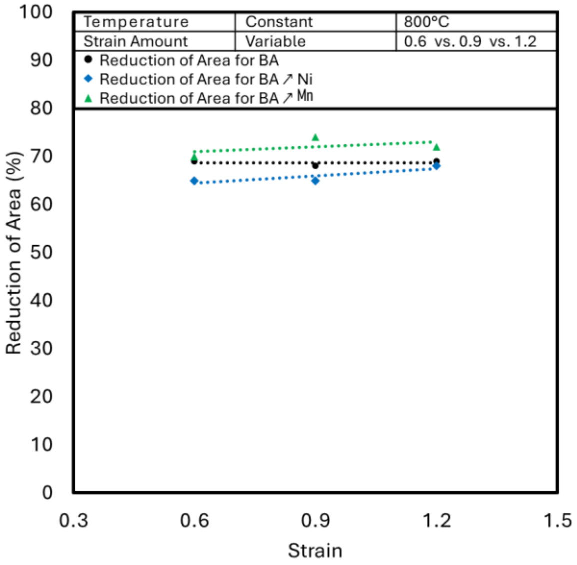

Figure 4.46 Reduction of area for the three different compositions at a constant temperature of 800°C and a varied total strain of 0.6, 0.9, and 1.2.

Tensile testing results demonstrated the significant influence of alloy composition and deformation conditions on mechanical properties. The superior tensile strength and ductility of BA ↗ Mn, arising from the ability of manganese to reduce the SFE, suppress dynamic recovery, and promote the accumulation of dislocations that enable distributed strain accommodation, establish it as a candidate for applications requiring high strength and toughness.

These mechanisms collectively delay strain localization and allow greater plastic deformation before fracture, thereby increasing ductility while maintaining strength. Conversely, the slight improvement in ductility of BA ↗ Ni under certain conditions, reflecting the stabilizing effect of nickel on austenite and its tendency to facilitate partial recovery, indicates its suitability for applications requiring a balance between strength and ductility.

4.5.2 Nanoindentation

The particular conditions of interest in terms of hardness measurements were the extreme conditions as indicated by total S_v results, i.e. strain amounts of 0.6 and 1.2, for the two different deformation temperatures while taking into account that nickel has a limited contribution to hardness as opposed to manganese which has a substantial contribution; hence, BA along with BA ↗ Mn were considered to be the optimal candidates for investigation to understand the mechanical behavior of these alloys further[47].

Despite the considerable experimental scatter arising from the irregular rhythm of hardness measurements and the inherent uncertainty related to the complexity of the martensitic structure, the general trends presented in Figure 4.47 and Figure 4.48 alluded to a slight overall increase in hardness with the increase in total S_v when the temperature dropped from 1050°C to 800°C.

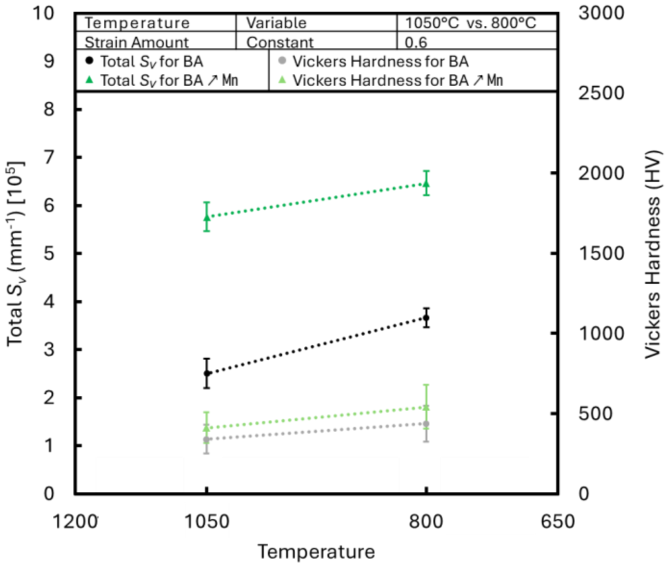

Figure 4.47 Vickers hardness numbers converted from the nanoindentation measurements (Equation 3.3) as a function of total S_v for two different compositions at a constant strain of 0.6 and a varied temperature of 1050°C and 800°C.

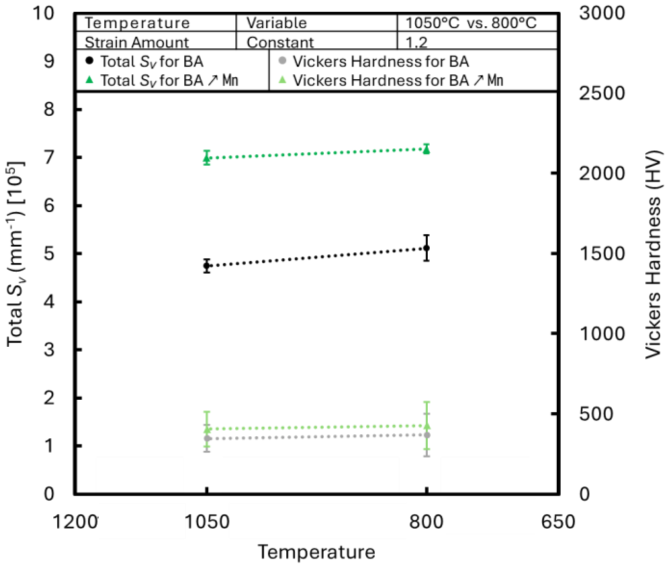

Figure 4.48 Vickers hardness numbers converted from the nanoindentation measurements (Equation 3.3) as a function of total S_v for two different compositions at a constant strain of 1.2 and a varied temperature of 1050°C and 800°C.

However, the correlation remained weak and inconclusive, as a decrease in the measured hardness was perceived when the strain raised from 0.6 to 1.2 which could be witnessed and became evident when comparing the hardness ranges against values of total S_v for the two mentioned strains, reinforcing the uncertainty in these measurements. This uncertainty may stem from the dilemma in distinguishing between grains and grain boundaries or in identifying possible precipitates present in the microstructure when measuring hardness, notwithstanding the high precision of the nanoindentation hardness test[159].

On the subject of the chemical compositions, the influence of manganese addition and its contribution towards increasing hardness had a tangible increase to a certain extent despite the fact that significant overlap between hardness measurements could be undoubtedly identified; on the basis of the fact that the alloy under study had a low-carbon content, i.e. less than 0.02 wt%, the effect of the additional small amount of manganese, i.e. less than 1 wt%, would definitely have a marginal influence on the overall hardness by the means of fundamental materials science principles where the majority of hardness increment was obtained as a result of martensitic transformation and there manganese effect on microstructural evolution was more apparent[76].

4.6 Summary of Results and Discussion

The relationship between processing parameters, i.e. deformation temperature, strain amount, and alloying additions, and the final microstructural and mechanical properties of the studied alloys, was systematically established through a detailed evaluation of microstructural evolution and mechanical behavior under a wide range of varied thermomechanical processing conditions. The martensitic transformation was identified as the dominant phase transformation mechanism upon cooling, as confirmed by dilatometric analysis and CCT simulations which verified the absence of diffusional transformation products.

The kinetics of martensitic transformation and the thermodynamic stability of austenite were notably influenced by the presence of manganese and nickel, with manganese exerting a more pronounced effect. Flow stress increased with decreasing deformation temperature, as revealed by stress-strain curves, particularly at 800°C where dynamic recrystallization was largely suppressed due to limited recovery and mobility. Among the three alloys, BA ↗ Mn exhibited a distinct softening behavior at high strain, which may suggest accelerated dynamic recrystallization and boundary migration facilitated by manganese through its influence on SFE and dislocation storage; however, this interpretation remains qualitative.

Microstructural evolution was primarily governed by deformation temperature and strain amount. As presented in Figure 4.49, which encapsulates the microstructural evolution during deformation across high and low temperatures at total strain amounts of 0.3, 0.6, 0.9, and 1.2, higher deformation temperatures resulted in fully recrystallized and equiaxed grains, while lower deformation temperatures produced unrecrystallized and elongated grains with residual substructures. Furthermore, grain refinement was observed at all processing conditions, with increasing strain consistently producing a finer grain size and a higher boundary density, irrespective of deformation temperature.

EBSD maps and corresponding reconstructed PAG maps presented in Figure 4.50 revealed that BA ↗ Mn developed a significantly finer and more equiaxed austenitic grain structure than BA, especially at high strain. In brief, the addition of manganese increased grain boundary misorientation, indicating higher resistance to boundary migration and a more uniform boundary distribution, although the underlying dislocation structures responsible for this stability were not directly characterized.

Quantitative analysis of total S_v demonstrated a marked increase with both higher strain and lower deformation temperature, although strain exerted a more dominant influence; moreover, BA ↗ Mn consistently exhibited the highest total S_v values across all processing conditions and among all alloys, followed by BA ↗ Ni and then BA. The contribution of reconstructed PAG to total S_v varied with processing conditions, i.e. increasing with strain at high temperatures due to active recrystallization and decreasing with strain at low temperatures due to retained deformation features and restricted boundary migration. It is therefore inferred that a balance between recrystallization and deformation-induced substructure formation governed the evolution of interfacial area density; however, the potential occurrence of dislocation saturation or dynamic recovery could not be experimentally confirmed, and should be regarded as an interpretation consistent with established thermomechanical models rather than a directly observed phenomenon.

Tensile testing results reinforced these microstructural observations where BA ↗ Mn demonstrated superior mechanical properties, including the highest yield strength, tensile strength, and reduction of area, confirming its greater ductility retention and fracture resistance. In contrast, BA ↗ Ni exhibited marginal strength increments but reduced ductility, while BA showed the highest overall work hardening capacity as indicated by its ratio of tensile strength to yield strength highlighting its ability to sustain further plastic deformation before failure.

Nevertheless, the inclusion of manganese in BA ↗ Mn provided a more compositionally balanced mechanical response, owing to the combined effect of grain size reduction and increased dislocation retention that likely contributed to higher strain hardening capacity, a behavior consistent with established deformation mechanisms in low SFE alloys, although not directly evidenced in this study. Nanoindentation measurements indicated a general correlation between hardness, total S_v, and microstructural refinement, particularly in BA ↗ Mn. This trend supports the hypothesis that increased grain boundary density contributes to localized strengthening through the restriction of dislocation glide and substructure movement.

However, it must be noted that nanoindentation data represent local responses and cannot directly quantify dislocation density; therefore, these interpretations are best viewed as consistent with, rather than conclusive evidence of, strain-induced microstructural strengthening. The data also revealed significant variability due to the intrinsic complexity of martensitic microstructures and measurement uncertainty, warranting careful interpretation of local hardness values.

Processing Parameters	BA	BA ↗ Ni	BA ↗ Mn
Rough Rolling Passes Single Finish Rolling Passes - Reheating Temperature 1200°C Rough Rolling Temperature 1150°C Finish Rolling Temperature - Strain Rate 10 s^{-1} Initial Strain ~0.3 Final Strain ~0.3	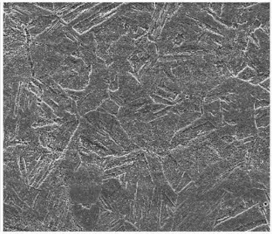	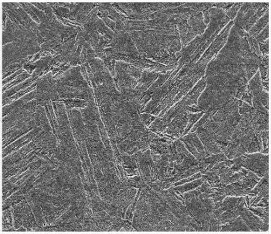	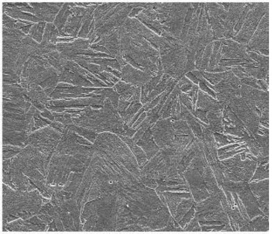
Rough Rolling Passes Single Finish Rolling Passes Single Reheating Temperature 1200°C Rough Rolling Temperature 1150°C Finish Rolling Temperature 1050°C Strain Rate 10 s^{-1} Initial Strain ~0.3 Final Strain ~0.6	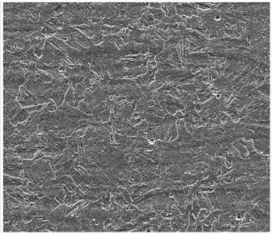	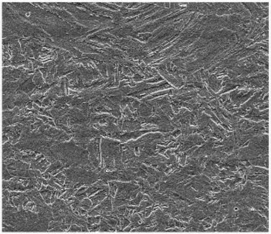	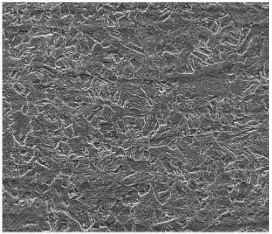
Rough Rolling Passes Single Finish Rolling Passes Single Reheating Temperature 1200°C Rough Rolling Temperature 1150°C Finish Rolling Temperature 800°C Strain Rate 10 s^{-1} Initial Strain ~0.3 Final Strain ~0.6	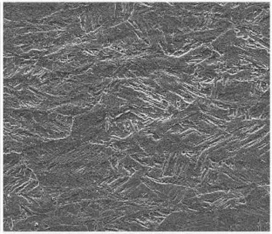	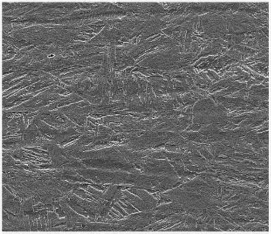	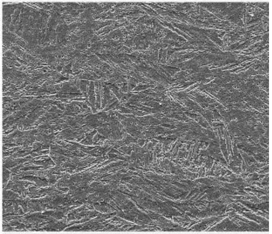
Rough Rolling Passes Single Finish Rolling Passes Double Reheating Temperature 1200°C Rough Rolling Temperature 1150°C Finish Rolling Temperature 1050°C Strain Rate 10 s^{-1} Initial Strain ~0.3 Final Strain ~0.9	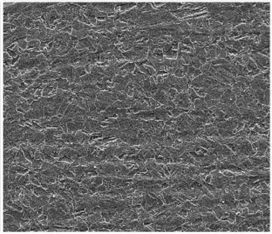	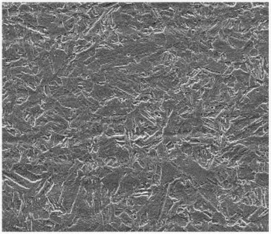	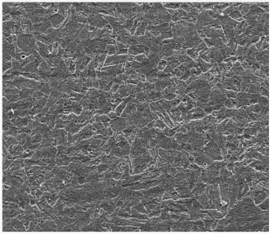
Rough Rolling Passes Single Finish Rolling Passes Double Reheating Temperature 1200°C Rough Rolling Temperature 1150°C Finish Rolling Temperature 800°C Strain Rate 10 s^{-1} Initial Strain ~0.3 Final Strain ~0.9	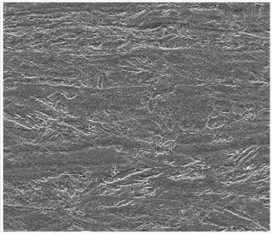	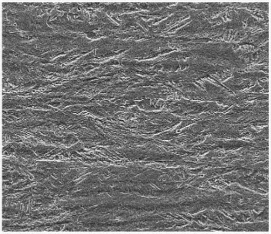	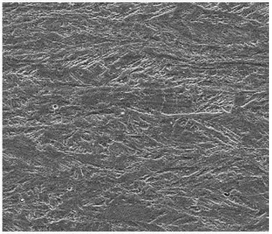
Rough Rolling Passes Single Finish Rolling Passes Triple Reheating Temperature 1200°C Rough Rolling Temperature 1150°C Finish Rolling Temperature 1050°C Strain Rate 10 s^{-1} Initial Strain ~0.3 Final Strain ~1.2	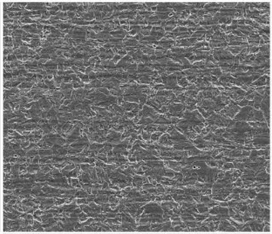	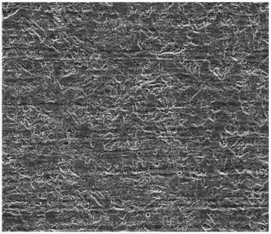	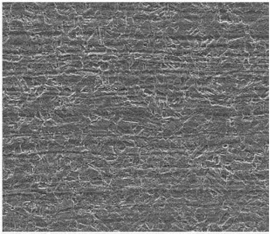
Rough Rolling Passes Single Finish Rolling Passes Triple Reheating Temperature 1200°C Rough Rolling Temperature 1150°C Finish Rolling Temperature 800°C Strain Rate 10 s^{-1} Initial Strain ~0.3 Final Strain ~1.2	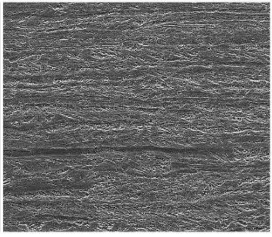	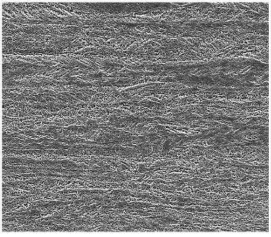	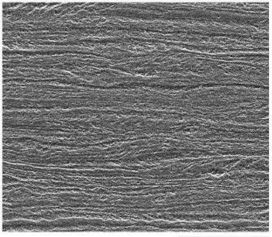

100 µm

Figure 4.49 SEM micrographs for all processing conditions presenting microstructural refinement with increased strain amount and decreased deformation temperature for the three studied alloys.

Processing Parameters	Reconstruction Status	BA	BA ↗ Mn
Rough Rolling Passes Single Finish Rolling Passes Single Reheating Temperature 1200˚C Rough Rolling Temperature 1150˚C Finish Rolling Temperature 1050˚C Strain Rate $10\ s^{-1}$ Initial Strain ~0.3 Final Strain ~0.6	Before PAG Reconstruction	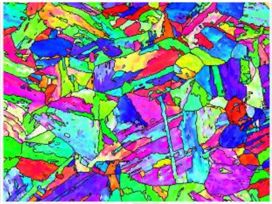	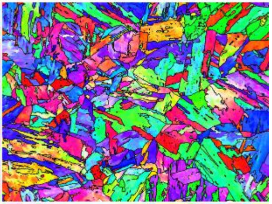
	After PAG Reconstruction	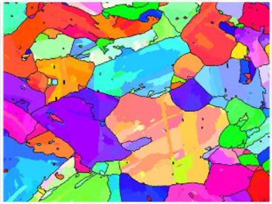	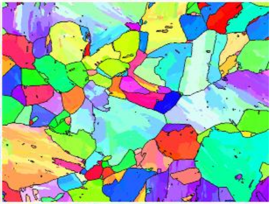
Rough Rolling Passes Single Finish Rolling Passes Single Reheating Temperature 1200˚C Rough Rolling Temperature 1150˚C Finish Rolling Temperature 800˚C Strain Rate $10\ s^{-1}$ Initial Strain ~0.3 Final Strain ~0.6	Before PAG Reconstruction	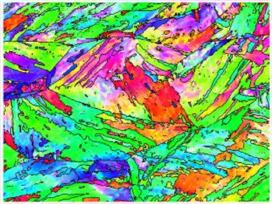	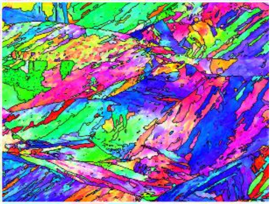
	After PAG Reconstruction	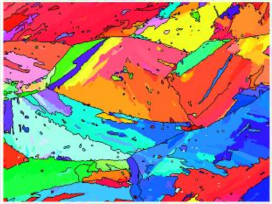	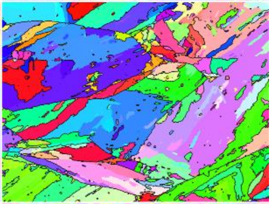
Rough Rolling Passes Single Finish Rolling Passes Triple Reheating Temperature 1200˚C Rough Rolling Temperature 1150˚C Finish Rolling Temperature 1050˚C Strain Rate $10\ s^{-1}$ Initial Strain ~0.3 Final Strain ~1.2	Before PAG Reconstruction	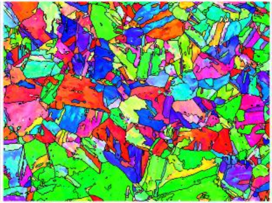	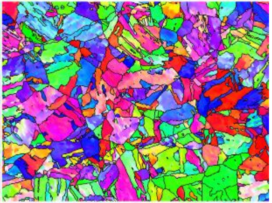
	After PAG Reconstruction	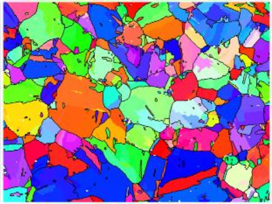	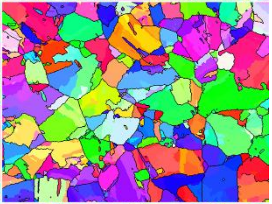
Rough Rolling Passes Single Finish Rolling Passes Triple Reheating Temperature 1200˚C Rough Rolling Temperature 1150˚C Finish Rolling Temperature 800˚C Strain Rate $10\ s^{-1}$ Initial Strain ~0.3 Final Strain ~1.2	Before PAG Reconstruction	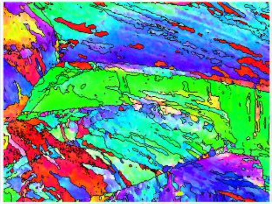	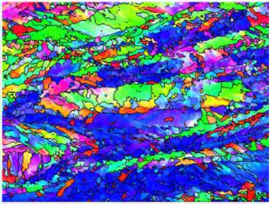
	After PAG Reconstruction	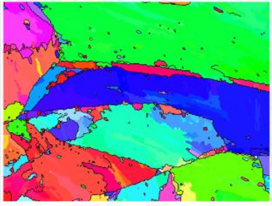	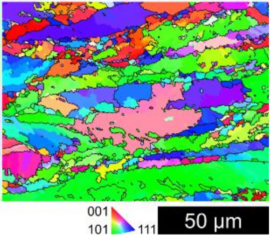

Figure 4.50 EBSD IPF maps for elected processing conditions presenting deformed microstructure along with corresponding reconstructed PAG maps for BA vs. BA ↗ Mn, processed using AZtecCrystal.

Chapter 5 Discussion

Finish deformation represents a critical stage in thermomechanical processing, directly associated with microstructural refinement and the evolution of mechanical properties. In this stage, the material is subjected to controlled deformation at specific temperatures and strain levels to develop the desired internal structure. The resulting microstructures, shaped by both chemical composition and processing conditions, were characterized primarily through the quantified parameter, i.e. total S_v, and were evaluated alongside corresponding mechanical property responses.

Direct measurements of martensite grain size, retained austenite fraction, or orientation-gradient metrics such as KAM were not undertaken; therefore, all references to refinement or dislocation activity are based on morphology-consistent trends and quantitative interfacial data derived from total S_v rather than on direct dislocation density measurements. In most cases, these microstructural and mechanical trends provided consistent and interpretable projections; however, a few instances exhibited uncertainty due to competing effects or experimental scatter.

In particular, yield strength variations were carefully interpreted only from specimens that fractured within the extensometer gauge length, while values from tests that fractured outside this region were reported solely for completeness and excluded from mechanistic discussion to ensure data integrity. Nevertheless, the observed behavioral differences helped establish a deeper understanding of how deformation temperature, strain amount, and alloy composition collectively influence the mechanical response of supermartensitic stainless steels under varying thermomechanical conditions.

5.1 Influence of Finish Deformation Temperature

Deformation temperature is a critical parameter in thermomechanical processing, particularly for supermartensitic stainless steels, as it governs dynamic restoration mechanisms, dislocation activity, and the final transformed microstructure. In this study, deformation at 1050°C (above $T_{95\%}$) favored recrystallization, as evidenced by the development of equiaxed grains and relatively lower dislocation storage, consistent with established thermomechanical processing behavior in austenitic matrices[160,161].

In contrast, deformation at 800°C (below $T_{5\%}$) significantly suppressed recrystallization and promoted dislocation retention, intragranular banding, referring to planar zones of localized plastic deformation that form within individual grains as dislocations accumulate along slip planes under restricted recovery, and grain elongation, in line with phenomena well documented in classical thermomechanical processing literature[102,155]. Although dislocation density was not directly quantified, these interpretations are supported by EBSD contrast and substructure morphology and should be regarded as qualitative yet consistent with established models.

5.1.1 Microstructural Morphology as a Function of Deformation Temperature

Deformation temperature exerted a pronounced influence on the microstructural morphology of supermartensitic stainless steels, as revealed by the EBSD orientation maps presented in Figure 4.21 to Figure 4.28. At 1050°C, recrystallization was clearly activated across all studied compositions resulting in the formation of equiaxed grains with reduced intragranular orientation gradients, particularly evident in BA and BA ↗ Mn (Figure 4.21 and Figure 4.23). The presence of such equiaxed, low-misorientation grain structures suggested that the higher thermal energy provided sufficient mobility for grain boundary migration and dislocation annihilation, supporting full recrystallization behavior. It should be emphasized that this interpretation was derived from EBSD-visible grain topology and misorientation contrast, rather than invoking quantitative martensite grain size measurements or KAM analysis.

Conversely, deformation at 800°C significantly suppressed recrystallization and altered grain morphology. For example, Figure 4.26 displayed elongated grains with pronounced intragranular orientation gradients and banded features in BA ↗ Mn. These microstructural characteristics indicate retention of deformation bands, high dislocation density, and limited grain boundary mobility, all of which are indicative of partial dynamic recovery in the absence of full recrystallization. While BA exhibited similar trends under these conditions, the severity of banding and misorientation was less pronounced than in BA ↗ Mn, highlighting the role of chemical composition in mediating thermally activated restoration processes.

Collectively, these EBSD-based observations confirmed that finish deformation temperature modulated the microstructural pathway, such that higher temperatures promoted recrystallization (equiaxed grains and lower intragranular misorientation), whereas lower temperatures favored substructure retention and elongation. This divergence in morphological outcomes reflected the interplay between thermal activation and deformation-driven mechanisms, which determined the extent of microstructural restoration. Altogether, these trends were consistent with classical hot deformation theories applied to low-carbon and martensitic systems, where atomic mobility, stacking fault energy, and dislocation interaction govern the restoration response during thermomechanical processing[160,161].

5.1.2 Response of Total S_v to Deformation Temperature

Total S_v exhibited a consistent increase as deformation temperature decreased across all compositions and strain amounts. At a strain of 0.6, for example, BA ↗ Mn showed an increase in total S_v at 800°C compared to 1050°C, as presented in Figure 4.30 and Figure 4.31, respectively. Similar temperature-dependent increases were also observed in BA and BA ↗ Ni, reinforcing the trend that lower deformation temperatures produced higher interfacial area density through intensified sub-grain formation and deformation banding. This behavior aligned with prior studies, which reported that deformation at reduced temperatures led to elevated dislocation densities and suppressed recrystallization, thereby contributing to increased boundary formation and interface area[162,163].

Nevertheless, the influence of temperature on total S_v diminished as the strain increased, where at higher strain amounts of 0.9 and 1.2, the differences in total S_v between the 1050°C and 800°C conditions became less significant, as illustrated in Figure 4.32, Figure 4.33, and Figure 4.34. This attenuation suggested that, beyond a certain strain threshold, dynamic recrystallization approached a steady state condition, and dislocation rearrangement together with substructure stabilization increasingly governed further microstructural evolution, overriding the apparent influence of thermal input, although dislocation density was not directly measured, this inference is consistent with EBSD-based substructure evidence and with comparable hot deformation behavior reported for martensitic systems[102,155]. Such behavior has also been observed in heavily deformed austenitic and martensitic steels, where strain-driven recovery and sub-grain formation dominate once recrystallization is saturated at advanced deformation levels[164–167].

5.1.3 Contribution of Reconstructed PAG to Total S_v

Total S_v was composed of contributions from both grain boundaries and intragranular features such as deformation bands and substructural interfaces. At 1050°C, the promotion of recrystallization resulted in significant PAG boundary reconstruction, which accounted for a greater share of the total S_v. In contrast, deformation at 800°C suppressed boundary migration, and the total S_v was predominantly derived from deformation-induced internal structures.

This trend was confirmed by the reconstructed PAG maps presented in Figure 4.37 to Figure 4.40, where a clear reduction in the fraction of PAG contribution to total S_v was observed at lower temperatures. For instance, at a strain of 1.2, BA ↗ Mn exhibited a PAG contribution of 41% at 1050°C, which dropped to 23% at 800°C. These differences reflected the temperature-dependent balance between boundary formation and substructural retention.

Further support was provided by the EBSD maps in Figure 4.21 to Figure 4.28, which illustrated equiaxed morphologies and lower misorientation gradients at 1050°C, consistent with extensive recrystallization. In contrast, the maps at 800°C revealed elongated grains with dense intragranular misorientation, particularly in BA ↗ Mn. This observation was indicative of strain-induced structural refinement without grain boundary replacement, a trend amplified by the lower stacking fault energy of manganese-rich compositions, which increased dislocation accumulation and suppressed recovery. Overall, the PAG reconstruction analysis substantiated the assertion that deformation at lower temperatures favors substructure dominated microstructures rather than grain boundary controlled configurations.

5.1.4 Mechanical Properties as a Function of Deformation Temperature

5.1.4.1 Yield Strength Evolution Across Deformation Temperature

Yield strength demonstrated a generally positive correlation with total S_v, particularly at moderate and high strain amounts. However, to maintain accuracy, interpretations were based only on yield strength data from specimens that fractured within the extensometer gauge length; furthermore, the results from out-of-gauge fractures were excluded from correlation analysis and discussed solely in descriptive context.

At a strain of 0.6, BA ↗ Mn exhibited a decrease in yield strength from 1030 MPa at 1050°C to 990 MPa at 800°C despite the increase in total S_v, as presented in Figure 5.1. This reduction may have reflected early-stage dynamic recovery processes that partially offset the strengthening effect of elevated interface density.

At a strain of 0.9, yield strength for BA ↗ Mn increased markedly from 660 MPa at 1050°C to 960 MPa at 800°C as presented in Figure 5.2, consistent with higher total S_v and greater dislocation retention. A similar trend was observed at a strain of 1.2, where yield strength rose from 800 MPa at 1050°C to 930 MPa at 800°C as presented in Figure 5.3, aligning with the increase in total S_v and suppressed recovery at a lower temperature. These results confirmed that the strengthening effect associated with deformation at a low temperature was most reliable at intermediate to high strain, while the minor deviations at low strain were within the expected scatter of thermomechanical tests.

5.1.4.2 Tensile Strength Evolution Across Deformation Temperature

Tensile strength followed a similar temperature-dependent trend, further supporting the influence of deformation temperature on mechanical performance. At a strain of 0.6, BA ↗ Mn reached 1103 MPa at 1050°C and maintained 1104 MPa at 800°C, as shown in Figure 5.4, indicating excellent strength retention under suppressed recrystallization. This stability indicated that the tensile response was not affected by the yield strength anomalies observed in a few isolated low-strain tests and that the overall mechanical trends remained internally consistent.

At a strain of 0.9, tensile strength remained stable with values of 1082 MPa at 1050°C and 1074 MPa at 800°C, as shown in Figure 5.5, suggesting that strain hardening and interfacial strengthening mechanisms were active at both conditions. This also implied that the transition from recovery-dominated to deformation-stabilized microstructures occurred gradually, preserving strength without substantial softening. At a strain of 1.2, tensile strength increased from 973 MPa at 1050°C to 1174 MPa at 800°C, as shown in Figure 5.6, aligning with the observed rise in total S_v and confirming that lower deformation temperatures contributed to increased tensile performance, particularly when paired with high strain. Hence, even though yield strength scatter was reliable for some low strain conditions, the tensile data validated the underlying consistency of the mechanical behavior and supported the credibility of the strength-temperature relationship.

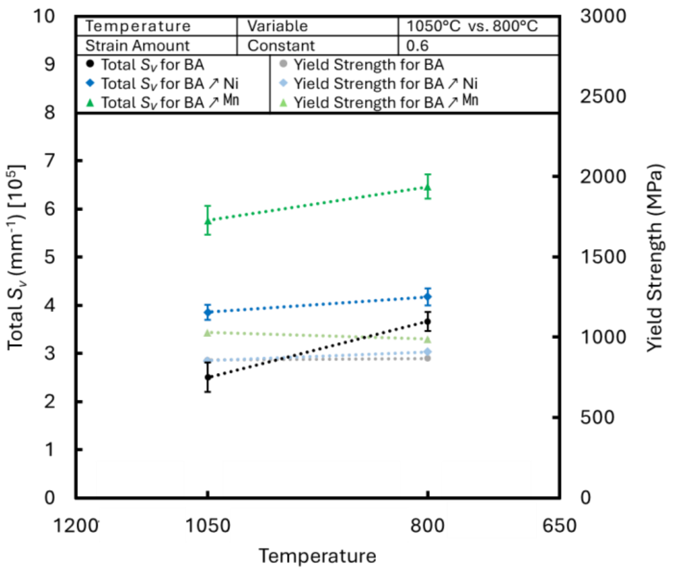

Figure 5.1 Yield strength as a function of total *S*$_v$ for the three different compositions at a constant strain of 0.6 and a varied temperature of 1050°C and 800°C.

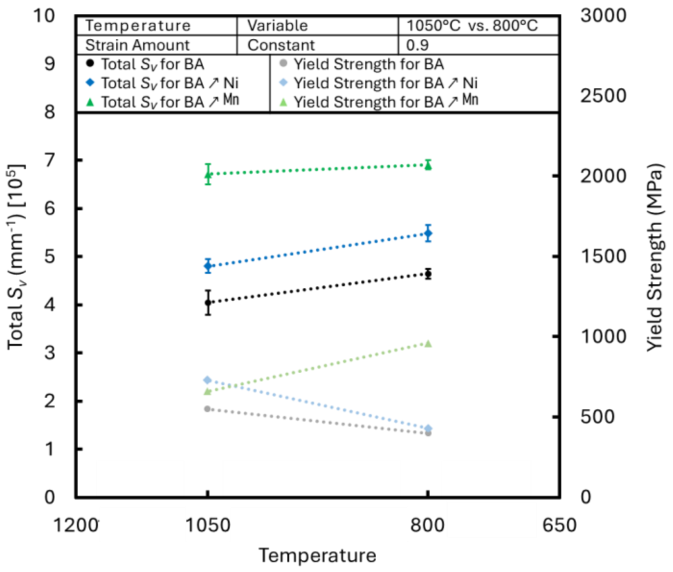

Figure 5.2 Yield strength as a function of total *S*$_v$ for the three different compositions at a constant strain of 0.9 and a varied temperature of 1050°C and 800°C.

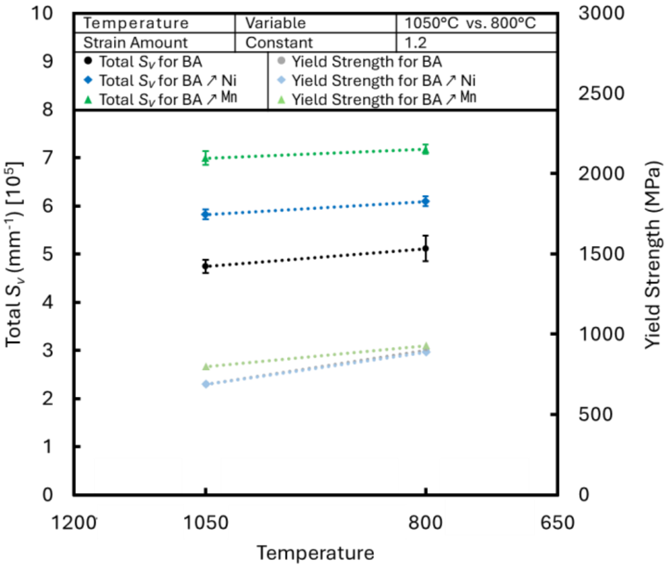

Figure 5.3 Yield strength as a function of total S_v for the three different compositions at a constant strain of 1.2 and a varied temperature of 1050°C and 800°C.

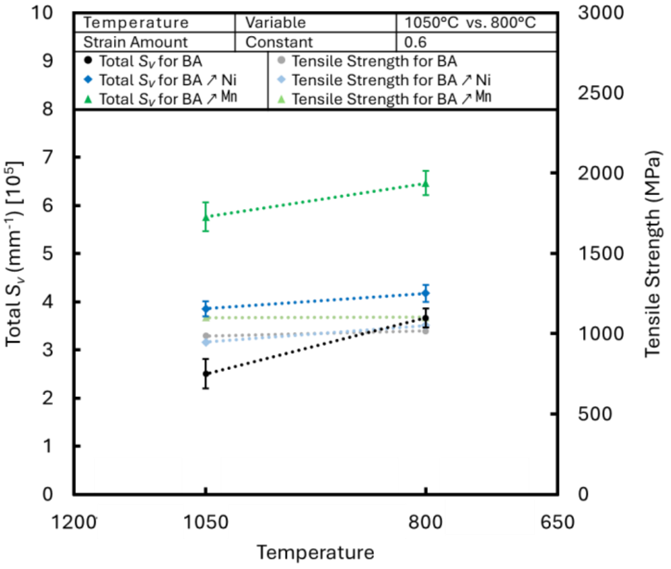

Figure 5.4 Tensile strength as a function of total S_v for the three different compositions at a constant strain of 0.6 and a varied temperature of 1050°C and 800°C.

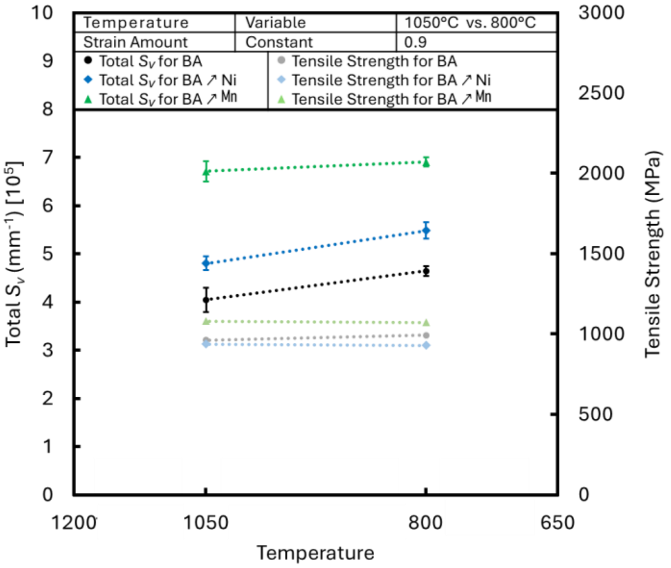

Figure 5.5 Tensile strength as a function of total S_v for the three different compositions at a constant strain of 0.9 and a varied temperature of 1050°C and 800°C.

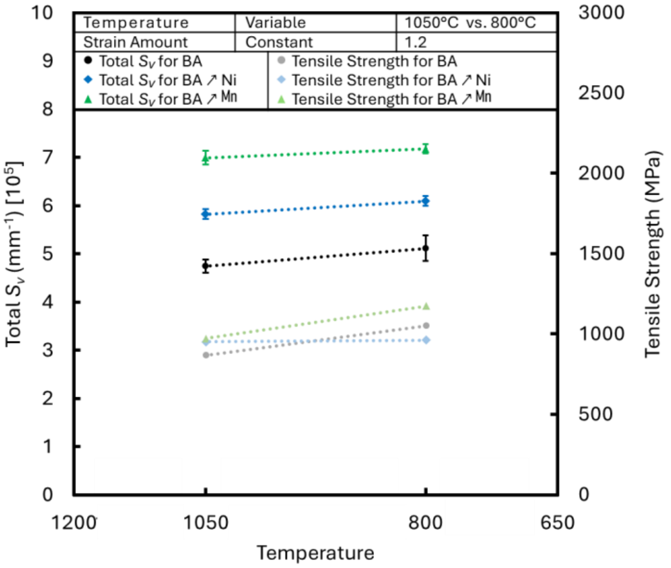

Figure 5.6 Tensile strength as a function of total S_v for the three different compositions at a constant strain of 1.2 and a varied temperature of 1050°C and 800°C.

5.1.4.3 Reduction of Area and Ductility Preservation

Despite the increase in strength at lower deformation temperatures, ductility, as measured by the reduction of area, remained remarkably consistent and relatively stable for BA ↗ Mn across all strain amounts. As shown in Figure 4.45 and Figure 4.46, RA values for BA ↗ Mn consistently ranged between 72% and 74%, indicating excellent plasticity retention even under high-strength regimes.

This observation clearly challenged the conventional strength-ductility trade-off and suggested that the refined martensitic lath structure, combined with extensive uniform intragranular subdivision distributed across laths/packets, contributed to greater resistance to crack initiation and propagation and increased strain accommodation through slip compatibility[168–170]. The preservation of ductility under these conditions was likely facilitated by a favorable synergistic interaction between high interfacial density and persistent substructural features, which delayed necking and localized failure.

In contrast, BA ↗ Ni exhibited more pronounced fluctuation in RA, with values ranging from 64% to 68%, and no clear correlation with total S_v or strain. This variability may have reflected the influence of nickel on dynamic recovery and substructural stability, where excessive nickel content could have promoted dislocation annihilation and reduced strain hardening, thereby limiting the capacity of material to sustain distributed plastic flow. However, BA maintained moderate ductility across all deformation conditions, with RA values between 67% and 69%. These results pointed to a conventional balance between strength and toughness, without the additional benefits of increased dislocation storage and suppressed recovery kinetics observed in the compositionally tailored alloys, which may partially account for the observed performance outcomes, particularly the superior ductility of BA ↗ Mn.

5.1.4.4 Composition-Specific Responses to Deformation Temperature

In contrast to BA ↗ Mn, which exhibited superior strength and stable ductility, BA ↗ Ni showed more variable RA responses and less consistent strength development, particularly under deformation below $T_{5\%}$. While moderate strength gains were recorded with decreasing temperature, the trend was comparatively subdued and exhibited limited sensitivity to strain. The observed modest fluctuations in yield strength for BA ↗ Ni were within the typical range of hot deformation scatter and are therefore not interpreted as anomalous. This inconsistency may be attributed to the influence of nickel on recovery and substructural stability, where higher nickel content can promote dynamic recovery and reduce dislocation density, thereby limiting work hardening and suppressing further strength evolution under severe deformation. All such interpretations are strictly based on in-gauge test data, excluding any anomalous yield strength points to ensure that composition-specific conclusions reflect genuine material behavior.

BA, by comparison, frequently exhibited lower strength values relative to BA ↗ Ni and BA ↗ Mn, especially under intermediate strain amounts and lower deformation temperatures. However, at 1050°C and a strain of 1.2, it unexpectedly achieved a yield strength of 900 MPa, surpassing both BA ↗ Ni and BA ↗ Mn. This localized increase may be linked to thermally assisted rearrangement of dislocations and sub-grain rearrangement under high deformation energy because this measurement was obtained from a fully compliant test where the increase is considered genuine rather than data error. Overall, the mechanical performance of BA appeared more dependent on processing conditions than on compositional effects to drive microstructural refinement and strength development.

5.1.5 Translational Insights for Processing Implications

Deformation at 800°C generally resulted in increased total S_v and yield strength, especially at higher strain amounts. This was most pronounced in BA ↗ Mn, where the yield strength increased from 660 MPa at 1050°C to 960 MPa at 800°C at a strain of 0.9, accompanied by a corresponding rise in interfacial density. At a strain of 1.2, a similar strengthening effect was observed, with BA ↗ Mn reaching 930 MPa at 800°C compared to 800 MPa at 1050°C. These observations suggested that deformation below $T_{5\%}$ increased dislocation accumulation and intragranular planar defect formation, raising yield strength without significantly compromising ductility.

However, some deviations from this trend were also apparent; for instance, at a strain of 0.6, BA ↗ Mn showed a slight decrease in yield strength at a lower temperature, which may be attributed to the onset of dynamic recovery, as suggested by reduced dislocation density and local orientation gradients observed in EBSD maps, partially offsetting the strengthening effect of increased total S_v[171,172]. In contrast, BA ↗ Ni exhibited reduced strength at an intermediate strain of 0.9, particularly under deformation below $T_{5\%}$, reflecting a limited hardening response despite elevated total S_v values. These findings indicate that the interplay between strain, temperature, and composition must be carefully considered in optimizing thermomechanical conditions.

These controlled and documented deviations were minor and expected within the normal experimental tolerance, thus do not undermine the validity of the overall strengthening trend. From an engineering perspective, lowering the finish deformation temperature offers practical advantages. Reducing the rolling temperature minimizes thermal energy input while raising strength, thereby creating favorable conditions for the use of supermartensitic stainless steels in offshore pipelines, high-pressure systems, and other components requiring high strength-to-weight ratios[161,173,174].

Nevertheless, the processing window must be carefully controlled and managed. Excessive deformation at a low temperature may lead to instability, localized cracking, or reduced workability. Therefore, an optimized strategy that combines lower deformation temperatures with tailored alloy design, particularly through manganese enrichment, may offer a balanced compromise between strength, ductility, and processing efficiency.

5.2 Influence of Finish Deformation Amount

Building upon the influence of deformation temperature, incremental strain accumulation played a fundamental role in shaping microstructural evolution, interfacial development, and mechanical performance during thermomechanical processing. With increasing strain, the microstructure experienced progressive defect accumulation and boundary refinement consistent with higher dislocation storage and enhanced strain partitioning[175]. Although dislocation density was not directly quantified in this study, its evolution was inferred exclusively from EBSD morphology and total S_v trends and the morphological evidence provided by EBSD.

These interpretations align with the expected thermomechanical response of steels under comparable deformation regimes where dynamic restoration processes, including sub-grain formation and partial recrystallization, were therefore considered qualitatively active, an inference supported by the morphological evolution and misorientation trends observed in EBSD maps, rather than in explicit dislocation or KAM measurements[176]. A systematic investigation across total strain amounts of 0.6, 0.9, and 1.2 was conducted to evaluate the influence of strain on total S_v, yield strength, PAG reconstruction, and ductility across the three studied alloys.

5.2.1 Microstructural Morphology as a Function of Strain Amount

Strain amount played a fundamental role in driving microstructural refinement during hot deformation. As strain increased from 0.6 to 1.2, a progressive rise in total S_v was observed across all temperatures and compositions, as detailed in Figure 4.29 to Figure 4.31. This increase reflected not only the elongation of grains but also the development of internal sub-grain boundaries and the accumulation of deformation-induced defect structures.

EBSD maps provided clear visual evidence of this refinement process. For example, Figure 4.26 showed that deformation at 800°C and a strain of 0.6 produced elongated grains in BA ↗ Mn with localized misorientation gradients. At a strain of 1.2, the same alloy exhibited more pronounced internal misorientation distributed across finer substructures, suggesting intensified strain partitioning and greater microstructural subdivision. A similar misorientation increase was observed in BA, as presented in Figure 4.28, although with a less refined structure and lower total S_v, consistent with its comparatively reduced dislocation storage capacity.

Both BA and BA ↗ Ni exhibited strain-induced morphological changes, but with lower refinement intensity. While BA ↗ Ni reached a comparable total S_v at 800°C and a strain of 1.2, the absence of EBSD data for this alloy precluded direct morphological interpretation. Nonetheless, its more moderate increase in total S_v across different strain amounts indicated a reduced degree of substructural refinement relative to BA ↗ Mn.

The general refinement trend with increasing strain was confirmed across all alloys and remained consistent with the associated strengthening responses, once non-representative yield strength data were excluded. Increasing strain overall favored intragranular subdivision and planar defect proliferation, driving up total S_v while modifying the interface character where this shift in morphology corresponded to higher yield strength via dislocation boundary strengthening but might also reduce the effectiveness of recrystallization, particularly at lower temperatures. These observations along with the quantitative outcomes support the inference that strain was the dominant driver of microstructural refinement under hot deformation conditions.

5.2.2 Response of Total S_v to Strain Amount

Total S_v increased significantly with incremental strain for all alloys at both deformation temperatures, with the highest values consistently observed at a strain of 1.2, as presented in Figure 4.32, Figure 4.33, and Figure 4.34. Among the three studied alloys, BA ↗ Mn exhibited the greatest total S_v at each strain amount, outperforming both BA and BA ↗ Ni. For instance, at 800°C, total S_v in BA ↗ Mn increased from 6.47 x 10^5 mm^{-1} at a strain of 0.6 to 7.13 x 10^5 mm^{-1} at a strain of 1.2. Similar but less pronounced increases were also recorded for BA and BA ↗ Ni under identical conditions.

These results confirmed that strain amount had a stronger influence on total S_v than deformation temperature, particularly beyond strain of 0.9, where the rate of increase in total S_v appeared to plateau. This saturation trend at a strain of 1.2 may be attributed to a limiting stage of microstructural refinement, potentially governed by dislocation cell wall thickness and boundary pinning effects. This inference stemmed from total S_v trends and established deformation theory despite that the direct validation through dislocation analysis was not performed.

Although this interpretation is consistent with classical hot deformation behavior, it remains inferential, as no direct evidence of dislocation saturation was obtained within the current dataset. Such behavior is consistent with prior observations reported in low-carbon high-manganese steels where the refinement of deformation substructures eventually approaches a steady state at high strain levels[162,177]. Furthermore, this behavior is consistent with prior stereological modeling, which demonstrated that increasing strain refines the microstructure into smaller, more geometrically complex domains, resulting in higher surface-to-volume ratios[99].

5.2.3 Contribution of Reconstructed PAG to Total S_v

The effect of strain on the contribution of reconstructed PAG to total S_v was substantial. At the lower strain of 0.6, a significant fraction of total S_v was derived from reconstructed PAG boundaries, particularly at the high deformation temperature of 1050°C, reaching 66% in BA and 39% in BA ↗ Mn. These values indicated that at moderate strain, a large portion of the interfacial area remained associated with original high angle austenitic boundaries.

However, as the strain increased to 1.2, the contribution from reconstructed PAG declined markedly. This reduction reflected the increased formation of intragranular features such as low angle grain boundaries (sub-grains) and deformation bands which dominated the microstructure at higher strains. The reconstructed PAG fraction dropped sharply at a strain of 1.2, consistent with the progressive subdivision of grains and replacement of prior grain boundary interfaces with deformation-induced internal boundaries.

This reduction in reconstructed PAG contribution explained the modest decrease in yield strength observed for BA ↗ Mn at high strain, confirming that the apparent softening originated from microstructural transformation rather than experimental error. The trends presented in Figure 4.37 to Figure 4.40 confirmed that increasing strain reduced the persistence of large prior austenite grains, instead promoting finer structural units and higher densities of internal interfaces. Comparable microstructural refinement behavior has been reported in other martensitic steels subjected to severe plastic deformation, where strain-induced subdivision of the parent austenitic structure diminishes the relative contribution of prior grain boundaries to the total interfacial area[30,170,178].

5.2.4 Mechanical Properties as a Function of Strain Amount

5.2.4.1 Yield Strength Evolution Across Strain Amount

Yield strength exhibited a generally positive correlation with increasing strain for BA and BA ↗ Ni, particularly at 800°C, as illustrated in Figure 5.1, Figure 5.2, and Figure 5.3. At this temperature, BA and BA ↗ Ni showed a progressive rise in yield strength with increasing strain from 0.6 to 1.2, where these outcomes, overall, correspond to fully valid in-gauge tests rather than out-of-gauge results which were excluded from interpretation, confirming that yield strength evolution with strain follows the expected strengthening pattern.

In contrast, BA ↗ Mn displayed a non-monotonic and composition-dependent trend with increasing strain at both temperatures. At 1050°C, yield strength dropped from 1030 MPa at a strain of 0.6 to 660 MPa at a strain of 0.9, then slightly recovered to 800 MPa at a strain of 1.2. At 800°C, BA ↗ Mn exhibited a more gradual decrease in yield strength, dropping from 990 MPa at a strain of 0.6 to 960 MPa at a strain of 0.9, and further to 930 MPa at a strain of 1.2.

These fluctuations, while modest, remained within the normal experimental scatter for hot deformation tensile tests and are attributed to competing effects between strain-induced substructure refinement and thermally assisted recovery. This deviation from typical strain hardening behavior suggested that recovery processes or dislocation rearrangement had become dominant, counteracting the strengthening normally conferred by finer interfacial features.

The coupling of increased total S_v and yield strength at higher strain amounts in BA and BA ↗ Ni supported the Hall-Petch strengthening mechanism, wherein finer effective grain boundaries act as effective barriers to dislocation motion[93,168]. However, BA ↗ Mn deviated from this trend, showing a progressive decline in yield strength despite the continued rise in total S_v. This behavior was possibly due to dynamic recovery, dislocation rearrangement into lower-energy configurations, or partial sub-grain coalescence[169].

5.2.4.2 Tensile Strength Evolution Across Strain Amount

Tensile strength trends followed a similar pattern, reinforcing the connection between interface development and mechanical performance. For BA ↗ Mn, tensile strength at 800°C slightly increased from 1104 MPa at a strain of 0.6 to 1174 MPa at a strain of 1.2, with a minor dip to 1074 MPa at a strain of 0.9, as shown in Figure 5.4, Figure 5.5, and Figure 5.6. This response aligned with the alloy’s ability to sustain elevated strength under high strain while maintaining a refined substructure.

In contrast, BA ↗ Ni demonstrated a gradual decrease in tensile strength with increasing strain, starting at 1054 MPa at a strain of 0.6, dropping to 930 MPa at a strain of 0.9, and reaching 963 MPa at a strain of 1.2. This behavior may have reflected limited substructure densification under increasing strain. BA showed non-monotonic behavior, with tensile strength increasing from 1019 MPa at a strain of 0.6 to 1052 MPa at a strain of 1.2, despite a dip to 869 MPa at a strain of 0.9. This trend suggested that deformation-induced structural refinement at high strain levels partially compensated for softening effects. Notably, tensile strength trends were unaffected by the yield strength exclusions and thus corroborate the overall mechanical consistency across the test matrix.

5.2.4.3 Reduction of Area and Ductility Preservation

Despite the progressive strain, ductility, as measured by the reduction of area, remained relatively stable for BA ↗ Mn, which consistently exhibited values between 70% and 74% across all strain amounts, as shown in Figure 4.45 and Figure 4.46. This preservation of ductility under high-strength regimes challenged the conventional strength-ductility trade-off. The retention of plasticity was likely supported by broadly distributed strain-accommodating substructures, such as refined lath martensite packets and dislocation cell networks, which collectively improved strain compatibility and delayed crack initiation and growth[168–170].

In contrast, BA ↗ Ni exhibited more variable RA values between 64% and 68%, with no consistent correlation to strain or strength. This inconsistency may have resulted from the influence of nickel on recovery and austenite stability, which could have moderated dislocation accumulation and reduced work-hardening capacity, thereby limiting distributed plastic flow[66,73]. BA showed moderately stable ductility across the strain range, with RA between 67% and 69%, indicating a traditional balance between strength and toughness without the benefits of extensive microstructural refinement or transformation mechanisms seen in compositionally tailored alloys.

5.2.4.4 Composition-Specific Responses to Strain Amount

Alloy composition exerted a clear influence on the mechanical response to increasing strain. BA ↗ Mn, while initially strong at lower strain amounts, demonstrated a decline in yield strength at higher strain amounts despite continued total S_v increase. This implied that strain-induced microstructural refinement alone was insufficient to sustain strength when recovery mechanisms were active, as inferred from morphology and interface trends rather than direct microstructural verification. In contrast, BA ↗ Ni exhibited consistent strength and moderate ductility across the strain range, although its improvement was less dramatic than that of BA. The influence of nickel likely promoted recovery and local rearrangement of dislocations, resulting in a modest strength increase, i.e. conservative response, compared with manganese-containing alloys.

BA achieved a notable strength increase at a temperature of 1050°C and a strain of 1.2, reaching 900 MPa and surpassing both BA ↗ Ni and BA ↗ Mn under those conditions. This suggested that even in the absence of alloying additions, the combined effect of high strain and elevated thermal energy could drive sufficient substructural evolution to raise mechanical properties. Therefore, for BA, deformation energy appeared to be a more critical factor in strength development than alloy chemistry.

5.2.5 Combined Influence of Strain and Temperature

A comparison of total S_v evolution at strains of 0.6 and 1.2 across both deformation temperatures of 800°C and 1050°C confirmed that strain exerted a more dominant effect than temperature on interfacial development. This trend was particularly evident in BA ↗ Mn, where at 1050°C, total S_v increased from 5.77 x 10^5 mm^{-1} at a strain of 0.6 to 7.00 x 10^5 mm^{-1} at a strain of 1.2. At 800°C, the total S_v increased from 6.47 x 10^5 mm^{-1} at a strain of 0.6 to 7.18 x 10^5 mm^{-1} at a strain of 1.2. Comparable patterns were also observed in BA and BA ↗ Ni, though the magnitude of the change was less pronounced, consistent with their lower dislocation storage capability and more limited substructural refinement.

These findings reinforced the conclusion that once a critical strain threshold was exceeded, further refinement in microstructure was driven primarily by deformation rather than thermal input. This was consistent with geometric recrystallization models, wherein the accumulation of strain promotes dislocation interaction, sub-grain rotation, and boundary formation independent of temperature[179]. Hence, the combined effect of high strain and controlled thermal input defined the microstructural transition pathway, balancing dislocation accumulation, substructural refinement, and the stabilization or transformation of phase boundaries.

5.2.6 Translational Insights for Processing Implications

From an engineering standpoint, optimizing the strain amount during hot deformation proved essential for achieving high strength without compromising ductility. Among the studied conditions, BA ↗ Mn subjected to a strain of 1.2 at 800°C yielded the most favorable combination of properties: balancing high yield strength, elevated tensile performance, and stable ductility. This indicated that thermomechanical conditions involving high strain at moderately low temperatures were especially advantageous for supermartensitic stainless steel components used in critical applications requiring strength, toughness, and microstructural stability.

However, it remained important to avoid excessive deformation, as uncontrolled strain accumulation could promote damage accumulation or microstructural degradation. The consistent performance of BA ↗ Mn under high strain was linked to its capacity to preserve elevated total S_v and ductility, which in turn pointed to the contribution of manganese in facilitating a refined and strain-compatible martensitic structure. This behavior was likely influenced by changes in stacking fault energy and greater dislocation glide accommodation mechanisms, both of which have been reported to support substructure stability under large strains[180–182].

5.3 Influence of Chemical Composition

Chemical composition played a critical role in governing the thermomechanical response of supermartensitic stainless steels. Subtle variations in alloying elements, particularly nickel and manganese, distinctly influenced phase stability, stacking fault energy, dislocation behavior, and transformation pathways. These compositional effects, in turn, shaped the evolution of microstructure and mechanical properties during hot deformation. The influence of nickel and manganese additions was assessed by comparing key parameters including total S_v, PAG contribution, yield strength, and ductility across BA, BA ↗ Ni, and BA ↗ Mn, based on experimental evidence and quantitative analysis.

5.3.1 Microstructural Morphology as Influenced by Alloying Elements

The influence of chemical composition on grain morphology and internal misorientation was evident in the EBSD maps presented in Figure 4.21 to Figure 4.28. Among the three studied alloys, BA ↗ Mn exhibited the most refined and strain-responsive microstructure. At 800°C, Figure 4.26 revealed highly elongated grains in BA ↗ Mn with pronounced intragranular misorientation and banding, suggesting suppressed recrystallization and greater strain localization. This morphology was consistent with the low SFE associated with manganese additions, which promoted dislocation storage and hindered recovery, thereby facilitating the development of deformation substructures, although these mechanisms are inferred from total S_v trends and EBSD evidence rather than direct dislocation density measurement[181,183,184]. No quantitative assessment of martensite grain size or retained austenite fraction was conducted; therefore, composition-dependent refinement is interpreted from qualitative morphology and total S_v metrics.

A more moderate degree of morphological refinement was observed in BA at 1050°C where its microstructure, shown in Figure 4.21, displayed equiaxed grains with relatively low intragranular orientation gradients, indicative of active recrystallization. At 800°C, however, Figure 4.22 demonstrated that the grains in BA became elongated and partially deformed, though not to the extent seen in BA ↗ Mn under similar processing conditions. This intermediate behavior corresponded with total S_v values presented in Figure 4.30 to Figure 4.36, where BA consistently recorded lower values than BA ↗ Mn. These findings reflected limited substructure evolution and less extensive interfacial development in BA.

Although EBSD data were not acquired for BA ↗ Ni, the observed mechanical response and total S_v trends offered indirect insight into its microstructural behavior. Across the different strain and temperature conditions, BA ↗ Ni exhibited less variation in total S_v and more subdued increases compared to BA ↗ Mn. This suggested a lower degree of strain-induced subdivision and a tendency toward greater structural stability, which aligned with the established role of nickel in raising SFE, accelerating recovery, and stabilizing austenite. In particular, the increase in SFE induced by nickel was likely to promote dislocation mobility and facilitate dynamic recovery, thereby limiting the formation of deformation bands and high-angle boundaries. In contrast, manganese is known to reduce SFE, impede recovery, and promote dislocation storage, contributing to more intense substructural refinement[102,180,185–190].

5.3.2 Response of Total S_v to Alloying Elements

Chemical composition exerted a systematic and measurable influence on total S_v, with BA ↗ Mn consistently displaying the highest total S_v values across all strain amounts and deformation temperatures, as presented in Figure 4.30 to Figure 4.34. For instance, at a temperature of 800°C and a strain of 1.2, BA ↗ Mn reached 7.18 x 10^5 mm^{-1}, compared to 6.10 x 10^5 mm^{-1} for BA ↗ Ni, and 5.12 x 10^5 mm^{-1} for BA. These results confirmed that manganese promoted microstructural refinement more effectively than nickel or the base composition. This effect was likely attributed to the ability of manganese to reduce SFE, thereby increasing dislocation storage and encouraging the formation of deformation substructures such as twins and dislocation cells, despite that the degree of dislocation accumulation was not directly quantified in this work[177,180–182]. The observed total S_v variations therefore reflect interface-density evolution rather than absolute grain size or dislocation-density measurements.

In contrast, BA ↗ Ni exhibited intermediate total S_v values across all conditions. The presence of nickel increased SFE, which may have facilitated dynamic recovery and suppressed sub-grain boundary formation, leading to a more stable and less subdivided microstructure. This behavior is consistent with the known role of nickel in promoting austenite stability and dislocation mobility. Additionally, BA consistently recorded the lowest total S_v values under all processing conditions, indicating a reduced tendency to form complex interfacial networks or undergo significant strain-induced subdivision. Its limited alloying content appeared to restrict the development of substructure and interface density, thus contributing to a coarser microstructural state.

5.3.3 Contribution of Reconstructed PAG to Total S_v

The contribution of reconstructed PAG to total S_v was found to be highly dependent on chemical composition, deformation temperature, and strain amount. As presented in Figure 4.37 to Figure 4.40, BA ↗ Mn consistently exhibited the lowest relative PAG contribution under high-strain, low-temperature conditions. Specifically, at 800°C and a strain of 1.2, PAG-derived interfaces accounted for only 23% of total S_v for BA ↗ Mn, compared to 26% for BA under the same condition, indicating a shift toward intragranular boundary generation and deformation-induced structure development.

In contrast, BA showed higher PAG contributions at an elevated temperature, particularly at 1050°C. At a strain of 1.2, PAG reconstruction in BA accounted for 50% of the total S_v, while BA ↗ Mn showed a lower value of 41%. These results highlight the role of manganese in driving substructural refinement by suppressing recrystallization and promoting dense intragranular boundary formation through deformation banding and dislocation accumulation.

The discussion of boundary density and substructural development is thus based on morphological evidence from EBSD and reconstructed PAG topology. These quantitative observations are supported by the EBSD maps shown in Figure 4.21 to Figure 4.28, where BA ↗ Mn exhibited elongated grains with high intragranular misorientation at 800°C, consistent with low SFE behavior and limited recovery. Literature on manganese-containing steels supports this interpretation, citing reduced recrystallization kinetics and greater substructural stability as key characteristics of manganese additions under hot deformation conditions[162,191–193].

5.3.4 Mechanical Properties Trends by Chemical Composition

5.3.4.1 Yield Strength Evolution Across Alloying Composition

Yield strength trends presented a pronounced dependence on alloying composition, as presented in Figure 5.1, Figure 5.2, and Figure 5.3. At a temperature of 800°C and a strain of 0.6, BA ↗ Mn displayed the highest yield strength of 990 MPa, then followed by BA ↗ Ni at 910 MPa and BA at 870 MPa. Although BA ↗ Mn demonstrated a modest reduction in strength with increased strain, declining to 960 MPa at a strain of 0.9 and 930 MPa at a strain of 1.2, it remained the strongest alloy across all tested conditions. This performance was attributed to its high dislocation retention and suppressed recovery, facilitated by manganese-induced reductions in stacking fault energy.

Conversely, BA ↗ Ni displayed a more monotonic response in yield strength. At 800°C, its yield strength rose from 910 MPa at a strain of 0.6 to 960 MPa at a strain of 0.9, before slightly decreasing to 890 MPa at a strain of 1.2. These results suggest that nickel contributed to solid solution strengthening and stabilized austenite, while its tendency to increase the SFE facilitated dynamic recovery through increased cross-slip activity and dislocation rearrangement, as commonly observed in high-nickel martensitic and austenitic systems, which may have limited further hardening at higher strains[180,181].

Additionally, BA generally exhibited the lowest yield strength under all deformation conditions. However, at a temperature of 1050°C and a strain of 1.2, it recorded an unexpected increase to 900 MPa, outperforming both BA ↗ Ni and BA ↗ Mn. This localized strengthening likely arose from sub-grain refinement under elevated deformation energy, highlighting the effect of temperature-driven mechanisms even in the absence of additional alloying elements.

5.3.4.2 Tensile Strength Evolution Across Alloying Composition

Tensile strength patterns similarly revealed composition-dependent behavior. At a strain of 0.6 and a temperature of 800°C, BA ↗ Mn recorded a tensile strength of 1104 MPa, compared to 1054 MPa for BA ↗ Ni and 1019 MPa for BA, as illustrated in Figure 5.4. At the same temperature of 800°C, tensile strength in BA ↗ Mn remained stable with a slight decrease to 1074 MPa at a strain of 0.9, followed by a significant increase to 1174 MPa at a strain of 1.2, indicating effective resistance to softening and sustained substructure strengthening under increasing strain.

BA ↗ Ni, in contrast, demonstrated a slight decline in tensile strength across the strain range, decreasing from 1054 MPa to 963 MPa, with an intermediate value of 930 MPa at a strain of 0.9, as presented in Figure 5.5. This trend reflected a balance between initial hardening and recovery-dominated behavior at higher strain. For BA, tensile strength increased, at a temperature of 800°C, from 1019 MPa at a strain of 0.6 to 1052 MPa at a strain of 1.2. This increase was likely due to deformation-driven substructural evolution, compensating for its lower initial strength compared to the alloyed compositions.

5.3.4.3 Reduction of Area and Ductility Preservation

RA data demonstrated that chemical composition significantly influenced ductility under strain, as presented in Figure 4.45 and Figure 4.46. BA ↗ Mn consistently exhibited the highest and most stable RA values, ranging between 72% and 74% across all strain and temperature conditions. This exceptional ductility, despite high strength and total S_v, indicated that manganese promoted intragranular structures that absorbed strain across packets and blocks and delayed crack propagation, possibly through greater dislocation storage, slip homogenization, and greater strain accommodation under multiaxial loading[168,170].

In contrast, BA ↗ Ni showed more variability in RA, with values ranging from 64% to 68%, and no consistent trend with strain or total S_v. The increased SFE resulting from nickel additions may have facilitated dynamic recovery and dislocation rearrangement, reducing strain hardening and limiting homogeneous plastic deformation. Nevertheless, BA displayed intermediate ductility, maintaining RA values between 67% and 69% across most conditions. Its performance reflected a conventional balance between strength and toughness, without the added benefits of strain-compatible microstructures introduced by manganese or nickel.

5.3.4.4 Composition-Specific Responses to Varying Deformation Conditions

The interplay between chemical composition and deformation conditions had a marked influence on the mechanical behavior of the studied alloys. BA ↗ Mn consistently exhibited the highest strength values across all tested temperatures and strain amounts, attributed to its ability to retain high dislocation density and develop refined substructures. However, a slight decrease in yield strength with increasing strain, despite rising total S_v, suggested the onset of recovery mechanisms or partial coalescence of sub-grains, which tempered the strengthening typically associated with interface density.

In contrast, BA ↗ Ni presented a more gradual mechanical response, with strength increasing from strain 0.6 to 0.9 before slightly declining at a strain of 1.2. This gradual trend was likely related to the known role of nickel in promoting austenite stability and facilitating dynamic recovery, which may have moderated dislocation buildup and delayed strain hardening saturation. Although BA ↗ Ni did not reach the strength levels of BA ↗ Mn, it maintained relatively moderate strength and ductility across a broader range of conditions.

BA exhibited the most temperature-sensitive and strain-sensitive behavior, achieving comparatively lower strength at mild deformation but showing a pronounced increase at a strain of 1.2 and 1050°C. This localized increase pointed to thermally assisted sub-grain rearrangement compensating for the absence of alloying-driven strengthening. The trends across all three alloys reinforced that mechanical performance under thermomechanical loading was composition-dependent, influenced by how each element modified stacking fault energy, dislocation dynamics, and the competition between recovery and hardening processes.

5.3.5 Translational Insights for Processing Implications

The superior performance of BA ↗ Mn in terms of total S_v, yield strength, and ductility retention underscored its potential for applications requiring refined microstructures and high energy absorption capacity. From an industrial standpoint, this alloy offered a balanced combination of mechanical robustness and formability, particularly under low-temperature and high-strain conditions. Such characteristics rendered BA ↗ Mn a strong candidate for structural components, offshore pipelines, and pressure containment systems exposed to severe loading environments. These findings suggested that alloy design strategies aimed at achieving microstructural refinement and deformation-induced strengthening should prioritize controlled manganese enrichment. Manganese not only reduced SFE but also promoted dislocation storage and substructure evolution, enabling strength development without sacrificing ductility, a relationship supported by literature but not directly evidenced within the current experimental scope.

Conversely, while nickel additions contributed to solid-solution strengthening and austenite stabilization, BA ↗ Ni demonstrated less predictable ductility, especially at elevated strains. This behavior indicated that an excessive nickel content may have facilitated recovery and reduced strain hardening capacity, thereby limiting the extent of distributed plastic flow unless balanced with other alloying elements that support dislocation retention and stabilize deformation substructures. Therefore, optimizing nickel levels in conjunction with other stabilizers was essential to achieve consistent mechanical performance. Collectively, these composition-dependent insights supported a processing approach that carefully integrates both alloy chemistry and deformation path to tailor microstructure, maximize interfacial area, and balance strength with toughness in supermartensitic stainless steel applications.

5.4 Summary and Integration of Discussion

The comprehensive evaluation of deformation temperature, strain amount, and chemical composition revealed a set of interdependent factors that governed the microstructural evolution and mechanical behavior of supermartensitic stainless steels during hot deformation. Rather than acting independently, these parameters interacted in a composition-sensitive and strain-dependent manner, producing microstructural and mechanical outcomes that could not be solely attributed to a single dominant variable.

Among the most critical findings was that strain amount emerged as the dominant driver of microstructural refinement and interfacial development. As incremental strain increased from 0.6 to 1.2, total S_v rose consistently across all alloys and temperatures, indicating finer grain subdivision and development of internal interfaces. This trend was most apparent in BA ↗ Mn, which recorded the highest total S_v values due to its manganese-induced suppression of recovery and facilitation of dislocation storage, although this interpretation remains inferential and based on established low SFE behavior. However, at higher strain levels, the benefits of additional deformation plateaued, and in some cases, yield strength decreased despite further total S_v increases. This indicated a shift in the dominant mechanism from interface strengthening to thermal-assisted recovery or strain-induced softening.

Reconstruction of PAG provided the clearest morphological evidence of these transitions. At 1050°C, deformation promoted equiaxed morphologies and high reconstructed PAG fractions, confirming that recrystallization was fully activated. At

800°C, however, the reconstructed PAG maps revealed elongated unrecrystallized morphologies with dense deformation banding, high local misorientation, and reduced PAG fractions; features consistent with sub-grain formation and suppressed boundary migration.

The measured decline in PAG contribution from 41%-66% at 1050°C to 23%-26% at 800°C quantitatively demonstrated that intragranular substructures, rather than inherited austenitic boundaries, became the dominant contributors to total S_v and, hence, to strength. These trends were particularly evident in BA ↗ Mn, which exhibited finer effective PAG thickness, shorter transverse intercept distances, and stronger segmentation at each strain level.

It should be emphasized that these interpretations derive from EBSD morphology, boundary topology, and total S_v analysis, rather than from direct measurements of dislocation density or orientation-gradient metrics such as KAM. Nonetheless, the consistency between qualitative contrast, reconstructed PAG statistics, and quantitative total S_v values provides strong indirect evidence of the strain-driven subdivision process and the compositional control of recovery and recrystallization kinetics.

Deformation temperature functioned as a secondary yet influential control. At 1050°C, recrystallization was activated, particularly in the base alloy BA, producing equiaxed grains and higher reconstructed PAG contributions. Conversely, deformation at 800°C led to deformation banding, dislocation storage, and elongated grain structures, particularly in BA ↗ Mn. The reduction of reconstructed PAG contributions with decreasing temperature and increasing strain confirmed that intragranular substructures became the dominant carriers of mechanical strength.

Chemical composition moderated the effect of temperature and strain. In general metallurgical terms, manganese is known to reduce SFE, thereby promoting planar slip, localized deformation, and suppression of dynamic recovery. This combination increased dislocation storage and produced high strength with sustained ductility, particularly at lower deformation temperatures. Nickel, in contrast, is known to increase SFE, thereby facilitating dislocation rearrangement and recovery, which produced steadier but smaller strength increments at elevated strain. As a result, BA ↗ Ni exhibited modest strength development compared with BA ↗ Mn.

Mechanical property trends reinforced these microstructural observations. BA ↗ Mn consistently showed the highest yield and tensile strength across most processing conditions, along with exceptional ductility retention. This performance was attributed to the formation of martensitic substructures that enabled effective strain accommodation and delayed localized failure. While BA ↗ Ni exhibited reliable strength development, its RA values fluctuated more, reflecting a distinct deformation response associated with recovery and interface character. BA followed intermediate trends, relying more heavily on processing conditions than compositional refinement to achieve mechanical performance.

The summarized interactions among strain, temperature, and chemical composition are captured in Table 5.1 which oulines how specific and critical thermomechanical conditions or compositional variations influenced both microstructural development and mechanical performance across the studied compositions.

Table 5.1 Summary of dominant thermomechanical conditions and their influence on microstructural development and mechanical response across the studied compositions.

Controlling Factor	Dominant Response	Resulting Outcome
↓ Strain, ↑ Temperature, BA	Activation of recrystallization and reduced dislocation density	↓ Total S_v, ↑ Reconstructed PAG contribution, ± Strength, ± Ductility
↑ Strain, ↓ Temperature, BA	Suppression of recrystallization and sub-grain formation	± Total S_v, ↓ Reconstructed PAG contribution, ↑ Strength, ± Ductility
↓ Strain, ↓ Temperature, BA ↗ Mn	Dislocation accumulation and limited recovery	± Total S_v, ± Reconstructed PAG contribution, ↑ Strength, ↑ Ductility
↑ Strain, ↓ Temperature, BA ↗ Mn	Dislocation storage and substructure development	↑ Total S_v, ↓ Reconstructed PAG contribution, ± Strength, ↑ Ductility
↑ Strain, ↓ Temperature, BA ↗ Ni	Recovery-dominated structure with austenite stabilization	↑ Total S_v, ± Development of substructure, ± Strength, ± Ductility
↓ Strain, ↑ Temperature, BA ↗ Ni	Recovery-dominated structure with boundary stabilization	↓ Total S_v, ↓ Development of substructure, ± Strength, ↓ Ductility

↑ Increased. ↓ Decreased. ± Intermediate.

Chapter 6 Conclusions and Future Work

6.1 Conclusions

In light of the compelling evidence and tangible outcomes of this research, achieved through slight alloy modifications combined with a systematic and quantitative approach that extended beyond conventional grain size metrics and delved into internal microstructural architecture, it is evident that the research objectives outlined in Section 1.4 have been fully addressed and successfully achieved. A structured evaluation of the research outcomes against the defined objectives is presented in Table 6.1. The comprehensive methodology, incorporating thermomechanical processing simulations, detailed microstructural quantification via total S_v, and mechanical property correlations, enabled a thorough and insightful assessment of supermartensitic stainless steels under varied processing conditions. The following conclusions were drawn from the investigation:

I. Influence of Deformation Temperature: Deformation at 1050°C (above $T_{95\%}$) activated recrystallization in BA and, to a lesser extent, in BA ↗ Mn. This resulted in equiaxed grains, elevated reconstructed PAG contributions, and moderate total S_v. In contrast, deformation at 800°C (below $T_{5\%}$) suppressed recrystallization, leading to grain elongation, high dislocation retention, and elevated total S_v, particularly in BA ↗ Mn, contributing to increased interface density and inferred dislocation-based strengthening through stored-energy accumulation.

II. Influence of Strain Amount: Strain was identified as the primary driver of total S_v evolution. As strain increased from 0.6 to 1.2, all compositions exhibited rising total S_v values, indicating progressive grain subdivision and development of intragranular interfaces. However, at high strain levels, this trend plateaued or reversed for some alloys. Specifically, BA ↗ Mn showed signs of softening at a strain of 1.2 despite continued total S_v increase, indicating the inferred onset of recovery or substructure coalescence mechanisms.

III. Influence of Chemical Composition: BA ↗ Mn exhibited the most favorable combination of high metrics, i.e. total S_v, strength, and ductility. Its reduced SFE promoted dislocation storage and suppressed dynamic recovery, resulting in refined martensitic morphologies and finer effective PAG thickness, especially under low-temperature, high-strain deformation. BA ↗ Ni, however, characterized by higher SFE, facilitated dislocation rearrangement and dynamic recovery, leading to smoother grain boundaries, steadier strength evolution, and more uniform ductility at elevated strain. BA demonstrated the most strain-sensitive and temperature-sensitive behavior, with its mechanical response governed more by deformation energy than by compositional modification.

IV. Microstructural-Mechanical Correlations: A generally positive correlation between total S_v and mechanical strength was observed in BA and BA ↗ Ni, where increasing interface density supported yield and tensile strength gains. However, in BA ↗ Mn, this relationship diverged at higher strain, where strength decreased despite continued total S_v increases, suggesting a shift toward recovery-dominated deformation. The contribution of reconstructed PAG to total S_v was highest at 1050°C, consistent with active recrystallization, but diminished with increasing strain, most notably under unrecrystallized elongated morphologies at 800°C, where deformation-induced substructures and high-angle boundaries became dominant.

V. Transformation Behavior: CCT diagrams and dilatometric analysis confirmed that all alloys achieved fully martensitic transformations, with M_s temperatures influenced by composition. Nickel suppressed M_s more significantly than manganese, consistent with its stronger austenite-stabilizing effect. A larger M_s depression can increase the prospect of residual austenite upon cooling; however, retained austenite was not quantified and is only inferred from thermodynamic expectations. Manganese produced a more moderate suppression of M_s and effectively reduced SFE, thereby facilitating planar slip and deformation-induced substructure formation during hot working. These effects collectively governed both the martensitic transformation and the refinement of the final microstructure.

Table 6.1 Key findings and supporting evidence from the investigation of modified supermartensitic stainless steels under varied thermomechanical processing conditions.

Objective	Key Findings	Supporting Evidence
Study the behavior of supermartensitic stainless steels against critical processing temperatures and evaluate the influence of nickel and manganese additions.	Nickel and manganese reduced critical transformation temperatures and altered austenite stability. Mn increased strength, dislocation storage, and substructural refinement. Ni facilitated recovery and austenite stability, with variable ductility responses.	Dilatometric analysis and CCT diagrams showed lower A_{c1}, A_{c3}, and M_s for BA ↗ Ni and BA ↗ Mn. Mechanical testing revealed that BA ↗ Mn achieved higher strength, whereas BA ↗ Ni showed lower RA but moderate strength.
Investigate and quantify the total S_v when deformed above or below critical processing temperatures and its effect on transformation microstructures.	Higher total S_v was consistently achieved at 800°C (below $T_{5\%}$) due to suppressed recrystallization and dense dislocation structures. However, at 1050°C (above $T_{95\%}$), total S_v was lower due to dynamic restoration and equiaxed grain formation.	Total S_v quantification across all conditions. EBSD maps confirmed grain morphology. Mechanical test data validated correlations between deformation temperature, total S_v, and resulting strength behavior.
Investigate and quantify PAG contribution to the total S_v for the extreme identified conditions and its effect on the transformation product.	PAG contribution to total S_v was highest at 1050°C and low strain, reflecting active recrystallization. At high strain and 800°C, PAG contribution decreased as substructural interfaces dominated.	Reconstructed PAG boundary maps and total S_v data demonstrated temperature-sensitive and strain-sensitive changes in interfacial carriers of strength. Supported by EBSD evidence and mechanical correlations.

6.2 Future Work

While this research followed a systematic methodology for investigating the processing-structure-property relationships in supermartensitic stainless steels and validated a composition-sensitive, strain-governed, and temperature-mediated framework for microstructural refinement and mechanical strengthening, it also uncovered several promising avenues for further exploration. By integrating thermomechanical processing simulations with quantitative interfacial analysis, the study offers a blueprint for future alloy and process design strategies. However, additional investigations are warranted to deepen the understanding of phase stability, interface evolution, and mechanical performance under industrially relevant conditions.

Building on the findings, the following research directions extend the core outcomes of this work and provide an applied foundation for developing next-generation supermartensitic stainless steel grades tailored for high-performance structural applications:

I. Industrial-scale validation and predictive modeling: To translate laboratory-scale insights into practical applications, pilot-scale trials, and multiscale modeling frameworks are essential. Simulations of hot rolling or forging under industrial conditions could validate the scalability of optimized thermomechanical schedules, particularly under variable strain rates and complex cooling trajectories. In parallel, atomistic and mesoscale models should be developed to predict SFE variations, dislocation interactions, and interfacial evolution as functions of temperature, strain, and chemical composition. These predictive tools would support the design of supermartensitic stainless steel alloys with customized microstructural responses and ensure their long-term mechanical reliability in real-world components such as offshore structures, pipelines, and welded joints.

II. Expanded mechanical performance assessments: This study primarily examined strength and ductility under monotonic loading. To complete the performance profile of supermartensitic stainless steels, future work should investigate additional properties, including fracture toughness, low-cycle fatigue resistance, creep strength, and thermal stability. In particular, understanding the stability of any residual or transformation-induced austenite and its influence on deformation behavior under cyclic and impact loading is crucial. Integrating these performance metrics with interfacial quantification via S_v could establish robust predictive correlations for supermartensitic stainless steels used in complex service environments.

III. Advanced characterization of dynamic microstructural evolution: Further research should leverage advanced characterization techniques to observe the real-time evolution of dislocation structures, sub-grains, and recrystallization fronts during thermomechanical processing. Techniques such as high-temperature EBSD, synchrotron X-ray diffraction, and TEM can offer dynamic insights into recovery mechanisms, interface migration, and strain accommodation, particularly in manganese-rich compositions where deformation structures show high thermal stability. Additionally, high-resolution EBSD analyses with a refined step size should be conducted to enable the quantitative extraction of KAM and the determination of martensitic lath, block, and packet size distributions with statistical reliability along with complementary X-ray diffraction analysis incorporating rietveld refinement to quantify the retained austenite fraction with higher precision, enabling a direct correlation between phase fractions, interfacial density, and mechanical response across different processing regimes.

References

---

(1) BP. *BP Statistical Review of World Energy 2022*, 71st ed.; BP: London, UK, 2022.

(2) McKinsey & Company. *Global Energy Perspective 2024*; McKinsey & Company: New York, NY, 2024.

(3) Parra, P. A. Y.; Ganti, G.; Brecha, R.; Hare, B.; Schaeffer, M.; Fuentes, U. *Global and Regional Coal Phase-Out Requirements of the Paris Agreement: Insights From the IPCC Special Report on 1.5°C*; Climate Analytics: Berlin, Germany, 2019.

(4) United Nations Framework Convention on Climate Change. *Paris Agreement*; United Nations: Paris, France, 2015.

(5) Rodger, C.; Radmall, P. *Environmental Statement Volume 1: Main Report*; Axis: Chester, UK, 2020.

(6) Department for Business, Energy & Industrial Strategy. *Coal Generation in Great Britain: The Pathway to a Low-Carbon Future*; HM Government: London, UK, 2016.

(7) Department for Business, Energy & Industrial Strategy. *Implementing the End of Unabated Coal by 2025: Government Response to Consultation and Statement of Policy*; HM Government: London, UK, 2018.

(8) Department for Business, Energy & Industrial Strategy. *Early Phase Out of Unabated Coal Generation in Great Britain: Response Consultation*; HM Government: London, UK, 2021.

(9) HM Government. *Net Zero Strategy: Build Back Greener*; HM Government: London, UK, 2021.

(10) Byers, L.; Friedrich, J.; Hennig, R.; Kressig, A.; Li, X.; McCormick, C.; Malaguzzi Valeri, L. *A Global Database of Power Plants*; World Resources Institute: Washington, DC, 2018.

(11) World Steel Association. *World Steel in Figures 2023*; World Steel Association: Brussels, Belgium, 2023.

(12) During, E. D. D. *Corrosion Atlas: A Collection of Illustrated Case Histories*, 3rd ed.; Elsevier: Amsterdam, Netherlands, 2018.

(13) Cobb, H. M. *The History of Stainless Steel*, 1st ed.; ASM International: Materials Park, OH, 2010.

(14) Cobb, H. M. *Stainless Steels: A Steel Products Manual*, 1st ed.; Association for Iron & Steel Technology: Warrendale, PA, 2008.

(15) American Iron and Steel Institute; Nickel Institute. *Design Guidelines for the Selection and Use of Stainless Steel: A Designers' Handbook Series*, 3rd ed.; Nickel Institute: Brussels, Belgium, 2020.

(16) Davis, J. R. *ASM Specialty Handbook: Stainless Steels*, 1st ed.; ASM International: Materials Park, OH, 1994.

(17) Farrar, J. C. M. *The Alloy Tree: A Guide to Low-Alloy Steels, Stainless Steels and Nickel-Base Alloys*, 1st ed.; CRC Press: Cambridge, England, 2004. https://doi.org/10.1533/9781855739925.

(18) Li, X.; Dai, Y.; Wang, X.; Liu, Y.; Chen, Y.; Wang, C.; Zhang, H.; Li, L.; Liu, H.; He, C.; Wang, Q. Effects of Local Microstructure on Crack Initiation in Super Martensitic Stainless Steel Under Very-High-Cycle Fatigue. *International Journal of Fatigue* **2022**, *163*, 107019. https://doi.org/10.1016/j.ijfatigue.2022.107019.

(19) Liu, Y.; Ye, D.; Yong, Q.; Su, J.; Zhao, K.; Jiang, W. Effect of Heat Treatment on Microstructure and Property of Cr13 Super Martensitic Stainless Steel. *Journal of Iron and Steel Research International* **2011**, *18* (11), 60–66. https://doi.org/10.1016/S1006-706X(11)60118-0.

(20) Caldwell, E.; Zhang, H.; Goodman, L. A Selection Methodology for 13Cr-Type Alloy Oil Country Tubular Goods. In *SPE International Oilfield Corrosion Conference and Exhibition*; SPE: Aberdeen, Scotland, 2014; pp 1–15. https://doi.org/10.2118/169633-MS.

(21) Miyata, Y.; Kimura, M.; Murase, F. Development of Martensitic Stainless Steel Seamless Pipe for Linepipe Application. *Kawasaki Steel Technical Report* **1998**, No. 38, 53–60.

(22) Pereda, M. D.; Gervasi, C. A.; Llorente, C. L.; Bilmes, P. D. Microelectrochemical Corrosion Study of Super Martensitic Welds in Chloride-Containing Media. *Corrosion Science* **2011**, *53* (12), 3934–3941. https://doi.org/10.1016/j.corsci.2011.07.040.

(23) Olden, V.; Thaulow, C.; Johnsen, R. Modelling of Hydrogen Diffusion and Hydrogen Induced Cracking in Supermartensitic and Duplex Stainless Steels. *Materials and Design* **2008**, *29* (10), 1934–1948. https://doi.org/10.1016/j.matdes.2008.04.026.

(24) Cumino, G.; Poli, A.; Ono, T.; Hashizume °, S.; Yamazaki, K.; Scoppio, L. Supermartensitic 13 %Cr Large Diameter Seamless Pipes: Mechanical Corrosion and Weldability Properties. *Latin American Applied Research* **2002**, *32* (3), 215–219.

(25) Sabará, C. V. L.; Prachedes, L. N. S.; Santos, L. C.; Sabará, M. A.; Souza, R. C.; Sene, A. F.; Caldeira, L.; Vaz, G. L.; Oliveira, J. R.; Gomes, J. A. C. P.; Bueno, A. H. S. Influence of Parameters Related to Microstructure, Chemical Composition and Environment Characteristics on Localized Corrosion Failure Susceptibility of Supermartensitic Stainless Steels. *Engineering Failure Analysis* **2021**, *127*, 105524. https://doi.org/10.1016/j.engfailanal.2021.105524.

(26) Ma, X. P.; Wang, L. J.; Liu, C. M.; Subramanian, S. V. Microstructure and Properties of 13Cr5Ni1Mo0.025Nb0.09V0.06N Super Martensitic Stainless Steel. *Materials Science and Engineering A* **2012**, *539*, 271–279. https://doi.org/10.1016/j.msea.2012.01.093.

(27) Ma, X. P.; Wang, L. J.; Liu, C. M.; Subramanian, S. V. Role of Nb in Low Interstitial 13Cr Super Martensitic Stainless Steel. *Materials Science and Engineering A* **2011**, *528* (22–23), 6812–6818. https://doi.org/10.1016/j.msea.2011.05.065.

(28) Barbosa, C.; Abud, I. Recent Developments on Martensitic Stainless Steels for Oil and Gas Production. *Recent Patents on Corrosion Science* **2013**, *3* (1), 27–38. https://doi.org/10.2174/22106839112029990004.

(29) Chales, R.; Cardoso, A. S. M.; Garcia, P. S. P.; Almeida, B. B.; Igreja, H. R.; Noris, L. F.; Pardal, J. M.; Tavares, S. S. M. Mechanical Properties and Strain-Hardening Models of Supermartensitic Stainless Steels Alloyed to Nitrogen and Vanadium. *Materials Research* **2023**, *26*, e20230198. https://doi.org/10.1590/1980-5373-mr-2023-0198.

(30) Voort, G. F. V. *Metallography: Principles and Practice*, 1st ed.; ASM International: Materials Park, OH, 1999.

(31) Porter, D. A.; Easterling, K. E.; Mohamed, Y. S. *Phase Transformations in Metals and Alloys*, 3rd ed.; CRC Press: Boca Raton, FL, 2009.

(32) ISO/TC 67 Committee. *NACE MR0175/ISO 15156-1:2015: Petroleum, Petrochemical, and Natural Gas Industries — Materials for Use in H2S-Containing Environments in Oil and Gas Production — Part 1: General Principles for Selection of Cracking-Resistant Materials*; NACE International: Houston, TX, 2015.

(33) SUSTAIN. *Annual Review 2023/2024*; EPSRC Strategic University Steel Technology and Innovation Network Future Manufacturing Research Hub: Swansea, UK, 2024.

(34) Hougardy, H. P. Transformation of Steels During Cooling. In *Theory and Technology of Quenching*; Liščić, B., Tensi, H. M., Luty, W., Eds.; Springer: New York, NY, 1992; pp 1–18. https://doi.org/10.1007/978-3-662-01596-4_1.

(35) Fisher, J. C.; Hollomon, J. H. Kinetics of the Austenite → Martensite Transformation. *Metals Transactions* **1949**, *185* (10), 691–700.

(36) Gomez, M.; Rancel, L.; Escudero, E.; Medina, S. F. Phase Transformation under Continuous Cooling Conditions in Medium Carbon Microalloyed Steels. *Journal of Materials Science & Technology* **2014**, *30* (5), 511–516. https://doi.org/10.1016/j.jmst.2014.03.015.

(37) Christian, J. W. *The Theory of Transformation in Metals and Alloys*, 3rd ed.; Elsevier: Oxford, UK, 2002.

(38) Krauss, G. Microstructure and Transformations in Steel. In *Materials Science and Technology: A Comprehensive Treatment Volume 7: Constitution and Properties of Steels*; Wiley: Weinheim, Germany, 1992; pp 1–40.

(39) Nishiyama, Z.; Fine, M. E.; Meshii, M.; Wayman, C. M. *Martensitic Transformation*, 1st ed.; Academic Press: New York, NY, 1978.

(40) Timokhina, I. B.; Hodgson, P. D.; Pereloma, E. V. Effect of Microstructure on the Stability of Retained Austenite in Transformation-Induced-Plasticity Steels. *Metallurgical and Materials Transactions A* **2004**, *35A*, 2331–2341. https://doi.org/10.1007/s11661-006-0213-9.

(41) Pereloma, E.; Edmonds, D. V. *Phase Transformations in Steels. Volume 1: Fundamentals and Diffusion-Controlled Transformations*, 1st ed.; Woodhead Publishing: Cambridge, UK, 2012.

(42) Pero-Sanz Elorz, J. A.; Quintana Hernández, M. J.; Verdeja González, L. F. *Solidification and Solid-State Transformations of Metals and Alloys*, 1st ed.; Elsevier: Amsterdam, Netherlands, 2017.

(43) Kelly, A.; Knowles, K. M. *Crystallography and Crystal Defects*, 2nd ed.; Wiley: West Sussex, UK, 2012. https://doi.org/10.1002/9781119961468.

(44) McGuire, M. F. *Stainless Steels for Design Engineers*, 1st ed.; ASM International: Materials Park, OH, 2008.

(45) Zhu, C.; Xu, L.; Xie, H.; Shi, R.; Yin, L.; Wei, S. Effect of Heat Treatment Processes on the Microstructure and Mechanical Properties of 00Cr13Ni5Mo Super Martensitic Stainless Steel (SMSS). *Journal of Materials Research and Technology* **2024**, *32*, 2006–2021. https://doi.org/10.1016/j.jmrt.2024.08.030.

(46) Hashmi, S. *Comprehensive Materials Processing*, 1st ed.; Elsevier: Amsterdam, Netherlands, 2014.

(47) Davis, J. R.; Park, M. *Alloying: Understanding the Basics*, 1st ed.; ASM International: Materials Park, OH, 2001.

(48) Campbell, F. C. *Elements of Metallurgy and Engineering Alloys*, 1st ed.; ASM International: Materials Park, OH, 2008.

(49) Verdeja González, J. I.; Fernández-González, D.; Verdeja González, L. F. *Physical Metallurgy and Heat Treatment of Steel*, 1st ed.; Springer: Cham, Switzerland, 2023. https://doi.org/10.1007/978-3-031-05702-1.

(50) Varga, I.; Kuzmann, E.; Vértes, A. Kinetics of A→γ Phase Transformation of Fe-12Cr-4Ni Alloy Aged Between 500-650°C. *Hyperfine Interactions* **1998**, *112* (1), 169–174. https://doi.org/10.1023/A:1011073602566.

(51) Peddle, B. E.; Pickles, C. A. Carbide Development in the Heat Affected Zone of Tempered and Post-Weld Heat Treated 2.25Cr-1Mo Steel Weldments. *Canadian Metallurgical Quarterly* **2001**, *40* (1), 105–126. https://doi.org/10.1179/cmq.2001.40.1.105.

(52) Falodun, O. E.; Oke, S. R.; Okoro, A. M.; Olubambi, P. A. Characterization of Cast Manganese Steels Containing Varying Manganese and Chromium Additions. *Materials Today: Proceedings* **2020**, *28*, 730–733. https://doi.org/10.1016/j.matpr.2019.12.288.

(53) Taneike, M.; Sawada, K.; Abe, F. Effect of Carbon Concentration on Precipitation Behavior of M23C6 Carbides and MX Carbonitrides in Martensitic 9Cr Steel during Heat Treatment. *Metallurgical and Materials Transactions A* **2004**, *35* (4), 1255–1262. https://doi.org/10.1007/s11661-004-0299-x.

(54) Eun, J.-C. *Handbook of Engineering Practice of Materials and Corrosion*, 1st ed.; Springer International Publishing: Cham, Switzerland, 2020. https://doi.org/10.1007/978-3-030-36430-4.

(55) Uhlig, H. H. Passivity in Metals and Alloys. *Corrosion Science* **1979**, *19*, 777–791. https://doi.org/10.1016/S0010-938X(79)80075-X.

(56) Bruemmer, S. M.; Arey, B. W.; Charlot, L. A. Influence of Chromium Depletion on Intergranular Stress Corrosion Cracking of 304 Stainless Steel. *CORROSION* **1992**, *48* (1), 42–49. https://doi.org/10.5006/1.3315917.

(57) Pumpyanskii, D. A.; Pyshmintsev, I. Yu.; Bityukov, S. M.; Gervas’ev, M. A.; Gusev, A. A. Features of Microstructure, Phase Composition and Strengthening Capability of Stainless Steels with Chromium Content of 13–17%. *Steel in Translation* **2022**, *52* (9), 844–851. https://doi.org/10.3103/S0967091222090091.

(58) Maisuradze, M. V.; Kuklina, A. A.; Nazarova, V. V.; Ryzhkov, M. A.; Antakov, E. V. Microstructure and Mechanical Property Formation of Heat Treated Low-Carbon Chromium-Nickel-Molybdenum Steels. *Metallurgist* **2024**, *68* (3), 322–335. https://doi.org/10.1007/s11015-024-01732-3.

(59) Tian, J.; Chen, K.; Li, H.; Jiang, Z. Suppressing Grain Boundary Embrittlement via Mo-Driven Interphase Precipitation Mechanism in Martensitic Stainless Steel. *Materials Science and Engineering A* **2022**, *833*, 142529. https://doi.org/10.1016/j.msea.2021.142529.

(60) Huang, T.; Zhang, Y.; Zhang, Z.; Du, K.; Li, J.; Liu, L.; Wang, X.; Sun, L. Effects of Mo Content on the Precipitation Behavior and Martensitic Transformation in FeNiCoAlMo Alloy. *Materials Characterization* **2023**, *199*, 112787. https://doi.org/10.1016/j.matchar.2023.112787.

(61) Michaud, P.; Delagnes, D.; Lamesle, P.; Mathon, M. H.; Levaillant, C. The Effect of the Addition of Alloying Elements on Carbide Precipitation and Mechanical

Properties in 5% Chromium Martensitic Steels. *Acta Materialia* **2007**, *55* (14), 4877–4889. https://doi.org/10.1016/j.actamat.2007.05.004.

(62) Oksiuta, Z.; Lewandowska, M.; Kurzydlowski, K. J.; Baluc, N. Effect of Vanadium Addition on the Microstructure and Mechanical Properties of the ODS Ferritic Steels. *Journal of Nuclear Materials* **2013**, *442* (1–3), S84–S88. https://doi.org/10.1016/j.jnucmat.2012.10.022.

(63) Wu, Z.; Ushioda, K.; Liu, H.; Li, Y.; Fujii, H. Effect of V and Mn Addition on the HAZ Softening and Tensile Properties of Friction Stir Welded Martensitic Steel. *Materials Science and Engineering A* **2024**, *903*, 146602. https://doi.org/10.1016/j.msea.2024.146602.

(64) Li, H.; Wen, G.; Cai, Z.; Feng, Y.; Ma, L.; Han, A.; Zhang, K. The Effect of Vanadium Content on Hierarchical Martensite Structure and Yield Strength of Petroleum Casing Steels. *Journal of Materials Research and Technology* **2022**, *18*, 4522–4532. https://doi.org/10.1016/j.jmrt.2022.04.129.

(65) Jing, T.; Ning, Y. T.; Liu, H. L.; Yang, B.; Chen, Y. Effect of Vanadium on Austenite Grain Refinement and Martensite Structure. In *Proceedings of the 6th International Conference on Advanced High Strength Steel and Press Hardening (ICHSU 2022)*; Zhang, Y., Ma, M., Eds.; Atlantis Press: Dordrecht, Netherlands, 2023; pp 36–41. https://doi.org/10.2991/978-94-6463-114-2_5.

(66) Bedekar, V.; Voothaluru, R.; Yu, D.; Wong, A.; Galindo-Nava, E.; Gorti, S. B.; An, K.; Hyde, R. S. Effect of Nickel on the Kinematic Stability of Retained Austenite in Carburized Bearing Steels - In-Situ Neutron Diffraction and Crystal Plasticity Modeling of Uniaxial Tension Tests in AISI 8620, 4320 and 3310 Steels. *International Journal of Plasticity* **2020**, *131*, 102748. https://doi.org/10.1016/j.ijplas.2020.102748.

(67) Niessen, F.; Tiedje, N. S.; Hald, J. Kinetics Modeling of Delta-Ferrite Formation and Retainment During Casting of Supermartensitic Stainless Steel. *Materials and Design* **2017**, *118*, 138–145. https://doi.org/10.1016/j.matdes.2017.01.026.

(68) Niessen, F.; Grumsen, F. B.; Hald, J.; Somers, M. A. J. Formation and Stabilization of Reverted Austenite in Supermartensitic Stainless Steel. *Metallurgical Research and Technology* **2018**, *115* (4), 1–9. https://doi.org/10.1051/metal/2018051.

(69) Tolchard, J. R.; Sømme, A.; Solberg, J. K.; Solheim, K. G. On the Measurement of Austenite in Supermartensitic Stainless Steel by X-Ray Diffraction. *Materials Characterization* **2015**, *99*, 238–242. https://doi.org/10.1016/j.matchar.2014.12.005.

(70) Slamani, F.; Thibault, D.; Verreman, Y.; Bocher, P. A New Morphology of Retained Austenite Obtained by Intercritical Tempering of 13Cr-4Ni Martensitic Stainless Steel. *Materials Characterization* **2022**, *193*, 112255. https://doi.org/10.1016/j.matchar.2022.112255.

(71) Shirazi, H.; Miyamoto, G.; Hossein Nedjad, S.; Chiba, T.; Nili Ahmadabadi, M.; Furuhara, T. Microstructure Evolution During Austenite Reversion in Fe-Ni Martensitic Alloys. *Acta Materialia* **2018**, *144*, 269–280. https://doi.org/10.1016/j.actamat.2017.10.068.

(72) Rodrigues, C. A. D.; Bandeira, R. M.; Duarte, B. B.; Tremiliosi-Filho, G.; Roche, V.; Jorge, A. M. The Influence of Ni Content on the Weldability, Mechanical, and Pitting Corrosion Properties of a High-Nickel-Bearing Supermartensitic Stainless Steel. *Journal of Materials Engineering and Performance* **2021**, *30* (4), 3044–3053. https://doi.org/10.1007/s11665-021-05600-y.

(73) Godin, S.; Hamel-Akré, J.; Thibault, D.; Serventi, A. M.; Bocher, P. Ni and Mn Enrichment Effects on Reformed Austenite: Thermodynamical and Low Cycle Fatigue Stability of 13%Cr–4%Ni and 13%Cr–6%Ni Stainless Steels. *SN Applied Sciences* **2020**, *2* (3), 382. https://doi.org/10.1007/s42452-020-2180-y.

(74) Klueh, R. L.; Maziasz, P. J.; Lee, E. H. Manganese as an Austenite Stabilizer in Fe-Cr-Mn-C Steels. *Materials Science and Engineering A* **1988**, *102* (1), 115–124. https://doi.org/10.1016/0025-5416(88)90539-3.

(75) Folkhard, E. *Welding Metallurgy of Stainless Steels*, 1st ed.; Springer: Vienna, Austria, 1988.

(76) Grange, R. A.; Hribal, C. R.; Porter, L. F. Hardness of Tempered Martensite in Carbon and Low-Alloy Steels. *Metallurgical Transactions A* **1977**, *8* (11), 1775–1785. https://doi.org/10.1007/BF02646882.

(77) Raghavan, V. *Physical Metallurgy: Principles and Practice*, 2nd ed.; PHI: New Delhi, India, 2012.

(78) Seetharaman, S.; McLean, A.; Guthrie, R. I. L.; Sridhar, S. *Treatise on Process Metallurgy: Industrial Processes*, 1st ed.; Elsevier: Oxford, UK, 2014.

(79) Bain, E. C. *Functions of the Alloying Elements in Steel*, 1st ed.; American Society for Metals: Cleveland, OH, 1939.

(80) Navarro-López, A.; Sietsma, J.; Santofimia, M. J. Effect of Prior Athermal Martensite on the Isothermal Transformation Kinetics Below Ms in a Low-C High-Si Steel. *Metallurgical and Materials Transactions A* **2016**, *47* (3), 1028–1039. https://doi.org/10.1007/s11661-015-3285-6.

(81) Bhadeshia, H. K. D. H.; Honeycombe, R. W. K. *Steels Structure, Properties and Design*, 5th ed.; Elsevier: Cambridge, MA, 2024.

(82) Jaffee, R. I.; Wilcox, B. A. *Fundamental Aspects of Structural Alloy Design*, 1st ed.; Springer US: Boston, MA, 1977. https://doi.org/10.1007/978-1-4684-2421-8.

(83) Durand-Charre, M. *Microstructure of Steels and Cast Irons*, 1st ed.; Derby, B., Series Ed.; Springer Berlin Heidelberg: Berlin, Germany, 2004. https://doi.org/10.1007/978-3-662-08729-9.

(84) Pickering, F. B. High Strength Low Alloy Steels. In *Materials Science and Technology: A Comprehensive Treatment Volume 7: Constitution and Properties of Steels*; Pickering, F. B., Ed.; Wiley: Weinheim, Germany, 1992; pp 335–399.

(85) DeArdo, A. J.; Garcia, C. I.; Palmiere, E. J. Thermomechanical Processing of Steels. In *ASM Handbook Volume 4: Heat treatment*; ASM International: Materials Park, OH, 1991; pp 237–255.

(86) Cohen, M.; Hansen, S. S. Microstructural Control in Microalloyed Steels. In *MiCon 78: Optimization of Processing, Properties, and Service Performance Through Microstructural Control*; ASTM International: Philadelphia, PA, 1979; pp 34–52.

(87) Yue, S. Thermomechanical Processing of Ferrous Alloys. In *ASM Handbook Volume 14A: Metalworking: Bulk Forming*; Semiatin, S. L., Ed.; ASM International: Materials Park, OH, 2005; pp 286–296. https://doi.org/10.31399/asm.hb.v14a.a0003995.

(88) Weng, Y. *Ultra-Fine Grained Steels*, 1st ed.; Springer: Beijing, China, 2009.

(89) Tamura, I.; Sekine, H.; Tanaka, T.; Ouchi, C. *Thermomechanical Processing of High-Strength Low-Alloy Steels*, 1st ed.; Butterworths: London, UK, 1988.

(90) Gottstein, G.; Shvindlerman, L. S. *Grain Boundary Migration in Metals: Thermodynamics, Kinetics, Applications*, 2nd ed.; Taylor & Francis: Boca Raton, FL, 2010.

(91) Meyers, M. A.; Chawla, K. K. *Mechanical Behavior of Materials*, 2nd ed.; Cambridge University Press: Cambridge, UK, 2008.

(92) Hall, E. O. The Deformation and Ageing of Mild Steel: III Discussion of Results. *Proceedings of the Physical Society* **1951**, *64* (9), 747–753.

(93) Petch, N. J. The Cleavage Strength of Polycrystals. *Journal of the Iron and Steel Institute* **1953**, *174*, 25–28.

(94) Hall, E. O. *Yield Point Phenomena in Metals and Alloys*, 1st ed.; Springer: New York, NY, 1970.

(95) Takaki, S. Review on the Hall-Petch Relation in Ferritic Steel. *Materials Science Forum* **2010**, *654–656*, 11–16. https://doi.org/10.4028/www.scientific.net/MSF.654-656.11.

(96) Takaki, S. Influence of Alloying Elements on the Hall-Petch Coefficient in Ferritic Steel. *Materials Science Forum* **2012**, *706–709*, 181–185. https://doi.org/10.4028/www.scientific.net/MSF.706-709.181.

(97) Sevillano, J. G.; van Houtte, P.; Aernoudt, E. Large Strain Work Hardening and Textures. *Progress in Materials Science* **1980**, *25* (2–4), 69–134. https://doi.org/10.1016/0079-6425(80)90001-8.

(98) Vander Voort, G. F. Quantitative Metallography. In *Materials Characterization*; ASM International: Materials Park, OH, 2019; pp 528–540. https://doi.org/10.31399/asm.hb.v10.a0006682.

(99) Underwood, E. E. *Quantitative Stereology*, 1st ed.; Addison-Wesley: Reading, MA, 1970.

(100) Speich, G. R.; Cuddy, L. J.; Gordon, C. R.; DeArdo, A. J. Formation of Ferrite from Controlled-Rolled Austenite. In *Phase Transformations in Ferrous Alloys: Proceedings of an International Conference*; Metallurgical Society of AIME: Warrendale, PA, 1984; pp 341–390.

(101) Ouchi, C.; Sampei, T.; Kozasu, I. The Effect of Hot Rolling Condition and Chemical Composition on the Onset Temperature of γ-α Transformation After Hot Rolling. *Transactions of the Iron and Steel Institute of Japan* **1982**, *22* (3), 214–222. https://doi.org/10.2355/isijinternational1966.22.214.

(102) Humphreys, F. J.; Rohrer, G. S.; Rollett, A. *Recrystallization and Related Annealing Phenomena*, 3rd ed.; Elsevier: Amsterdam, Netherlands, 2017.

(103) Huang, K.; Logé, R. E. A Review of Dynamic Recrystallization Phenomena in Metallic Materials. *Materials & Design* **2016**, *111*, 548–574. https://doi.org/10.1016/j.matdes.2016.09.012.

(104) Dieter, G. E. *Mechanical Metallurgy*, 1st ed.; McGraw-hill: New York, NY, 1961.

(105) Honeycombe, R. W. K. *The Plastic Deformation of Metals*, 2nd ed.; Edward Arnold: London, UK, 1984.

(106) Gottstein, G. *Physical Foundations of Materials Science*, 1st ed.; Springer: New York, NY, 2004. https://doi.org/10.1007/978-3-662-09291-0.

(107) Ebrahimi, G. R.; Keshmiri, H.; Maldad, A. R.; Momeni, A. Dynamic Recrystallization Behavior of 13%Cr Martensitic Stainless Steel under Hot Working Condition. *Journal of Materials Science & Technology* **2012**, *28* (5), 467–473. https://doi.org/10.1016/S1005-0302(12)60084-X.

(108) Zener, C.; Smith, C. Grains, Phases and Interfaces: Interpretation of Microstructures. *Metallurgical and Materials Transactions A* **1948**, *175*, 15–51.

(109) Burke, J. Some Factors Affecting the Rate of Grain Growth in Metals. *Transactions of the American Institute of Mining Engineers* **1949**, *180*, 73–91.

(110) Balluffi, R. W.; Allen, S. M.; Carter, W. C.; Kemper, R. A. *Kinetics of Materials*, 1st ed.; J. Wiley & Sons: Hoboken, NJ, 2005.

(111) Hersent, E.; Marthinsen, K.; Nes, E. The Effect of Solute Atoms on Grain Boundary Migration: A Solute Pinning Approach. *Metallurgical and Materials Transactions A* **2013**, *44* (7), 3364–3375. https://doi.org/10.1007/s11661-013-1690-2.

(112) Sevillano, J. G.; van Houtte, P.; Aernoudt, E. Large Strain Work Hardening and Textures. *Progress in Materials Science* **1980**, *25* (1–2), 135–221. https://doi.org/10.1016/0079-6425(80)90001-8.

(113) Derazkola, H. A.; García Gil, E.; Murillo-Marrodán, A.; Méresse, D. Review on Dynamic Recrystallization of Martensitic Stainless Steels during Hot Deformation: Part I—Experimental Study. *Metals* **2021**, *11* (4), 572. https://doi.org/10.3390/met11040572.

(114) Akhmed'yanov, A. M.; Rushchits, S. V.; Smirnov, M. A. Hot Deformation of Martensitic and Supermartensitic Stainless Steels. *Materials Science Forum* **2016**, *870*, 259–264. https://doi.org/10.4028/www.scientific.net/MSF.870.259.

(115) Hillert, M. On the Theory of Normal and Abnormal Grain Growth. *Acta Metallurgica* **1965**, *13* (3), 227–238. https://doi.org/10.1016/0001-6160(65)90200-2.

(116) Toda-Caraballo, I.; Capdevila, C.; Pimentel, G.; De Andrés, C. G. Drag Effects on Grain Growth Dynamics. *Computational Materials Science* **2013**, *68*, 95–106. https://doi.org/10.1016/j.commatsci.2012.10.012.

(117) Singh, R. *Applied Welding Engineering: Processes, Codes, and Standards*, 3rd ed.; Butterworth-Heinemann: Oxford, UK, 2020.

(118) Rodrigues, C. A. D.; Lorenzo, P. L. D.; Sokolowski, A.; Barbosa, C. A.; Rollo, J. M. D. A. Titanium and Molybdenum Content in Supermartensitic Stainless Steel. *Materials Science and Engineering A* **2007**, *460–461*, 149–152. https://doi.org/10.1016/j.msea.2007.01.016.

(119) Totten, G. E. *Steel Heat Treatment: Metallurgy and Technologies*, 2nd ed.; CRC Press: Boca Raton, FL, 2006.

(120) Campbell, F. C. *Phase Diagrams: Understanding the Basics*, 1st ed.; ASM International: Materials Park, OH, 2012.

(121) David, F. F.; Vasconcelos, L. M. C.; Silvestre, V. A.; David, S. F. Determination of the Transformation Temperatures AR1 and AR3 for Hot Rolled CA50 Steel Rebars. *Brazilian Journal of Development* **2020**, *6* (11), 89375–89385. https://doi.org/10.34117/bjdv6n11-383.

(122) Dutta, B.; Palmiere, E. J. Effect of Prestrain and Deformation Temperature on the Recrystallization Behavior of Steels Microalloyed with Niobium. *Metallurgical and Materials Transactions A* **2003**, *34* (6), 1237–1247. https://doi.org/10.1007/s11661-003-0234-6.

(123) Romano-Acosta, L. F.; García-Rincon, O.; Pedraza, J. P.; Palmiere, E. J. Influence of Thermomechanical Processing Parameters on Critical Temperatures to Develop an Advanced High-Strength Steel Microstructure. *Journal of Materials Science* **2021**, *56* (33), 18710–18721. https://doi.org/10.1007/s10853-021-06444-6.

(124) Krauss, G. *Steels: Processing, Structure, and Performance*, 2nd ed.; ASM International: Materials Park, OH, 2015.

(125) Ericsson, T. Principles of Heat Treating of Steels. In *ASM Handbook Volume 4: Heat treatment*; ASM International: Materials Park, OH, 1991; pp 22–34.

(126) Mishiro, Y.; Yutaka, O. R410NI5 High Strength Heavy Section Stainless Steel Plate with Excellent Weldability. *Kawasaki Steel Technical Report* **1991**, *23* (1), 78–81.

(127) Vyazovkin, S.; Koga, N.; Schick, C. *Handbook of Thermal Analysis and Calorimetry. Volume 6: Recent Advances, Techniques and Applications*, 2nd ed.; Elsevier: Amsterdam, Netherlands, 2018.

(128) Zhao, J.-C. *Methods of Phase Diagram Determination*, 1st ed.; Elsevier: Oxford, UK, 2007.

(129) ASTM Committee A01. *A1033 Standard Practice for Quantitative Measurement and Reporting of Hypoeutectoid Carbon and Low-Alloy Steel Phase Transformations*; ASTM International, 2023.

(130) Loveday, M. S.; Mahon, G. J.; Roebuck, B.; Lacey, A. J.; Palmiere, E. J.; Sellers, C. M.; Van Der Winden, M. R. Measurement of Flow Stress in Hot Plane Strain Compression Tests. *Materials at High Temperatures* **2006**, *23* (2), 85–118. https://doi.org/10.3184/096034006782739394.

(131) ASTM Committee E04. *E3 Standard Guide for Preparation of Metallographic Specimens*; ASTM International, 2017. https://doi.org/10.1520/E0003-11R17.

(132) Vander Voort, G. F. Mechanical Grinding and Polishing. In *ASM Handbook Volume 9: Metallography and Microstructures*; ASM International: Materials Park, OH, 2004; pp 257–280. https://doi.org/10.31399/asm.hb.v09.a0003747.

(133) ASTM Committee E04. *E407 Standard Practice for Microetching Metals and Alloys*; ASTM International, 2015. https://doi.org/10.1520/E0407-07R15E01.

(134) Goldstein, J. I.; Newbury, D. E.; Echlin, P.; Joy, D. C.; Lyman, C. E.; Lifshin, E.; Sawyer, L.; Michael, J. R. *Scanning Electron Microscopy and X-Ray Microanalysis*, 3rd ed.; Springer US: Boston, MA, 2003. https://doi.org/10.1007/978-1-4615-0215-9.

(135) *Electron Backscatter Diffraction in Materials Science*, 2nd ed.; Schwartz, A. J., Kumar, M., Adams, B. L., Field, D. P., Eds.; Springer US: Boston, MA, 2009. https://doi.org/10.1007/978-0-387-88136-2.

(136) Collins, J.; Taylor, M.; Scarlett, A. L.; Palmiere, E. J.; Pickering, E. J. Prior Austenite Grain Measurement: A Direct Comparison of EBSD Reconstruction, Thermal Etching and Chemical Etching. *Materials Characterization* **2024**, *208*, 113656. https://doi.org/10.1016/j.matchar.2024.113656.

(137) Feng, H.; Wang, H.; Li, H.; Zhu, H.; Zhang, S.; Jiang, Z. Parent Austenite Grain Reconstruction in Martensitic Steel. *Journal of Materials Science & Technology* **2025**, *215*, 244–257. https://doi.org/10.1016/j.jmst.2024.07.032.

(138) Taylor, M.; Smith, A. D.; Donoghue, J. M.; Burnett, T. L.; Pickering, E. J. In-Situ Heating-Stage EBSD Validation of Algorithms for Prior-Austenite Grain Reconstruction in Steel. *Scripta Materialia* **2024**, *242*, 115924. https://doi.org/10.1016/j.scriptamat.2023.115924.

(139) Nyyssönen, T.; Peura, P.; Kuokkala, V.-T. Crystallography, Morphology, and Martensite Transformation of Prior Austenite in Intercritically Annealed High-Aluminum Steel. *Metallurgical and Materials Transactions A* **2018**, *49* (12), 6426–6441. https://doi.org/10.1007/s11661-018-4904-9.

(140) Niessen, F.; Nyyssönen, T.; Gazder, A. A.; Hielscher, R. Parent Grain Reconstruction from Partially or Fully Transformed Microstructures in MTEX. *Journal of Applied Crystallography* **2022**, *55* (1), 180–194. https://doi.org/10.1107/S1600576721011560.

(141) ASTM Committee E04. *ASTM E2627 Standard Practice for Determining Average Grain Size Using Electron Backscatter Diffraction (EBSD) in Fully Recrystallized Polycrystalline Materials*; ASTM International, 2019.

(142) ASTM Committee E04. *E112 Standard Test Methods for Determining Average Grain Size*; ASTM International, 2021. https://doi.org/10.1520/E0112-13R21.

(143) Bhadeshia, H. K. D. H. Length Scales and Alloys of Iron. *IOP Conference Series: Materials Science and Engineering* **2019**, *580* (1), 012002. https://doi.org/10.1088/1757-899X/580/1/012002.

(144) Higginson, R. L.; Sellars, C. M. *Worked Examples in Quantitative Metallography*, 1st ed.; Maney: London, UK, 2003.

(145) Fischer-Cripps, A. C. *Nanoindentation*, 3rd ed.; Frederick, F. L., Winer, W. O., Bergles, A. E., Klutke, G. A., Wang, K. K., Finnie, I., Welty, J. R., Bryant, M. D., Yang, H. T., Mow, V. C., Leckie, F. A., Gross, D., Series Eds.; Springer New York: New York, NY, 2011. https://doi.org/10.1007/978-1-4419-9872-9.

(146) ASTM Committee E28. *E2546 Standard Practice for Instrumented Indentation Testing*; ASTM International, 2023.

(147) ASTM Committee E28. *E8 Standard Test Methods for Tension Testing of Metallic Materials*; ASTM International, 2022. https://doi.org/10.1520/E0008_E0008M-22.

(148) Davis, J. R. *Tensile Testing*, 2nd ed.; ASM International: Materials Park, OH, 2004.

(149) Christien, F.; Telling, M. T. F.; Knight, K. S. A Comparison of Dilatometry and In-Situ Neutron Diffraction in Tracking Bulk Phase Transformations in a Martensitic Stainless Steel. *Materials Characterization* **2013**, *82*, 50–57. https://doi.org/10.1016/j.matchar.2013.05.002.

(150) Bojack, A.; Zhao, L.; Morris, P. F.; Sietsma, J. In-Situ Determination of Austenite and Martensite Formation in 13Cr6Ni2Mo Supermartensitic Stainless Steel. *Materials Characterization* **2012**, *71*, 77–86. https://doi.org/10.1016/j.matchar.2012.06.004.

(151) Roberts, W.; Ahlblom, B. A Nucleation Criterion for Dynamic Recrystallization during Hot Working. *Acta Metallurgica* **1978**, *26* (5), 801–813. https://doi.org/10.1016/0001-6160(78)90030-5.

(152) Bain, E. C.; Paxton, H. W. *Alloying Elements in Steel*, 2nd ed.; American Society for Metals: Metals Park, OH, 1961.

(153) Verhoeven, J. D. *Fundamentals of Physical Metallurgy*, 1st ed.; Wiley: New York, NY, 1975.

(154) Maresca, F.; Kouznetsova, V. G.; Geers, M. G. D.; Curtin, W. A. Contribution of Austenite-Martensite Transformation to Deformability of Advanced High Strength Steels: From Atomistic Mechanisms to Microstructural Response. *Acta Materialia* **2018**, *156*, 463–478. https://doi.org/10.1016/j.actamat.2018.06.028.

(155) Doherty, R. D.; Hughes, D. A.; Humphreys, F. J.; Jonas, J. J.; Jensen, D. J.; Kassner, M. E.; King, W. E.; McNelley, T. R.; McQueen, H. J.; Rollett, A. D. Current Issues in Recrystallization: A Review. *Materials Science and Engineering A* **1997**, *238* (2), 219–274. https://doi.org/10.1016/S0921-5093(97)00424-3.

(156) Cai, Z. H.; Ding, H.; Misra, R. D. K.; Ying, Z. Y. Austenite Stability and Deformation Behavior in a Cold-Rolled Transformation-Induced Plasticity Steel with

Medium Manganese Content. *Acta Materialia* **2015**, *84*, 229–236. https://doi.org/10.1016/j.actamat.2014.10.052.

(157) Bhattacharyya, M.; Brechet, Y.; Purdy, G. R.; Zurob, H. S. Austenite Grain Growth in High Manganese Steels. *Metallurgical and Materials Transactions A* **2019**, *50* (12), 5760–5766. https://doi.org/10.1007/s11661-019-05460-1.

(158) Birch, R. M.; Britton, T. B.; Poole, W. J. Improving Parent-Austenite Twinned Grain Reconstruction Using Electron Backscatter Diffraction in Low Carbon Austenite. *Scripta Materialia* **2025**, *257*, 116459. https://doi.org/10.1016/j.scriptamat.2024.116459.

(159) Taylor, M. D.; Choi, K. S.; Sun, X.; Matlock, D. K.; Packard, C. E.; Xu, L.; Barlat, F. Correlations between Nanoindentation Hardness and Macroscopic Mechanical Properties in DP980 Steels. *Materials Science and Engineering A* **2014**, *597*, 431–439. https://doi.org/10.1016/j.msea.2013.12.084.

(160) Gourdet, S.; Montheillet, F. A Model of Continuous Dynamic Recrystallization. *Acta Materialia* **2003**, *51* (9), 2685–2699. https://doi.org/10.1016/S1359-6454(03)00078-8.

(161) Suwas, S.; Ray, R. K. *Crystallographic Texture of Materials*, 1st ed.; Engineering Materials and Processes; Springer: London, UK, 2014.

(162) Kozłowska, A.; Stawarczyk, P.; Grajcar, A.; Radwański, K.; Matus, K.; Samek, L. Microstructure Evolution and Strain Hardening Behavior of Thermomechanically Processed Low-C High-Manganese Steels: An Effect of Deformation Temperature. *Archiv.Civ.Mech.Eng* **2023**, *23* (3), 184. https://doi.org/10.1007/s43452-023-00722-7.

(163) Peng, Y.; Liu, C.; Wang, N. Effect of Deformation on Microstructure and Mechanical Properties of Medium Carbon Steel During Heat Treatment Process. *Chinese Journal of Mechanical Engineering* **2021**, *34* (1), 113. https://doi.org/10.1186/s10033-021-00634-8.

(164) Ghazani, M. S.; Eghbali, B. Characterization of the Hot Deformation Microstructure of AISI 321 Austenitic Stainless Steel. *Materials Science and Engineering: A* **2018**, *730*, 380–390. https://doi.org/10.1016/j.msea.2018.06.025.

(165) Ren, F.; Chen, F.; Chen, J. Investigation on Dynamic Recrystallization Behavior of Martensitic Stainless Steel. *Advances in Materials Science and Engineering* **2014**, 1–16. https://doi.org/10.1155/2014/986928.

(166) Kumar, B. R.; Das, S. K.; Sharma, S.; Sahu, J. K. Effect of Thermal Cycles on Heavily Cold Deformed AISI 304L Austenitic Stainless Steel. *Materials Science and Engineering: A* **2010**, *527* (4–5), 875–882. https://doi.org/10.1016/j.msea.2009.08.075.

(167) Isao Kozasu; Chiaki Ouchi; Tetsuya Sampei; Tomoyoshi Okita. Hot Rolling as a High-Temperature Thermo-Mechanical Process. In *Proceedings of an International Symposium on High-Strength, Low-Alloy Steels*; Washington, DC, 1975; pp 120–135.

(168) Li, S.; Zhu, G.; Kang, Y. Effect of Substructure on Mechanical Properties and Fracture Behavior of Lath Martensite in 0.1C–1.1Si–1.7Mn Steel. *Journal of Alloys and Compounds* **2016**, *675*, 104–115. https://doi.org/10.1016/j.jallcom.2016.03.100.

(169) Morris, Jr., J. W. Comments on the Microstructure and Properties of Ultrafine Grained Steel. *ISIJ International* **2008**, *48* (8), 1063–1070. https://doi.org/10.2355/isijinternational.48.1063.

(170) Misra, R. D. K.; Injeti, V. S. Y.; Somani, M. C. The Significance of Deformation Mechanisms on the Fracture Behavior of Phase Reversion-Induced Nanostructured Austenitic Stainless Steel. *Sci Rep* **2018**, *8* (1), 7908. https://doi.org/10.1038/s41598-018-26352-1.

(171) Polkowski, W.; Jóźwik, P.; Bojar, Z. Electron Backscatter Diffraction Study on Microstructure, Texture, and Strain Evolution in Armco Iron Severely Deformed by the Differential Speed Rolling Method. *Metallurgical and Materials Transactions A* **2015**, *46* (5), 2216–2226. https://doi.org/10.1007/s11661-015-2760-4.

(172) Wang, N.; Zhang, Z.; Geng, J.; Chen, Y.; Wu, G.; Zhao, Q.; Zhu, L.; Luo, J. Influence of Deformation Substructure on the Strain Compatibility of Ferrite and Bainite in a Commercial Pipeline Steel. *Materials Science and Engineering: A* **2023**, *885*, 145596. https://doi.org/10.1016/j.msea.2023.145596.

(173) Taban, E.; Kaluc, E.; Ojo, O. O. Properties, Weldability and Corrosion Behavior of Supermartensitic Stainless Steels for on- and Offshore Applications. *Materials Testing* **2016**, *58* (6), 501–518. https://doi.org/10.3139/120.110884.

(174) Malik, S.; Radwan, A. B.; Al-Qahtani, N.; Abdullah, A.; Haddad, M. E.; Case, R.; Castaneda, H.; Al-Thani, N.; Bhadra, J. Focused Review on Factors Affecting Martensitic Stainless Steels and Super Martensitic Stainless Steel Passive Film in the Oil and Gas Field. *Journal of Solid State Electrochemistry* **2024**, *28* (10), 3533–3557. https://doi.org/10.1007/s10008-024-05984-6.

(175) Chen, Z.; Cao, Y.; Miao, Y.; Liu, H.; Fu, P.; Chen, Y.; Zhao, Z.; Lei, C.; Li, D. Thermo-Mechanics Driven Dynamic Recrystallization Behavior and Mechanism in High Strength Martensitic Stainless Steel. *Metallurgical and Materials Transactions A* **2023**, *54* (9), 3503–3518. https://doi.org/10.1007/s11661-023-07106-9.

(176) Sun, T.; Chen, H.; Shi, R.; Zhang, B.; Shi, H. Study on Dynamic Recrystallization Behavior and Numerical Simulation Prediction of Martensite Stainless Steel 04Cr13Ni5Mo. *Materials* **2025**, *18* (17), 4047. https://doi.org/10.3390/ma18174047.

(177) Grajcar, A.; Kozłowska, A.; Topolska, S.; Morawiec, M. Effect of Deformation Temperature on Microstructure Evolution and Mechanical Properties of Low-Carbon High-Mn Steel. *Advances in Materials Science and Engineering* **2018**, *2018* (1), 7369827. https://doi.org/10.1155/2018/7369827.

(178) Hidalgo, J.; Santofimia, M. J. Effect of Prior Austenite Grain Size Refinement by Thermal Cycling on the Microstructural Features of As-Quenched Lath Martensite. *Metallurgical and Materials Transactions A* **2016**, *47* (11), 5288–5301. https://doi.org/10.1007/s11661-016-3525-4.

(179) McQueen, H. J. Development of Dynamic Recrystallization Theory. *Materials Science and Engineering: A* **2004**, *387–389*, 203–208. https://doi.org/10.1016/j.msea.2004.01.064.

(180) Medvedeva, N. I.; Park, M. S.; Van Aken, D. C.; Medvedeva, J. E. First-Principles Study of Mn, Al and C Distribution and Their Effect on Stacking Fault Energies in Fcc Fe. *Journal of Alloys and Compounds* **2014**, *582*, 475–482. https://doi.org/10.1016/j.jallcom.2013.08.089.

(181) Pierce, D. T.; Jiménez, J. A.; Bentley, J.; Raabe, D.; Oskay, C.; Wittig, J. E. The Influence of Manganese Content on the Stacking Fault and Austenite/ε-Martensite Interfacial Energies in Fe–Mn–(Al–Si) Steels Investigated

by Experiment and Theory. *Acta Materialia* **2014**, *68*, 238–253. https://doi.org/10.1016/j.actamat.2014.01.001.

(182) Chandan, A. K.; Mishra, G.; Mahato, B.; Chowdhury, S. G.; Kundu, S.; Chakraborty, J. Stacking Fault Energy of Austenite Phase in Medium Manganese Steel. *Metall Mater Trans A* **2019**, *50* (10), 4851–4866. https://doi.org/10.1007/s11661-019-05367-x.

(183) Choi, H.-N.; Choi, J.-W.; Kang, H.; Fujii, H.; Lee, S.-J. Effect of Stacking-Fault Energy on Dynamic Recrystallization, Textural Evolution, and Strengthening Mechanism of Fe—Mn Based Twinning-Induced Plasticity (TWIP) Steels during Friction-Stir Welding. *Journal of Advanced Joining Processes* **2024**, *10*, 100236. https://doi.org/10.1016/j.jajp.2024.100236.

(184) Kim, S.-D.; Park, J. Y.; Park, S.-J.; Jang, J. H.; Moon, J.; Ha, H.-Y.; Lee, C.-H.; Kang, J.-Y.; Shin, J.-H.; Lee, T.-H. Direct Observation of Dislocation Plasticity in High-Mn Lightweight Steel by in-Situ TEM. *Scientific Report* **2019**, *9* (1), 15171. https://doi.org/10.1038/s41598-019-51586-y.

(185) Nakano, J.; Jacques, P. J. Effects of the Thermodynamic Parameters of the Hcp Phase on the Stacking Fault Energy Calculations in the Fe–Mn and Fe–Mn–C Systems. *Calphad* **2010**, *34* (2), 167–175. https://doi.org/10.1016/j.calphad.2010.02.001.

(186) Chauhan, A. K.; Goel, D. B.; Prakash, S. Solid Particle Erosion Behaviour of 13Cr–4Ni and 21Cr–4Ni–N Steels. *Journal of Alloys and Compounds* **2009**, *467* (1–2), 459–464. https://doi.org/10.1016/j.jallcom.2007.12.053.

(187) Lu, J.; Hultman, L.; Holmström, E.; Antonsson, K. H.; Grehk, M.; Li, W.; Vitos, L.; Golpayegani, A. Stacking Fault Energies in Austenitic Stainless Steels. *Acta Materialia* **2016**, *111*, 39–46. https://doi.org/10.1016/j.actamat.2016.03.042.

(188) Cotes, S. M.; Guillermet, A. F.; Sade, M. Fcc/Hcp Martensitic Transformation in the Fe-Mn System: Part II. Driving Force and Thermodynamics of the Nucleation Process. *Metallurgical and Materials Transactions A* **2004**, *35* (1), 83–91. https://doi.org/10.1007/s11661-004-0111-y.

(189) Saeed-Akbari, A.; Imlau, J.; Prahl, U.; Bleck, W. Derivation and Variation in Composition-Dependent Stacking Fault Energy Maps Based on Subregular Solution Model in High-Manganese Steels. *Metallurgical and Materials Transactions A* **2009**, *40* (13), 3076–3090. https://doi.org/10.1007/s11661-009-0050-8.

(190) Mazancová, E.; Mazanec, K. Stacking Fault Energy in High Manganese Alloys. *Materials Engineering* **2009**, *16* (2), 26–31.

(191) Morito, S.; Huang, X.; Furuhara, T.; Maki, T.; Hansen, N. The Morphology and Crystallography of Lath Martensite in Alloy Steels. *Acta Materialia* **2006**, *54* (19), 5323–5331. https://doi.org/10.1016/j.actamat.2006.07.009.

(192) Haase, C.; Kühbach, M.; Barrales-Mora, L. A.; Wong, S. L.; Roters, F.; Molodov, D. A.; Gottstein, G. Recrystallization Behavior of a High-Manganese Steel: Experiments and Simulations. *Acta Materialia* **2015**, *100*, 155–168. https://doi.org/10.1016/j.actamat.2015.08.057.

(193) Sun, B.; Aydin, H.; Fazeli, F.; Yue, S. Microstructure Evolution of a Medium Manganese Steel During Thermomechanical Processing. *Metall Mater Trans A* **2016**, *47* (4), 1782–1791. https://doi.org/10.1007/s11661-016-3338-5.

Appendix I

For transparency, accuracy, and consistency in quantifying total S_v, it is fundamental to analyze four fields-of-view of the deformed microstructure along the long transverse direction for each processing condition. Figure I.1 to Figure I.21 provide a comprehensive visual representation of this data, incorporating SEM micrographs alongside schematic diagrams that illustrate the specific processing conditions applied. Additionally, the corresponding stress-strain flow curves are provided to correlate the deformation history with the observed microstructural evolution, thereby enabling an in-depth analysis of how variations in strain and temperature influence the resulting phase transformations or morphological changes within the microstructure represented by total S_v.

In addition, for processing conditions where deformation was performed at a temperature of 800°C, another set of four fields-of-view along the short transverse direction was analyzed to ensure that the measured total S_v values accurately reflect the structural changes occurring at this deformation temperature. Figure I.22 to Figure I.30 provide a comprehensive visual representation of this data, incorporating SEM micrographs alongside schematic diagrams that illustrate the specific processing conditions applied. Additionally, the corresponding stress-strain flow curves are provided to, once again, establish a direct correlation between the deformation history and the observed microstructural evolution.

Detailed total S_v quantification along the long transverse direction, including values for each of the four fields-of-view, their calculated average, and their associated standard deviation, is systematically provided in Table I.1 to enable direct and meaningful comparison between different processing conditions, facilitating a more precise evaluation of how strain and temperature influence total S_v. In light of the significance of analyzing multiple orientations to fully capture microstructural characteristics, a detailed breakdown of total S_v quantification along the short transverse direction is presented in Table I.2. It should be emphasized that field A, field B, field C, and field D correspond to the top-left, top-right, bottom-left, and bottom-right SEM micrographs, respectively, ensuring a structured and consistent approach to the quantification process.

Table I.1 Detailed total S_v (mm^{-1}) [10^5] quantification compiling data captured from the different fields-of-view, towards the long transverse direction.

Temperature	Strain	Material Identification	Field A	Field B	Field C	Field D	Avg.	Std Dev
1150°C	0.3	BA	1.24	1.12	1.28	1.36	1.25	0.10
		BA ↗ Ni	1.52	1.52	1.56	1.60	1.55	0.04
		BA ↗ Mn	1.88	1.68	1.92	1.84	1.83	0.11
1050°C	0.6	BA	2.40	2.28	2.40	2.96	2.51	0.31
		BA ↗ Ni	3.92	3.88	4.00	3.64	3.86	0.15
		BA ↗ Mn	6.12	5.92	5.56	5.48	5.77	0.30
1050°C	0.9	BA	4.32	4.16	3.72	4.00	4.05	0.26
		BA ↗ Ni	4.88	4.64	4.76	4.96	4.81	0.14
		BA ↗ Mn	6.88	6.52	6.56	6.92	6.72	0.21
1050°C	1.2	BA	4.80	4.76	4.56	4.88	4.75	0.14
		BA ↗ Ni	5.88	5.92	5.68	5.84	5.83	0.11
		BA ↗ Mn	7.00	7.08	6.80	7.12	7.00	0.14
800°C	0.6	BA	3.88	3.68	3.72	3.40	3.67	0.20
		BA ↗ Ni	4.40	4.00	4.08	4.24	4.18	0.18
		BA ↗ Mn	6.80	6.20	6.48	6.40	6.47	0.25
800°C	0.9	BA	4.80	4.64	4.56	4.60	4.65	0.11
		BA ↗ Ni	5.56	5.60	5.24	5.56	5.49	0.17
		BA ↗ Mn	6.92	7.04	6.84	6.84	6.91	0.09
800°C	1.2	BA	5.20	5.12	5.40	4.76	5.12	0.27
		BA ↗ Ni	6.12	6.20	5.96	6.12	6.10	0.10
		BA ↗ Mn	7.16	7.12	7.12	7.32	7.18	0.10

Table I.2 Detailed total S_v (mm^{-1}) [10^5] quantification compiling data captured from the different fields-of-view, towards the short transverse direction.

Temperature	Strain	Material Identification	Field A	Field B	Field C	Field D	Avg.	Std Dev
800°C	0.6	BA	2.00	1.80	1.72	1.96	1.87	0.13
		BA ↗ Ni	2.32	1.88	2.40	2.56	22.9	0.29
		BA ↗ Mn	3.12	3.04	3.44	2.88	3.12	0.24
800°C	0.9	BA	2.44	2.32	2.12	2.56	2.36	0.19
		BA ↗ Ni	3.00	2.80	2.60	2.92	2.83	0.17
		BA ↗ Mn	3.56	3.68	3.24	3.88	3.59	0.27
800°C	1.2	BA	2.60	2.76	2.88	2.36	2.65	0.22
		BA ↗ Ni	3.32	2.60	2.96	3.00	2.97	0.29
		BA ↗ Mn	3.92	3.68	3.68	4.48	3.94	0.38

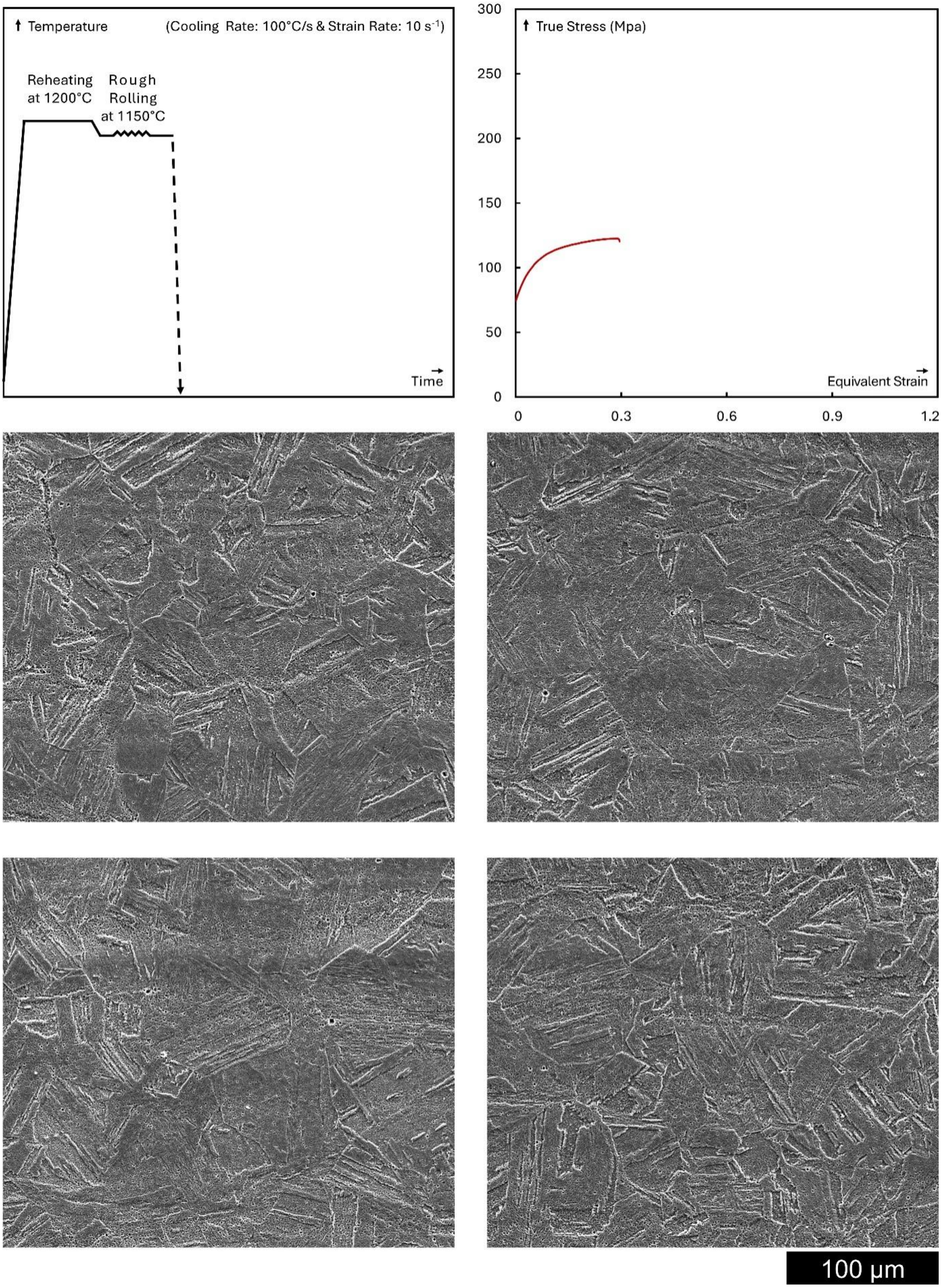

Figure I.1 SEM micrographs representing four separate fields-of-view of BA microstructure, towards the long transverse direction, deformed at 1150°C with a final strain reaching ~0.3 followed by rapid cooling at a rate of 100°C/s; the processing conditions schematic diagram along with the stress-strain flow curve are presented on top-left and top-right, respectively.

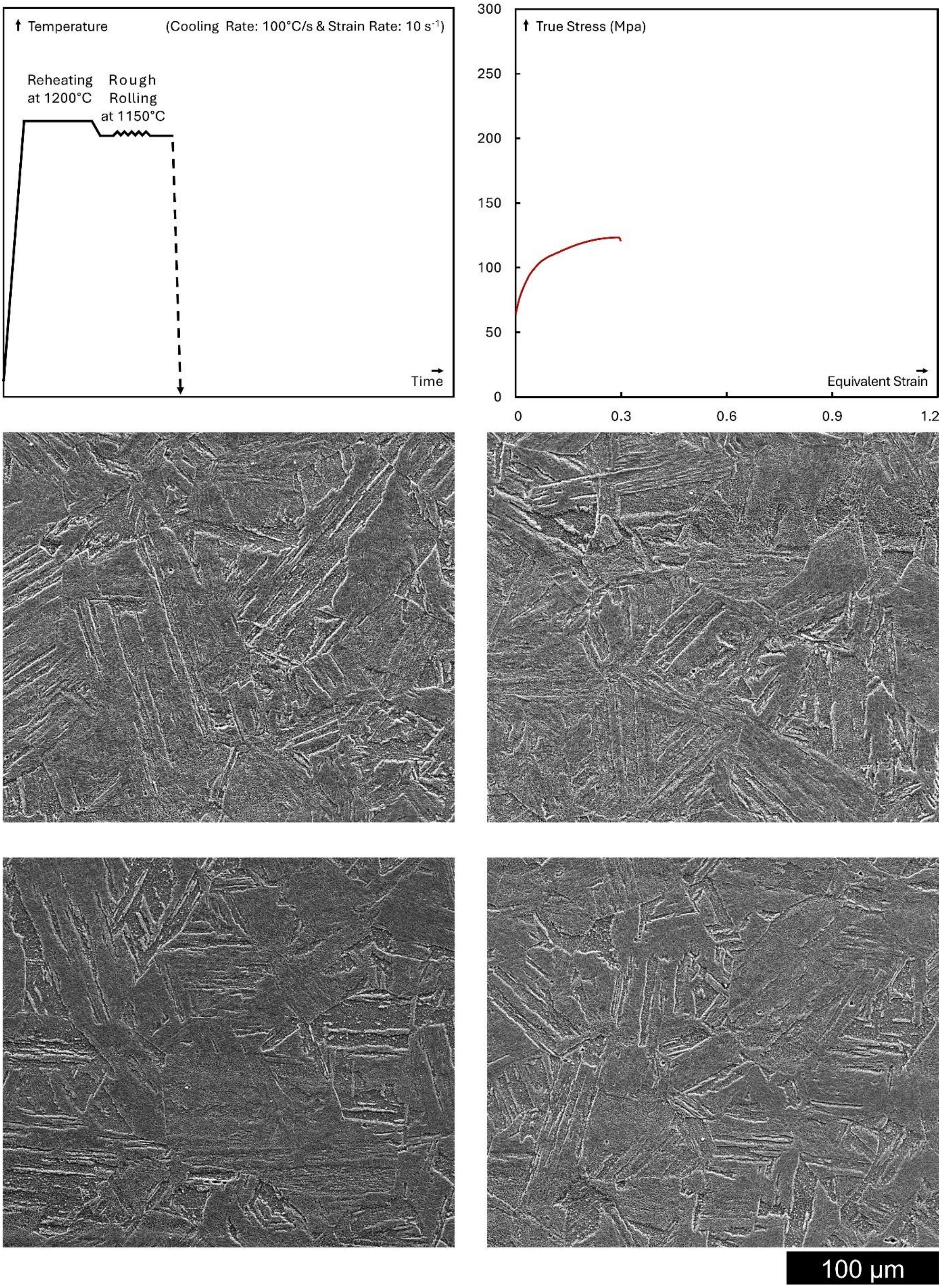

Figure I.2 SEM micrographs representing four separate fields-of-view of BA ↗ Ni microstructure, towards the long transverse direction, deformed at 1150°C with a final strain reaching ~0.3 followed by rapid cooling at a rate of 100°C/s; the processing conditions schematic diagram along with the stress-strain flow curve are presented on top-left and top-right, respectively.

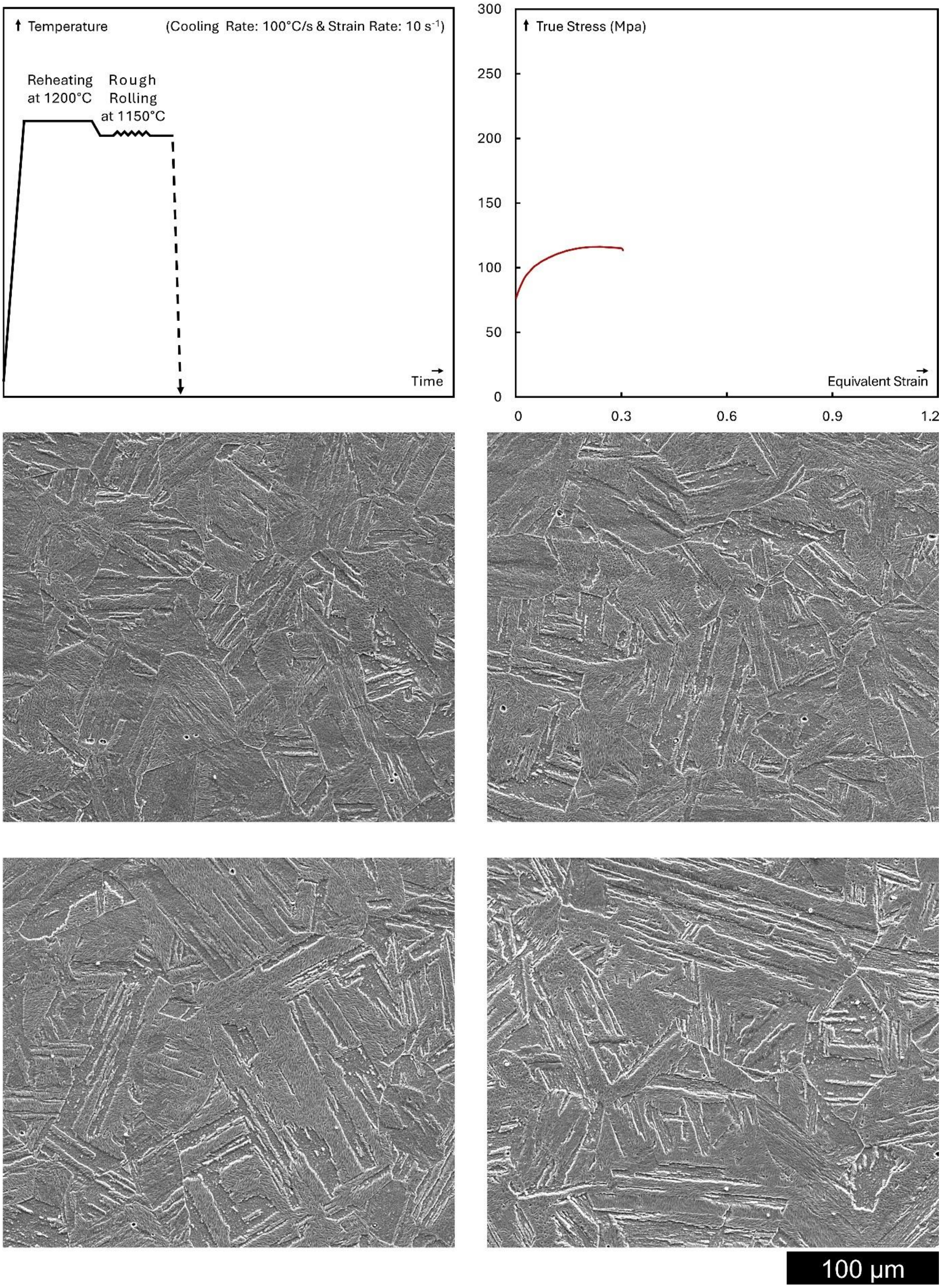

Figure I.3 SEM micrographs representing four separate fields-of-view of BA ↗ Mn microstructure, towards the long transverse direction, deformed at 1150°C with a final strain reaching ~0.3 followed by rapid cooling at a rate of 100°C/s; the processing conditions schematic diagram along with the stress-strain flow curve are presented on top-left and top-right, respectively.

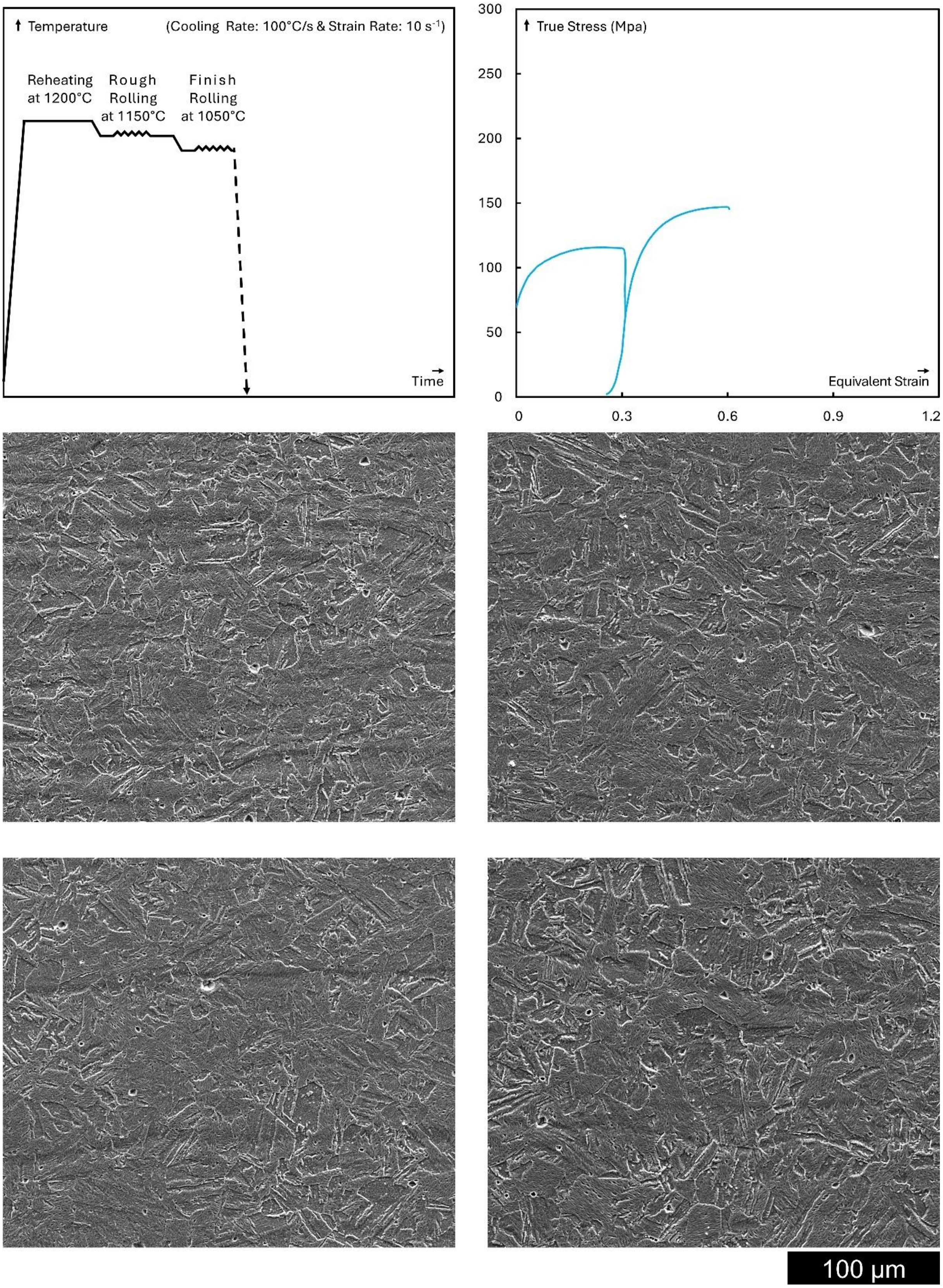

Figure I.4 SEM micrographs representing four separate fields-of-view of BA microstructure, towards the long transverse direction, deformed at 1050°C with a final strain reaching ~0.6 followed by rapid cooling at a rate of 100°C/s; the processing conditions schematic diagram along with the stress-strain flow curve are presented on top-left and top-right, respectively.

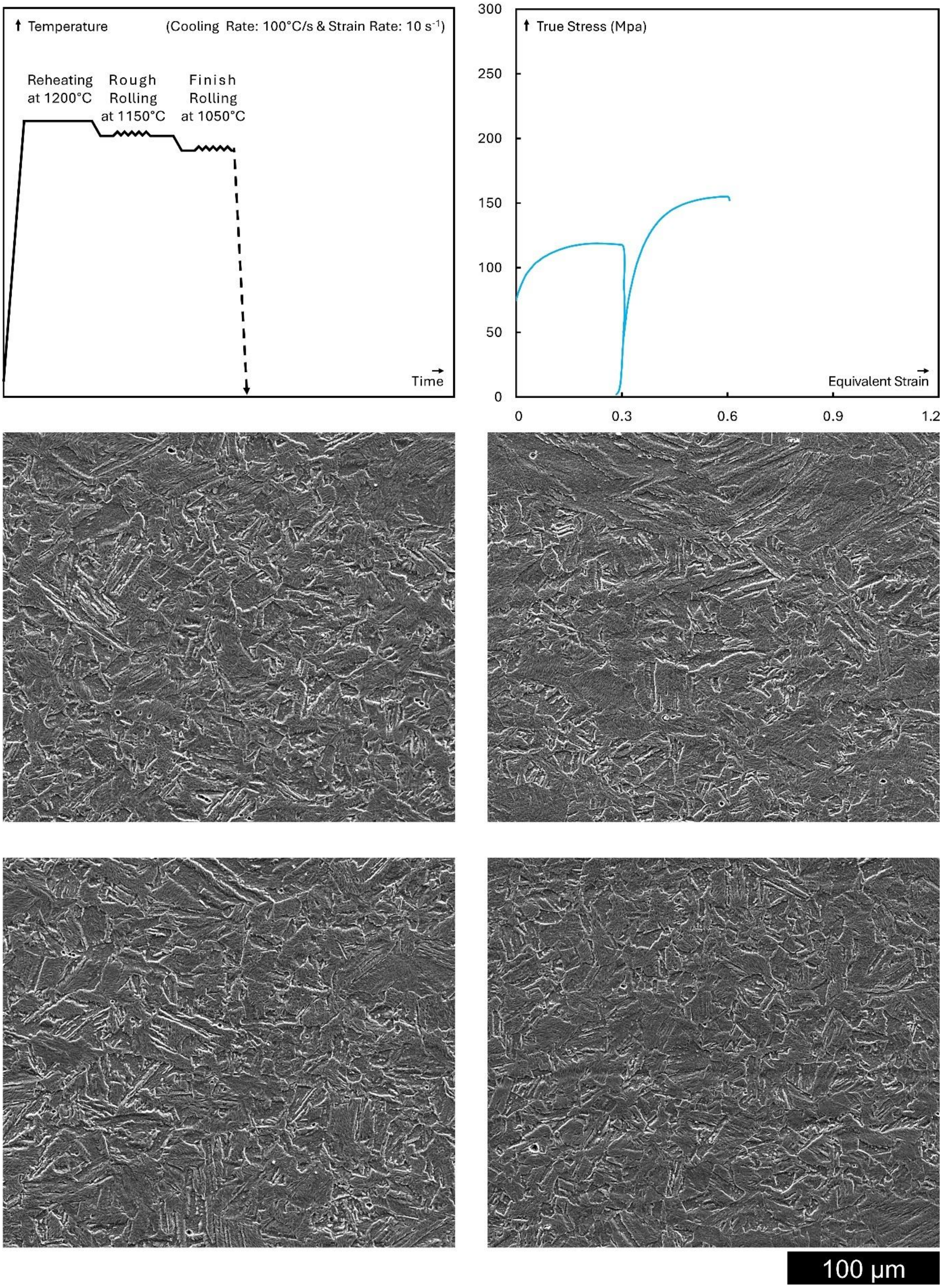

Figure I.5 SEM micrographs representing four separate fields-of-view of BA ↗ Ni microstructure, towards the long transverse direction, deformed at 1050°C with a final strain reaching ~0.6 followed by rapid cooling at a rate of 100°C/s; the processing conditions schematic diagram along with the stress-strain flow curve are presented on top-left and top-right, respectively.

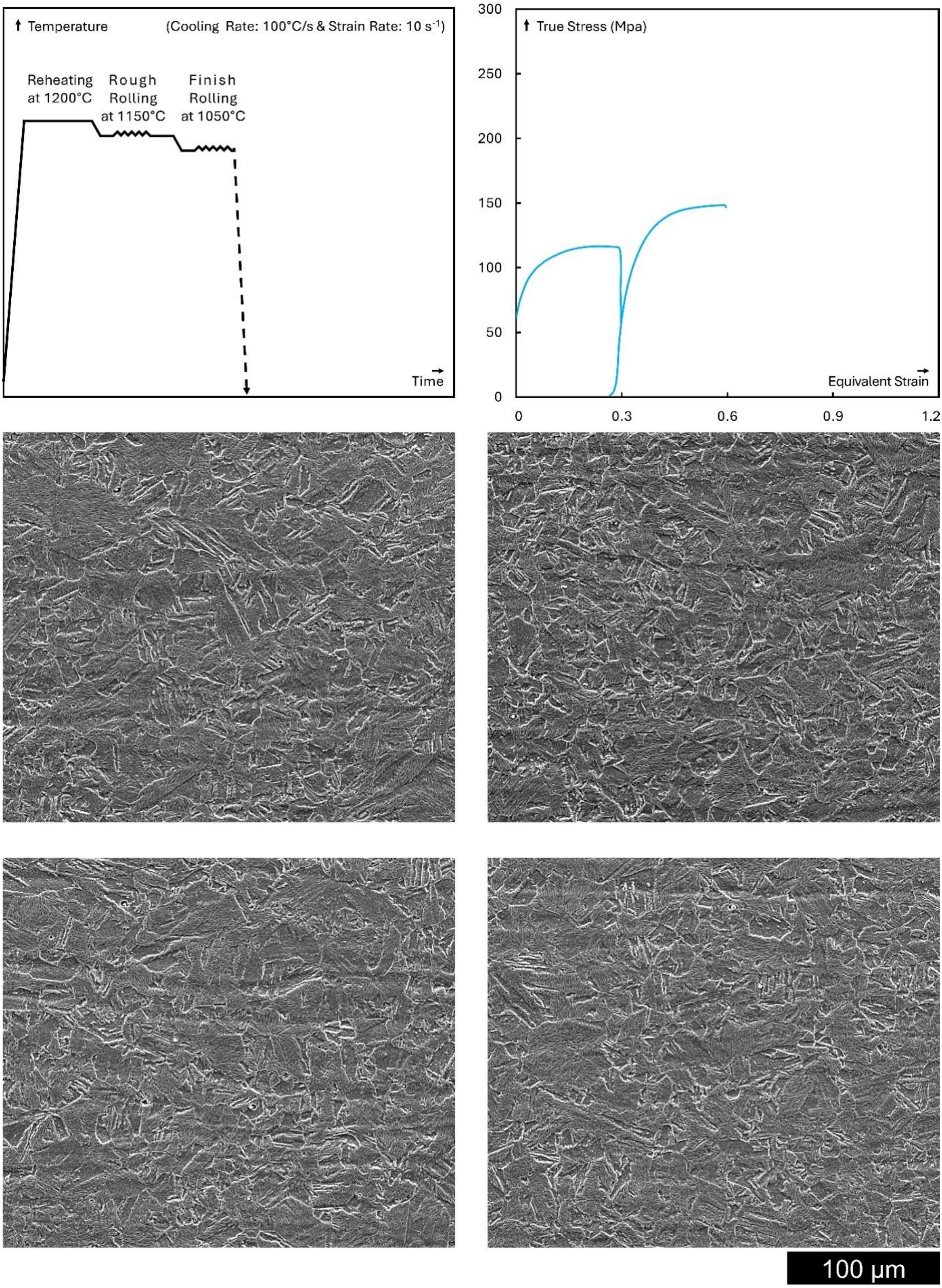

Figure I.6 SEM micrographs representing four separate fields-of-view of BA ↗ Mn microstructure, towards the long transverse direction, deformed at 1050°C with a final strain reaching ~0.6 followed by rapid cooling at a rate of 100°C/s; the processing conditions schematic diagram along with the stress-strain flow curve are presented on top-left and top-right, respectively.

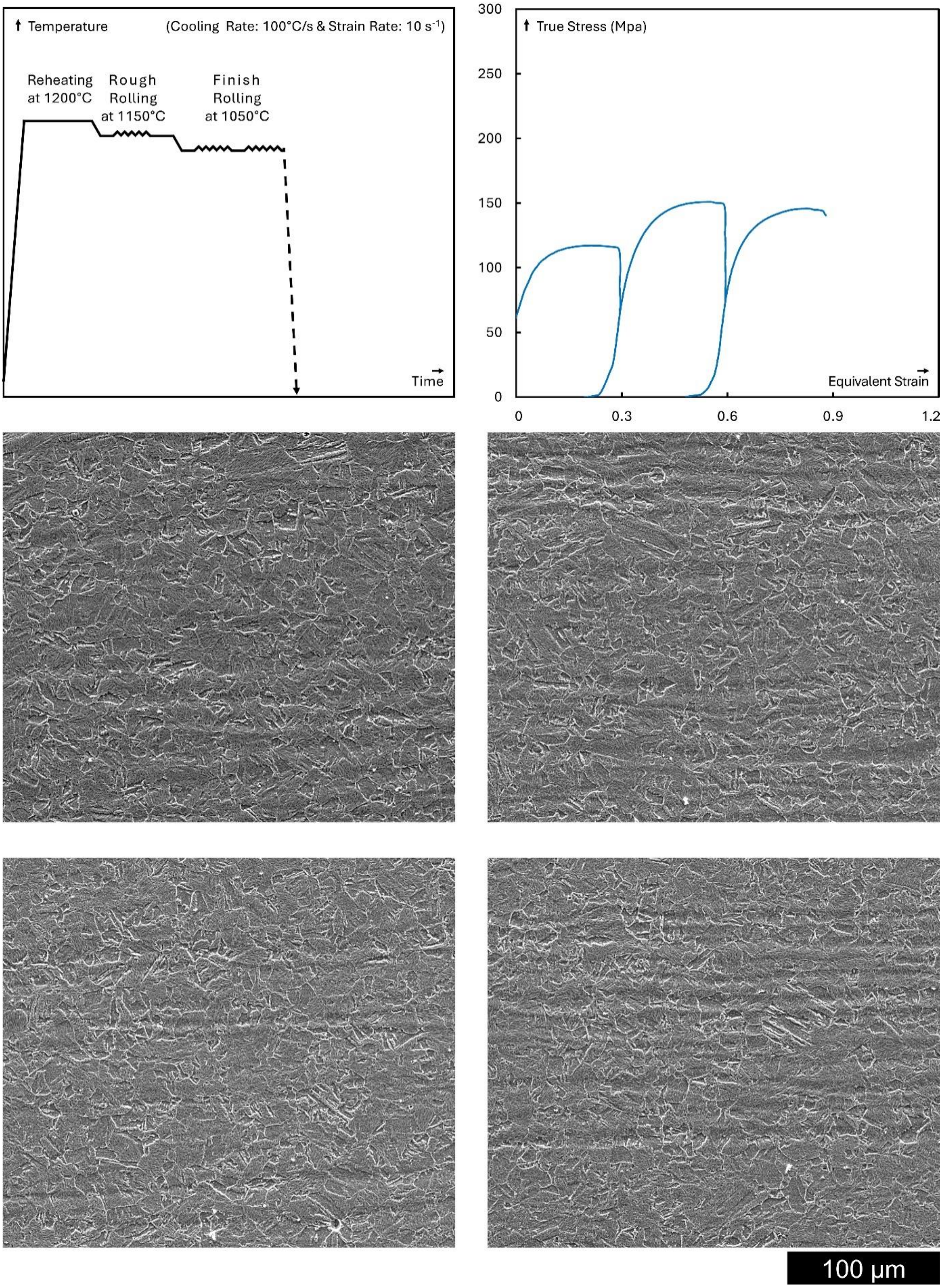

Figure I.7 SEM micrographs representing four separate fields-of-view of BA microstructure, towards the long transverse direction, deformed at 1050°C with a final strain reaching ~0.9 followed by rapid cooling at a rate of 100°C/s; the processing conditions schematic diagram along with the stress-strain flow curve are presented on top-left and top-right, respectively.

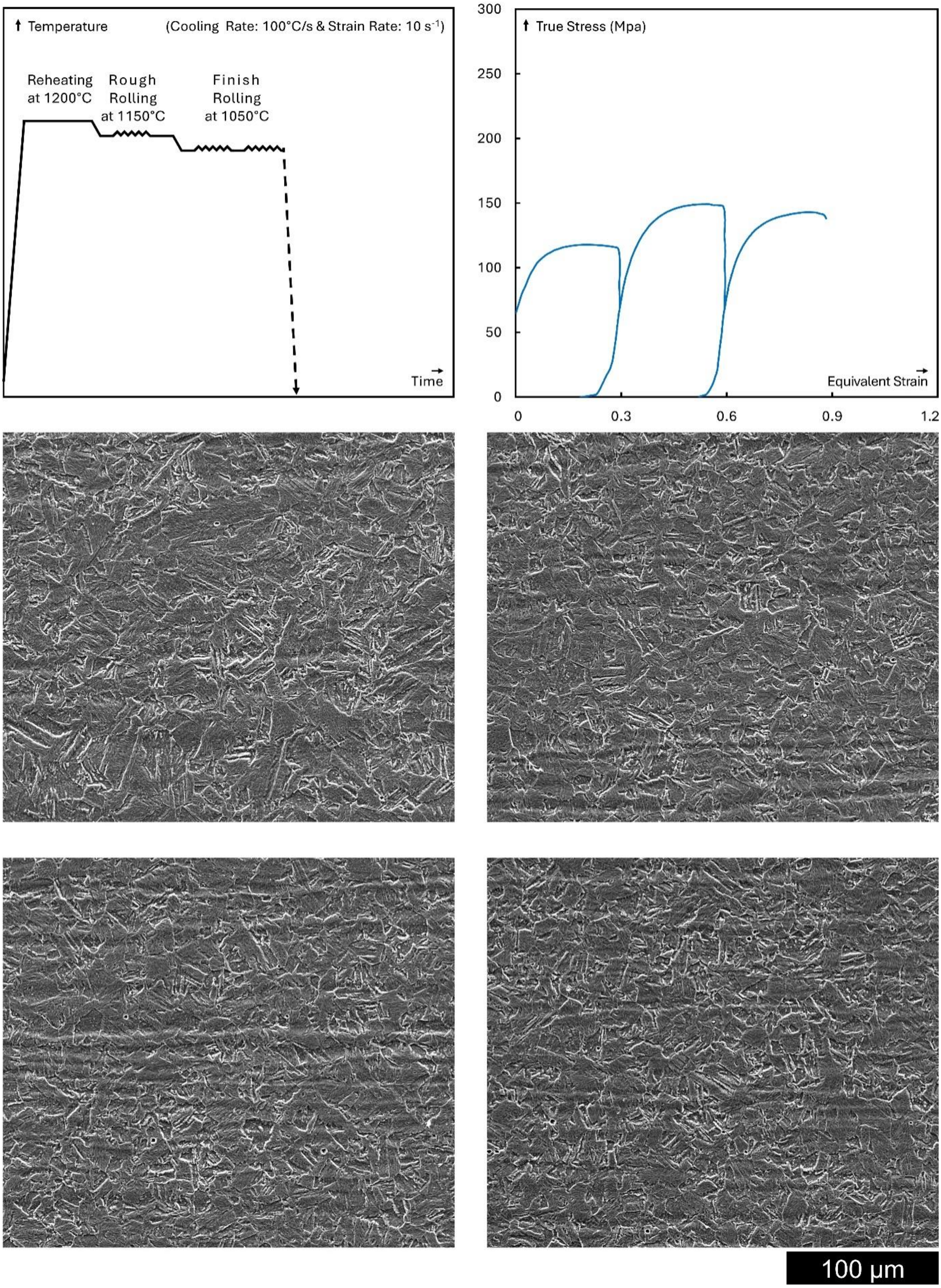

Figure I.8 SEM micrographs representing four separate fields-of-view of BA ↗ Ni microstructure, towards the long transverse direction, deformed at 1050°C with a final strain reaching ~0.9 followed by rapid cooling at a rate of 100°C/s; the processing conditions schematic diagram along with the stress-strain flow curve are presented on top-left and top-right, respectively.

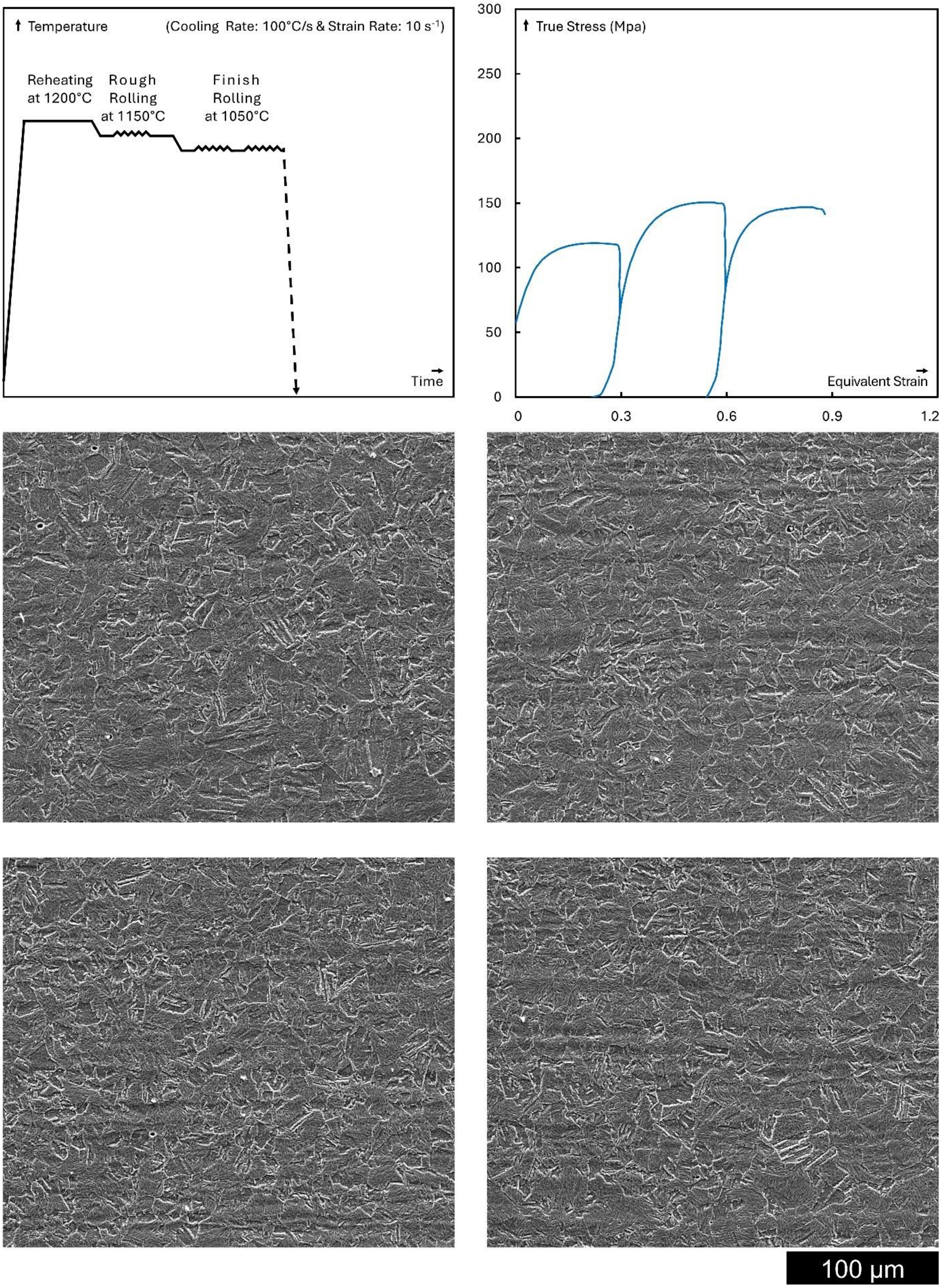

Figure I.9 SEM micrographs representing four separate fields-of-view of BA ↗ Mn microstructure, towards the long transverse direction, deformed at 1050°C with a final strain reaching ~0.9 followed by rapid cooling at a rate of 100°C/s; the processing conditions schematic diagram along with the stress-strain flow curve are presented on top-left and top-right, respectively.

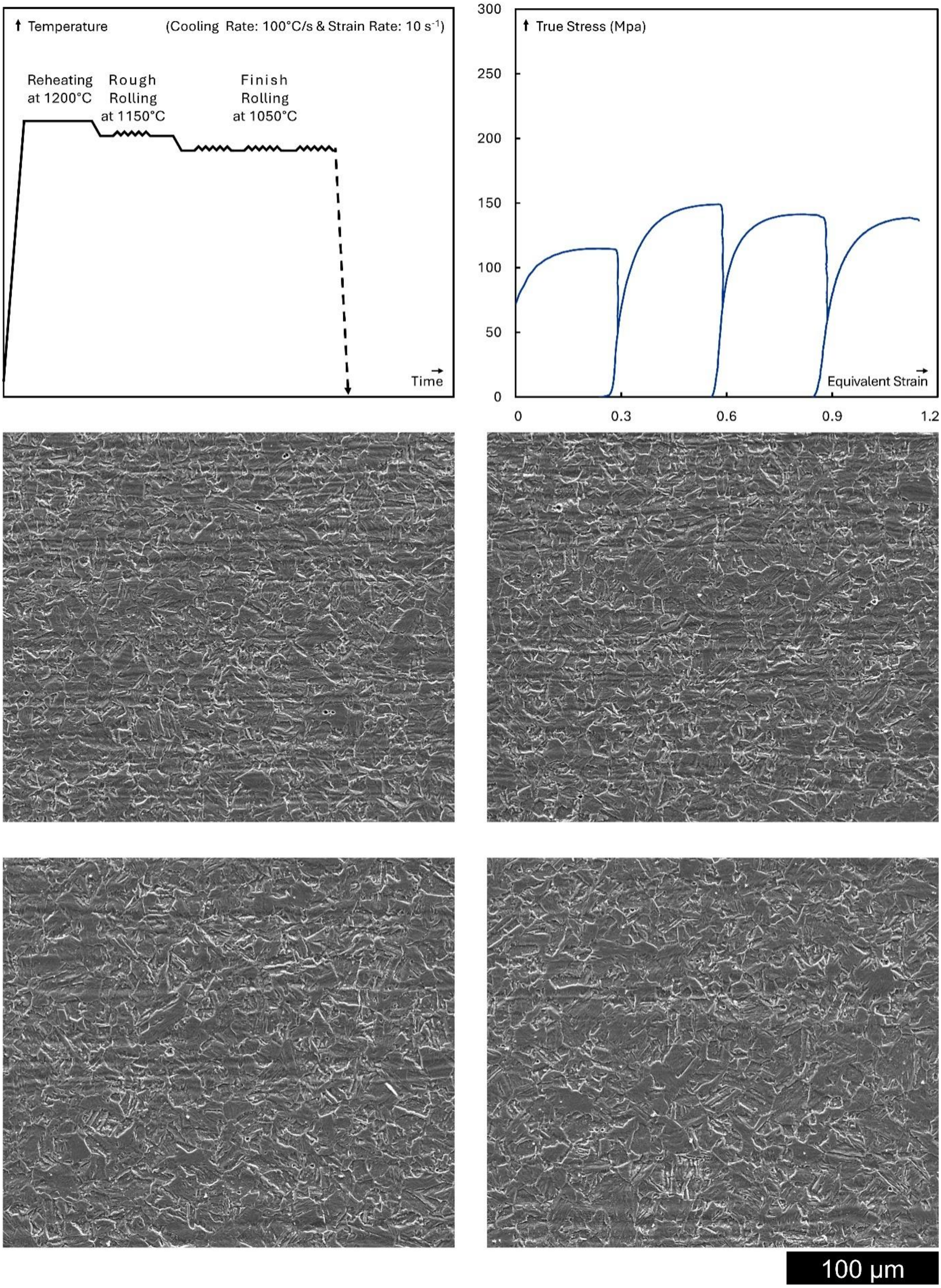

Figure I.10 SEM micrographs representing four separate fields-of-view of BA microstructure, towards the long transverse direction, deformed at 1050°C with a final strain reaching ~1.2 followed by rapid cooling at a rate of 100°C/s; the processing conditions schematic diagram along with the stress-strain flow curve are presented on top-left and top-right, respectively.

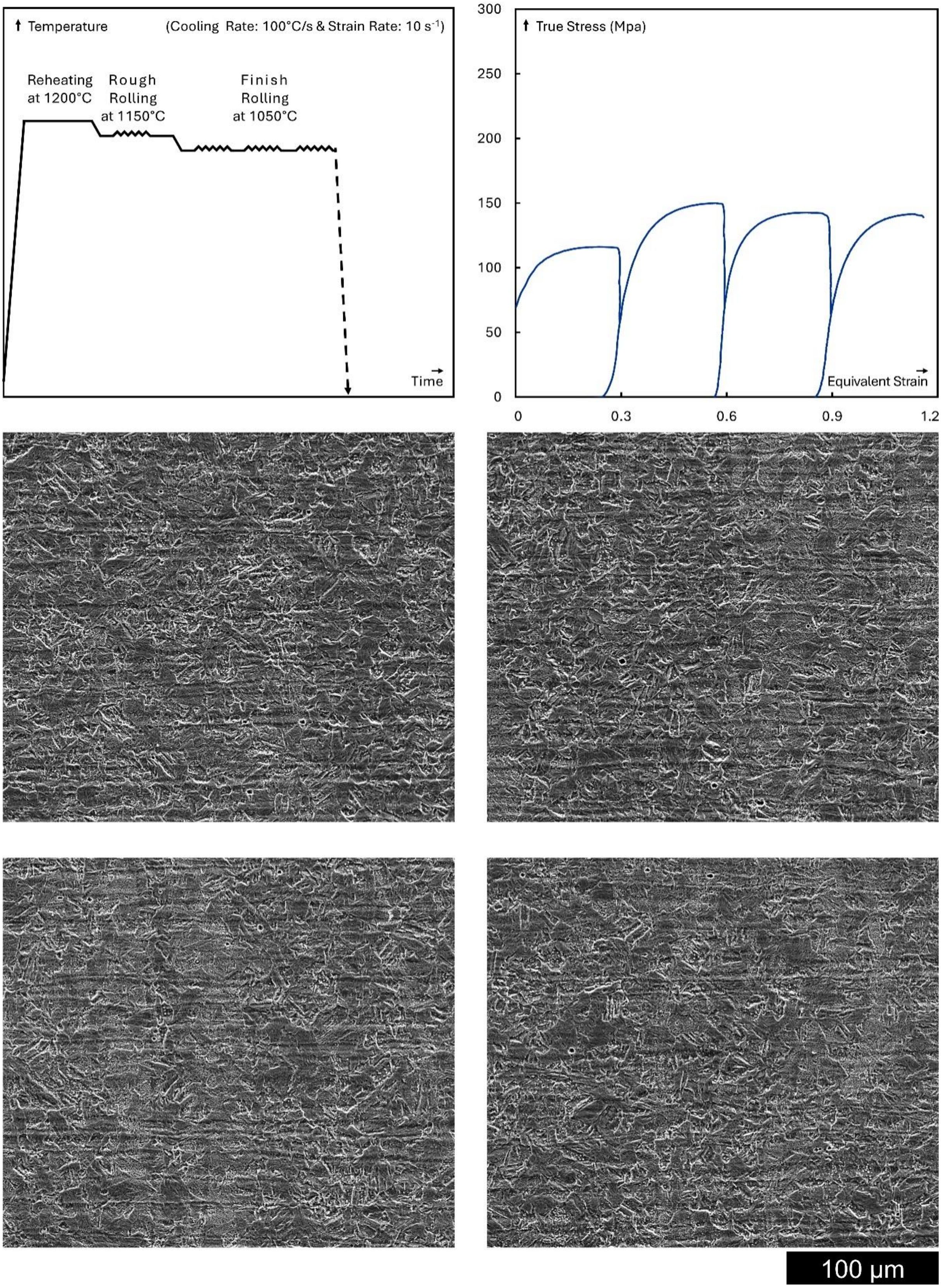

Figure I.11 SEM micrographs representing four separate fields-of-view of BA ↗ Ni microstructure, towards the long transverse direction, deformed at 1050°C with a final strain reaching ~1.2 followed by rapid cooling at a rate of 100°C/s; the processing conditions schematic diagram along with the stress-strain flow curve are presented on top-left and top-right, respectively.

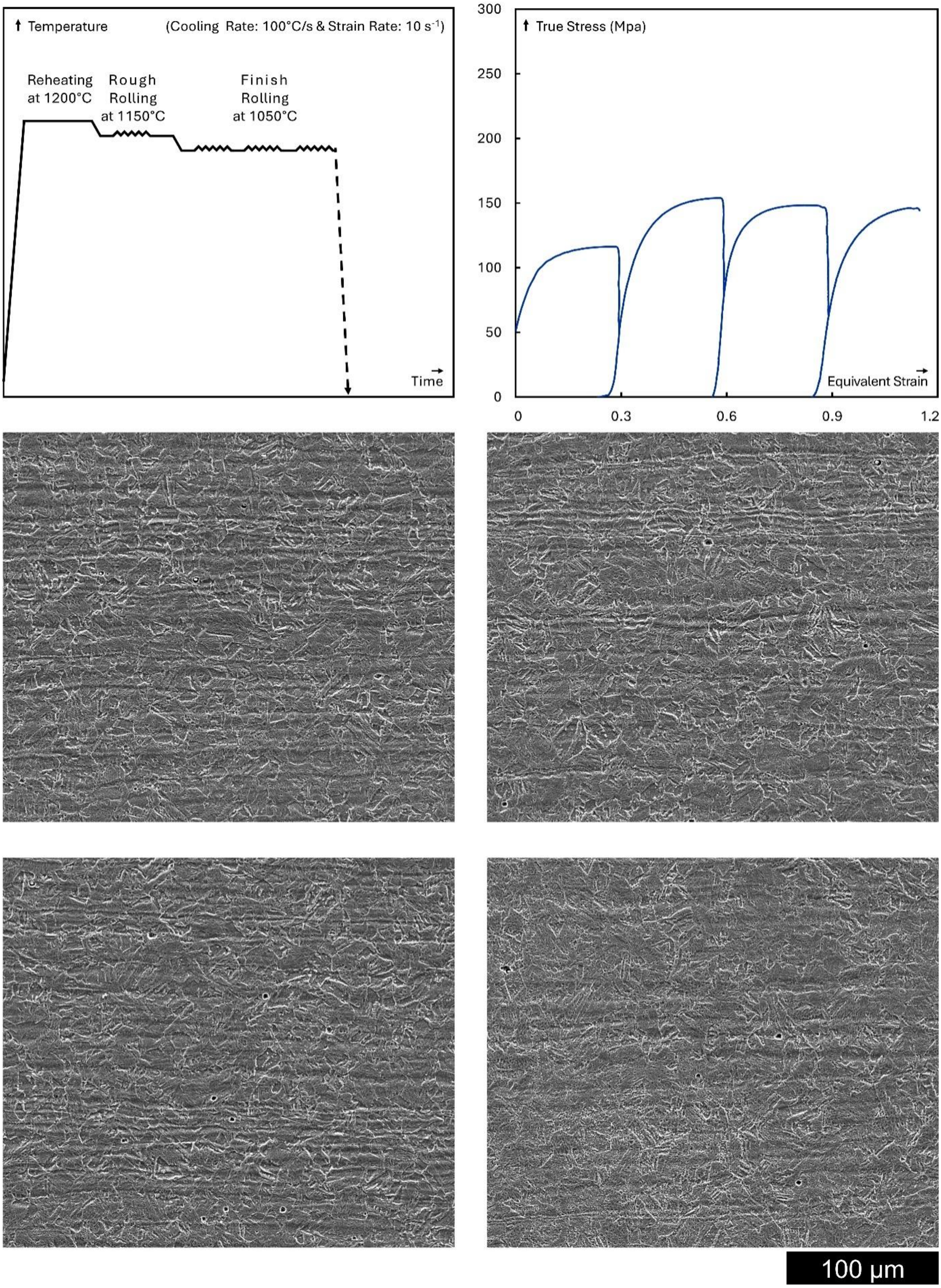

Figure I.12 SEM micrographs representing four separate fields-of-view of BA ↗ Mn microstructure, towards the long transverse direction, deformed at 1050°C with a final strain reaching ~1.2 followed by rapid cooling at a rate of 100°C/s; the processing conditions schematic diagram along with the stress-strain flow curve are presented on top-left and top-right, respectively.

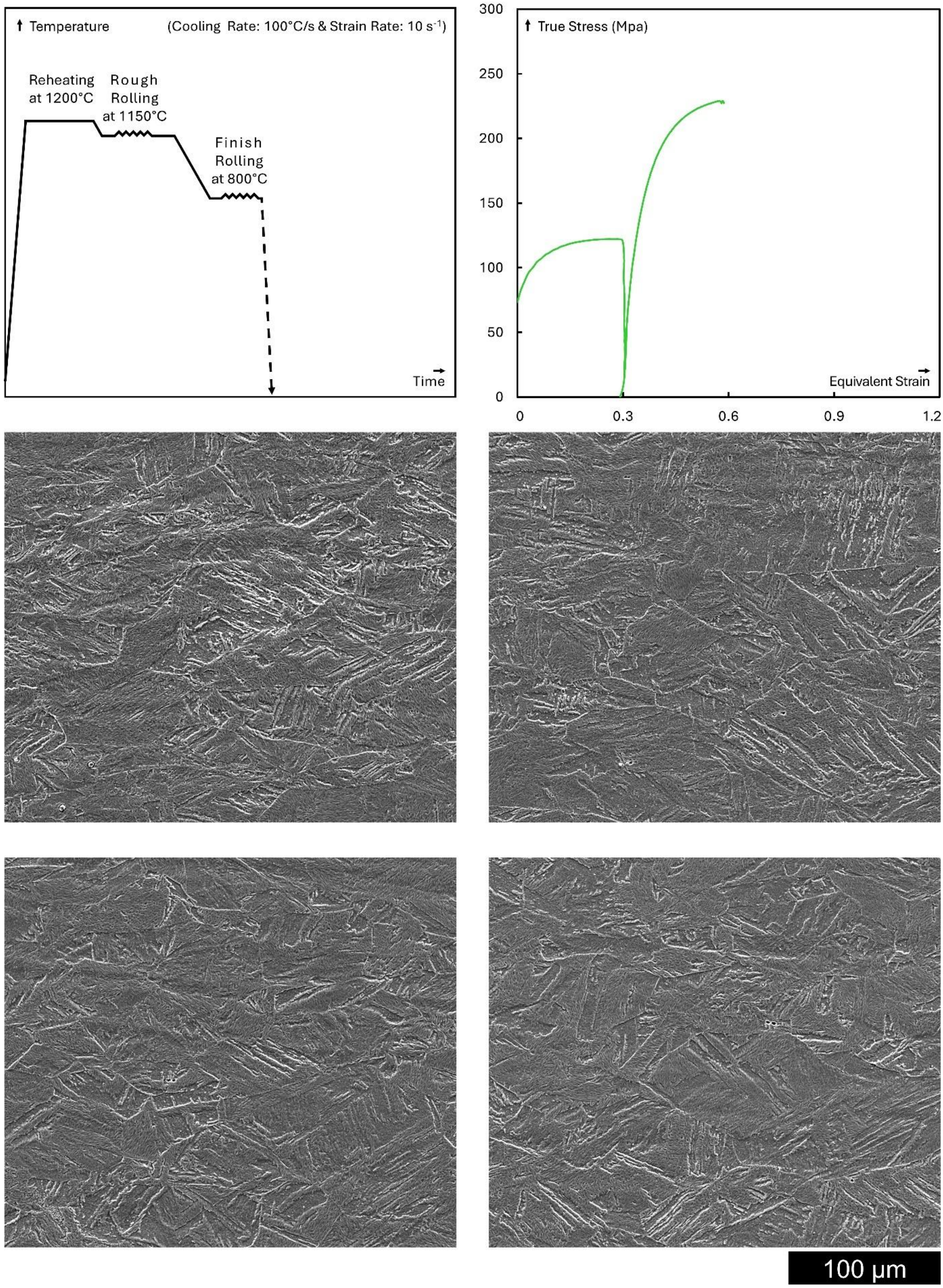

Figure I.13 SEM micrographs representing four separate fields-of-view of BA microstructure, towards the long transverse direction, deformed at 800°C with a final strain reaching ~0.6 followed by rapid cooling at a rate of 100°C/s; the processing conditions schematic diagram along with the stress-strain flow curve are presented on top-left and top-right, respectively.

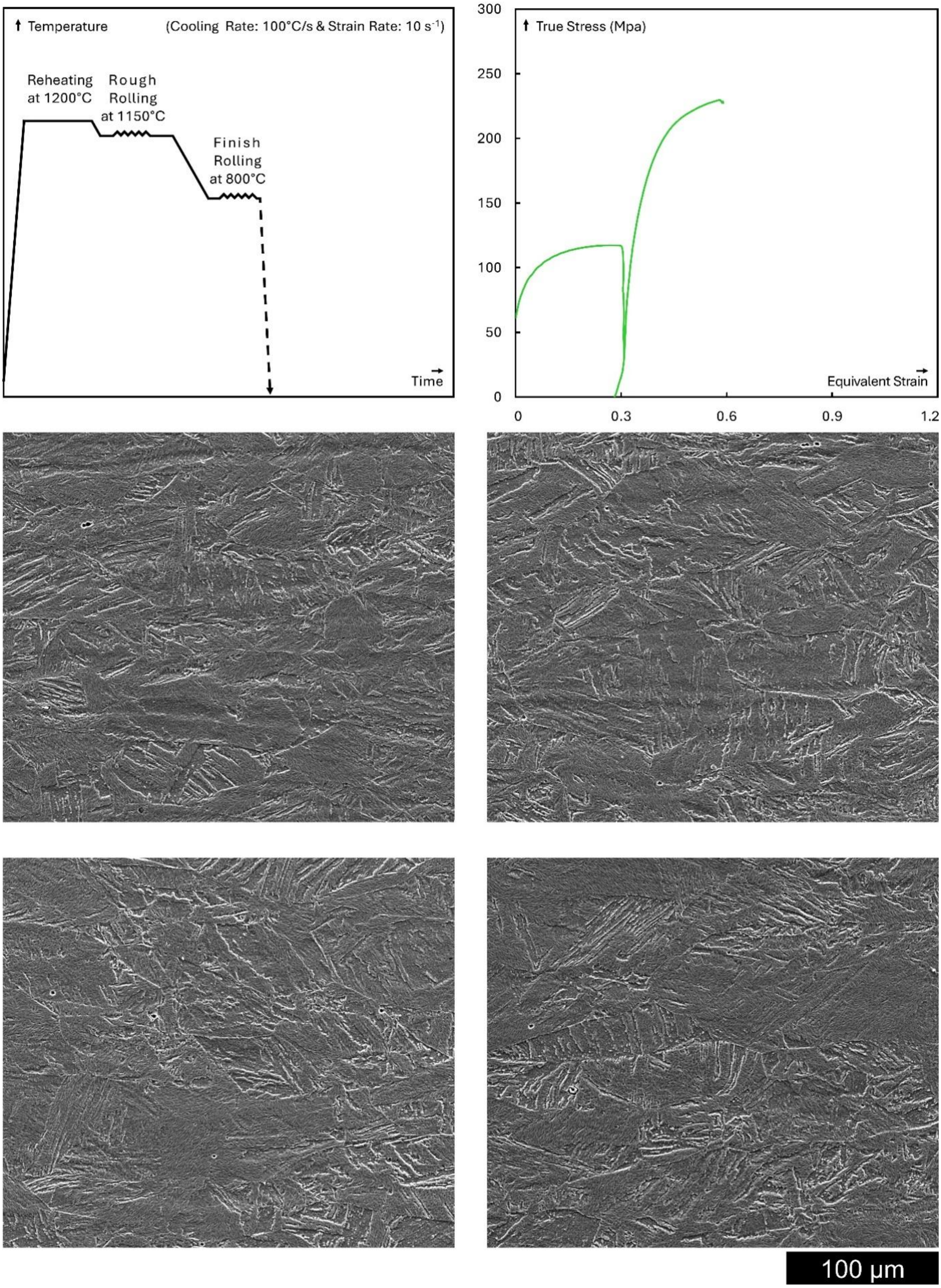

Figure I.14 SEM micrographs representing four separate fields-of-view of BA ↗ Ni microstructure, towards the long transverse direction, deformed at 800°C with a final strain reaching ~0.6 followed by rapid cooling at a rate of 100°C/s; the processing conditions schematic diagram along with the stress-strain flow curve are presented on top-left and top-right, respectively.

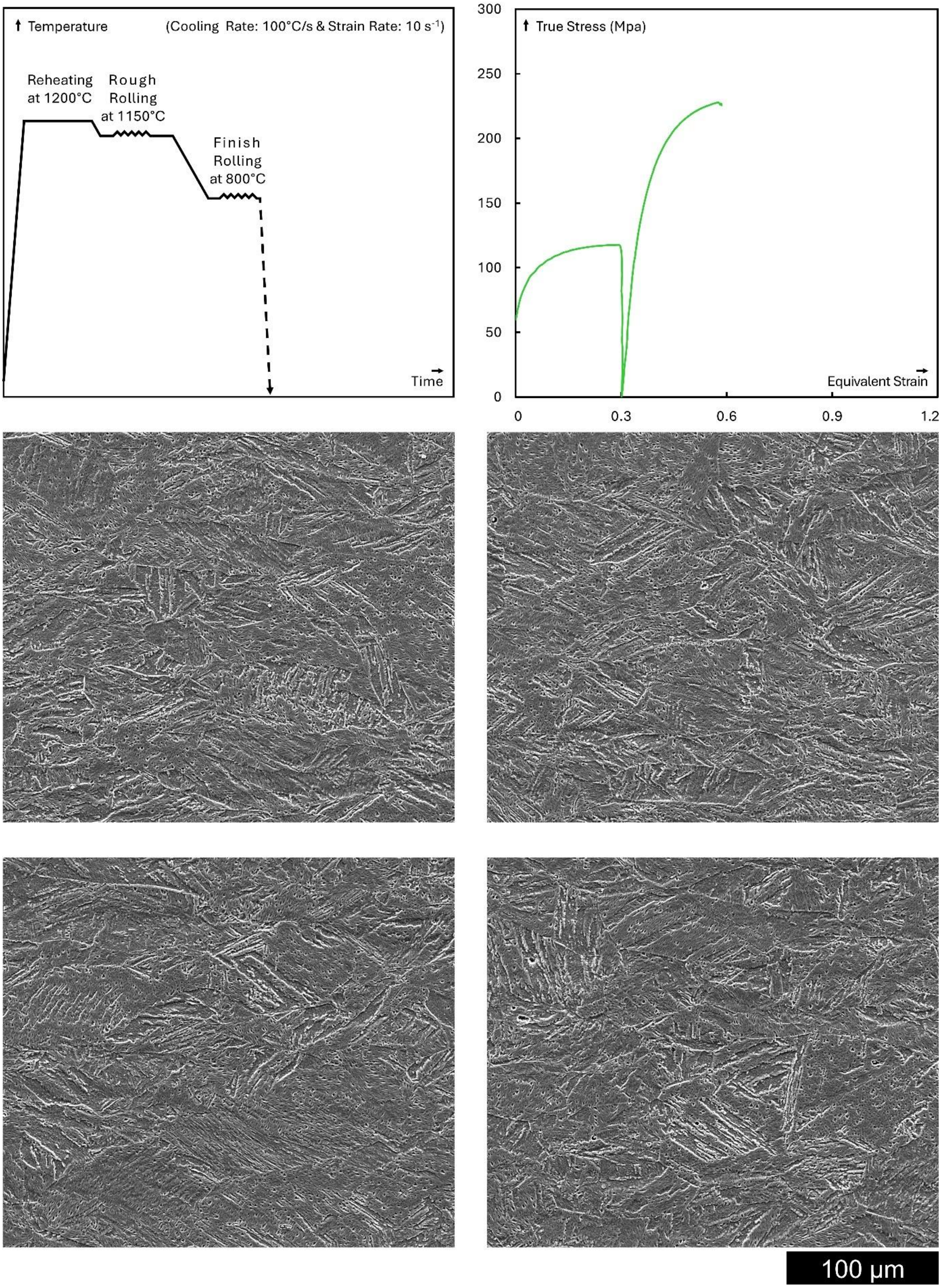

Figure I.15 SEM micrographs representing four separate fields-of-view of BA ↗ Mn microstructure, towards the long transverse direction, deformed at 800°C with a final strain reaching ~0.6 followed by rapid cooling at a rate of 100°C/s; the processing conditions schematic diagram along with the stress-strain flow curve are presented on top-left and top-right, respectively.

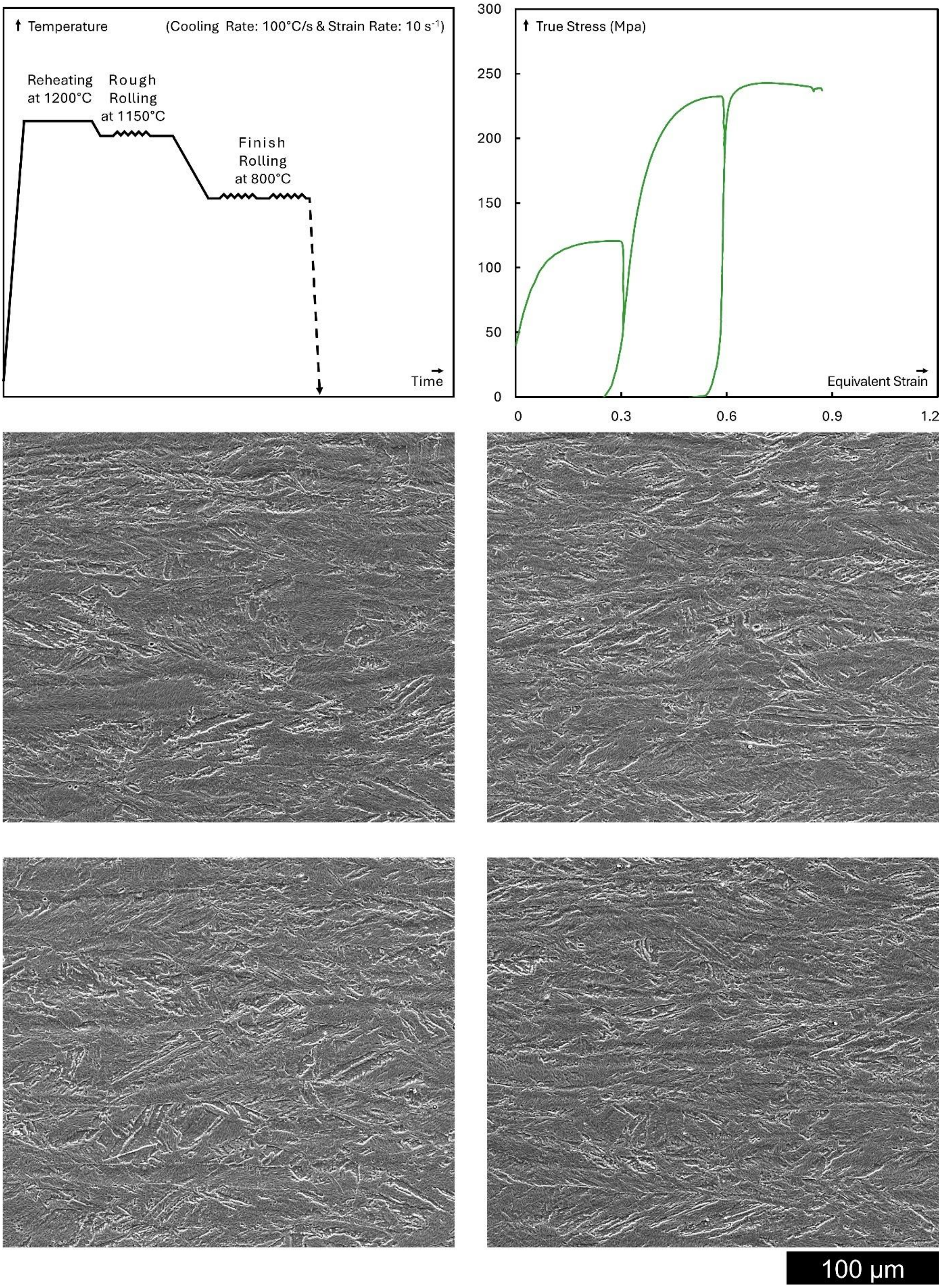

Figure I.16 SEM micrographs representing four separate fields-of-view of BA microstructure, towards the long transverse direction, deformed at 800°C with a final strain reaching ~0.9 followed by rapid cooling at a rate of 100°C/s; the processing conditions schematic diagram along with the stress-strain flow curve are presented on top-left and top-right, respectively.

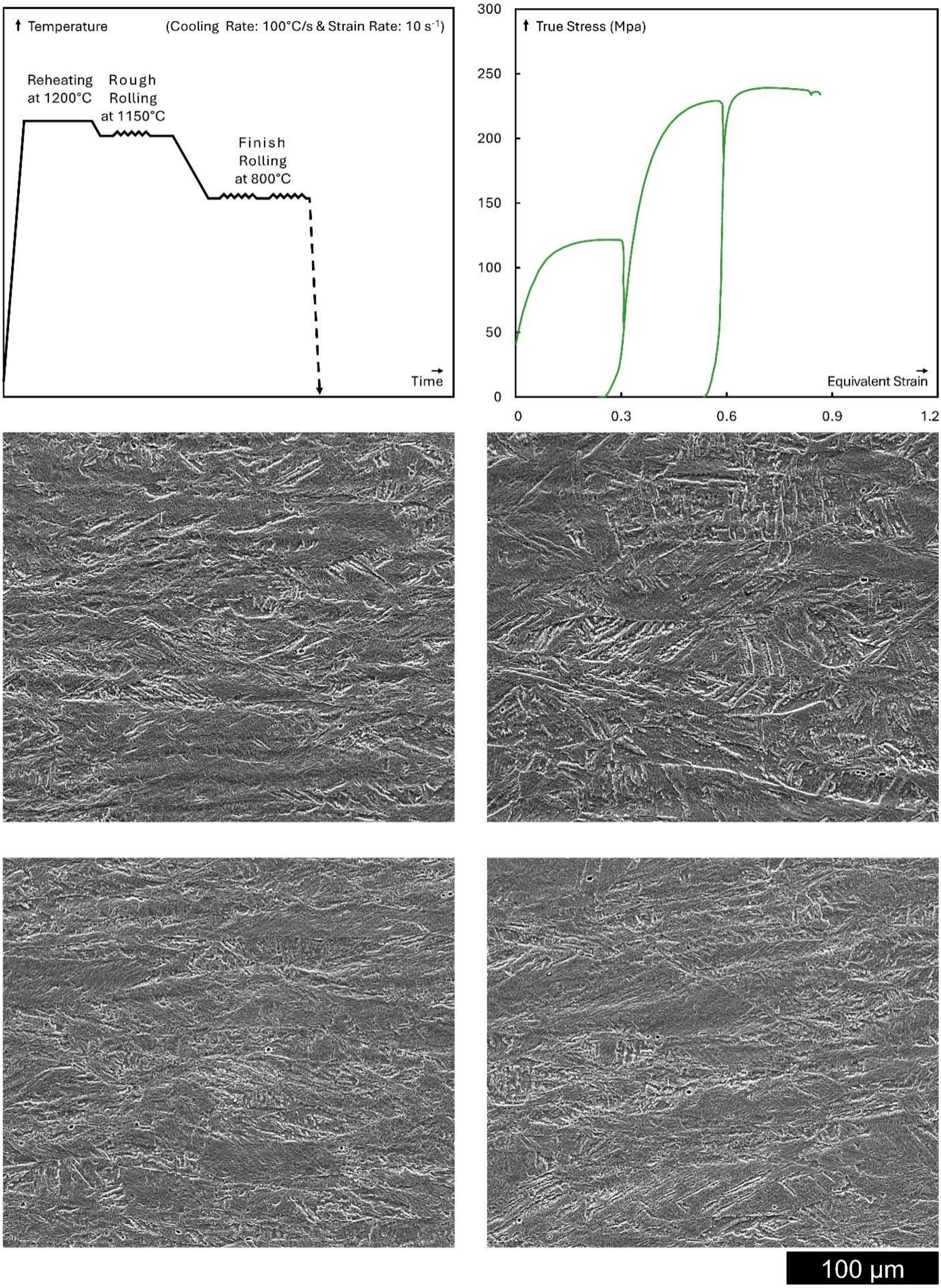

Figure I.17 SEM micrographs representing four separate fields-of-view of BA ↗ Ni microstructure, towards the long transverse direction, deformed at 800°C with a final strain reaching ~0.9 followed by rapid cooling at a rate of 100°C/s; the processing conditions schematic diagram along with the stress-strain flow curve are presented on top-left and top-right, respectively.

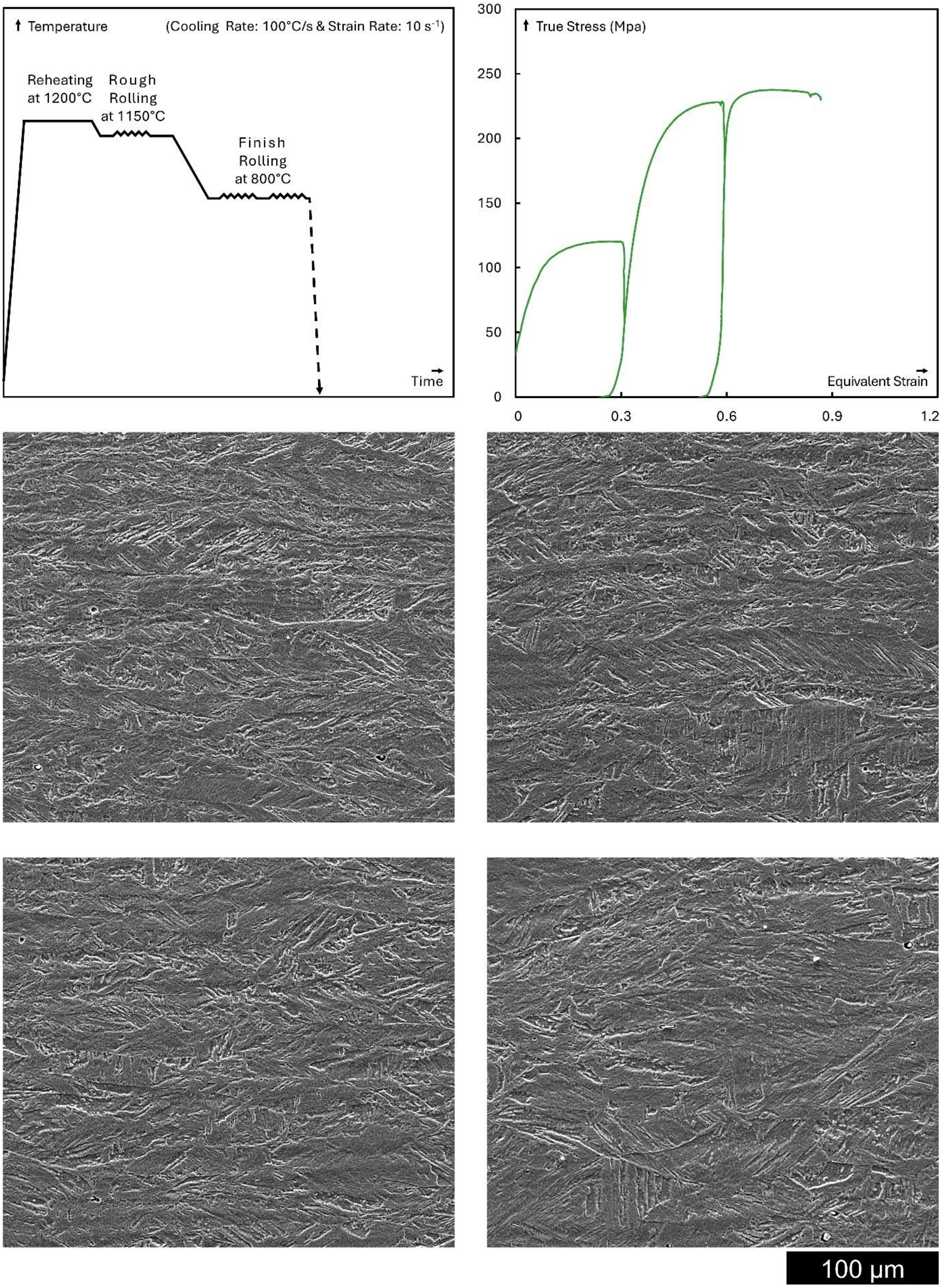

Figure I.18 SEM micrographs representing four separate fields-of-view of BA ↗ Mn microstructure, towards the long transverse direction, deformed at 800°C with a final strain reaching ~0.9 followed by rapid cooling at a rate of 100°C/s; the processing conditions schematic diagram along with the stress-strain flow curve are presented on top-left and top-right, respectively.

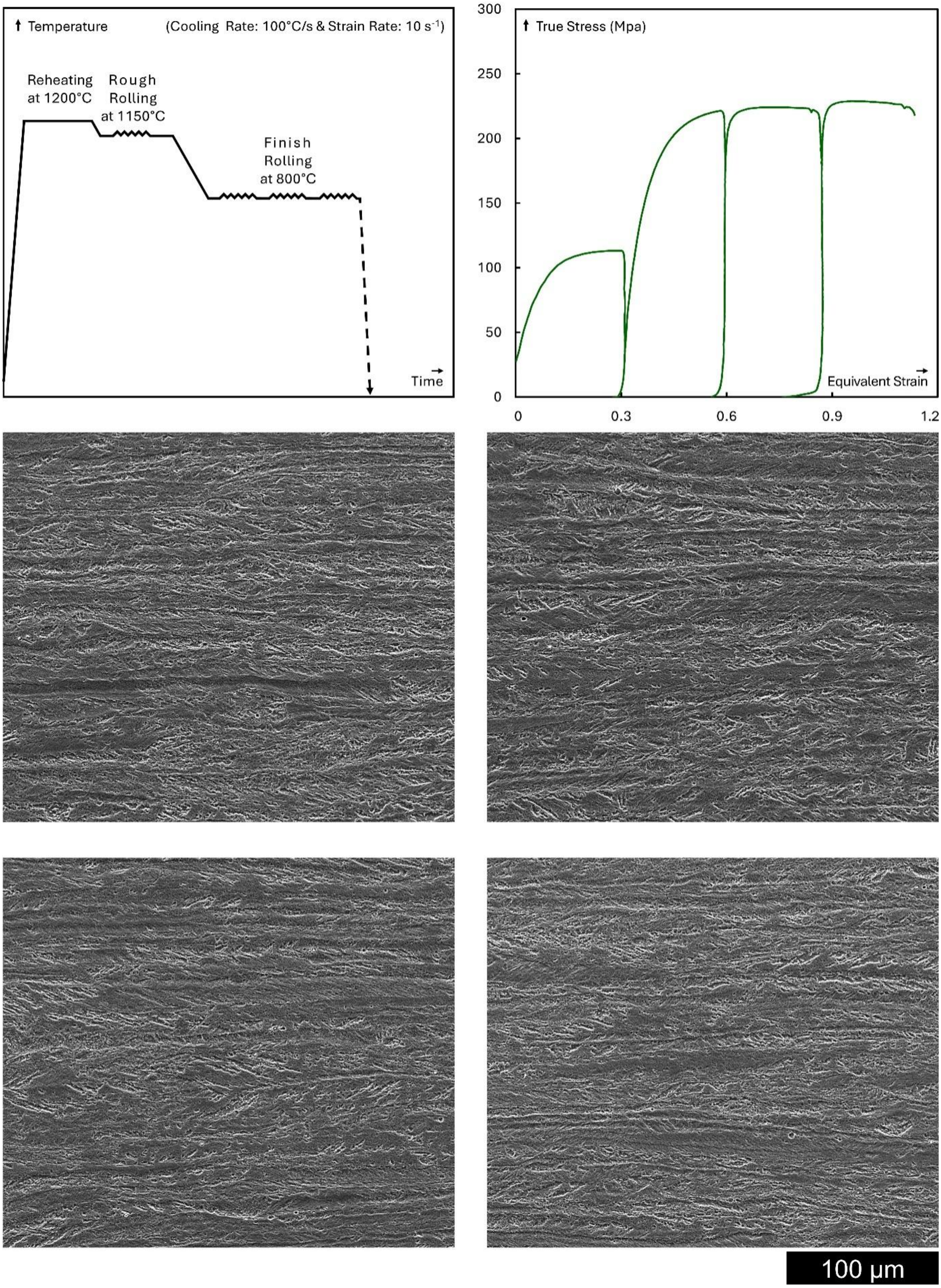

Figure I.19 SEM micrographs representing four separate fields-of-view of BA microstructure, towards the long transverse direction, deformed at 800°C with a final strain reaching ~1.2 followed by rapid cooling at a rate of 100°C/s; the processing conditions schematic diagram along with the stress-strain flow curve are presented on top-left and top-right, respectively.

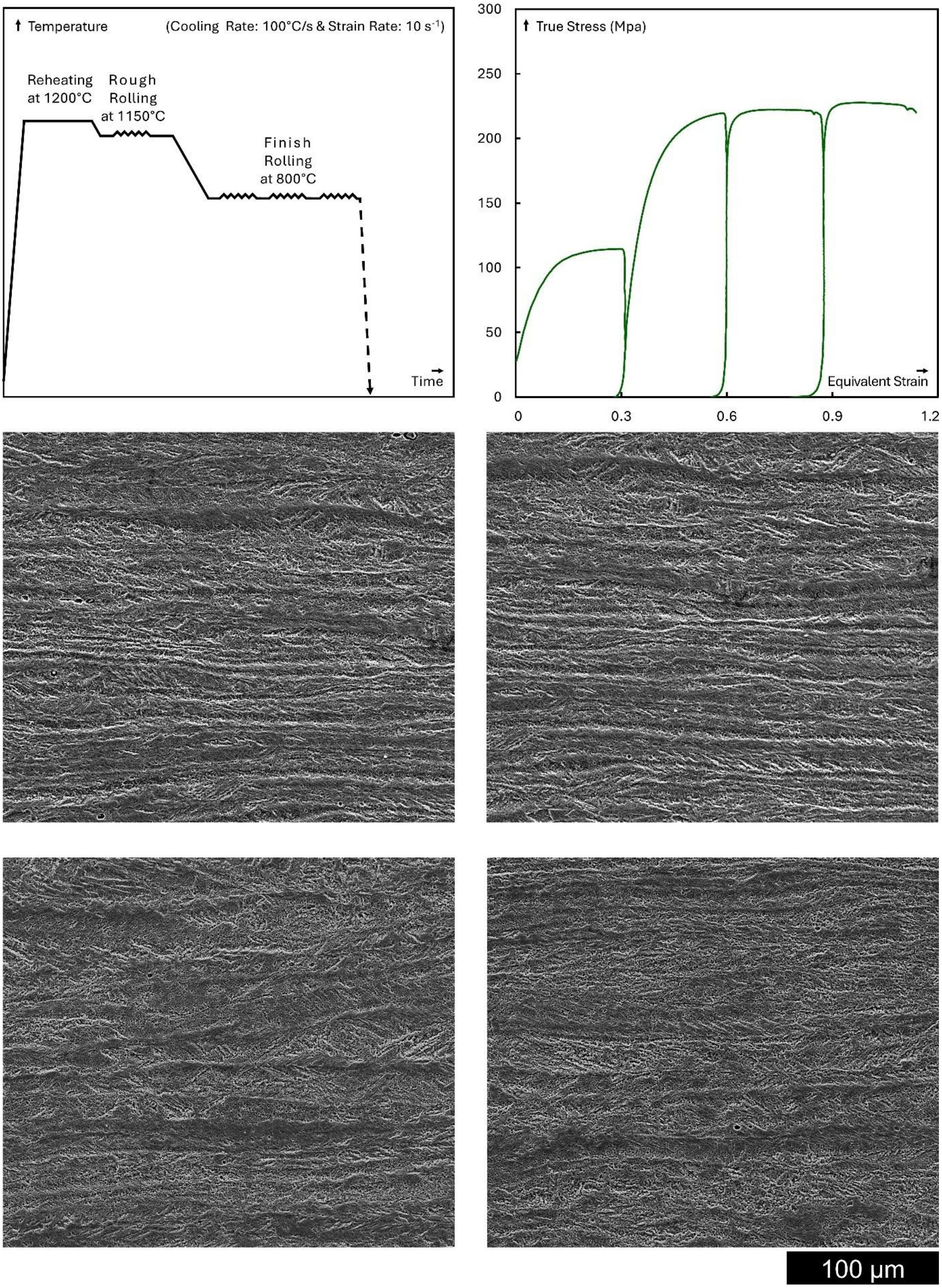

Figure I.20 SEM micrographs representing four separate fields-of-view of BA ↗ Ni microstructure, towards the long transverse direction, deformed at 800°C with a final strain reaching ~1.2 followed by rapid cooling at a rate of 100°C/s; the processing conditions schematic diagram along with the stress-strain flow curve are presented on top-left and top-right, respectively.

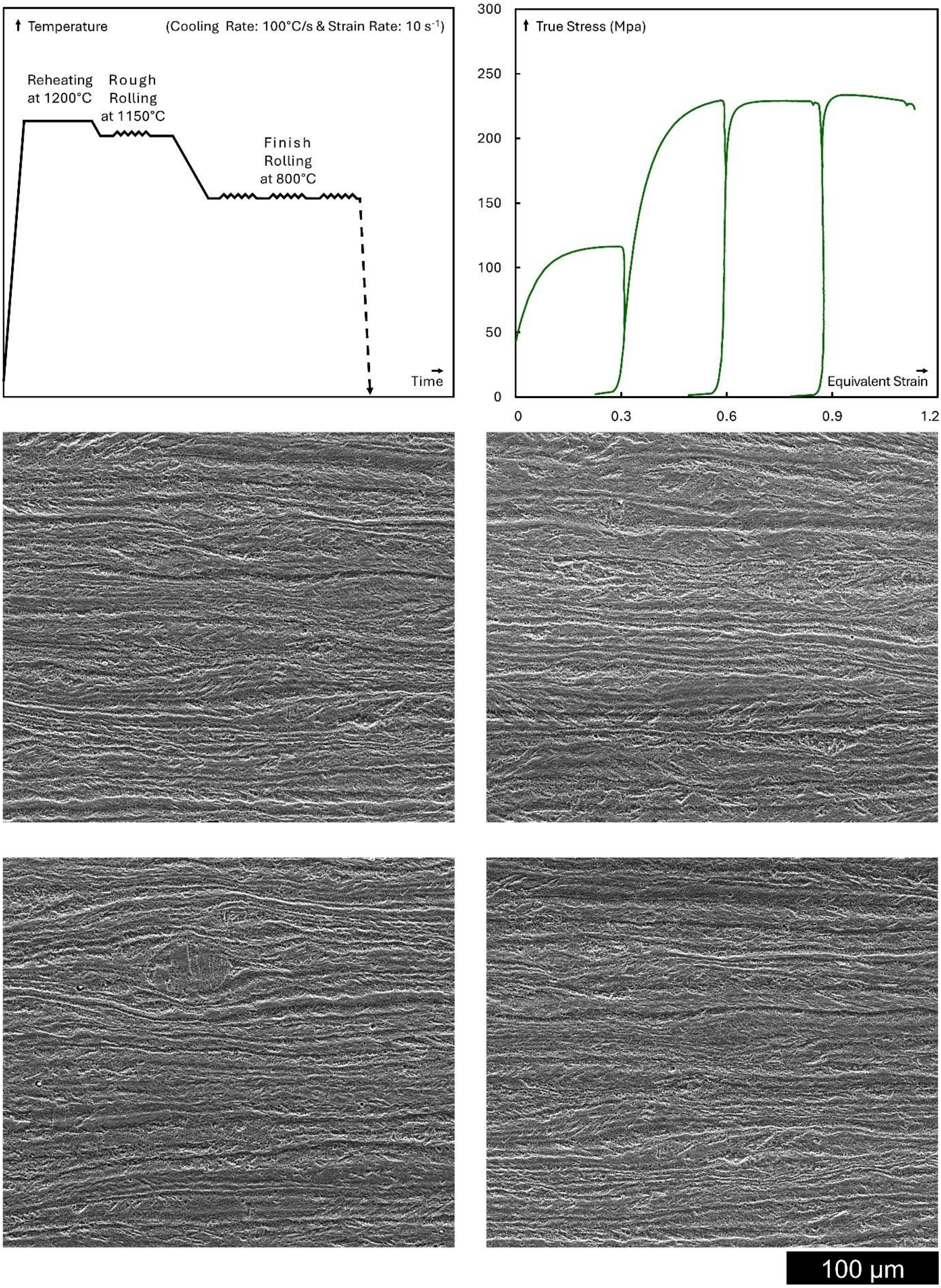

Figure I.21 SEM micrographs representing four separate fields-of-view of BA ↗ Mn microstructure, towards the long transverse direction, deformed at 800°C with a final strain reaching ~1.2 followed by rapid cooling at a rate of 100°C/s; the processing conditions schematic diagram along with the stress-strain flow curve are presented on top-left and top-right, respectively.

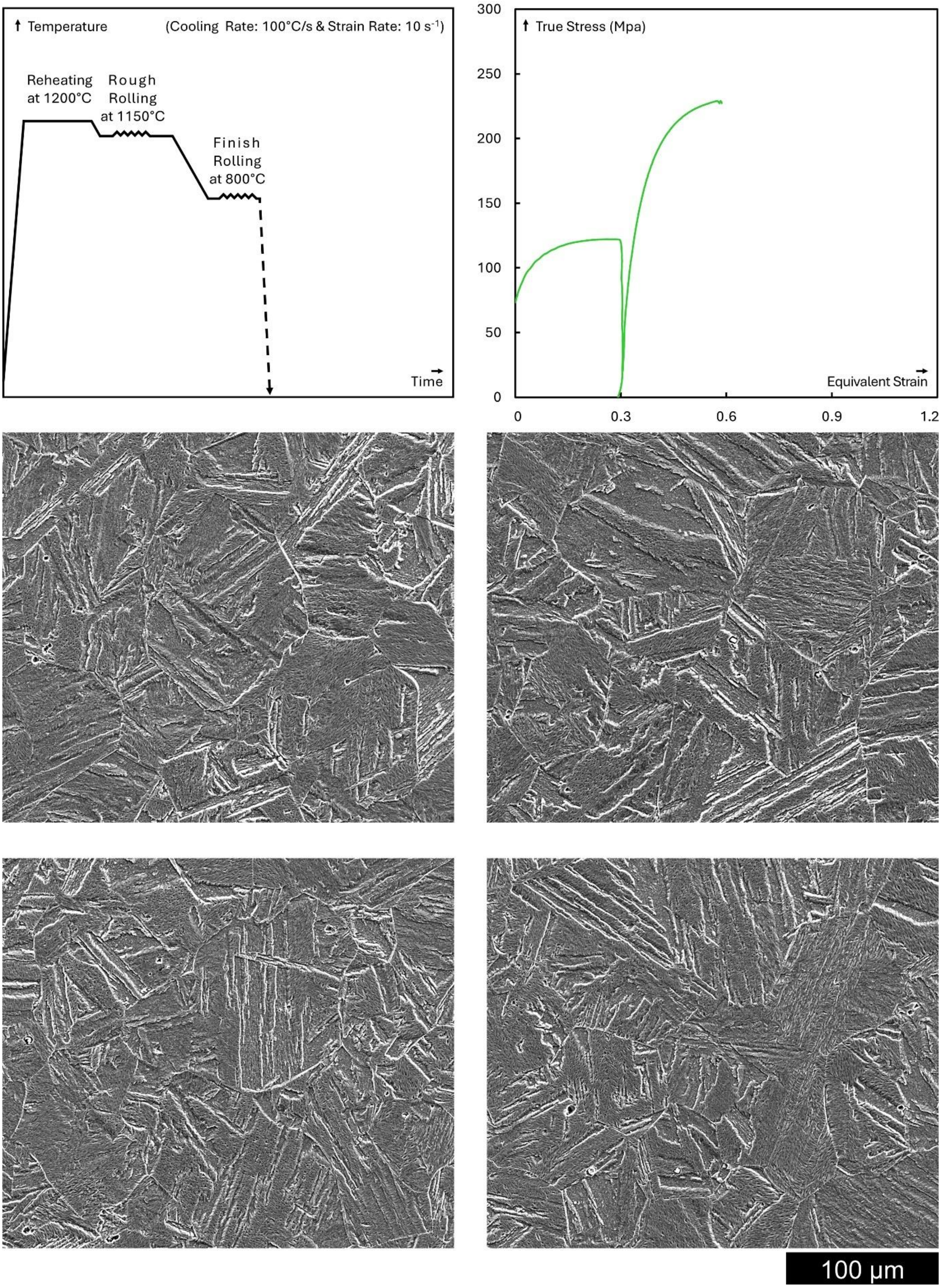

Figure I.22 SEM micrographs representing four separate fields-of-view of BA microstructure, towards the short transverse direction, deformed at 800°C with a final strain reaching ~0.6 followed by rapid cooling at a rate of 100°C/s; the processing conditions schematic diagram along with the stress-strain flow curve are presented on top-left and top-right, respectively.

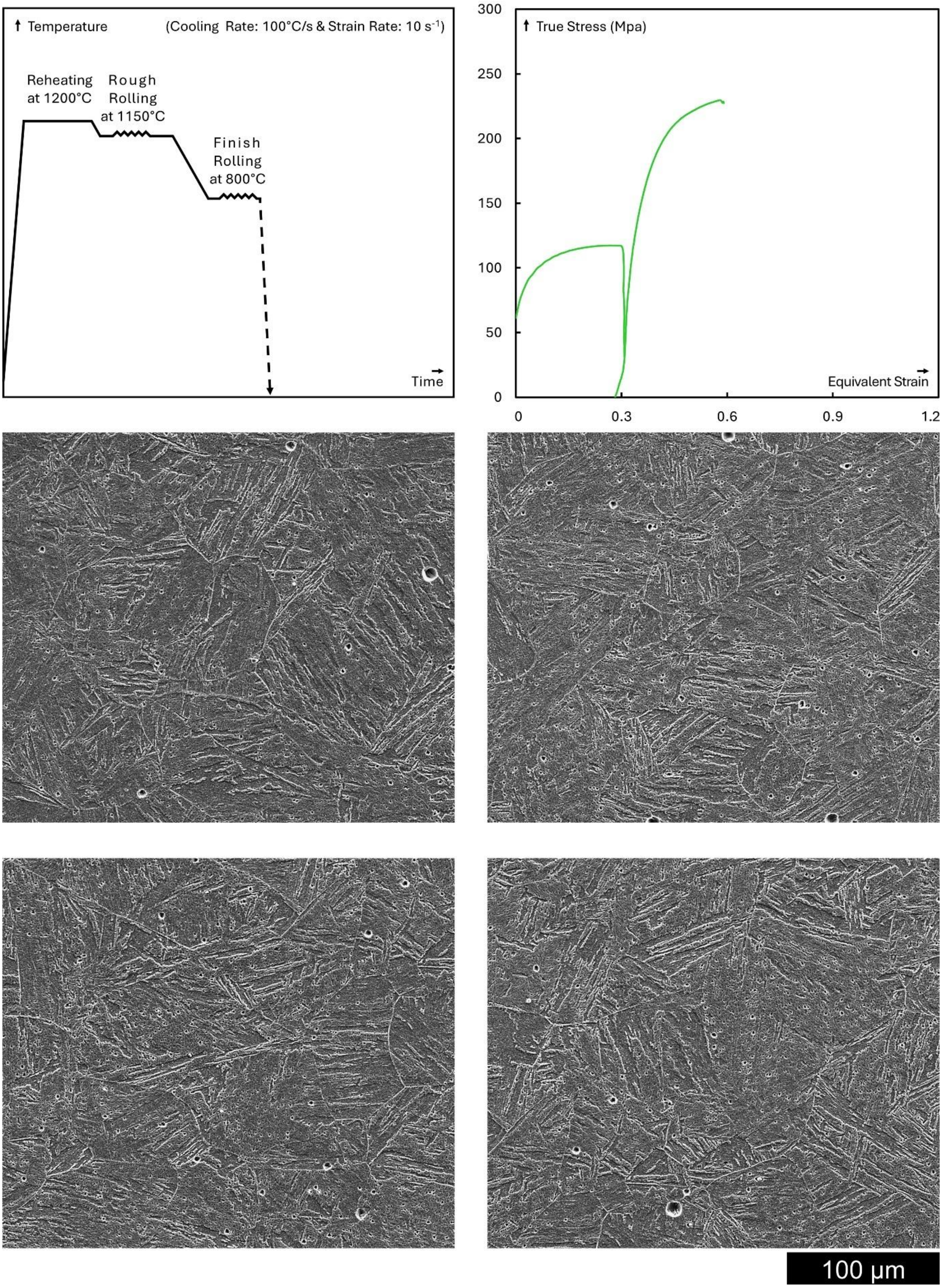

Figure I.23 SEM micrographs representing four separate fields-of-view of BA ↗ Ni microstructure, towards the short transverse direction, deformed at 800°C with a final strain reaching ~0.6 followed by rapid cooling at a rate of 100°C/s; the processing conditions schematic diagram along with the stress-strain flow curve are presented on top-left and top-right, respectively.

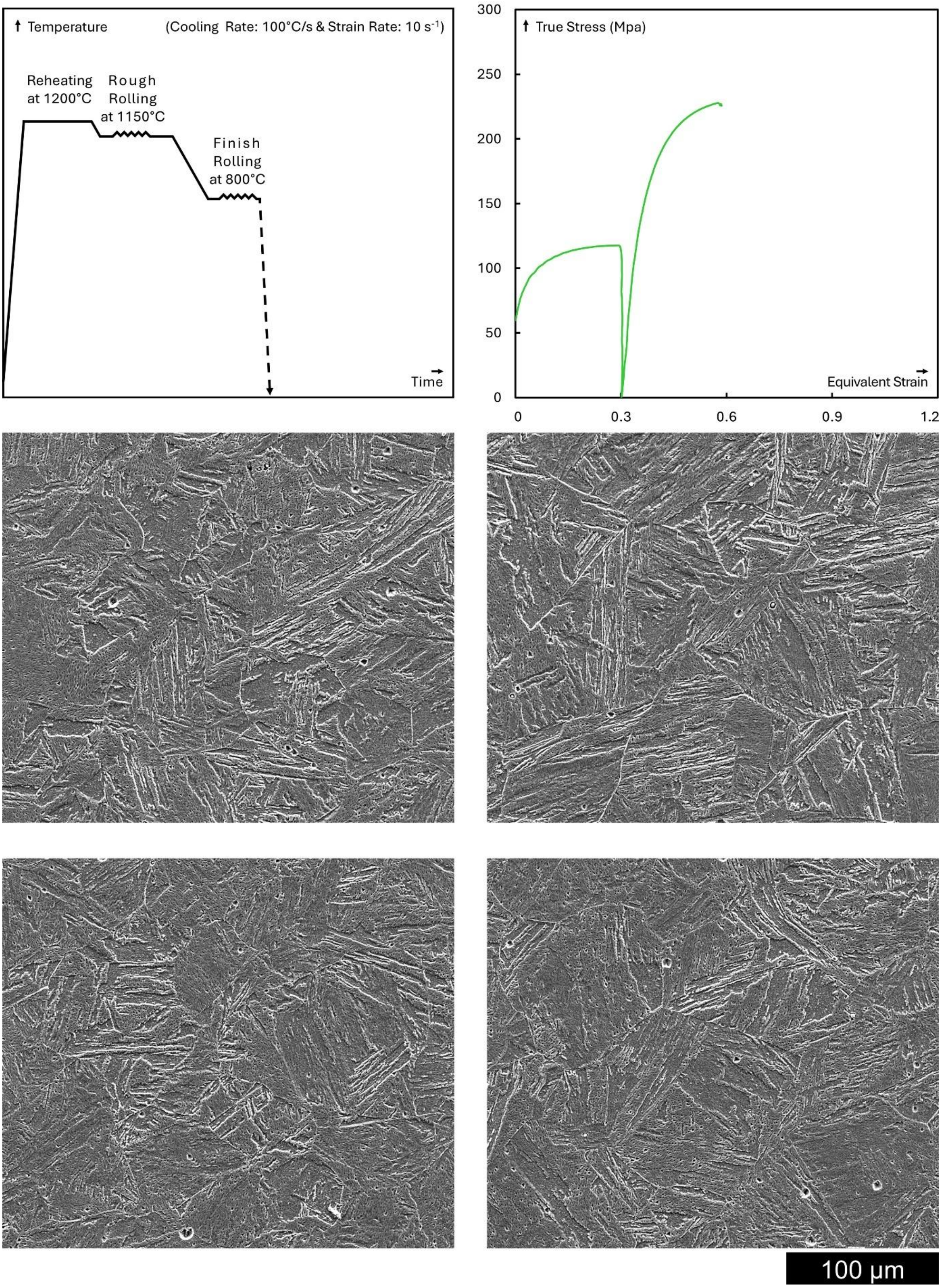

Figure I.24 SEM micrographs representing four separate fields-of-view of BA ↗ Mn microstructure, towards the short transverse direction, deformed at 800°C with a final strain reaching ~0.6 followed by rapid cooling at a rate of 100°C/s; the processing conditions schematic diagram along with the stress-strain flow curve are presented on top-left and top-right, respectively.

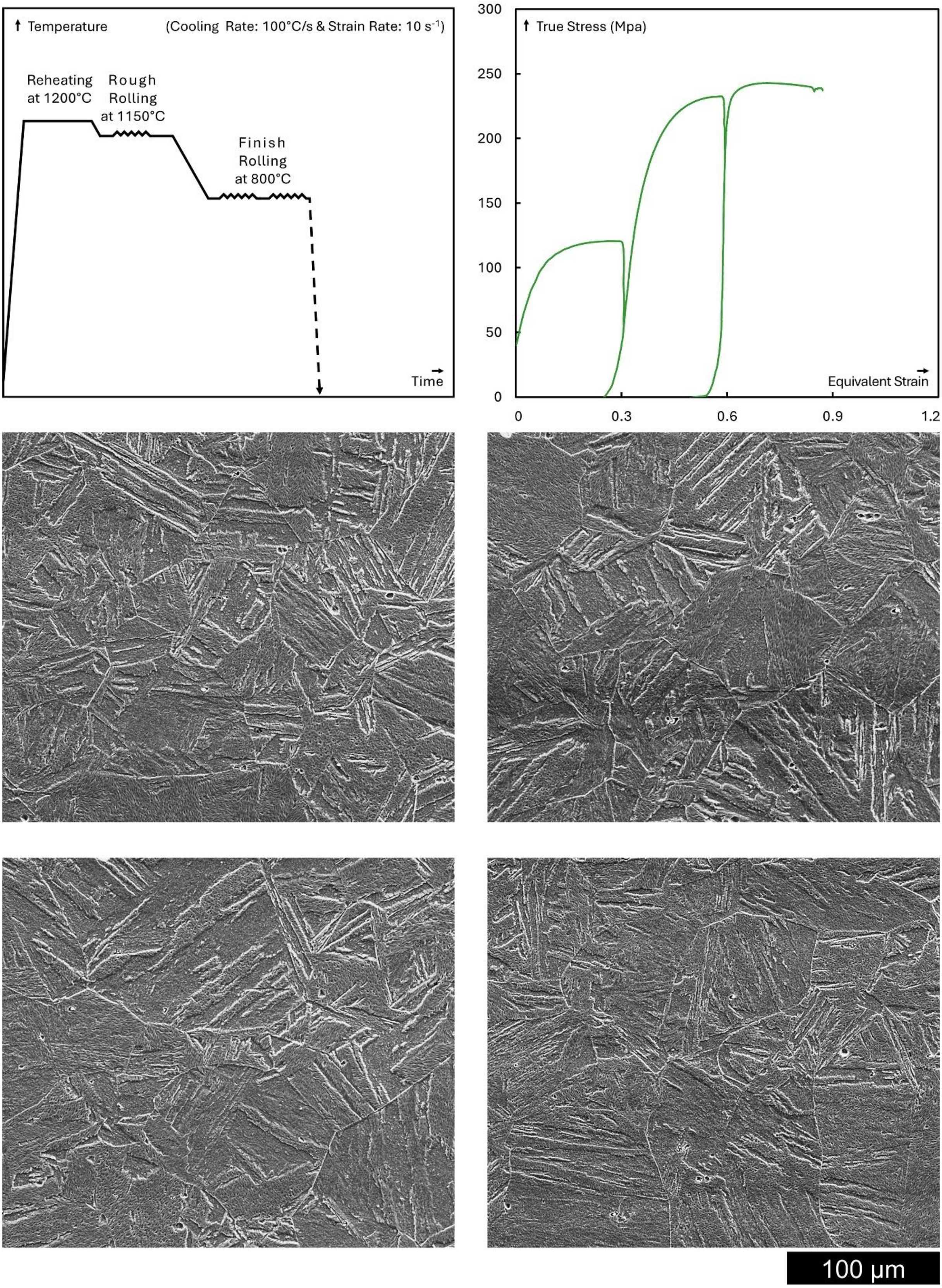

Figure I.25 SEM micrographs representing four separate fields-of-view of BA microstructure, towards the short transverse direction, deformed at 800°C with a final strain reaching ~0.9 followed by rapid cooling at a rate of 100°C/s; the processing conditions schematic diagram along with the stress-strain flow curve are presented on top-left and top-right, respectively.

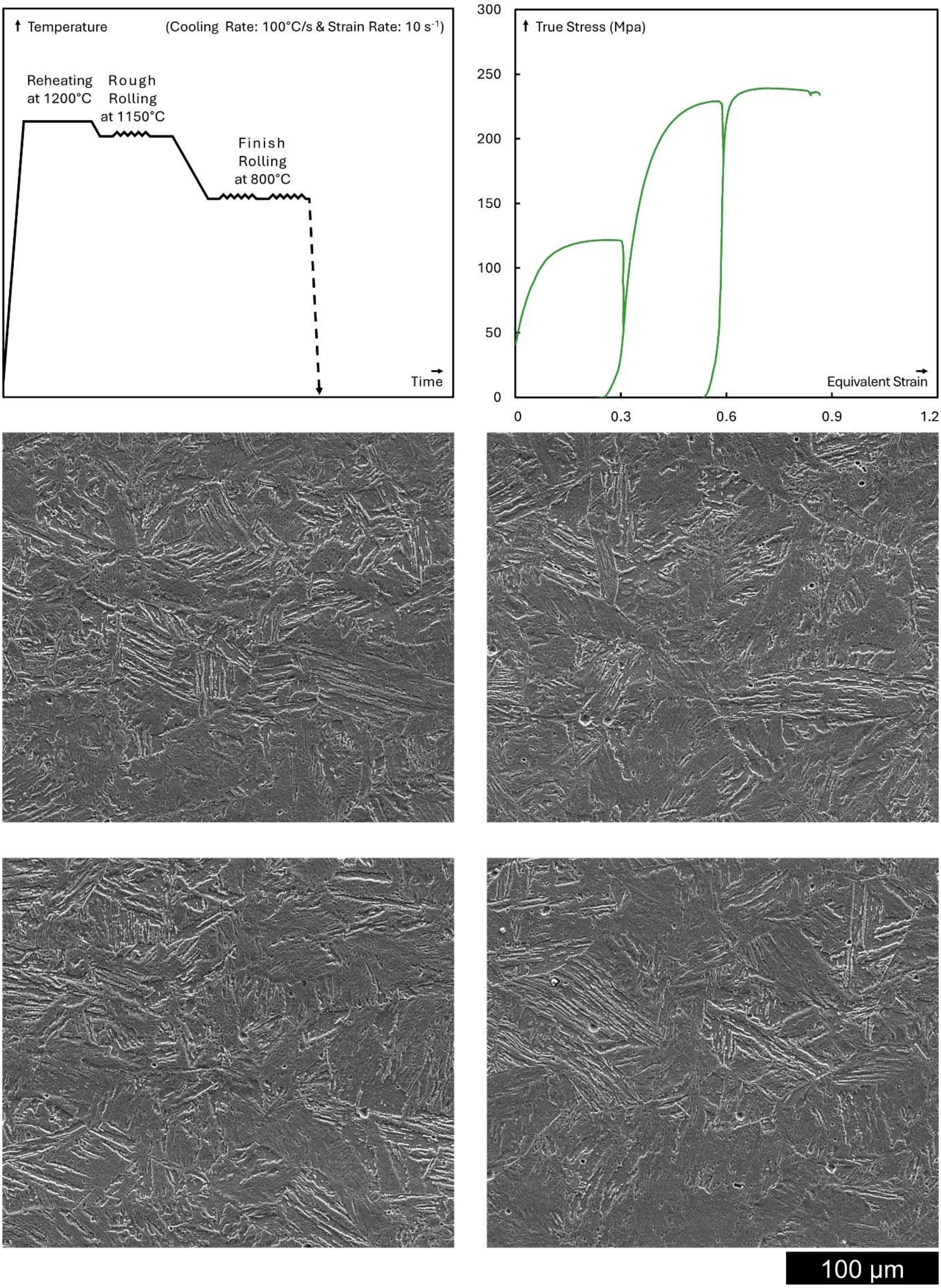

Figure I.26 SEM micrographs representing four separate fields-of-view of BA ↗ Ni microstructure, towards the short transverse direction, deformed at 800°C with a final strain reaching ~0.9 followed by rapid cooling at a rate of 100°C/s; the processing conditions schematic diagram along with the stress-strain flow curve are presented on top-left and top-right, respectively.

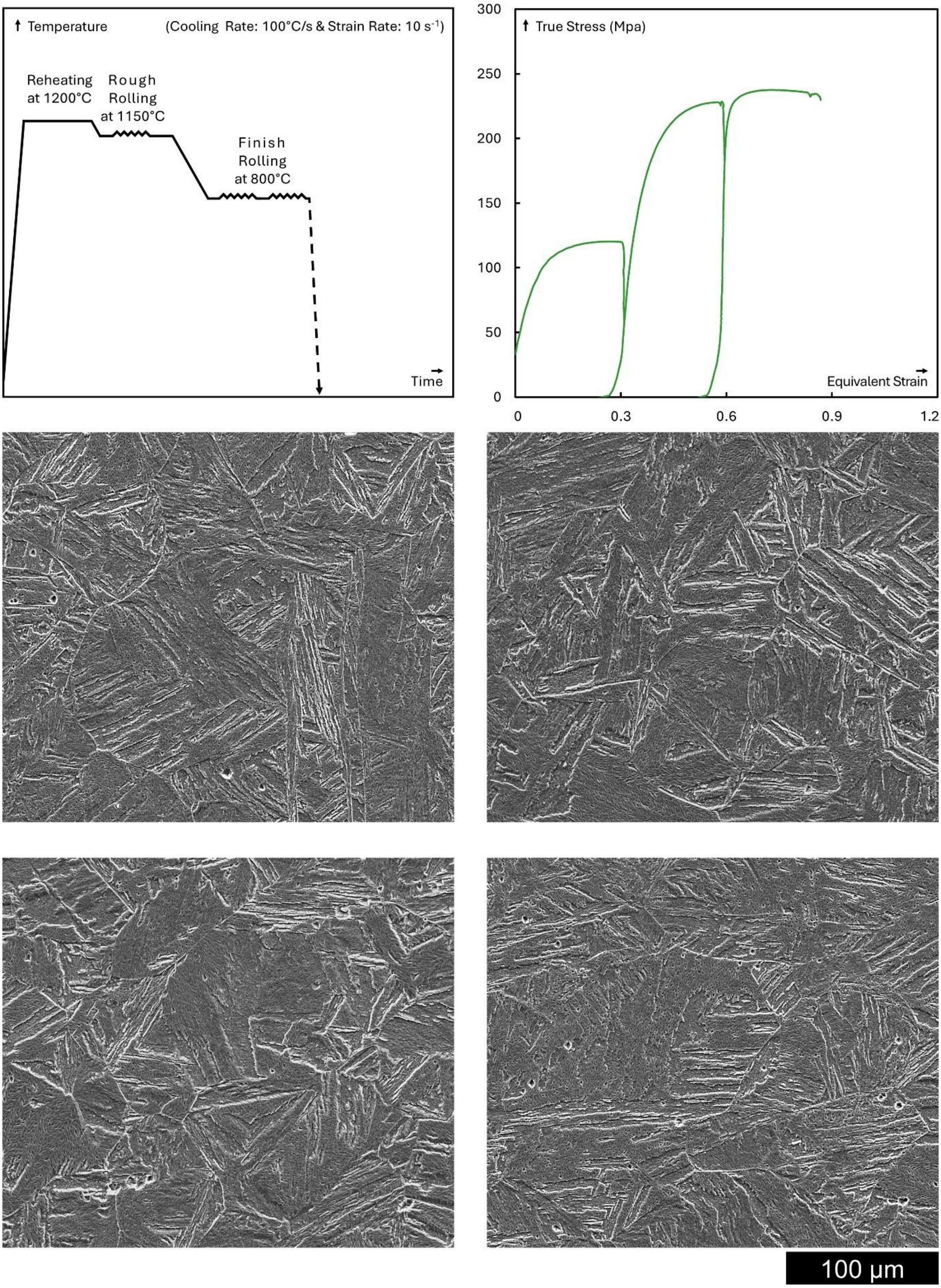

Figure I.27 SEM micrographs representing four separate fields-of-view of BA ↗ Mn microstructure, towards the short transverse direction, deformed at 800°C with a final strain reaching ~0.9 followed by rapid cooling at a rate of 100°C/s; the processing conditions schematic diagram along with the stress-strain flow curve are presented on top-left and top-right, respectively.

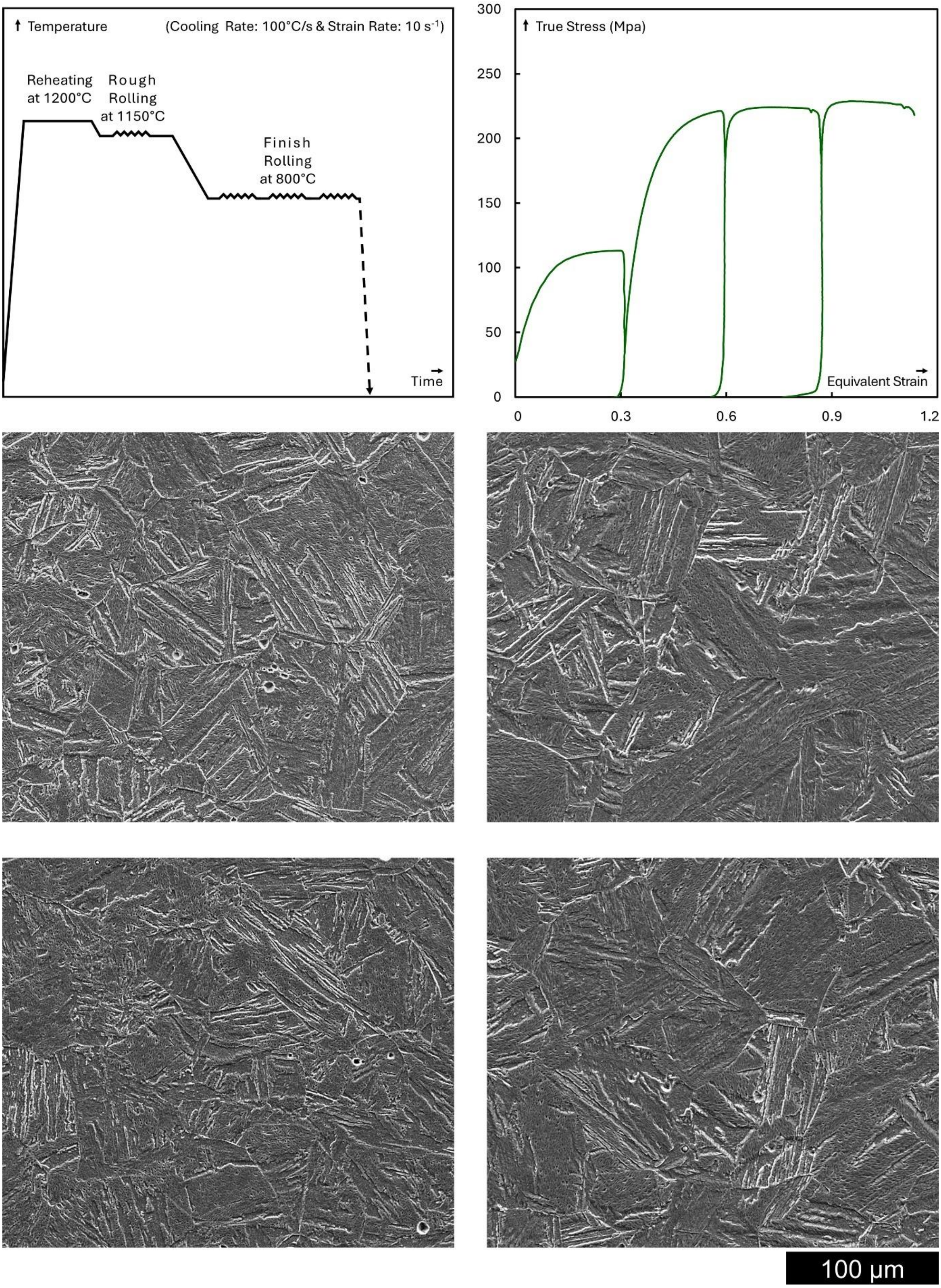

Figure I.28 SEM micrographs representing four separate fields-of-view of BA microstructure, towards the short transverse direction, deformed at 800°C with a final strain reaching ~1.2 followed by rapid cooling at a rate of 100°C/s; the processing conditions schematic diagram along with the stress-strain flow curve are presented on top-left and top-right, respectively.

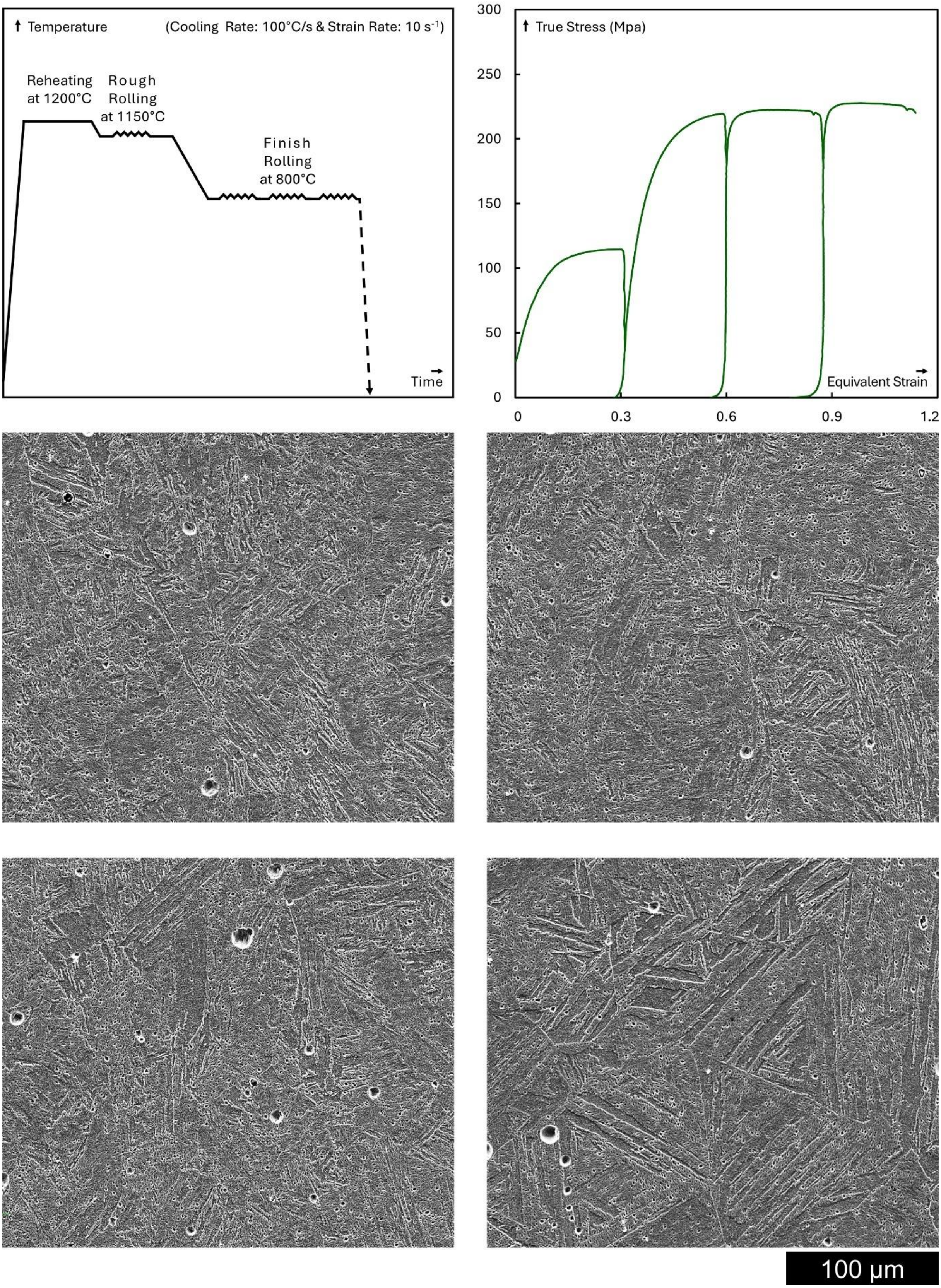

Figure I.29 SEM micrographs representing four separate fields-of-view of BA ↗ Ni microstructure, towards the short transverse direction, deformed at 800°C with a final strain reaching ~1.2 followed by rapid cooling at a rate of 100°C/s; the processing conditions schematic diagram along with the stress-strain flow curve are presented on top-left and top-right, respectively.

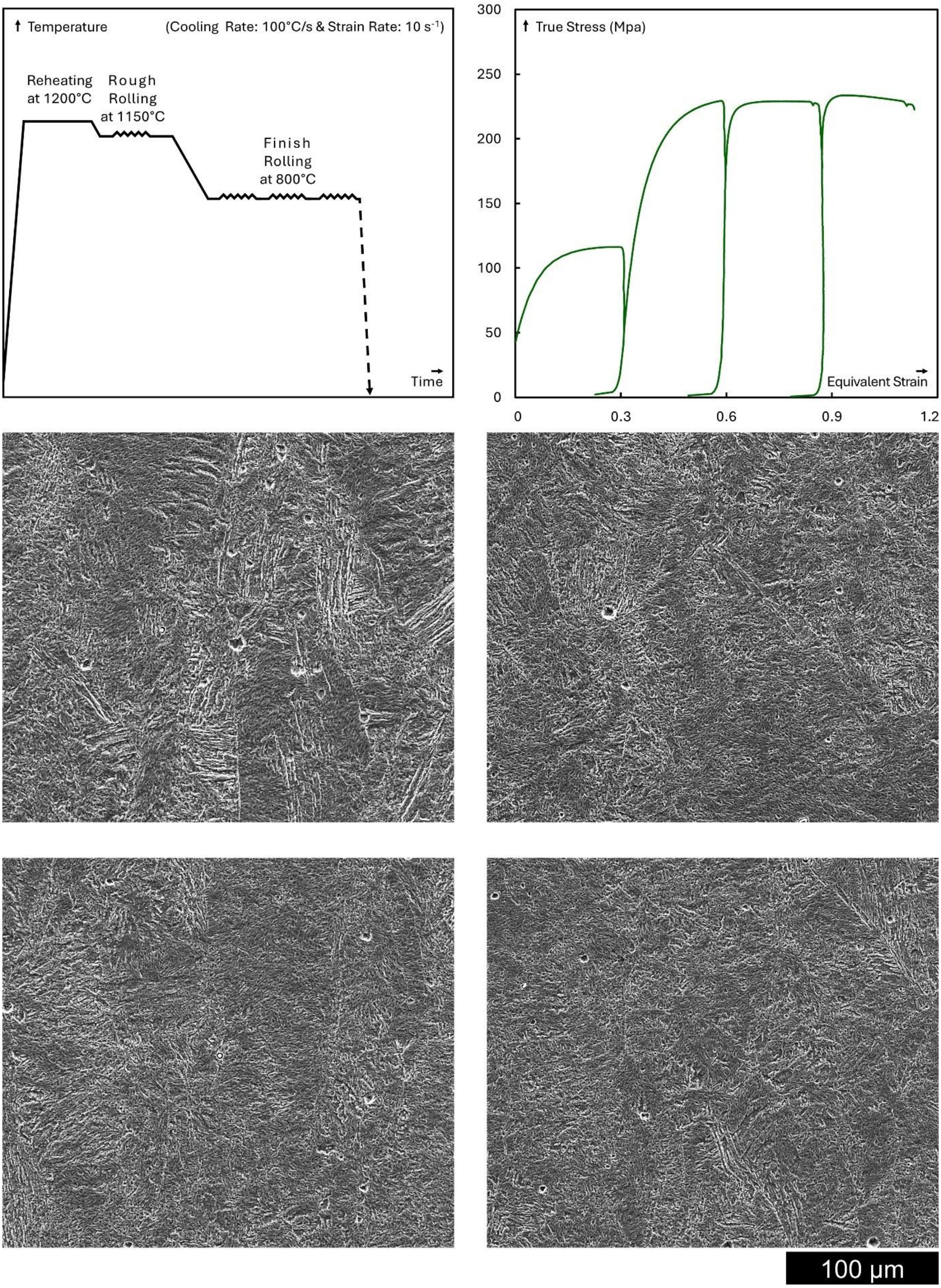

Figure I.30 SEM micrographs representing four separate fields-of-view of BA ↗ Mn microstructure, towards the short transverse direction, deformed at 800°C with a final strain reaching ~1.2 followed by rapid cooling at a rate of 100°C/s; the processing conditions schematic diagram along with the stress-strain flow curve are presented on top-left and top-right, respectively.